POLITECHNIKA POZNAŃSKA

Wydział Inżynierii Materiałowej i Fizyki Technicznej

ROZPRAWA DOKTORSKA

mgr inż. Maciej J. Szary

Struktura elektronowa i spinowa wybranych układów dwuwymiarowych – badanie DFT

Promotor
dr hab. Arkadiusz Ptak, prof. PP

Promotor pomocniczy
dr Marek T. Michalewicz

Poznań 2022

Finansowanie

Autor rozprawy doktorskiej był słuchaczem Interdyscyplinarnego Studium Doktoranckiego Nauka o Materiałach utworzonego przez Politechnikę Poznańską w ramach projektu *"Inżynier Przyszłości. Wzmocnienie potencjału naukowo-dydaktycznego Politechniki Poznańskiej"* finansowanego ze środków Europejskiego Funduszu Społecznego w ramach Programu Operacyjnego *"Kapitał Ludzki"*.

Zasoby obliczeniowe

Obliczenia, przeprowadzone w ramach badań wchodzących w skład rozprawy doktorskiej, zrealizowane zostały przy wsparciu: Polskiej Infrastruktury Gridowej PL-Grid, Interdyscyplinarnego Centrum Modelowania Matematycznego i Komputerowego Uniwersytetu Warszawskiego (ICM) oraz singapurskiego A*STAR Computational Resource Centre (A*CRC).

Podziękowania

Dziękuję Panu Profesorowi Arkadiuszowi Ptakowi za pomoc i opiekę.

Dziękuję Panu Profesorowi Marianowi Radnemu za opiekę naukową, wkład merytoryczny wniesiony we wspólne badania oraz liczne rady i uwagi. Jestem szczególnie wdzięczny za wspólne dyskusje, z których miałem przyjemność nauczyć się wiele, zarówno w kontekście aktualnie realizowanych badań, jak i ogólnego spojrzenia na naturę pracy naukowej.

Dziękuję Panu Doktorowi Markowi Michalewiczowi za opiekę naukową, sugestie badawcze oraz wnikliwe uwagi. Dziękuję również za liczne rady dotyczące rozwoju kariery naukowej.

Dziękuję Pani Doktor Barbarze Pieczyrak i Panu Profesorowi Leszkowi Jurczyszynowi za współpracę w moich pierwszych pracach badawczych.

Dziękuję Panu Doktorowi Michałowi Hermanowiczowi za pomoc w pierwszych obliczeniach oraz późniejsze liczne dyskusje o metodach obliczeniowych, pracy naukowej oraz życiu akademickim.

Dziękuję Rodzinie za pomoc, cierpliwość i poczucie humoru, w szczególności, Kaśce za logistykę, Mamie za żarty, Ojcu za prąd, Babci za liczne wałówki i Dziadkowi za troskę.

Dziękuję Przyjaciołom za zainteresowanie oraz liczne rady.

Streszczenie

Niniejsza rozprawa doktorska składa się z cyklu siedmiu artykułów naukowych poświęconych modyfikacji właściwości elektronowych i spinowych wybranych struktur dwuwymiarowych. Badanymi materiałami były monowarstwy ołowiu na powierzchniach półprzewodników (krzemu i germanu) i modyfikowane warstwy dwutellurku molibdenu, silicenu oraz germacenu. Układy te zostały zbadane z wykorzystaniem metod obliczeniowych opartych na teorii funkcjonału gęstości (z ang. *Density Functional Theory*, DFT) z użyciem fal płaskich oraz pseudopotencjałów.

Badania przeprowadzone w ramach rozprawy doktorskiej pokazały, że olbrzymie rozszczepienie spinowe elektronowych pasm metalicznych w układach Pb/Si(111)-1×1 oraz Pb/Ge(111)-1×1 może osiągnąć wartość rzędu setek meV, bądź zostać wygaszone w zależności od miejsca adsorpcyjnego ołowiu. Efekt ten jest wynikiem niezerowej wartości orbitalnego momentu pędu $\boldsymbol{L}$, który w połączeniu ze spinowym momentem pędu $\boldsymbol{S}$ prowadzi do rozszczepienia poprzez sprzężenie spin-orbita. Różnice obserwowane między konfiguracjami układu wynikają z charakteru oddziaływań na powierzchni. Powstające wiązania prowadzą do sprzężenia różnych orbitali atomowych i tym samym różnych wartości $\boldsymbol{L}$ dla stanów powierzchniowych. Analogiczne rozszczepienie wywołane adsorpcją Pb pokazano również dla układu Pb/germacen, dla którego faza 1×1 przewidziana została jako stabilna w oparciu o rachunek energii swobodnej oraz analizę widma fononów. Wpływ oddziaływań powierzchniowych na rozszczepienie spinowe został zbadany również dla słabo związanego układu Pb/$MoTe_2$. W tym przypadku oddziaływania powierzchniowe ograniczają się wyłącznie do sił van der Waalsa, jednakże złamana symetria inwersyjna prowadzi do olbrzymiego rozszczepienia spinowego stanów elektronowych zarówno w warstwie Pb jak i $MoTe_2$. Przeprowadzone badania ilustrują istotną rolę fizykochemii powierzchni w mechanizmie prowadzącym do rozszczepienia spinowego oraz wysoką zdolność do jego indukcji warstwami atomowymi metali ciężkich, co może znaleźć zastosowanie w spintronice.

Pokazano również, że małą aktywność chemiczną powierzchni $MoTe_2$ można zwiększyć poprzez naprężenie. Kontrolowana w ten sposób warstwa ułatwia zajście silnych interakcji na granicy układów $MoTe_2$/Ge(111)-1×1 oraz dla heterostruktury materiałów dwuwymiarowych silicen/$MoTe_2$. Powstałe wiązania mają istotny wpływ na stany elektronowe struktur w pobliżu poziomu Fermiego, a także na rozkład gęstości ładunku na granicy materiałów. W rezultacie naprężenie może mieć znaczący wpływ na właściwości struktury, więc powinno być brane pod uwagę przy projektowaniu układów elektrycznych bazujących na $MoTe_2$.

Słowa kluczowe: *struktura elektronowa, rozszczepienie spinowe, fizykochemia powierzchni, materiały dwuwymiarowe, german, krzem*

Abstract

This doctoral thesis comprises seven scientific articles on the modification of electronic and spin properties of selected two-dimensional structures. The research included monolayers of lead on semiconductor surfaces (silicon and germanium) and modified sheets of molybdenum ditelluride, silicene, and germanene. The systems were investigated using computational methods based on density functional theory (DFT) employing the plane-wave and pseudopotential methods.

The study predicts that the giant spin splitting of metallic bands in Pb/Si(111)-1×1 and Pb/Ge(111)-1×1 systems can reach values of hundreds of meV or be suppressed depending on the adsorption site of lead. The effect originates from non-zero values of the orbital angular momentum $\boldsymbol{L}$ present in the spin-split states, which in combination with the spin angular momentum $\boldsymbol{S}$ gives rise to a spin splitting facilitated directly by the spin-orbit coupling. The differences observed between configurations of the system are due to the character of chemical bonds facilitated at the surface, which couple different atomic orbitals, and thus give rise to different values of $\boldsymbol{L}$. A similar splitting caused by Pb adsorption was also predicted for the Pb/germanene system, for which phase 1×1 was shown stable based on the surface formation free energy and phonon spectra analysis. The impact of surface interactions on spin splitting has also been studied for the weakly-bonded system of Pb/$MoTe_2$. In this case, the surface interactions are predicted weak i.e, limited only to the van der Waals forces. However, the interface formation gives rise to a giant spin splitting of electronic bands in both the Pb and $MoTe_2$ layers. The conducted research illustrates the important role of surface interactions on spin splitting and also the high effectiveness of heavy-atomic layers in inducing the effect.

It has also been shown that the low chemical activity of $MoTe_2$ can be increased with the use of homogeneous tensile strain. The strain was shown to facilitate a strong chemical bonding at the interface of $MoTe_2$/Ge(111)-1×1 and for a heterostructure of two-dimensional materials silicene/$MoTe_2$. The resulting bonds have a significant impact on the electronic states of the system in the vicinity of the Fermi level, and also on the charge-density distribution on the interface. As a result, strain can have a significant impact on the electron properties of the structure. Hence, it should be accounted for when designing electronic devices based on $MoTe_2$.

Keywords: *electronic band structure, spin splitting, surface science, 2D materials, Germanium, Silicon*

Spis skrótów i oznaczeń

2DEG (ang. *2D electron gas*) – dwuwymiarowy gaz elektronowy

DFPT (ang. *Density Functional Perturbation Theory*) – perturbacyjna teoria funkcjonału gęstości

DFT (ang. *Density Functional Theory*) – teoria funkcjonału gęstości

DFT-D2 – półempiryczna poprawka oddziaływań dyspersyjnych Grimmego (człon C6)

DFT-D3 – półempiryczna poprawka oddziaływań dyspersyjnych Grimmego (człony C6 i C8)

DOS (ang. *density of states*) – gęstość stanów

FET (ang. *Field-Effect Transistor*) – tranzystor polowy

GGA (ang. *Generalized Gradient Approximation*) – uogólnione przybliżenie gradientowe potencjału XC

GSS (ang. *Giant Spin Splitting*) – gigantyczne rozszczepienie spinowe

HB strain (ang. *homogeneous biaxial strain*) – jednorodne dwuosiowe odkształcenie

HSE – hybrydowy funkcjonał XC Heyda-Scuseria-Ernzerhofa

IF (ang. *Impact Factor*) – wskaźnik cytowań

LCPAO (ang. *linear combination of pseudo-atomic orbitals*) – kombinacja liniowa pseudoorbitali atomowych

LDA (ang. *local density approximation*) – przybliżenie lokalnej gęstości potencjału XC

ML (ang. *monolayer*) – monowarstwa

NC, NCPP (ang. *norm-conserving pseudopotentials*) – pseudopotencjały typu NC; orbitale zbudowane są w bazie fal płaskich; założenia (i) energia prawdziwego orbitalu równa jest energi pseudoorbitalu, (ii) obie funkcje muszą być sobie równe poza zadanym promieniem odcięcia, (iii) wewnątrz odciętego obszaru obie funcje muszą dawać jednakowy ładunek

OAM (ang. *Orbital Angular Momentum*) – orbitalny moment pędu

PAW (ang. *Projector Augmented Wave*) – pseudopotencjały typu PAW; zachowują strukturę węzłową orbitali, ponieważ nie są budowane wyłącznie z fal płaskich

PBE – funkcjonał XC typu GGA z parametryzacją Perdew-Burke-Ernzerhofa

PBEsol – funkcjonał XC typu GGA z parametryzacją Perdew-Burke-Ernzerhofa dla powierzchni

PZ – funkcjonał XC typu LDA z parametryzacją Perdew-Zungera

QE – QUANTUM ESPRESSO

RB – Rashba-Bychkov

SAM (ang. *spin angular momentum*) – spinowy moment pędu

SBZ (ang. *surface Brillouin zone*) – powierzchniowa komórka Brillouina

JCR – Journal Citation Reports

SCF (ang. *self-consistent field*) – metoda pola samouzgodnionego

Sil – silicen

SJR – Scimago Journal & Country Rank

SOC (ang. *spin-orbit coupling*) – sprzężenie spin-orbita

TMD (ang. *Transition-Metal Dichalcogenide*) – chalkogenki metali przejściowych

TS-vdW – poprawka dyspersyjna Tkatchenko-Schefflera

US, USPP (ang. *ultrasoft pseudopotential*) – pseudopotencjały typu US; modyfikują warunek normalizacji potencjałów NC i wprowadzają poprawkę gęstości ładunku

VDOS (ang. *vibrational density of states*) – gęstość stanów fononowych

vdW – van der Waals

XC (ang. *exchange-correlation*) – oddziaływanie korelacyjno-wymienne

XDM (ang. *exchange-hole dipole moment*) – poprawka oddziaływań dyspersyjnych Becke

Spis treści

1. Forma rozprawy doktorskiej

Na niniejszą rozprawę doktorską składa się cykl siedmiu artykułów naukowych opublikowanych w recenzowanych czasopismach, których metryki śledzone są w bazach Journal Citation Reports (JCR), Scopus oraz Scimago Journal & Country Rank (SJR). Artykuły te są poświęcone modyfikacji właściwości elektronowych i spinowych wybranych struktur powierzchniowych oraz materiałów dwuwymiarowych. Ich lista wraz ze wskaźnikiem cytowań (IF) i CiteScore za rok 2021 oraz ich punktacją przyznaną przez Ministerstwo Edukacji i Nauki w 2021 roku (MEiN_{2021}) umieszczona jest poniżej:

P1 Barbara Pieczyrak*, **Maciej J. Szary**, Leszek Jurczyszyn, and Marian W. Radny*, *"Spin polarization of two-dimensional electronic gas decoupled from structural asymmetry environment"*, Physical Review B 93, 195318 (2016); $\text{IF}_{2021} = 3.908$, $\text{CiteScore}_{2021} = 6.9$, $\text{MEiN}_{2021} = 140$

P2 **Maciej J. Szary***, Barbara Pieczyrak, Leszek Jurczyszyn, Marian W. Radny*, *"Suppressed and enhanced spin polarization in the 1ML-Pb/Ge(111)-1×1 system"*, Applied Surface Science 466 224–229 (2019); $\text{IF}_{2021} = 7.392$, $\text{CiteScore}_{2021} = 12.1$, $\text{MEiN}_{2021} = 140$

P3 **Maciej J. Szary***, *"Role of coupling between surface orbitals in SOC enhanced spin splitting"*, Surface Science 684 12–17 (2019); $\text{IF}_{2021} = 2.07$, $\text{CiteScore}_{2021} = 3.9$, $\text{MEiN}_{2021} = 100$

P4 **Maciej J. Szary***, *"Giant Rashba spin splitting induced by heavy element adsorption at germanene"*, FlatChem 18 100141 (2019); $\text{IF}_{2021} = 5.829$, $\text{CiteScore}_{2021} = 6.3$, $\text{MEiN}_{2021} = 20$

P5 **Maciej J. Szary***, Marek T. Michalewicz, Marian W. Radny* *"Giant spin splitting induced by a symmetry-braking van der Waals interaction"*, Applied Surface Science 494 619–626 (2019); $\text{IF}_{2021} = 7.392$, $\text{CiteScore}_{2021} = 12.1$, $\text{MEiN}_{2021} = 140$

P6 **Maciej J. Szary***, Marek T. Michalewicz, Marian W. Radny* *"Bonding and electronics of the $MoTe_2$/Ge interface under strain"*, Physical Review B 95, 205421 (2017); $\text{IF}_{2021} = 3.908$, $\text{CiteScore}_{2021} = 6.9$, $\text{MEiN}_{2021} = 140$

P7 **Maciej J. Szary*** *"Bonding and electronics of the silicene/$MoTe_2$ interface under strain"*, Applied Surface Science 491 469–477 (2019); $\text{IF}_{2021} = 7.392$, $\text{CiteScore}_{2021} = 12.1$, $\text{MEiN}_{2021} = 140$

W artykule **P1** autor rozprawy doktorskiej wykonał rachunki potrzebne do sporządzenia rysunków 2a, 2b oraz 4 w oparciu o samodzielnie przygotowane pliki wsadowe. Autor napisał

również skrypty do programu gnuplot, które posłużyły do złożenia rysunków 2 i 4. Ponadto, autor brał udział w dyskusji wyników przed napisaniem manuskryptu oraz w przygotowaniu odpowiedzi na recenzje.

W artykule **P2** autor rozprawy doktorskiej wykonał rachunki potrzebne do sporządzenia rysunków 2–5 oraz tabel 1 i 2 w oparciu o samodzielnie przygotowane pliki wsadowe. Napisał także skrypty do programu gnuplot, które zostały użyte do przygotowania rysunków 1 i 5. Autor miał znaczący wkład w interpretację uzyskanych wyników, napisał również pierwszą wersję manuskryptu oraz brał udział w jego kolejnych rewizjach. Odpowiedzialny był za wysłanie manuskryptu, korespondencję z edytorem oraz przygotowanie pierwszej wersji odpowiedzi na uwagi recenzentów. Uczestniczył również w pracach uzupełniających przygotowaną odpowiedź.

W artykułach **P5** i **P6** autor rozprawy jest współpomysłodawcą badań i miał znaczący wkład w interpretację uzyskanych wyników. Był odpowiedzialny za wykonanie wszystkich obliczeń oraz opracowanie wszystkich danych przedstawionych w artykułach. Napisał pierwszą wersję obu manuskryptów oraz brał udział w ich kolejnych poprawkach. Ponadto, autor odpowiedzialny był za wysłanie manuskryptów i korespondencję z edytorami. Przygotował pierwsze wersję odpowiedzi na uwagi recenzentów oraz brał aktywny udział w przygotowaniu ich finalnej formy.

Autor rozprawy doktorskiej jest jedynym autorem artykułów **P3**, **P4** i **P7**. Oznacza to, że jest on pomysłodawcą badań, wykonawcą wszystkich obliczeń, osobą odpowiedzialną za opracowanie wyników i ich interpretację, wyłącznym autorem tekstów oraz osobą odpowiedzialną za przeprowadzenie artykułów przez proces recenzji.

2. Motywacja i cele

Rozwój mikroelektroniki to jedno z największych osiągnięć XX wieku. Jej postęp zrewolucjonizował wiele gałęzi nauki i techniki pozwalając m.in. na automatyzację i cyfryzację przemysłu oraz rozwój technologii komunikacyjnych. Elektronika stała się integralną częścią większości aspektów ludzkiego życia. Na skutek tego jej rynek stale rośnie, podobnie jak zapotrzebowanie na postępującą miniaturyzację oraz nowe energooszczędne rozwiązania [1]. Krzem jest głównym materiałem półprzewodnikowym stosowanym obecnie w elektronice [2]. Jest to skutek m.in. jego stosunkowo dużej dostępności oraz rozwiniętego procesu technologicznego, pozwalającego na produkcję wysokiej jakości kryształów [3–5]. Jednakże materiał ten jest obarczony również ograniczeniami, które sprawiają, że postęp elektroniki staje się systematycznie coraz trudniejszy [6].

Integracja większej liczby tranzystorów w jeden układ scalony pozwala na zwiększenie jego szybkości przetwarzania informacji. Jednakże, wzrost ten jest przede wszystkim zdeterminowany przez mobilność nośników ładunku w materiale półprzewodnikowym, z którego wykonany jest tranzystor. Krzem charakteryzuje się wysoką ruchliwością elektronów, ale również niską ruchliwością dziur [3, 7, 8], co istotnie ogranicza parametry opartych na nim układów. Kolejnym problemem elektroniki krzemowej jest relatywnie niski próg temperatury, powyżej którego jej elementy przejawiają widoczny spadek wydajności [9, 10]. W przypadku urządzeń dużej mocy i elektroniki wysokotemperaturowej narzuca to konieczność użycia kosztownych metod pasywnego lub aktywnego chłodzenia [11–13], a w skrajnych przypadkach zastosowania innych materiałów niż krzem [14, 15]. Krzem posiada również skośną przerwę energetyczną [16]. Przyczynia się to do mało wydajnej generacji światła, co zawęża możliwości wykorzystania tego materiału w optoelektronice [17–19]. W konsekwencji tych ograniczeń, badania materiałów na potrzeby elektroniki stanowią jedną z największych gałęzi inżynierii materiałowej.

Jednym z potencjalnych rozwiązań aktualnych problemów elektroniki jest znalezienie materiałów pozwalających na jej ewolucję w spintronikę. Ta ostatnia stara się przezwyciężyć ograniczenia materiałowe krzemu poprzez zastąpienie ładunku polaryzacją spinu jako nośnika informacji. Dzięki temu układy spintroniczne powinny charakteryzować się wyższą wydajnością przy mniejszym poborze mocy. Jednym z głównych wyzwań stojących przed spintroniką jest uzyskanie i transport spolaryzowanych spinowo elektronów w temperaturze pokojowej [20, 21]. To wymaga (i) dużego rozszczepienia spinowego (>100 meV) metalicznych pasm na

(ii) powierzchni półprzewodnika [22]. Pierwszy punkt związany jest z efektywnym transportem, natomiast drugi jest konieczny ze względu na to, że duży prąd płynący przez metaliczne podłoże zaburzyłby spolaryzowany spinowo sygnał na powierzchni.

Spinowe rozszczepienie pasm elektronowych występuje w układach niemagnetycznych, gdy symetria inwersyjna struktury krystalicznej zostaje złamana przez zewnętrzne pole elektryczne najczęściej będące wynikiem obecności powierzchni [23–27]. Dla większości układów efekt ten jest niewielki (zwykle między 0,01 a 1 meV), jednak dla niektórych struktur może on osiągać wartości powyżej 100 meV. W takich przypadkach nazywa się go gigantycznym rozszczepieniem spinowym (ang. *Giant Spin Splitting*, GSS). GSS zaobserwowane zostało w wielu układach pokrytych warstwami ciężkich atomów [28–35], wliczając powierzchnie popularnych półprzewodników – Si(111) oraz Ge(111) [22, 24, 26, 36].

W oryginalnej interpretacji GSS, zaproponowanej w modelu Rashby-Bychkova (RB, lub po prostu Rashby) [37], spin elektronu oddziałuje z efektywnym polem magnetycznym wynikającym z ruchu elektronu w polu elektrycznym, co prowadzi do rozszczepienia analogicznego do efektu Zeemana. Model RB przewiduje, m.in. zniesienie degeneracji spinowej oraz chiralną strukturę wektora spinu. Efekty te zostały eksperymentalnie zweryfikowane dla stanów powierzchniowych metali [38–41], izolatorów topologicznych [42] oraz heterostruktur ze złamaną symetrią inwersyjną [43]. Jednakże, pomimo licznych sukcesów, model RB pozostawił wiele niewyjaśnionych problemów. Po pierwsze, przewidywane w nim wartości energii rozszczepienia pasm są często znacznie mniejsze od wielkości mierzonych eksperymentalnie np. $\sim 10^5$ razy mniejsze dla stanów na powierzchni Au (111) [38]. Po drugie, nie tłumaczy on jednoznacznie dlaczego efekt obserwowany jest wyłącznie w materiałach zawierających atomy pierwiastków o dużej masie atomowej [38–40]. W celu rozwinięcia modelu zasugerowano wiele poprawek m.in. uwzględnienie: iloczynu gęstości ładunku i gradientu potencjału wzdłuż normalnej do powierzchni [22, 44] oraz gradientu pola krystalicznego w jej płaszczyźnie [41, 45, 46]. Jednak żadna ze sugerowanych zmian nie pozwoliła na wyjaśnienie wszystkich aspektów zjawiska, co przyczyniło się do sformułowania jego alternatywnego opisu. W nowym ujęciu zaproponowanym przez Kima et al. [23, 47, 48] rozszczepienie spinowe wynika z niezerowego orbitalnego momentu pędu (ang. *Orbital Angular Momentum*, OAM), który w sprzężeniu ze spinowym momentem pędu oraz polem elektrycznym na powierzchni może być źródłem rozszczepienia rzędu setek meV [25–27].

Innym potencjalnym rozwiązaniem problemów technologii krzemowej jest oparcie nowych rozwiązań na materiałach dwuwymiarowych (ang. *two-dimensional*, 2D). Ze względu na unikatowe właściwości i postęp w ich wytwarzaniu, heterostruktury 2D zyskały duże zainteresowanie w obszarze nanotechnologii, spintroniki, elastycznej elektroniki i magazynowania energii [49–55]. Układy oparte na grafenie, silicenie, germacenie i chalkogenkach metali przejściowych (ang. *Transition-Metal Dichalcogenide*, TMD) stanowią atrakcyjne platformy dla tranzystorów polowych (ang. *Field-Effect Transistor*, FET) i przestrajalnych złącz

metal-półprzewodnik. Pokazano, że zewnętrzne pole elektryczne może zwiększyć siłę oddziaływania między warstwami i kontrolować rozmiar bariery Schottky'ego w heterostrukturach grafen/MoS_2 [56], silicen/MoS_2 [57] i germacen/MoS_2 [58]. Ponadto, dla układów MoS_2/Nb_2CO_2 i MoS_2/Nb_2CF_2, wykazano kontrolowany rozmiar przerwy energetycznej [59]. Na heterostrukturze silicen/MoS_2 wyprodukowano działający tranzystor typu FET [60, 61]. Natomiast grafen/MoS_2/grafen został użyty w wysokowydajnym fotodetektorze [62]. W wymienionych badaniach [56–62] oddziaływania między warstwami materiałów 2D traktowane są jako słabe tzn. ograniczone do oddziaływań van der Waalsa (vdW). Jednakże, w niektórych warunkach silne wiązania chemiczne mogą mieć miejsce na granicy tych materiałów, co może mieć istotne znaczenie dla ich właściwości elektrycznych. Problem ten został częściowo omówiony w przypadku silicenu i germacenu na MoS_2 [63]. Zmiany rozkładu gęstości ładunku zaobserwowane między warstwami sugerowały lokalny charakter oddziaływań na granicy warstw. To, w połączeniu z pokryciem powierzchni ciężkimi atomami, powinno, w myśl modelu Kima, pozwolić również na funkcjonalizację heterostruktur materiałów 2D na potrzeby spintroniki.

W ramach niniejszej rozprawy doktorskiej zostały przeprowadzone badania obliczeniowe, oparte na teorii funkcjonału gęstości (ang. *density functional theory*, DFT), których przedmiotem były powierzchnie krzemu oraz germanu pokryte monowarstwą ołowiu Pb/Si(111)-1$\times$1, Pb/Ge(111)-1$\times$1, oraz heterostruktur $MoTe_2$/Ge(111)-1$\times$1, Pb/$MoTe_2$, silicen/$MoTe_2$ i Pb/germacen. Zrealizowane badania miały następujące cele:

1. zbadanie mechanizmu odpowiedzialnego za rozszczepienie spinowe wywołane adsorpcją ołowiu na powierzchni wybranych materiałów;
2. określenie relacji między obserwowanym rozszczepieniem spinowym a oddziaływaniami mającymi miejsce na powierzchni układu;
3. zbadanie roli oddziaływań vdW w kontekście łamania symetrii inwersyjnej w heterostrukturach materiałów 2D;
4. zbadanie stabilności faz Pb na powierzchni germacenu oraz wpływu Pb na strukturę pasmową warstwy;
5. zbadanie wpływu naprężenia rozciągającego na aktywność chemiczną warstwy $MoTe_2$;
6. zbadanie wpływu naprężenia rozciągającego na właściwości elektronowe heterostruktury silicen/$MoTe_2$.

3. Metody

Badania w ramach rozprawy doktorskiej zostały przeprowadzone z wykorzystaniem metod obliczeniowych opartych na teorii funkcjonału gęstości (DFT) zaimplementowanych w pakiecie QUANTUM ESPRESSO [64, 65]. W celu rozwiązania równania Kohna-Shama została wykorzystana metoda fal płaskich. Pseudopotencjały zostały użyte do opisu oddziaływań elektrostatycznych jonów, natomiast oddziaływania korelacyjno-wymienne (ang. *exchange-correlation*, XC) elektronów zostały opisane przez parametryzowane funkcjonały. W ramach przeprowadzonych badań użyto pseudopotencjałów typu PAW (ang. *Projector Augmented Wave*) [66, 67], US (ang. *ultrasoft*) [68] i NC (ang. *Norm-Conserving*) [69], oraz funkcjonałów XC typu LDA (ang. *Local-Density Approximations*) z parametryzacją Perdew-Zungera (PZ) [70], GGA (ang. *Generalized Gradient Approximations*) z parametryzacją Perdew-Burke-Ernzerhofa (PBE) [71, 72], oraz hybrydowego HSE (Heyd-Scuseria-Ernzerhof) [73]. W badaniach uwzględniono również różne poprawki dla oddziaływań vdW: półempiryczne metody Grimmego DFT-D2 [74, 75] i DFT-D3 [76], korekcję dyspersyjną Tkatchenko-Schefflera (ts-vdW) [77], oraz model dipolowy Beckea (XDM) [78, 79]. Do generacji siatki punktów k, na podstawie której była wykonywana integracja strefy Brillouina, użyto metody Monkhorst-Packa [80]. W badaniach zostały wykorzystane energie odcięcia fali i gęstości, rozmiar siatki punktów k oraz odległości między sąsiadującymi układami uzyskane w testach zbieżności. Podobnie, dobór odpowiednich XC oraz poprawek vdW oparty był na wynikach obliczeń wykonanych dla układów testowych, dla których uzyskane parametry odniesione zostały do danych literaturowych.

Wszystkie zbadane struktury zbudowano w modelu periodycznie powtórzonej komórki elementarnej, tj. z użyciem periodycznych warunków brzegowych. Dla układów Pb/Si(111)-1$\times$1 oraz Pb/Ge(111)-1$\times$1 jedną z powierzchni kryształu pokryto ołowiem, a na drugiej pary elektronów wysycono adsorbując atomy wodoru. Wysokość badanych komórek zależała od grubości układu oraz optymalnego obszaru próżni. Dodatkowo zastosowano odcięcie interakcji kulombowskiej w kierunku osi z, aby uniknąć interakcji między sąsiednimi układami [81]. Dla większości zbadanych układów położenie wszystkich atomów w strukturze zostało zoptymalizowane do zadanego kryterium sił. Wyjątkiem są struktury Pb/Si(111)-1$\times$1 oraz Pb/Ge(111)-1$\times$1, dla których zoptymalizowano położenia adsorbatu oraz pierwszych pięciu warstw podłoża.

4. Skrócony opis badań

Przedmiotem badań prowadzonych w ramach rozprawy doktorskiej były powierzchnie krzemu oraz germanu pokryte monowarstwą ołowiu Pb/Si(111)-1×1, Pb/Ge(111)-1×1 oraz heterostruktury Pb/germacen, Pb/$MoTe_2$, $MoTe_2$/Ge(111)-1×1 i silicen/$MoTe_2$.

W ramach pracy **P1** zbadane zostało rozszczepienie spinowe powierzchniowych pasm metalicznych struktury Pb/Si(111)-1×1. Adsorpcja ołowiu została rozważona dla trzech miejsc adsorpcyjnych na powierzchni Si(111)-1×1: T_1, T_4, H_3. Najstabilniejsza energetycznie okazała się konfiguracja T_1, w której atomy ołowiu znajdują się centralnie nad atomami pierwszej warstwy podłoża (Rysunek 4.1a). Obserwowane w tym przypadku wiązanie chemiczne zachodzi z udziałem elektronów zajmujących orbitale typu p_z w Pb oraz Si. Dla struktur T_4 i H_3, atomy Pb adsorbują centralnie nad atomami, odpowiednio, drugiej (Rysunek 4.1b) oraz czwartej warstwy podłoża (Rysunek 4.1c). W obu konfiguracjach wiązanie Pb–Si zachodzi poprzez hybrydyzację orbitali p_x/p_y ołowiu oraz p_z krzemu, co skutkuje zbliżoną energią całkowitą obu konfiguracji. Przeprowadzona dla układu analiza elektronowej struktury pasmowej pozwoliła przewidzieć, że w zależności od konfiguracji powierzchniowej, GSS metalicznych pasm obserwowany wzdłuż $\Gamma - K - M$ może osiągnąć wartości rzędu setek meV (konfiguracje

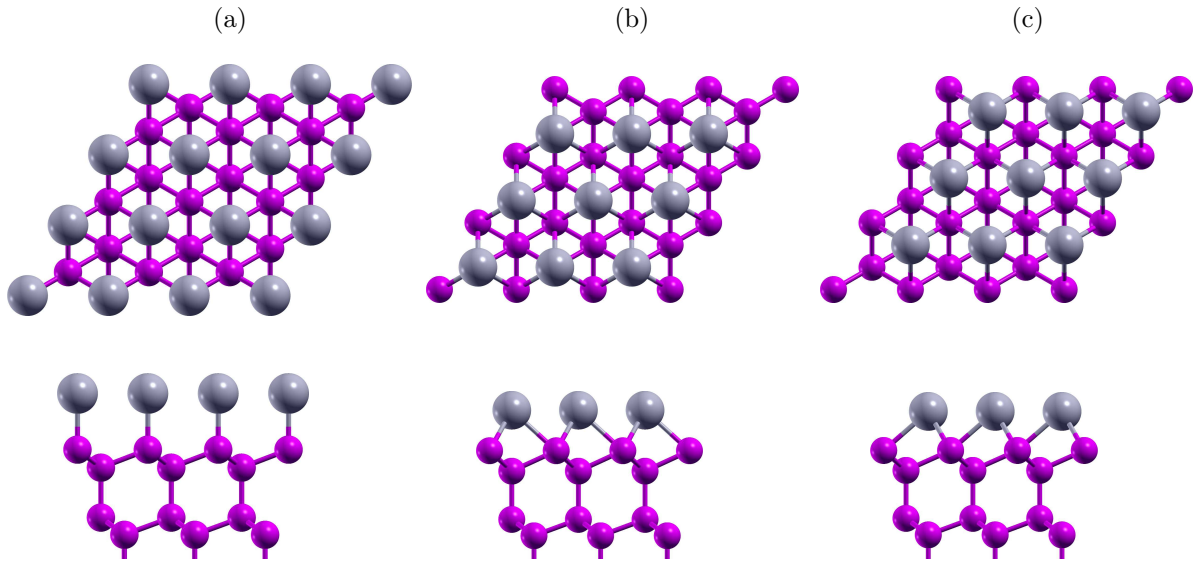

Rysunek 4.1. Schematyczna ilustracja miejsc adsorpcyjnych T_1 (a), T_4 (b) i H_3 (c) na powierzchniach Si(111) i Ge(111). Rysunek przygotowany został w oparciu o dane z pracy **P2**.

T_4 i H_3), bądź ulec niemal całkowitemu wygaszeniu (konfiguracja T_1). Efekt ten powiązany został z różnym charakterem wiązań chemicznych, które dla konfiguracji T_4 i H_3 łamią symetrię dwuwymiarowego gazu elektronowego (ang. *two-dimensional electron gas*, 2DEG) w warstwie Pb. Złamana symetria stanowi źródło pola elektrycznego, które może sprzęgać spin elektronów w gazie dwuwymiarowym poprzez efektywne pole magnetyczne obecne ze względu na ruch elektronów. Efekt ten nie ma miejsca w konfiguracji T_1, gdyż dla tej struktury symetria 2DEG zostaje zachowana.

Praca **P2** jest kontynuacją badań nad GSS powierzchniowych pasm metalicznych warstw ołowiu wzdłuż $\Gamma - K - M$ przeprowadzonych w pracy **P1**. Jednakże, w tym badaniu, analiza rozszczepienia spinowego została oparta na modelu Kima [23, 47, 48], który wiąże ten efekt jawnie z atomowym sprzężeniem spin-orbita. W pracy **P2** zbadano wpływ orbitalnego momentu pędu $\boldsymbol{L}$ na GSS powierzchniowych pasm metalicznych struktury Pb/Ge(111)-1×1. Adsorpcja Pb na powierzchni Ge(111)-1×1 przebiega w sposób podobny do tej, opisanej dla Si(111)-1×1. Ołów może zostać zaadsorbowany w jednym z trzech miejsc adsorpcyjnych: T_1, T_4, H_3, które strukturalnie są analogiczne do tych na Si(111)-1×1 (Rysunek 4.1). Konfiguracja T_1 okazała się najstabilniejszą z powierzchniowych struktur Pb/Ge(111)-1×1, po niej plasują się odpowiednio konfiguracje H_3 i T_4. Niższa energia konfiguracji T_1 jest skutkiem wiązań chemicznych Pb–Ge, które dla tej struktury powstają z hybrydyzacji orbitali p_z i na skutek tego nie zrywają metalicznych wiązań między atomami ołowiu będących hybrydą orbitali p_x/p_y. Te ostatnie ulegają natomiast zerwaniu w konfiguracjach T_4 i H_3, w których przewidzano powstanie stanów hybrydowych między orbitalami p_x/p_y ołowiu oraz p_z germanu. Prowadzi to do zerwania części wiązań Pb–Pb i tym samym podniesienia energii całkowitej układu. Analogiczne wiązania chemiczne przekładają się na podobny GSS obserwowany w Pb/Ge(111)-1×1 oraz Pb/Si(111)-1×1. Dla konfiguracji T_4 oraz H_3 największe rozszczepienie pasm metalicznych zachodzi wzdłuż $\Gamma - K - M$, natomiast dla konfiguracji T_1 efekt ten zostaje niemal całkowicie wygaszony. Wyniki obliczeń przewidują, że OAM odpowiada bezpośrednio za zaobserwowany efekt, prowadząc do rozszczepienia spinowego w pasmach z niezerową wartością $\boldsymbol{L}$ poprzez sprzężenie spin-orbita (ang. *spin-orbit coupling*, SOC) $\alpha \boldsymbol{L} \cdot \boldsymbol{S}$. Różne wartości $\boldsymbol{L}$ obserwowane dla metalicznych pasm konfiguracji T_1 oraz T_4/H_3 są skutkiem różnego składu pasm, który wynika z typu wiązań chemicznych na powierzchni. Przeprowadzona analiza pokrywa się z głównymi wnioskami z pracy **P1** ($\sigma \cdot \boldsymbol{B} \sim \boldsymbol{L} \cdot \boldsymbol{S}$) oraz rozszerza w znacznym stopniu jej opis fizyczny.

Praca **P3** stanowi kontynuację analizy GSS pasm metalicznych warstw ołowiu w ujęciu modelu Kima [23, 47, 48]. Jednakże, dzięki wiedzy zdobytej w pracy **P2**, analiza przeniesiona została na rozszczepienie wzdłuż $M - \Gamma - M'$ i skupia się na relacji wartości GSS z kompozycją orbitali składających się na rozszczepione pasma. W przeciwieństwie do rozszczepienia wzdłuż $\Gamma - K - M$, zbadanego w pracach **P1** i **P2**, GSS wzdłuż $M - \Gamma - M'$ jest obserwowany dla wszystkich konfiguracji powierzchniowych Pb/Ge(111)-1×1, a jego wartość silnie zależy od

miejsca adsorpcyjnego ołowiu. Różnice w GSS między konfiguracjami są rzędu setek meV i zachodzą na tej samej powierzchni, przy tym samym adsorbacie oraz jego pokryciu. Oznacza to, że są one najprawdopodobniej rezultatem różnych wiązań chemicznych Pb–Ge. GSS osiąga największą wartość dla konfiguracji H_3. Po niej kolejno plasują się konfiguracje T_4 oraz T_1. Wartość GSS jest silnie związana z wartością $\boldsymbol{L}$ elektronów okupujących rozszczepione stany. Niezerowa wartość orbitalnego momentu pędu w badanych stanach jest rezultatem sprzężenia orbitali atomowych o różnej parzystości względem łamiącego symetrię pola elektrycznego powierzchni. Zatem, różna jego wartość wynika z wkładu orbitali atomowych tworzących poziomy energetyczne w strukturze krystalicznej, który dla rozszczepionych stanów metalicznych zależy przede wszystkim od typu wiązań na powierzchni układu. Analiza GSS w ujęciu OAM pokazała, że jest to głównie produktem oddziaływania spin-orbita.

Praca **P4** wykorzystuje informacje o adsorpcji warstw Pb na Ge(111), pochodzące z artykułów **P2** i **P3**, do problemu adsorpcji tych warstw na germacenie. W pracy tej zbadano stabilność faz ołowiu oraz wpływ adsorbatu na właściwości elektryczne układu. Badania te dotyczyły trzech potencjalnych faz Pb/germacen wzorowanych na stabilnych strukturach Pb/Ge(111), tj. dwóch faz $\sqrt{3} \times \sqrt{3}$ (α i β), odpowiednio, o pokryciu 1/3 i 4/3 monowarstwy (ML), oraz fazy 1×1 o pokryciu 1 ML (Rysunek 4.2). Dodatkowo, każda z faz została zbadana w trzech różnych konfiguracjach. Dla każdego z układów przeprowadzono pełną relaksację struktury atomowej. W oparciu o wartości energii całkowitej przewidziano, że w rozważanych fazach atomy Pb zajmują inne miejsca adsorpcyjne na powierzchni germacenu niż ich odpowiedniki na Ge(111). Na podstawie przeprowadzonych badań został sporządzony diagram fazowy energii swobodnej powierzchni γ w funkcji potencjału chemicznego ołowiu μ_{Pb}. Przewidziano, że fazy 1×1 i β są korzystniejsze energetycznie, mając najniższe γ w odpowiednich przedziałach μ_{Pb}. Ponadto, energie swobodne tych faz są niższe od energii ich odpowiedników, co dodatkowo sugeruje potencjalną stabilność tych układów. Ze względu na przyjęte przybliżenia w analizie nie

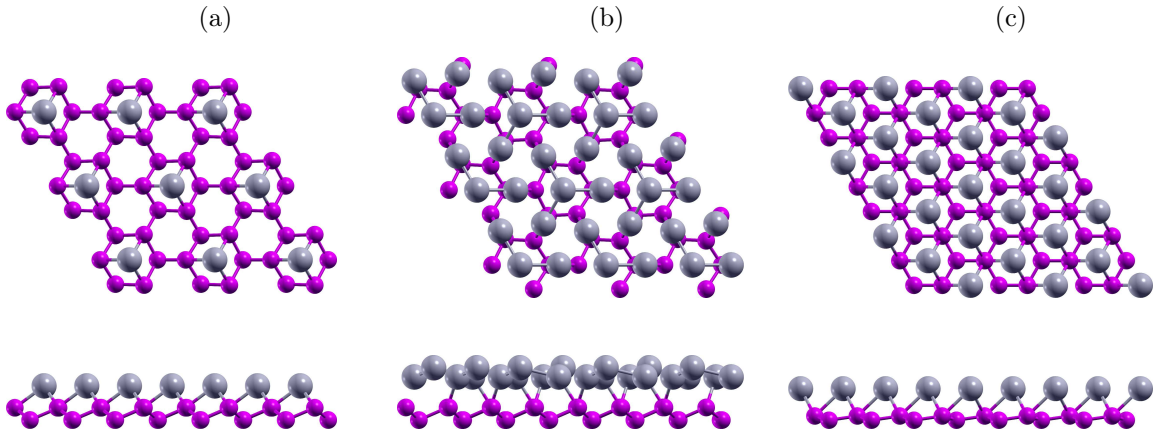

Rysunek 4.2. Schemat struktury atomowej ilustrujący fazy α, β i 1×1. Każda z faz pokazana w jednej z trzech zbadanych konfiguracji. Rysunek przygotowany został w oparciu o dane z pracy **P4**.

uwzględniono entropii, ciśnienia oraz temperatury. Z tego powodu dla faz 1×1 oraz β wykonano dodatkowo rachunki gęstości stanów fononowych, na podstawie których przewidziano, że jedynie faza 1×1 jest stabilna dynamicznie. Dla struktury tej został zbadany również charakter wiązań chemicznych Pb–Ge oraz ich wpływ na właściwości elektronowe układu. Pokazano, że faza 1×1 Pb/germacen zawdzięcza swoją stabilność dwóm wiązaniom Pb–Ge przypadającym na atom ołowiu, co jest rezultatem niewielkiej odległości warstw Pb i Ge w porównaniu do Pb/Ge(111), gdzie obserwowano tylko jedno wiązanie z podłożem przypadające na atom adsorbatu. Silna hybrydyzacja stanów Pb i Ge ma znaczący wpływ na właściwości elektronowe układu, które zostały zbadane z użyciem funkcjonałów PBE oraz HSE. Dla obu funkcjonałów policzono struktury pasmowe z oraz bez oddziaływań spin-orbita. Otrzymane wyniki pokazały, że układ Pb/germacen jest metalem z GSS pasm metalicznych.

Wszystkie zbadane dotąd układy charakteryzowały się GSS pasm metalicznych w układach, w których atomy Pb silnie wiązały się z podłożem. Praca **P5** jest kontynuacją badań nad efektami prowadzącymi do GSS. Jednakże, w przeciwieństwie do poprzednich prac, w **P5** efekt został przeanalizowany dla układu bez silnych wiązań chemicznych pomiędzy warstwą Pb i substratem. W pracy tej zbadano potencjał słabych sił dyspersyjnych do indukowania GSS poprzez złamanie symetrii inwersyjnej na granicy dwóch materiałów. Jako powierzchnię, na której spodziewane były tylko słabe oddziaływania dyspersyjne wybrano monowarstwę $MoTe_2$. Symetria inwersyjna warstwy została złamana poprzez adsorpcję na jednej z jej powierzchni monowarstwy atomów Pb. Ołów wybrano gdyż: (i) jego elektrony charakteryzują się silnym oddziaływaniem spinowo-orbitalnym oraz (ii) teoretyczna stała sieci warstwy Pb zbliżona jest do stałej $MoTe_2$. Ze względu na to, że interfejsy vdW nie mają zazwyczaj jednego stabilnego miejsca adsorpcyjnego, powierzchnia $MoTe_2$ została spróbkowana siatką 9×9. Każdy z punktów siatki stanowił położenie początkowe ołowiu podczas relaksacji struktury $Pb/MoTe_2$. Otrzymane wyniki badań pokazały, że atomy Pb wykazują tendencję do relaksacji wzdłuż kierunku [110], który spróbkowano używając dodatkowo trzydziestu jeden równo oddalonych punktów. Na podstawie tej analizy określono konfigurację układu o najniższej energii. Ze względu na słabe oddziaływania między warstwami, bariera przejścia między stabilnymi miejscami adsorpcyjnymi to jedynie 14 i 43 meV. Dalszą część pracy **P5** poświęcono właściwością elektronowym $Pb/MoTe_2$. W pierwszym kroku omówiono elektronową strukturę pasmową izolowanych warstw, a GSS $MoTe_2$ opisano w ramach modelu OAM. Następnie, elektronowe struktury pasmowe układów izolowanych porównano z wynikami uzyskanymi dla heterostruktury. Właściwości elektronowe $Pb/MoTe_2$ policzono dla charakterystycznych miejsc adsorpcyjnych na powierzchni $MoTe_2$. Uzyskane struktury pasmowe okazały się jakościowo identyczne dla wszystkich zbadanych miejsc adsorpcyjnych, co jest charakterystyczne dla interfejsów bez silnych, lokalnych wiązań chemicznych między warstwami. Struktury pasmowe $Pb/MoTe_2$ składają się przede wszystkim z sumy pasm struktur izolowanych. Jedyne nowe pasma nieobecne w układach izolowanych zaobserwowano w okolicy punktu Γ. Nie są one jednak

rezultatem silnych lokalnych oddziaływań między atomami Pb oraz Te, a jedynie wynikiem sił dyspersyjnych, które łamią symetrię orbitali p_z ołowiu, co w konsekwencji podnosi ich energię. Uwzględnienie oddziaływań spin-orbita znosi degenerację ze względu na spin dla stanów pochodzących zarówno od warstwy Pb jak i $MoTe_2$. Obserwowany efekt jest rzędu setek meV i pokrywa się z obecnością niezerowego $\boldsymbol{L}$ w rozszczepionych stanach. Wartość GSS przewidziana przez obliczenia DFT pokrywa się dobrze, z wartością rozszczepienia wynikającego bezpośrednio z oddziaływania spin-orbita w modelu Kima.

Praca **P6** łączy wiedzę uzyskaną w artykułach **P2**, **P3** i **P5**. Jej celem było zbadanie wpływu naprężenia $MoTe_2$ na adsorpcję warstw Ge. Nienaprężony $MoTe_2$ jest półprzewodnikiem, którego pary elektronów walencyjnych są wysycone wiązaniami wewnątrz warstwy, a oddziaływania z otoczeniem ograniczają się głównie do słabych sił vdW. Pod wpływem naprężenia rozciągającego, rozmiar przerwy energetycznej TMD może ulec zmniejszeniu [82], na skutek zmiany rozkładu ładunku w warstwie. Zwiększona ilość ładunku na powierzchni TMD powinna zwiększyć jej aktywność i ułatwić powstanie silnych wiązań chemicznych nieobserwowanych dla warstwy nienaprężonej. W pracy **P6**, $MoTe_2$ naprężony został tak, aby dopasować jego stałą sieci krystalicznej do stałej Ge(111)-1×1. W tych warunkach naprężenie skutkuje zamknięciem przerwy energetycznej $MoTe_2$ oraz przeniesieniem 0.13 e^- z atomów Mo do Te. W pierwszym kroku dla warstwy naprężonej i nienaprężonej zbadano adsorpcję atomów H, Si, Ge oraz Pb. Otrzymane wyniki pokazały, że dla każdego z atomów energia wiązania wzrasta średnio dwukrotnie po naprężeniu, co sugeruje, że zwiększa ono aktywność chemiczną warstwy. Dla układu $MoTe_2$/Ge przeprowadzono dodatkowo analizę populacji Lödwina, która wskazała na duży przeniesienie ładunku między sąsiadującymi atomami Ge i Te w warunkach naprężonych i na jego brak, gdy warstwa $MoTe_2$ jest nienaprężona. Następnie, została zbadana adsorpcja kolejnych warstw Ge aż do uzyskania struktury składającej się z czternastu warstw atomowych Ge(111). Wyniki obliczeń pokazały, że niezależnie od ilości warstw, układ osiąga minimum energii całkowitej dla konfiguracji T_1, jednakże, ilość warstw ma wpływ na różnice w energii między konfiguracjami. W kolejnej części badań została policzona elektronowa struktura pasmowa $MoTe_2$/Ge(111)-1×1 dla konfiguracji o najniższej (T_1) oraz najwyższej (H_3) energii. W przypadku adsorpcji w H_3 struktura pasmowa $MoTe_2$/Ge(111)-1×1 składa się z prostej sumy pasm układów izolowanych. Natomiast, w przypadku adsorpcji w T_1, struktura pasmowa heterostruktury posiada pasma nieobecne dla izolowanych $MoTe_2$ oraz Ge(111). Analiza nowych stanów pokazała, że dla konfiguracji T_1 powstają nowe wiązania chemiczne, które współtworzone są przez elektrony orbitalii p_z Te oraz Ge. Jednakże, dzieje się to kosztem części wiązań Te–Mo w warstwie $MoTe_2$.

Praca **P7** jest kontynuacją badań nad wpływem naprężeń na aktywność chemiczną $MoTe_2$. Jednakże, w przeciwieństwie do pracy **P6**, w tych badaniach powierzchnię germanu zastąpiono silicenem. W konsekwencji, wybrany układ stał się heterostrukturą materiałów 2D, która wymaga mniejszych naprężeń warstwy $MoTe_2$. Adsorpcję silicenu rozważono dla trzech różnych

miejsc adsorpcyjnych podłoża. Naprężenie dobrano tak, aby dopasować stałą sieci $MoTe_2$ do stałej silicenu. Dodatkowo dla każdego z miejsc adsorpcyjnych, silicen zbadano w dwóch orientacjach względem $MoTe_2$. Dla każdej z sześciu konfiguracji przeprowadzono pełną optymalizację struktury atomowej oraz analizę energii całkowitej zrelaksowanych układów. Zaobserwowane między nimi różnice w energii były rzędu setek meV, co sugeruje różne typy interakcji zachodzące między warstwami. Analizę rozszerzono o wyznaczenie barier przejścia między konfiguracjami. Pozwoliło to na określenie relatywnej stabilności wszystkich miejsc adsorpcyjnych. Następnie zbadano charakter oddziaływań między silicenem i $MoTe_2$. W tym celu przeprowadzono analizę struktur pasmowych oraz populacji ładunku metodą Löwdina. Analiza składu pasm wskazała, na które z orbitali atomowych adsorpcja miała największy wpływ oraz które stany w strukturze pasmowej silicen/$MoTe_2$ składają się głównie z kombinacji orbitali Te i Si. Zaobserwowane w układzie zmiany odpowiadają przewidzianym wartościom przeniesienia ładunku między atomami na granicy warstw. Wyniki badań wskazały na występowanie trzech różnych typów oddziaływań, które zilustrowano konturami gęstości ładunku. W najstabilniejszej konfiguracji zaobserwowano wiązanie z udziałem elektronów obsadzających orbitale p_z w Si oraz Te. Mniej korzystne energetycznie okazały się konfiguracje, dla których hybrydyzacja zachodzi między orbitalami p_x/p_y Si oraz p_z Te. Natomiast, najmniej korzystne były konfiguracje, dla których wiązania chemiczne między Si i Te nie powstają. Opisane interakcje mają duży wpływ na transfer ładunku między warstwami oraz na charakter stanów w okolicy poziomu Fermiego. Ponadto, otrzymane wyniki przewidują, że w zależności od konfiguracji powierzchniowej adsorpcja silicenu może zmniejszać wartość GSS w $MoTe_2$.

5. Podsumowanie

W ramach rozprawy doktorskiej zbadano wpływ funkcjonalizacji chemicznej na właściwości elektronowe struktur: Pb/Si(111)-1×1, Pb/Ge(111)-1×1, Pb/germacen, Pb/$MoTe_2$, $MoTe_2$/Ge(111)-1×1 oraz silicen/$MoTe_2$. Badania zostały przeprowadzone z wykorzystaniem metod obliczeniowych opartych na DFT. Metody te zastosowano do relaksacji struktur atomowych, zbadania energii oddziaływań, określenia elektronowej struktury pasmowej, populacji elektronów na orbitalach atomowych (w tym ładunków cząstkowych atomów) oraz kompozycji stanów elektronowych w strukturze pasmowej. Na podstawie przeprowadzonych obliczeń przewidziano typy oddziaływań między adsorbatem a powierzchnią oraz ich wpływ na właściwości układu, szczególnie, w kontekście zniesienia degeneracji stanów elektronowych ze względu na spin. Najważniejsze osiągnięcia prac, wchodzących w skład rozprawy doktorskiej, zostały wymienione poniżej.

P1. Pokazano, w oparciu o przewidywania teoretyczne, że dwuwymiarowy gaz elektronowy, indukowany w monowarstwach Pb i Tl zaadsorbowanych na powierzchni Si(111), jest niewrażliwy na asymetrię strukturalną podłoża, a jego polaryzacja spinowa zależy od oddziaływania między adsorbatem i substratem. Wyniki obliczeń pokazały, że oddziaływanie to zmienia symetrię inwersyjną rozkładu ładunku w monowarstwie i może tłumić [Pb/Si(111)], albo wzmocnić [Tl/Si(111)], oddziaływanie spin-orbita i tym samym GSS obserowowany w stabilnych konfiguracjach układu.

P2. Zbadano GSS powierzchniowych stanów elektronowych wzdłuż $\Gamma - K - M$, indukowane przez monowarstwę Pb na powierzchni Ge(111)-1×1. Pokazano, że GSS zależy od charakteru wiązań Pb–Ge, tj. może ono być stłumione (T_1), bądź osiągać wartości rzędu setek meV (H_3/T_4). W oparciu o analizę funkcji falowych rozszczepionych pasm, zaproponowano że w drugim przypadku konfiguracja wiązań Pb–Ge pozwala na pojawienie się niezerowego orbitalnego momentu pędu $\boldsymbol{L}$ wzdłuż kierunku $\Gamma - K - M$, który znosi degenerację spinową stanów elektronowych poprzez sprzężenie spinowo-orbitalne.

P3. Przewidziano, że w układzie Pb/Ge(111)-1×1 wielkość GSS wzdłuż $M - \Gamma - M'$ zależy od rodzaju wiązań Pb–Ge, przyjmując wartości z przedziału od 242 do 667 meV dla metalicznych pasm powierzchniowych. Przeprowadzona analiza pokazała, że $\sim$93% GSS jest bezpośrednim efektem SOC. Natomiast, różnice w wartości GSS są wynikiem różnego sprzężenia między orbitalami p_x/p_y i p_z, które odpowiada za niezerowe wartości L rozszczepionych pasm.

P4. Przewidziano stabilną dynamicznie konfigurację układu Pb/germacen. Układ charakteryzuje to samo pokrycie i geometria, co warstw ołowiu w Pb/Ge(111)-1×1. Jednakże, w przeciwieństwie do powierzchni germanu, faworyzowane są miejsca adsorpcyjne, dla których możliwe jest powstanie kilku wiązań Pb–Ge przypadających na atom adsorbatu. Powoduje to, że stabilna faza Pb/germacen ma niższą energię swobodną powierzchni niż jej odpowiednik na Ge(111). Ponadto przewidziano, że struktura Pb/germacen jest metalem o GSS metalicznych pasm rzędu setek meV.

P5. Pokazano, że oddziaływania typu vdW między monowarstwami Pb i $MoTe_2$ są wystarczająco silne, żeby, łamiąc ich symetrię inwersyjną, prowadzić do GSS w obu warstwach. Wyniki te kontrastują z konwencjonalnym spojrzeniem na rozszczepienie spinowe w układach adsorpcyjnych, w których efekt zwykle jest związany z asymetrią ładunku elektrycznego w pobliżu jąder adsorbatu w obecności silnych wiązań powierzchniowych. Analiza oparta na efektywnym Hamiltonianie wykazała, że obserwowane GSS pochodzi bezpośrednio z atomowego sprzężenia spin-orbita.

P6. Pokazano, że pod wpływem naprężenia rozciągającego monowarstwa $MoTe_2$ ulega przejściu półprzewodnik-metal i w tej formie wiąże się kowalencyjnie z dwuwarstwami Ge ułożonymi w kierunku [111] kryształu. Nowe wiązania Ge–Te powstają kosztem części wiązań Te–Mo, co ma znaczący wpływ na strukturę elektronową warstwy oraz transfer ładunku między materiałami.

P7. Przeprowadzone badania pozwoliły zilustrować trzy możliwe typy interakcji na granicy faz naprężonego układu silicen/$MoTe_2$. Wyniki wskazują, że w zależności od konfiguracji tego układu, oddziaływania mogą być słabe i ograniczać się do sił vdW, bądź być silne i prowadzić do hybrydyzacji stanów elektronowych Si i Te. Modyfikuje to ich charakter w okolicy poziomu Fermiego oraz ułatwia transfer ładunku między warstwami, co w konsekwencji może mieć znaczący wpływ na efektywne parametry urządzeń elektronicznych opartych na heterostrukturze.

Badania przeprowadzone w ramach rozprawy doktorskiej dostarczyły informacji w dziedzinie modyfikacji właściwości elektronowych i spinowych struktur dwuwymiarowych. Pozwoliły one na opisanie mechanizmu odpowiedzialnego za rozszczepienie spinowe metalicznych pasm elektronowych w układach funkcjonalizowanych ołowiem. Przewidywana w ramach modelu Kima wartość GSS pokryła się z wynikami DFT, co jest znaczącą poprawą w porównaniu do oryginalnego modelu Rashby. Uzyskane wyniki zilustrowały rolę niezerowego orbitalnego momentu pędu w obserwowanym rozszczepieniu, które w zbadanych przypadkach wynikało głównie z atomowego oddziaływania spin-orbita. W przeprowadzonych badaniach, duża uwaga została poświęcona oddziaływaniom powierzchniowym i ich roli w mechanizmie odpowiadającym za niezerową wartość L. Pokazano, że zarówno silne wiązania chemiczne, jak i słabe siły vdW potrafią być decydującym czynnikiem odpowiedzialnym za pojawienie się GSS. Efekt ten jest szczególnie widoczny w układach Pb/Si(111)-1×1 oraz Pb/Ge(111)-1×1, gdzie w zależności od miejsca adsorpcyjnego Pb, GSS wzdłuż $\Gamma - K - M$ może zostać wygaszone, bądź

osiągać wartości rzędu setek meV. Ponadto, rozszczepienie opisane wzdłuż $M - \Gamma - M'$ dla Pb/Ge(111)-1$\times$1 ma podobny charakter do rozszczepień w innych strukturach adsorpcyjnych, m.in.: Tl/Si(111)-1$\times$1, Bi/Si(111)–$\sqrt{3} \times \sqrt{3}$ i Pb/Ge(111)–$\sqrt{3} \times \sqrt{3}$, co sugeruje, że ich GSS również może być skutkiem wzmocnienia przez SOC.

W ramach rozprawy doktorskiej zbadano również wpływ modyfikacji chemicznej powierzchni na właściwości elektronowe $MoTe_2$. Przewidziano, że naprężenie rozciągające zwiększa aktywność chemiczną warstwy umożliwiając hybrydyzację zachodzącą między orbitalami atomowymi adsorbatu oraz Te. Powoduje to wzrost energii adsorpcji i tym samym wpływa na stabilność konfiguracji powierzchniowych. Zachodząca hybrydyzacja znacząco modyfikuje elektronową strukturę pasmową w okolicy poziomu Fermiego. Oznacza to, że w warunkach naprężonych modyfikowane warstwy $MoTe_2$ mogą zmieniać swoje właściwości elektryczne. To z kolei sugeruje możliwość sterowania poprzez naprężenie właściwościami układów bazujących na $MoTe_2$ oraz sygnalizuje potencjalną trudność utrzymania właściwości układu po naprężeniu. Ponadto, ze względu na hybrydyzację stanów na granicy adsorbat/$MoTe_2$ naprężenie pozwala na zwiększenie efektywności transferu ładunku między warstwami, co ma kluczowe znaczenie przy projektowaniu heterostruktur materiałów dwuwymiarowych na potrzeby elektroniki np. dla zastosowań w tranzystorach typu FET.

6. Dorobek naukowy

6.1. Publikacje

Dorobek publikacyjny autora stanowi osiemnaście artykułów opublikowanych w recenzowanych czasopismach naukowych, których metryki śledzone są w bazach JCR, Scopus oraz SJR. W pietnastu z nich autor rozprawy jest autorem pierwszym i korespondencyjnym, z czego w siedmiu jest jedynym autorem. Lista artykułów wraz z IF i CiteScore za rok 2021 oraz ich punktacją przyznaną przez Ministerstwo Edukacji i Nauki w 2021 roku umieszczona jest poniżej.

1. Barbara Pieczyrak*, **Maciej J. Szary**, Leszek Jurczyszyn, and Marian W. Radny*, *"Spin polarization of two-dimensional electronic gas decoupled from structural asymmetry environment"*, Physical Review B 93, 195318 (2016); $\text{IF}_{2021} = 3.908$, $\text{CiteScore}_{2021} = 6.9$, $\text{MEiN}_{2021} = 140$
2. **Maciej J. Szary***, Marek T. Michalewicz, Marian W. Radny* *"Bonding and electronics of the $MoTe_2$/Ge interface under strain"*, Physical Review B 95, 205421 (2017); $\text{IF}_{2021} = 3.908$, $\text{CiteScore}_{2021} = 6.9$, $\text{MEiN}_{2021} = 140$
3. **Maciej J. Szary***, Barbara Pieczyrak, Leszek Jurczyszyn, Marian W. Radny*, *"Suppressed and enhanced spin polarization in the 1ML-Pb/Ge(111)-1×1 system"*, Applied Surface Science 466, 224–229 (2019); $\text{IF}_{2021} = 7.392$, $\text{CiteScore}_{2021} = 12.1$, $\text{MEiN}_{2021} = 140$
4. **Maciej J. Szary***, *"Role of coupling between surface orbitals in SOC enhanced spin splitting"*, Surface Science 684, 12–17 (2019); $\text{IF}_{2021} = 2.07$, $\text{CiteScore}_{2021} = 3.9$, $\text{MEiN}_{2021} = 100$
5. **Maciej J. Szary*** *"Bonding and electronics of the silicene/$MoTe_2$ interface under strain"*, Applied Surface Science, 491 469–477 (2019); $\text{IF}_{2021} = 7.392$, $\text{CiteScore}_{2021} = 12.1$, $\text{MEiN}_{2021} = 140$
6. **Maciej J. Szary***, *"Giant Rashba spin splitting induced by heavy element adsorption at germanene"*, FlatChem 18, 100141 (2019); $\text{IF}_{2021} = 5.829$, $\text{CiteScore}_{2021} = 6.3$, $\text{MEiN}_{2021} = 20$
7. **Maciej J. Szary***, Marek T. Michalewicz, Marian W. Radny* *"Giant spin splitting induced by a symmetry-braking van der Waals interaction"*, Applied Surface Science 494, 619–626 (2019); $\text{IF}_{2021} = 7.392$, $\text{CiteScore}_{2021} = 12.1$, $\text{MEiN}_{2021} = 140$

8. **Maciej J. Szary***, *"Adsorption of heavy-element monolayers of Tl, Pb, and Bi at silicene: A DFT study"*, Surface Science 697, 121604 (2020); $\text{IF}_{2021} = 2.07$, $\text{CiteScore}_{2021} = 3.9$, $\text{MEiN}_{2021} = 100$
9. **Maciej J. Szary*** *"Al doped MoS_2 for adsorption-based water collection"*, Applied Surface Science 529, 147083 (2020); $\text{IF}_{2021} = 7.392$, $\text{CiteScore}_{2021} = 12.1$, $\text{MEiN}_{2021} = 140$
10. **Maciej J. Szary***, Semir El-Ahmar, Tymoteusz Ciuk *"The impact of partial H intercalation on the quasi-free-standing properties of graphene on SiC(0001)"*, Applied Surface Science 541, 148668 (2021); $\text{IF}_{2021} = 7.392$, $\text{CiteScore}_{2021} = 12.1$, $\text{MEiN}_{2021} = 140$
11. **Maciej J. Szary***, *"Adsorption of ethylene oxide on doped monolayers of MoS_2: A DFT study"*, Materials Science and Engineering B: Solid-State Materials for Advanced Technology 265, 115009 (2021); $\text{IF}_{2021} = 3.407$, $\text{CiteScore}_{2021} = 4.5$, $\text{MEiN}_{2021} = 100$
12. **Maciej J. Szary*** *"MoS_2 doping for enhanced H_2S detection"*, Applied Surface Science 547, 149026 (2021); $\text{IF}_{2021} = 7.392$, $\text{CiteScore}_{2021} = 12.1$, $\text{MEiN}_{2021} = 140$
13. Tymoteusz Ciuk*, Wawrzyniec Kaszub, Kinga Kosciewicz, Artur Dobrowolski, Jakub Jagiello, Adrianna Chamryga, Jaroslaw Gaca, Marek Wojcik, Dariusz Czolak, Beata Stanczyk, Krystyna Przyborowska, Roman Kozlowski, Michal Kozubal, Pawel P. Michalowski, **Maciej J. Szary**, Pawel Kaminski *"Highly-doped p-type few-layer graphene on UID off-axis homoepitaxial 4H–SiC"*, Current Applied Physics 27, 17-24 (2021); $\text{IF}_{2021} = 2.856$, $\text{CiteScore}_{2021} = 4.5$, $\text{MEiN}_{2021} = 70$
14. **Maciej J. Szary***, Jakub A. Bąbelek, Dominik M. Florjan *"Adsorption and dissociation of NO_2 on MoS_2 doped with p-block elements"*, Surface Science 712, 121893 (2021); $\text{IF}_{2021} = 2.07$, $\text{CiteScore}_{2021} = 3.9$, $\text{MEiN}_{2021} = 100$
15. **Maciej J. Szary***, Dominik M. Florjan, Jakub A. Bąbelek *"Sheet doping for improved sensitivity of HCl on $MoTe_2$"*, Surface Science 716, 121964 (2022); $\text{IF}_{2021} = 2.07$, $\text{CiteScore}_{2021} = 3.9$, $\text{MEiN}_{2021} = 100$
16. **Maciej J. Szary***, Dominik M. Florjan, Jakub A. Bąbelek *"Selective Detection of Carbon Monoxide on P-Block Doped Monolayers of $MoTe_2$"*, ACS Sensors 7(1), 272–285 (2022); $\text{IF}_{2021} = 9.618$, $\text{CiteScore}_{2021} = 12.2$, $\text{MEiN}_{2021} = 140$
17. Semir El-Ahmar*, **Maciej J. Szary**, Tymoteusz Ciuk, Rafał Prokopowicz, Artur Dobrowolski, Jakub Jagiełło, Maciej Ziemba *"Graphene on SiC as a promising platform for magnetic field detection under neutron irradiation"*, Applied Surface Science 590, 152992 (2022); $\text{IF}_{2021} = 7.392$, $\text{CiteScore}_{2021} = 12.1$, $\text{MEiN}_{2021} = 140$
18. **Maciej J. Szary***, Jakub A. Bąbelek, Dominik M. Florjan *" Dopant-sheet interaction and its role in the enhanced chemical activity of doped $MoTe_2$"*, Surface Science 723, 122093 (2022); $\text{IF}_{2021} = 2.07$, $\text{CiteScore}_{2021} = 3.9$, $\text{MEiN}_{2021} = 100$

6.2. Wystąpienia

Autor rozprawy prezentował wyniki badań sześciokrotnie – trzy razy ustnie i trzy razy w formie plakatu. Trzy wystąpienia miały charakter międzynarodowy, a pozostałe trzy krajowy. Dodatkowo, autor rozprawy jest współautorem dwóch wystąpień w formie plakatu.

1. **Maciej J. Szary**, Barbara Pieczyrak, Leszek Jurczyszyn, Marian W. Radny, *DFT studies of spin polarized surface states at Pb/Ge(111)-1×1 system*, 4th Summer Symposium on Nanomaterials and their application to Biology and Medicine (2014), Poznań, Polska (plakat)
2. **Maciej J. Szary**, Michał Hermanowicz, Barbara Pieczyrak, Leszek Jurczyszyn, Marian W. Radny, *Badania metodami DFT spolaryzowanych spinowo stanów powierzchniowych w układach Pb/Ge(111)1×1*, I Poznańskie Sympozjum Młodych Naukowców Nowe Oblicze Nauk (2014), Poznań, Polska (plakat)
3. **Maciej J. Szary**, Barbara Pieczyrak, Leszek Jurczyszyn, Marian W. Radny, *DFT studies of spin polarized surface states at Pb/Ge(111)-1×1 system*, 7th International Conference on Scanning Probe Spectroscopy and Related Methods SPS'15 (2015), Poznań, Polska (plakat)
4. **Maciej J. Szary** *The nature of a strain-induced covalent bonding at the $MoTe_2$/Ge(111) interface*, NanoTech Poland International Conference and Exhibition (2017), Poznań, Polska (referat ustny)
5. **Maciej J. Szary**, Barbara Pieczyrak, Leszek Jurczyszyn, Marian W. Radny, *Wpływ orbitalnego moment pędu na rozszczepienie spinowe na powierzchni Pb/Ge(111)-1×1*, X Seminarium Badania prowadzone metodami skaningowej mikroskopii bliskich oddziaływań STM/AFM (2018), Zakopane, Polska (referat ustny)
6. **Maciej J. Szary**, *Domieszkowany MoS_2 jako materiał do detekcji H_2S*, XXI Sesja Użytkowników Komputerów Dużej Mocy ICM (2021), Warszawa, Polska (referat ustny, online)
7. Dominik M. Florjan, **Maciej J. Szary**, *$MoTe_2$ doping for enhanced HCl detection*, NanoTech Poland 2021 – 11th International Conference (2021), Poznań, Polska (plakat)
8. Dominik M. Florjan, **Maciej J. Szary**, *Impact of doping on chemical activity of $MoTe_2$*, NanoTech Poland 2022 – 12th International Conference (2022), Poznań, Polska (plakat)

6.3. Staże i praktyki

Autor rozprawy brał udział w jednym jedenastodniowym szkoleniu zagranicznym oraz jednym sześciomiesięcznym stażu zagranicznym.

1. 45th IFF Spring School Computing Solids: Models, Ab-initio Methods and Supercomputing (Julich, Niemcy) *III 2014*
2. Staż w centrum komputerowym A*CRC, A*STAR (Singapur) *VIII 2015 – II 2016*

6.4. Recenzje publikacji

Autor rozprawy wykonał dwadzieścia jeden recenzji artykułów naukowych dla czasopism, których metryki śledzone są w bazach JCR, Scopus oraz SJR. Recenzje przeprowadzono dla czasopism:

1. Physical Chemistry Chemical Physics (9),
2. Journal of Physics: Condensed Matter (4),
3. Journal of Physics D: Applied Physics (3),
4. Surface Science (2),
5. Applied Surface Science (1),
6. Frontiers in Chemistry (1),
7. The European Physical Journal Plus (1).

7. Działalność akademicka

Autor rozprawy doktorskiej w ramach studium doktoranckiego prowadził zajęcia laboratoryjne z *Fizyki*. Od 1 października 2019 roku autor jest zatrudniony na stanowisku asystenta badawczo-dydaktycznego w Instytucie Fizyki Politechniki Poznańskiej. W ramach pensum autor, oprócz laboratoriów z *Fizyki*, współprowadził:

— wykład specjalistyczny z *Modelowania Komputerowego Materiałów w Skali Atomowej* (studia inżynierskie na kierunku Fizyka Techniczna),
— laboratorium z *Modelowania Komputerowego Materiałów w Skali Atomowej* (studia inżynierskie na kierunku Fizyka Techniczna) ,
— laboratorium z *Symulacji Komputerowych z Pierwszych Zasad* (studia inżynierskie na kierunku Fizyka Techniczna),
— *Zaawansowane Laboratorium Specjalistyczne* (studia magisterskie na kierunku Fizyka Techniczna),
— laboratorium z *Podstaw Informatyki* (studia inżynierskie na kierunku Fizyka Techniczna).

Autor był opiekunem pięcu prac inżynierskich, czterech realizowanych w roku akademickim 2020/2021 i jednej w 2021/2022. Jest również opiekunem dwóch prac magisterskich (2021/2022).

1. Jakub Bąbelek, *Adsorpcja NO_2 i SO_2 na powierzchni domieszkowanego MoS_2: badania DFT*, praca inżynierska, 2020/2021
2. Dominik Florjan, *Adsorpcja CO oraz CO_2 na powierzchni domieszkowanego $MoTe_2$: badania DFT*, praca inżynierska, 2020/2021
3. Maciej Kozłowski, *Adsorpcja Cl_2 oraz HCl na powierzchni domieszkowanego $MoTe_2$: badania DFT*, praca inżynierska, 2020/2021
4. Adam Szelerski, *Adsorpcja H_2S na powierzchni domieszkowanych TMD: badania DFT*, praca inżynierska, 2020/2021
5. Michał Kanak, *Wpływ modyfikacji struktury grafenu na oddziaływanie z wodą: badania DFT*, praca inżynierska, 2021/2022
6. Jakub Bąbelek, *Wpływ pola elektrycznego na populację stanów elektronowych modyfikowanych warstw MoS_2*, praca magisterska, 2021/2022
7. Dominik Florjan, *Modyfikacja aktywności chemicznej $MoTe_2$ domieszkowanego elementami z bloku p (B–Bi)*, praca magisterska, 2021/2022

Od 2019 autor rozprawy jest również opiekunem pracowni komputerowej oraz Koła Naukowego Fizyki Obliczeniowej (KNFO).

8. Przedruki artykułów naukowych

P1. Spin polarization of two-dimensional electronic gas decoupled from structural asymmetry environment

Spin polarization of two-dimensional electronic gas decoupled from structural asymmetry environment

B. Pieczyrak,[1,*] M. Szary,[2] L. Jurczyszyn,[1] and M. W. Radny[2,3,†]
[1]*Institute of Experimental Physics, University of Wroclaw pl. Maxa Borna 9, 50-204 Wrocław, Poland*
[2]*Institute of Physics, Poznan University of Technology, ul. Piotrowo 3, 60-965 Poznan, Poland*
[3]*School of Mathematical and Physical Sciences, The University of Newcastle, Callaghan 2308, Australia*
(Received 4 February 2016; revised manuscript received 14 April 2016; published 31 May 2016)

It is shown, using density functional theory, that a 2D electron gas induced in a monolayer of Pb or Tl adatoms on the Si(111) $-$ 1 $\times$ 1 surface is insensitive to the structural asymmetry of the system and its spin polarization is governed by the interaction between the adlayer and the substrate. It is demonstrated that this interaction changes the in-plane inversion symmetry of the charge distribution within the monolayer and can either suppress [Pb/Si(111)] or enhance [Tl/Si(111)] the adatom intra-atomic spin-orbit effect on a Rashba-Bychkov-type spin splitting.

DOI: 10.1103/PhysRevB.93.195318

The formation and properties of a spin polarized 2D electron gas (2DEG) on surfaces of nonmagnetic solids continues to attract a great deal of interest due to anticipated spintronic applications [1]. Of special interest are substrates of elemental (Si, Ge) semiconductors, with the spin polarized 2DEG originating from the spin-split electronic surface states induced by the adsorption of heavy metal elements [with large intra-atomic spin-orbit coupling (SOC)] and a structural inversion asymmetric environment [1–17].

At a crystal surface, the electric field perpendicular to the surface plane acts as a magnetic field in the rest frame of a moving electron and the spin degeneracy of electronic states is lifted [18,19]. In real systems the magnitude of this effect, usually called Rashba-Bychkov (RB) effect, is governed by various types of structural asymmetries at the solid-vacuum interface and the magnitude of intra-atomic SOC [12,13]. A single layer of Bi on Ge(111) within the $\sqrt{3} \times \sqrt{3} - R30^\circ$ reconstruction induces the RB effect in the adatom derived surface states enhanced by a strong asymmetry of the charge density perpendicular to the surface in close proximity of the adatom (Bi) nuclei [20]. In a trimer configuration on the Bi/Si(111)$\sqrt{3} \times \sqrt{3} - R30^\circ$ surface the large RB effect was attributed to an in-plane structural inversion asymmetry that induces a large in-plane potential gradient [14,15]. Typically, the RB spin splitting arises around the k-points in the (111) surface Brillouin zone (SBZ) with the time reversal symmetry (Γ and M). However, a peculiar RB effect was also reported at point K with no such symmetry. This was attributed to the change in 2D symmetry of SBZ in the transition from 1 $\times$ 1 to the adsorption induced $\sqrt{3} \times \sqrt{3} - R30^\circ$ surface reconstruction [3]. Here we add the new RB-type of spin polarization demonstrated for a 2DEG induced by a 1 $\times$ 1 monolayer of Pb and Tl adatoms (adlayer) on the Si(111) $-$ 1 $\times$ 1 surface. We show that the 2DEG formed at the interface is effectively decoupled from the system structural asymmetry and its spin polarization is governed by the symmetry of the bonding structure within the adlayer. We also show that the latter can either suppress or enhance the intra-atomic SOC effect on the RB spin splitting.

Our results were obtained for Pb/Si(111) and can be extended to the Tl/Si(111) system; both studied in literature before [16,17]. Here, we investigate the changes to the energetics and the electronic and spin structures of the systems caused by a commensurate shift of the 1 $\times$ 1 adlayer with respect to the unreconstructed Si(111) $-$ 1 $\times$ 1 substrate. Schematics of the studied configurations are shown in Fig. 1. In the T_4 and H_3 configurations each adatom of the monolayer sits above the second and the fourth substrate atom, respectively. In both configurations each adatom interacts directly with three topmost Si atoms. In the T_1 geometry, each adatom interacts directly with one topmost Si atom. These adsorption systems were modeled using a 3-bilayer slab of Si with one side covered by a 1 $\times$ 1 adlayer and the other terminated by H atoms. The slabs were separated along [111] direction by a 10 Å vacuum (the x and y axes are chosen to be parallel and z axis perpendicular to the surface (111) plane). DFT plane wave (cutoff 450 eV) calculations were performed using the PAW potential [21,22], PBE for exchange and correlation [23], and SOC as implemented in the VASP code [24–27]. In the total-energy calculations the five topmost slab layers and the adlayer were relaxed until the forces present were less than 0.01 eV/Å. The irreducible part of SBZ was sampled by 16 k-points.

Figure 2 shows the relativistic and nonrelativistic electronic band structures for Pb/Si(111) in the T_1 and T_4 geometries. The band structure for configuration H_3 is very similar to that for T_4 and is not shown. In all of the presented band structures the states that are located in the bulk energy gap are the surface states exclusively of the Pb 6p character. The Pb 6s states were calculated to form a nondispersive band located $\sim$6 eV below the Fermi level (not shown in Fig. 2). Such behavior is typical for heavy elements of the p-block metals where the energy separation between s and p orbitals makes the s-p hybridization energetically too costly to occur [20]. The nonrelativistic and relativistic electronic structures of a free Pb monolayer compatible with the 1 $\times$ 1 periodicity of the Si(111) substrate are also shown in Fig. 2 to clarify the effects of intra-atomic SOC and the structural symmetries on

*meghan@ifd.uni.wroc.pl
†marian.radny@newcastle.edu.au

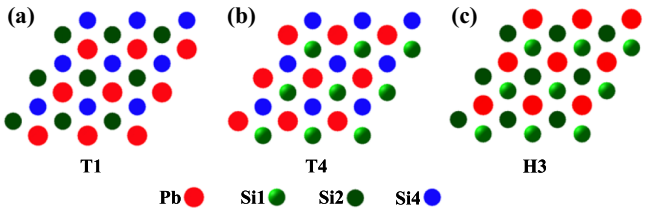

FIG. 1. Top views of a 1×1-Pb (Tl) monolayer deposited on the Si(111) surface at three adsorptions sites (a) T_1, (b) T_4, and (c) H_3. The Pb (Tl) adatoms are marked by large red spheres, first-layer Si atoms by green spheres, second-layer Si atoms by dark-green spheres, and the fourth-layer Si atoms by blue spheres.

the electronic and spin structures of the Pb/Si(111) $-$ 1×1 adsorption systems.

In the nonrelativistic band structure of the free Pb monolayer [Fig. 2(b)], the parabolic-like bands with minima close to the K and M points have $6p_x/p_y$ character (blue squares and green triangles). This indicates that the $6p_x$ and $6p_y$ orbitals on neighboring Pb atoms are coupled, resulting in the in-plane σ bonds within the layer. The less dispersive parabolic-like band [red circles in Fig. 2(b)] with a minimum at the Γ point and maxima at the K and M points is of a $6p_z$ character. The

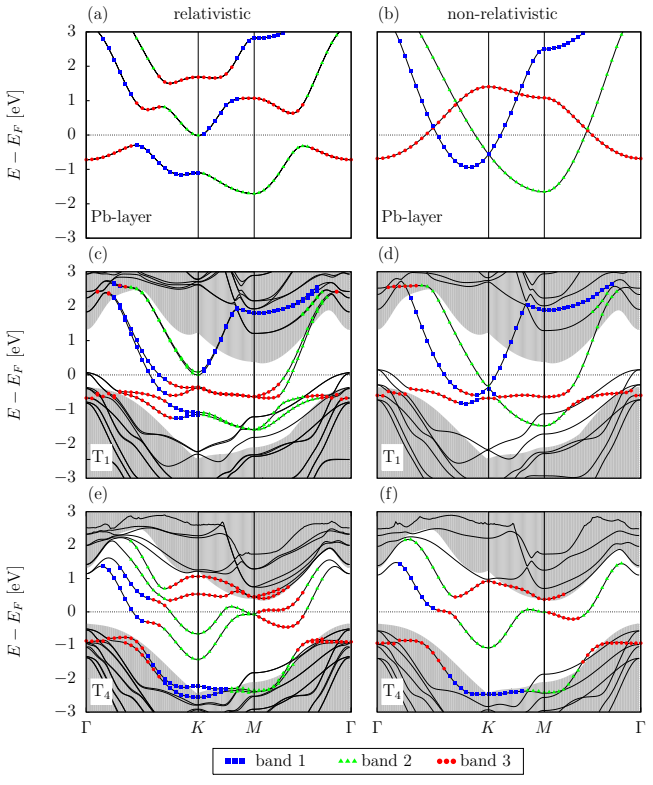

FIG. 2. Relativistic (left) and nonrelativistic (right) electronic band structures of the isolated Pb-1×1 monolayer (top), and the Pb/Si(111)-1×1 adsorption system in the T_1 (middle) and T_4 (bottom) configurations. The blue and green curves denote the bands of electronic surface states that originate from the Pb p_x/p_y orbitals, while the red band represents the surface states originating from the Pb p_z orbitals.

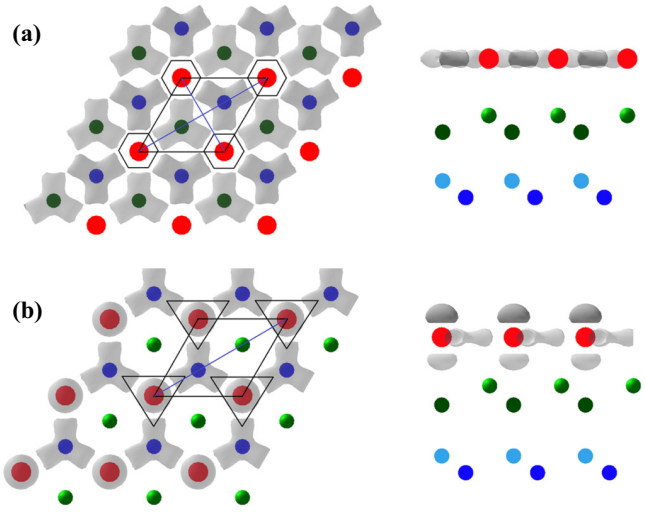

FIG. 3. Side (left) and top (right) views of the spatial charge distribution within the 2DEG in the Pb/Si(111)-1×1 adsorption system calculated at the K point for the nonrelativistic electronic band structure of configuration (a) T_1 [green and blue bands in Fig. 2(d)]; (b) T_4 [red and green bands in Fig. 2(f)]. The hexagons and triangles around the selected adatoms illustrate the difference in the in-plane symmetries of the charge distribution in configuration T_1 and T_4, respectively. Isosurface value: $0.15\,\mathrm{e/\AA^3}$.

gapless crossing points between the $6p_z$ and $6p_x/p_y$ bands indicate that the corresponding states do not couple. This is because both the in-plane bonding and the inversion structural symmetries are present, and remain unbroken, in the system.

In the nonrelativistic band structure of adsorption configuration T_1 [Fig. 2 (d)], the spin degenerate, dispersive surface bands that cross the Fermi level are of the Pb $6p_x/p_y$ character and are virtually identical to those seen in the band structure of the isolated Pb monolayer [compare blue and green lines in Figs. 2(b) and 2(d)]. This demonstrates that the in-plane Pb-Pb σ bonding within the monolayer is not altered upon adsorption and that the 2DEG represented by the Pb $6p_x/p_y$ bands in the vicinity of the Fermi level is essentially decoupled from the substrate. This is illustrated in Fig. 3(a), where the charge distribution calculated for these bands is shown to be almost completely localized within the Pb monolayer, with the in-plane symmetry of the Pb-Pb σ bonding preserved. By contrast, the surface band of the Pb $6p_z$ character [red line in Fig. 2(d)] is flattened and lowered in energy, indicating Pb-Si covalent bonding.

In the relativistic band structure of configuration T_1 [Fig. 2 (c)], all of the Pb $6p$-induced surface states have essentially their binding energies unaffected by the adatom intra-atomic SOC in the entire surface BZ. The only effect of SOC can be observed at the K point, where the three surface bands separate slightly in energy. Also, the states remain essentially spin degenerate except narrow regions in the vicinity of the crossing points—between Γ and K (near K), and between Γ and M (near M)—where there is a residual spin splitting. While the spin degeneracy of the Pb $6p_z$ band [red band in Fig. 2(c)] can be attributed to its overlap with the Si states, the spin degeneracy for the noninteracting with the substrate

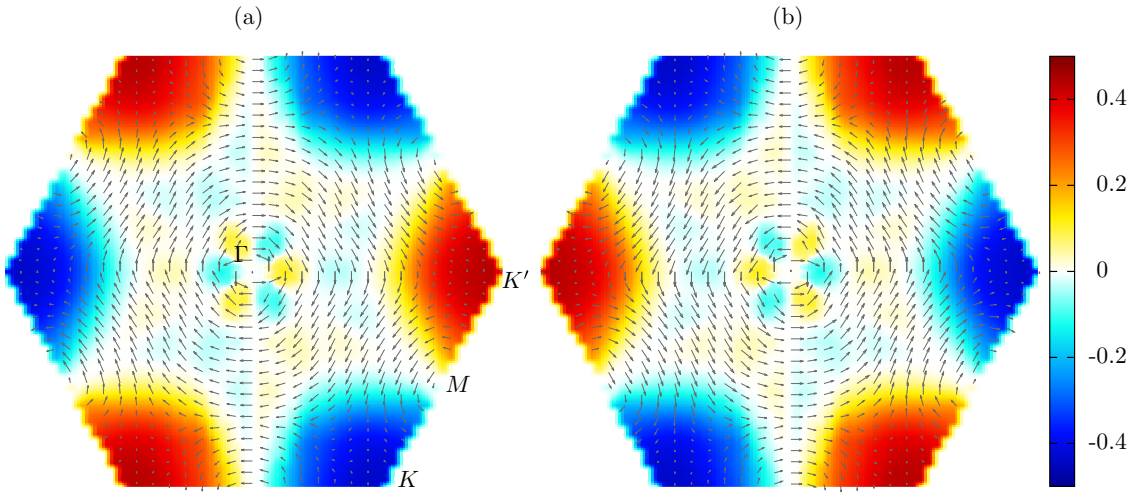

FIG. 4. Spin polarization vector projected onto the x/y plane (arrows) and z axis (color bar) in the surface Brillouin zone calculated for the spin-split surface states in the Pb/Si(111)-1 × 1 relativistic band structure of configuration T4 shown in Fig. 2(e): (a) upper green and red bands around the K and M points, respectively; (b) lower green and red bands around the K and M points, respectively.

Pb $6p_x/p_y$ bands [green and blue bands in Fig. 2(c)] must be a consequence of the fact that both time reversal and spatial inversion symmetries are preserved in the system. Our results indicate that the latter is preserved despite the fact that in the Pb/Si(111) system, the structural inversion symmetry of the Pb layer is broken by its interaction with the Si substrate. Apparently, the adsorption-induced structural asymmetry does not affect the in-plane Pb-Pb σ bonding symmetry within the adlayer [see Fig. 3(a)], resulting in the adatom-induced 2DEG being essentially decoupled from the substrate; i.e., the 2DEG remains, effectively, insensitive to the structural asymmetry environment within the system.

In adsorption configuration T_4, each Pb adatom interacts with three Si substrate atoms. This breaks the in-plane Pb-Pb σ bonding symmetry within the monolayer. As a result, the nonrelativistic band structure for this configuration [Fig. 2(f)] opens energy gaps at the crossing points between the Pb $6p$ bands near K (between Γ and K) and near M (between Γ and M). In addition, breaking the bonding symmetry within the Pb layer results in one of the $6p_x/p_y$ bands (the one that directly interacts with the Si states) being shifted well below the Fermi level [blue line in Fig. 2(f)]. By contrast, the energies of the bands that do not interact with Si, i.e., the second Pb $6p_x/p_y$ band (green line) and the Pb $6p_z$ band (red line) remain essentially unaltered. Also, these noninteracting with the Si substrate Pb $6p$ states are located in the energy gap and the 2DEG represented by these states in the vicinity of the Fermi level is decoupled from the rest of the system. This is illustrated in Fig. 3(b), where the charge distribution calculated for these states at the K point is presented.

By analogy to the T_1 configuration one might expect that as in geometry T4 the 2DEG is decoupled from the substrate-induced structural asymmetry, it will also remain spin unpolarized if the adatom SOC is taken into account. Surprisingly, the relativistic band structure for the T_4 configuration shown in Fig. 2(e) predicts otherwise—a large spin-split is observed for the unaltered (by adatom-substrate interation) Pb $6p_x/p_y$ (green line) and $6p_z$ (red line) bands around the K point. At the M point these spin-split surface bands merge and form a Dirac point. Figure 4 shows the momentum-dependent spin polarization vector components calculated for these spin-split surface bands of Fig. 2(e). One observes that near the M points the in-plane (x/y) spin component shows in-plane helicity (z component of the spin vector is zero), while at the K points the spin vector has only vertical z component. Spin splitting of the Pb $6p_x/p_y$ states involved in the Pb-Si interaction [blue band in Fig. 2(e)] is negligible due to its overlap with Si states.

Taken together, one should observe the following: In both configurations T_1 and T_4, (a) the structural inversion asymmetry (in z direction) of the Pb adlayer is broken due to its interaction with the substrate, (b) the structural inversion symmetry within the 1 × 1 Pb layer (in the x/y plane) is not altered by the adlayer interaction with the Si substrate, (c) the adlayer-induced 2DEG remains decoupled from the substrate-induced structural asymmetry; yet, the 2DEG is spin polarized in configuration T_4 [see Fig. 2(e)] but not in T_1 [see Fig. 2(c)]. In order to resolve this apparent inconsistency one needs to inspect Fig. 3 again. The analysis shows that there is in-plane x/y asymmetry in the charge distribution within the 2DEG induced in configuration T_4 [Fig. 3(b)] when compared with the corresponding charge distribution obtained for T_1 [Fig. 3(a)]. As the charge distribution of Fig. 3(b) was calculated at point K, where the overlap between the surface states is negligible due to the large energy separation between them [see Fig. 2(e)], it is clear that the charge asymmetry in configuration T_4 originates from the noninteracting, with the Si substrate, surface bands of the Pb $6p_x/p_y$ and Pb $6p_z$ character.

The in-plane asymmetry in charge distribution in configuration T_4 indicates that an electron of the 2DEG experiences an electric field, $\vec{E}$, and that this field will couple to the electronic spin $\vec{\sigma}$ as $-\vec{\sigma}\cdot\vec{B}$, with magnetic field $\vec{B} = (1/mc)(\vec{p}\times\vec{E})$. As the electric field, $\vec{E}$, and the electronic momentum, $\vec{p}$, have only in-plane x/y components, the effective magnetic field, $\vec{B}$, has only one, z component. As a result, the coupling term $-\vec{\sigma}\cdot\vec{B}$ should affect the vertical, z, component of the spin vector. At the K point, where the spin polarization vector has

only z component (see Fig. 4), the magnitude of the coupling term $-\vec{\sigma} \cdot \vec{B}$ is measured to be 0.77 eV [see Fig. 2(e)]. At point M, however, the effective magnetic field $\vec{B}$ couples to the spin vector differently. As shown in Fig. 4, the spin polarization vector rotates in x/y plane with zero z component, and the spin-split surface bands merge to form a Dirac point [see Fig. 2(e)]. Such behavior is a consequence of Kramers' theorem that requires the magnitude of the coupling term $-\vec{\sigma} \cdot \vec{B}$ to be zero at M point, even if $\vec{B} \neq 0$. This means that at point M the system responds to this symmetry constraint by forcing the spin polarization vector to rotate in x/y plane with both the z component and the coupling term $-\vec{\sigma} \cdot \vec{B}$ reduced to zero. These considerations show that the spin polarization of the Pb $6p$ states in configuration T_4 is of the Rashba-Bychkov origin despite the fact that the resulting 2DEG is not affected by the substrate-induced structural asymmetry.

In conclusion, we discussed a novel mechanism for the formation of the Rashba-Bychkow type of spin polarization in a 2DEG decoupled from any structural asymmetry environment in the systems. Based on the DFT calculations for Pb/Si(111) we showed that the gas can be decoupled from the substrate and its spin polarization can be induced by the in-plane bonding structure. It was demonstrated that the latter can change the in-plane symmetry of the charge distribution within a 2DEG and can suppress (geometry T_1) or enhance (geometry T_4) the adatom SOC effect on the magnitude of the RB spin polarization. It should be noted that both scenarios can be realized in real materials as the energetic order of the analyzed atomic configurations depends on the type of the adatom covering Si(111)—for Pb/Si(111) the most stable adlayer configuration is T_1 followed by T_4 and H_3 (less stable by 0.375 and 0.352 eV, respectively), while for Tl/Si(111) the most stable geometry is T_4, followed by H_3 and T_1 (less stable by 0.098 and 0.476 eV, respectively). As the topology of the electronic band structures are very similar for both systems, in real world the scenario related to spin polarization identified in configuration T_1 can be realized in the Pb/Si(111) system, while the one identified in the T_4 geometry can be found in the Tl/Si(111) system. The reported results open up the possibility to search for other adsorption systems with the RB-type of spin-split electronic surface states induced exclusively by the intra-atomic SOC within the adlayer and the bonding structure at the adlayer-substrate interface.

ACKNOWLEDGMENTS

This work is supported by University of Wroclaw under Contract No. 1010/S/IFD/16. Numerical calculations reported in this work have been performed at the Interdisciplinary Centre of Mathematical and Computational Modeling of the University of Warsaw under Grant No. G44-10. M.W.R. acknowledges the Polish Ministry of Science and Higher Education for support (Grant No. 06/62/DSPB/0216).

[1] A. Manchon, H. C. Koo, J. Nitta, S. M. Frolov, and R. A. Duine, Nat. Mater. **14**, 871 (2015).
[2] S. D. Stolwijk, A. B. Schmidt, M. Donath, K. Sakamoto, and P. Krüger, Phys. Rev. Lett. **111**, 176402 (2013).
[3] K. Sakamoto, T. Oda, A. Kimura, K. Miyamoto, M. Tsujikawa, A. Imai, N. Ueno, H. Namatame, M. Taniguchi, P. E. J. Eriksson, and R. I. G. Uhrberg, Phys. Rev. Lett. **102**, 096805 (2009).
[4] P. E. J. Eriksson, K. Sakamoto, and R. I. G. Uhrberg, Phys. Rev. B **81**, 205422 (2010).
[5] Y. Ohtsubo, S. Hatta, H. Okuyama, and T. Aruga, J. Phys.: Condens. Matter **24**, 092001 (2012).
[6] S. Hatta, T. Aruga, C. Kato, S. Takahashi, H. Okuyama, A. Harasawa, T. Okuda, and T. Kinoshita, Phys. Rev. B **77**, 245436 (2008).
[7] S. Hatta, C. Kato, N. Tsuboi, S. Takahashi, H. Okuyama, T. Aruga, A. Harasawa, T. Okuda, and T. Kinoshita, Phys. Rev. B **76**, 075427 (2007).
[8] K. Yaji, S. Hatta, T. Aruga, and H. Okuyama, Phys. Rev. B **86**, 235317 (2012).
[9] K. Sakamoto, T. H. Kim, T. Kuzumaki, B. Müller, Y. Yamamoto, M. Ohtaka, J. R. Osiecki, K. Miyamoto, Y. Takeichi, A. Harasawa, S. D. Stolwijk, A. B. Schmidt, J. Fujii, R. I. G. Uhrberg, M. Donath, H. W. Yeom, and T. Oda, Nat. Commun. **4**, 2073 (2013).
[10] K. Yaji, Y. Ohtsubo, S. Hatta, H. Okuyama, K. Miyamoto, T. Okuda, A. Kimura, H. Namatame, M. Taniguchi, and T. Aruga, Nat. Commun. **17**, 1 (2010).
[11] J. Ibañez-Azpiroz, A. Eiguren, and A. Bergara, Phys. Rev. B **84**, 125435 (2011).
[12] L. Petersen and P. Hedegard, Surf. Sci. **459**, 49 (2000).
[13] Y. M. Koroteev, G. Bihlmayer, J. E. Gayone, E. V. Chulkov, S. Blügel, P. M. Echenique, and P. Hofmann, Phys. Rev. Lett. **93**, 046403 (2004).
[14] I. Gierz, T. Suzuki, E. Frantzeskakis, S. Pons, S. Ostanin, A. Ernst, J. Henk, M. Grioni, K. Kern, and C. R. Ast, Phys. Rev. Lett. **103**, 046803 (2009).
[15] C. R. Ast, J. Henk, A. Ernst, L. Moreschini, M. C. Falub, D. Pacilé, P. Bruno, K. Kern, and M. Grioni, Phys. Rev. Lett. **98**, 186807 (2007).
[16] T. Zhang, P. Cheng, W.-J. Li, Y.-J. Sun, G. Wang, X.-G. Zhu, K. He, L. Wang, X. Ma, X. Chen, Y. Wang, Y. Liu, H.-Q. Lin, J.-F. Jia, and Q.-K. Xue, Nat. Phys. **6**, 104 (2010).
[17] K. Sakamoto, H. Kakuta, K. Sugawara, K. Miyamoto, A. Kimura, T. Kuzumaki, N. Ueno, E. Annese, J. Fujii, A. Kodama, T. Shishidou, H. Namatame, M. Taniguchi, T. Sato, T. Takahashi, and T. Oguchi, Phys. Rev. Lett. **103**, 156801 (2009).
[18] E. I. Rashba, Sov. Phys. Solid State **2**, 1109 (1960).
[19] Y. A. Bychkov and E. I. Rashba, JETP Lett. **39**, 78 (1984).
[20] S. Hatta, T. Aruga, Y. Ohtsubo, and H. Okuyama, Phys. Rev. B **80**, 113309 (2009).
[21] P. E. Blöchl, Phys. Rev. B **50**, 17953 (1994).
[22] G. Kresse and D. Joubert, Phys. Rev. B **59**, 1758 (1999).
[23] J. P. Perdew, K. Burke, and M. Ernzerhof, Phys. Rev. Lett. **77**, 3865 (1996).
[24] G. Kresse and J. Hafner, Phys. Rev. B **47**, 558 (1993).
[25] G. Kresse and J. Hafner, Phys. Rev. B **49**, 14251 (1994).
[26] G. Kresse and J. Furthmüller, Comput. Mater. Sci. **6**, 15 (1996).
[27] G. Kresse and J. Furthmüller, Phys. Rev. B **54**, 11169 (1996).

P2. Suppressed and enhanced spin polarization in the 1ML-Pb/Ge(111)–1 × 1

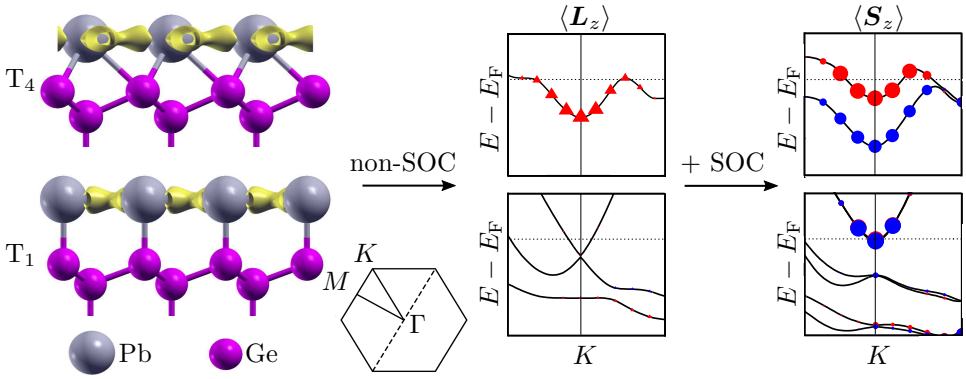

Applied Surface Science 466 (2019) 224–229

Contents lists available at ScienceDirect

Applied Surface Science

journal homepage: www.elsevier.com/locate/apsusc

Full Length Article

Suppressed and enhanced spin polarization in the 1ML-Pb/Ge(1 1 1)-1 × 1 system

Maciej J. Szary[a,*], Barbara Pieczyrak[b], Leszek Jurczyszyn[b], Marian W. Radny[a,c,**]

[a] Institute of Physics, Poznan University of Technology, 62-965 Poznan, Poland
[b] Institute of Experimental Physics, University of Wroclaw, pl. Maxa Borna 9, 50-204 Wrocław, Poland
[c] School of Mathematical and Physical Sciences, The University of Newcastle, Callaghan 2308, Australia

ARTICLE INFO

Keywords:
Density functional theory
Spin orbit coupling
Spin-split surface states
Band structure
Electronic spin
Rashba effect

ABSTRACT

It is shown, based on the density functional theory (DFT), that the spin splitting of surface electronic states induced by a Pb monolayer on the Ge(1 1 1)-1 × 1 surface depends on the bonding structure of the Pb/Ge interface and may be either significant, ~0.8 eV, (H_3/T_4) or completely suppressed (T_1). It is also shown that for the former the bonding configuration facilitates an emergence of unquenched orbital angular momentum ***L*** along Γ-*K*-*M* direction, which then lifts the spin degeneracy of the electronic states through the spin-orbit coupling (SOC) of electrons in Pb. Along with the DFT data, we present a complementary analysis conducted withing the orbital Rashba framework, which provides an additional insight into the SOC-induced splitting.

1. Introduction

Spin angular momentum (SAM, or simply spin) polarized electronic states induced on surfaces of elemental semiconductors by monolayers of metallic, nonmagnetic adatoms with large intra-atomic spin-orbit coupling (SOC) have attracted much attention due to possible spintronic application [1–7]. The latter requires that the spin polarized states are located within a semiconductor bulk energy gap to prevent mixing with the unpolarized states of the bulk. Also, the spin split of at least 100 meV is desirable to minimize the effect of thermal fluctuations and enable room temperature operations.

Experimentally observed spin splitting of electronic states at semiconductor surfaces are well reproduced by first principle calculations and the phenomenon is usually associated within a Zeeman-like effect described by the Rashba-Bychkov (RB, or simply Rashba) model. This approach, however, lacks predictive power to quantitatively account for spin split, as experiments and the original Rashba theory show large discrepancy in the energy scales reported. A number of proposals had also been put forward to amend the energy of the putative Zeeman-type splitting of the original Rashba model [7–11], however, no universal solution has yet been recognized. On the other conceptual side, recent observations of a direct correlation between unquenched orbital angular momentum (OAM) and the emergence of SAM splitting has led to the formulation of the so-called orbital Rashba model [12–15]. In this approach the unquenched OAM explicitly contributes to the spin-split pattern through both the atomic SOC and the surface electric-dipole/electric-field interaction at the surface. It was also shown that this model quantitatively accounts for the scale of the spin splitting in a variety of systems [14,16,15,17].

In this paper we investigate, based on the density functional theory (DFT), the spin and electronic structure of the Pb/Ge(1 1 1)-1 × 1 adsorption system. We observe that the predicted spin-split pattern depends on the bonding configuration at the Pb/Ge interface, and may be large (~0.8 eV) or completely suppressed in vicinity of the *K* point of the surface Brillouin zone (SBZ). The observed difference is also shown to be correlated with the magnitude of the unquenched adatomic OAM calculated for the SAM-split bands. Our DFT data indicate that the spin split in vicinity of *K* originates form the atomic SOC of Pb adatoms, which we further discuss within the orbital Rashba framework.

2. Methods

Total-energy and electronic structure calculations, were performed using Quantum Espresso [18] (QE), a DFT plane-waves code, employing ultrasoft pseudopotentials [19], local density approximation (LDA) for exchange and correlation of Perdew-Zunger [20], energy cutoffs of 544 and 3400 eV for wave functions and densities, respectively, and SOC. The SBZ was sampled using 12 × 12 × 1 Monkhorst–Pack [21] *k*-point grid scheme. The Pb/Ge(1 1 1) system was modeled by repeated asymmetric slab consisting of six Ge layers, Pb monolayer on one side of

* Corresponding author.
** Corresponding author at: Institute of Physics, Poznan University of Technology, 62-965 Poznan, Poland..
E-mail addresses: maciejjanszary@gmail.com, maciej.s.szary@doctorate.put.poznan.pl (M.J. Szary), marian.radny@newcastle.edu.au (M.W. Radny).

https://doi.org/10.1016/j.apsusc.2018.10.028
Received 22 August 2018; Received in revised form 1 October 2018; Accepted 3 October 2018
Available online 04 October 2018

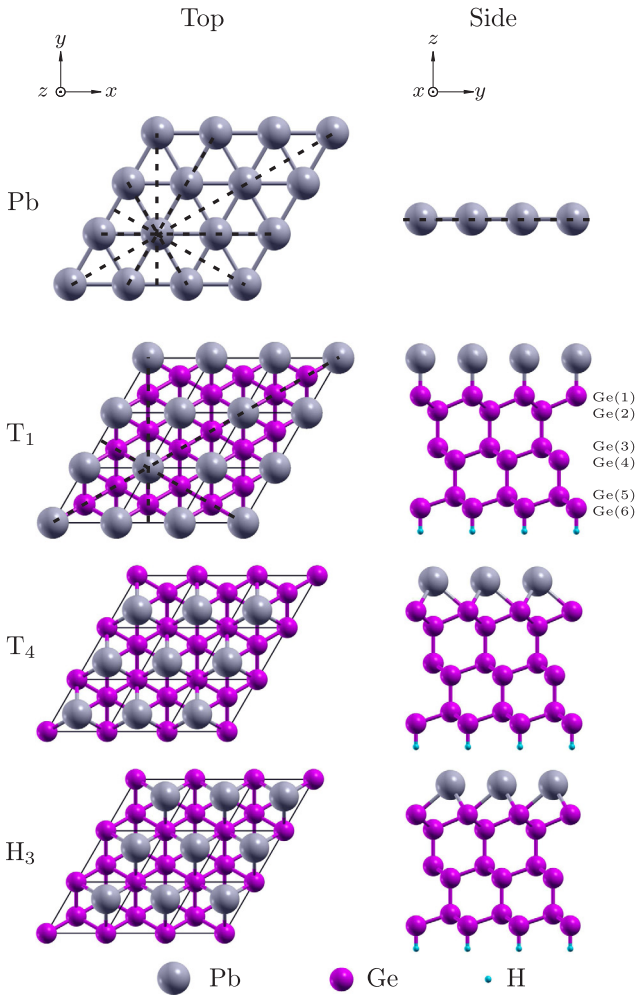

Fig. 1. Schematics of atomic structures of isolated Pb monolayer and configurations T_1, T_4 and H_3 of the Pb/Ge(1 1 1) adsorption system. Black dashed lines indicate mirror symmetry planes. Black lines in the top views indicate surface unit cell borders.

the slab and the hydrogen atoms on the other. The atomic positions, except for H and two bottom Ge layers of the slab, were fully optimized to an assumed criterion for atomic forces ($<1.36{\cdot}10^{-4}$ eV/a.u.). All calculations were performed with the optimized bulk Ge lattice constant of 5.658 Å(experimental value for bulk Ge is 5.64 Å[22]), and the spatial separation between the slabs of 20 Å. The spin-orbit interaction has been reported to have a considerable (~30 meV) impact on the stability of the surface configurations of the Pb-decorated surfaces of Ge (1 1 1) and Si(1 1 1) in the $\sqrt{3} \times \sqrt{3}$ surface reconstruction, and therefore the investigated configurations of Pb/Ge(1 1 1)-1 × 1 were relaxed in presence of SOC. The SAM and OAM projections for specific *k*-points were obtained with the use of the linear combination of pseudo-atomic orbitals (LCPAO) [23] coefficients of local atoms calculated in OpenMX code [24–27], with norm-conserving pseudopotentials [28].

3. Results

The calculations were carried out for three distinct atomic configurations of the Pb monolayer (ML) on a Ge(1 1 1) surface shown in Fig. 1. In the H_3 and T_4 geometries each Pb atom is located at the hollow sites of the Ge(1 1 1)-1 × 1 surface and interacts with three, first layer Ge atoms. The difference between these geometries is that in T_4 the Pb atoms are located above the second layer Ge atoms, while in H_3, above the fourth layer Ge atoms. In configuration T_1, the Pb atoms are placed directly above the topmost layer Ge atoms and each Pb interacts with one surface Ge atom.

Table 1
Calculated atomic distances and interlayer spacings (Δz) within the Pb/Ge (1 1 1) interface in configurations T_1, T_4, and H_3. The enumeration of Ge atoms is shown in Fig. 1.

Atom	Distance			Δz		
	T_1	T_4	H_3	T_1	T_4	H_3
	(Å)					
Pb-Ge(1)	2.754	3.129	3.053	2.754	2.109	1.996
Ge(1)-Ge(2)	2.462	2.530	2.516	0.851	1.030	0.997
Ge(2)-Ge(3)	2.453	2.487	2.466	2.487	2.487	2.466

The surfaces of configurations H_3 and T_4 are of p3m1 symmetry (the Pb adlayer and the first Ge layer being considered). In geometry T_1 the Pb atoms are directly on-top of the first Ge layer resulting in the p6mm symmetry of the two-layer structure. However, in this case first three atomic layers are to be included. It has been shown, that for the symmetry-equivalent surface T_1-Br/Ge(1 1 1)-1 × 1 the quasi-2D structure consists of the Br adlayer and two top atomic layers of the substrate, which give the surface a p3m1 symmetry [29,30] (compare the top views of the configurations shown in Fig. 1).

Geometry T_1 was found to be energetically the most favourable which agrees with experimental data [31]. This configuration is 0.178 and 0.213 eV lower in energy than geometries H_3 and T_4, respectively. The structural parameters of the calculated geometries are summarized in Table 1 and the corresponding electronic structures are shown in Fig. 2. The electronic structure of an isolated two-dimensional (2D) monolayer of Pb atoms (1ML-Pb) arranged in a hexagonal geometry with the lattice constant compatible with that for 1ML-Pb/Ge(1 1 1)-1 × 1 is also shown in the figure.

The electronic structures of 1ML-Pb with and without SOC are shown in Fig. 2a and b, respectively. In the structure without SOC (Fig. 2b), the states within the bands in the vicinity of the Fermi level (E_F) have $l = 1$ character (p type). Only one band, however, can be distinguished by the magnetic quantum number m_l (p_z) as the remaining two result from the in-plane interaction between the electrons in the p_x and p_y orbitals (denoted as p_x/p_y); see Fig. 2b, and also Table 2. The 2D crystal field (non-SOC case) does not couple the p_z and p_x/p_y orbitals so that the corresponding bands remain degenerate at the crossing points. By contrast, in the structure with SOC (Fig. 2a), the spin-orbit interaction couples the p_z and p_x/p_y states and the degeneracy at the crossing points is lifted, however, no spin-split bands are observed as the inversion symmetry of the isolated layer is preserved. When SOC is present, it would be customary to expand the electronic states around an atomic center with total angular momentum (j, m_j), rather than orbital angular momentum projections (l, m_l). As all the states within the bands of Fig. 2a are of $l = 1$ character, j and m_j can take the values of $\frac{1}{2}$ and $\frac{3}{2}$, and $\pm\frac{1}{2}$ and $\pm\frac{3}{2}$, respectively. As a result there are six possible (j, m_j) bands, however, due to lack of spin splitting, the bands in Fig. 2a are doubly degenerate with respect to m_j and are: $(\frac{1}{2}, \pm\frac{1}{2})$, $(\frac{3}{2}, \pm\frac{1}{2})$ and $(\frac{3}{2}, \pm\frac{3}{2})$ (see the color code in Fig. 2).

The electronic structures of the most stable configuration, T_1, with and without SOC, are shown in Fig. 2c and d, respectively. It is observed that in the band structure without SOC (Fig. 2d), the dispersion and binding energies of the bands of the Pb p_x/p_y character (16 and 17) located in the projected bulk band gap are essentially identical to that of the isolated Pb monolayer (Fig. 2b). This shows that these states are not part of the bonding structure of the Pb/Ge interface and that inversion asymmetry imposed by the Pb/Ge has little impact on the symmetry of these states. Fig. 3a and b, where the corresponding partial charge density are shown, illustrate this effect. Only the band of the Pb p_z character (18 in Fig. 2d) is affected by the interaction with the Ge dangling bonds (see Fig. 3c). As a result this band flattens and its binding energy is shifted down below the Fermi level. Analogous

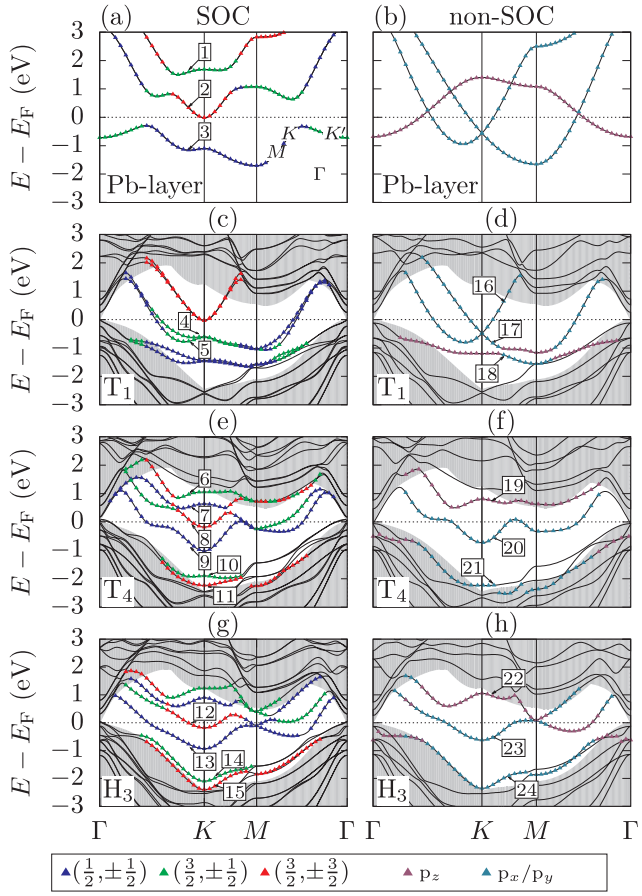

Fig. 2. SOC (left) and non-SOC (right) electronic band structures of (a,b) isolated Pb monolayer, (c,d) T_1, (e,f) T_4, and (g,f) H_3 configurations. The quantum numbers (j, m_j) and (l, m_l) indicating the character of the Pb induced surfaces states calculated with and without SOC, respectively; see bottom of the figure. SBZ is presented as an inset in (a). The shaded area represents the bulk Ge band structure projected on the [1 1 1] direction. The Fermi energy is at 0.0 eV.

Table 2
The s, p_z, p_{xy}, and d (total sum) projected wave function character of the Pb induced bands calculated at the K point for SOC band structures of (a) isolated monolayer (Fig. 5(a) and (b) configuration T_4 (Fig. 5e).

System	Band	s	p_z	p_x/p_y	d (total)
Pb	1	0.000	0.382	0.016	0.002
	2	0.000	0.010	0.324	0.008
	3	0.000	0.000	0.306	0.010
T_4	6	0.001	0.194	0.008	0.000
	7	0.000	0.144	0.070	0.000
	8	0.000	0.005	0.230	0.006
	9	0.000	0.024	0.236	0.004

behavior can be observed in the corresponding band structure with SOC (Fig. 2c). The bands $(\frac{1}{2}, \pm\frac{1}{2})$ and $(\frac{3}{2}, \pm\frac{3}{2})$, located in the bulk band gap, are virtually the same as those in the band structure of the isolated Pb monolayer (compare Fig. 2a and c); only the states within the $(\frac{3}{2}, \pm\frac{1}{2})$ band interact strongly with the substrate. Surprisingly, the inclusion of SOC, which is significant for Pb atom, and the inversion asymmetry of the Pb adlayer due to the adlayer-substrate interaction, have little impact on the electronic structure of the system, the two surface p_x/p_y bands of Pb separate slightly in energy at K, and only narrow regions—along Γ-K and M-Γ—exhibit a small, residual spin splitting.

The results for T_1 are unexpected. This is because the spin splitting of 0.2 eV has experimentally been observed in the 4/3 ML Pb/Ge(1 1 1)-$(\sqrt{3} \times \sqrt{3})R30°$ system and successfully reproduced by ab initio calculations [8]. It should be noted, however, that surface configuration can be decomposed to four Pb atoms per $(\sqrt{3} \times \sqrt{3})R30°$) unit cell with one adatom located at the H_3 site and the remaining three adatoms located on the off-centred bridge positions between the T_1 and T_4 sites. The fact that none of the Pb adatoms is located in the T_1 adsorption site suggests that an alteration of the bonding configuration at the Pb-Ge interface may induce a more prominent spin splitting. This is indeed the case for the Pb/Ge system studied here, as for the two energetically unfavorable configurations, T_4 and H_3—Fig. 2e and g, respectively—the electronic structures show: a spin split along M-Γ (also present in configuration T_1), and a new large spin splitting along the Γ-K-M direction. The M-Γ splitting is observed in all surface configurations, and thus can be associated with the inversion asymmetry of the Pb monolayer along z axis induced by the interface formation. However, this puts the mechanism of the Γ-K-M split at question as within the same system (differentiated only by the adsorption configuration) a large discrepancy in the SAM-split pattern is observed. This in itself poses an important problem to explore, as on surfaces comprised by the same atom types, and having the same surface symmetry (p3m1) one would expect to observe the same magnitude of Zeeman-like SAM splitting of corresponding surface stats. Thus, further insight into the system is instructive, in order to understand the underlining physics behind the Γ-K-M splitting.

Both the SOC and non-SOC electronic structures of T_4 and H_3 share similar band topology and the corresponding SOC structures exhibit comparable magnitude of spin-splitting—0.83 and 0.75 eV at the K point between bands 8 and 9 (T_4, Fig. 2e) and bands 12 and 13 (H_3, Fig. 2g). These similarities occur because the T_4 and H_3 geometries exhibit the same type of the Pb-Ge interaction—the p_x/p_y(Pb)-p_z(Ge) bonding takes place instead of the p_z(Pb)-p_z(Ge) one identified in configuration T_1—see Fig. 3d–f for T_4 and Fig. 3g–i for H_3. This indicates that the splitting on the Ge(1 1 1)-1 × 1 surface may be either significantly enhanced or completely suppressed depending on the bonding configuration of the Pb/Ge interface.

It should also be noted that in the T_4 (H_3) non-SOC band structures (Fig. 2f and h), the topology of the Pb bands representing the states that are not utilized in the Pb/Ge bonding configuration are very similar to the corresponding bands in the SOC band structure of the isolated monolayer (Fig. 2a). The only difference is that in the monolayer, the coupling between the p_x/p_y and p_z atomic orbitals is due to the spin-orbit interaction of electrons in Pb, while in the non-SOC T_4 (H_3) band structures, the degeneracy at the crossing points is lifted by the crystal field at the interface (in both cases the p_z-dominated band has a p_{xy}-type contribution, see Table 2 for SOC T_4 composition). Also, in the non-SOC band structures the bands have (l, m_l) representation and when SOC is included in the calculations for T_4 (H_3), the spin degeneracy is lifted between states of the same m_l—compare Fig. 5f and e (T_4), and Fig. 2h and g (H_3); see also Table 2. It is clear therefore, that the Γ-K-M spin splitting originate from Pb atomic SOC rather than the Zeeman-like effect where a splitting of degenerated j states over values of m_j would be expected.

Fig. 4 shows the spin-texture maps of the metallic bands of configurations T_1 and T_4 (H_3 has qualitatively the same pattern as T_4 and is not shown). The SAM vectors in the spin-split bands of configuration T_4 are aligned with the z axis in the vicinity of the K(K') points, while at point M where the states are degenerate and the SAM polarization vector rotates in x-y plane with an insignificant z component. In the map for configuration T_1 (Fig. 4a and b) no correlation of the orientation of the spin vector at K and M is observed.

The fact that in the DFT calculations the spin splitting is directly linked with the presence of atomic SOC leads us to the conclusion that the observed phenomenon may be of Rashba type and its origin could be elucidated within the so-called OAM approach. Within this model both, the atomic SOC ($\widehat{H}_{SOC} = \alpha \boldsymbol{L}\cdot\boldsymbol{S}$), where α is SOC strength, and the electric-dipole/electric-field interaction $\widehat{H}_{E_s} = \beta(\boldsymbol{k}_{\parallel} \times \boldsymbol{L})\cdot\boldsymbol{E}_s$, where β is

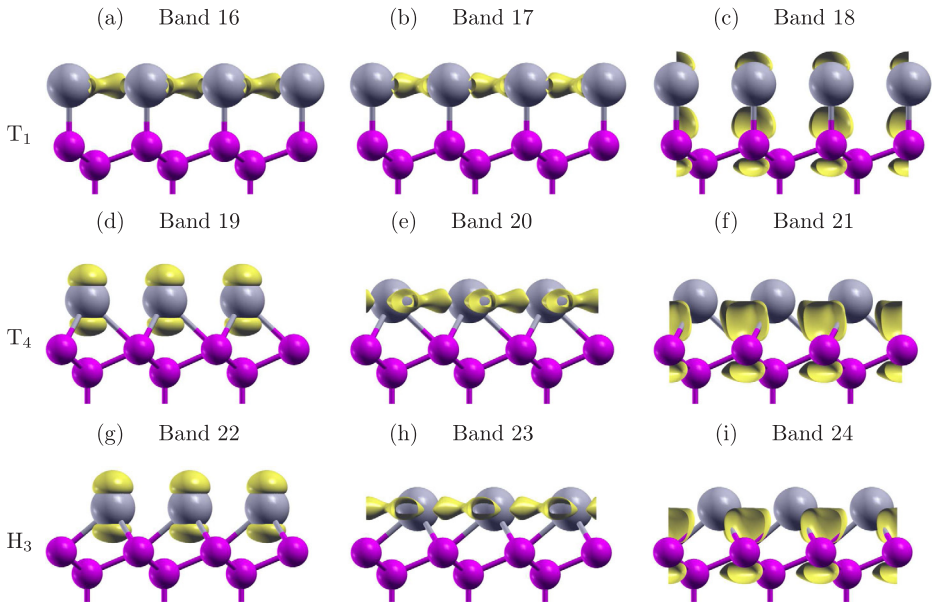

Fig. 3. Partial charge and probability densities ($|\Psi|^2$) calculated for the Pb-induced states at point *K* for bands 16–24 in Fig. 5d, f and h. Isosurface value: 0.005 e/a.u.^{3}. Atoms are represented as in Fig. 1.

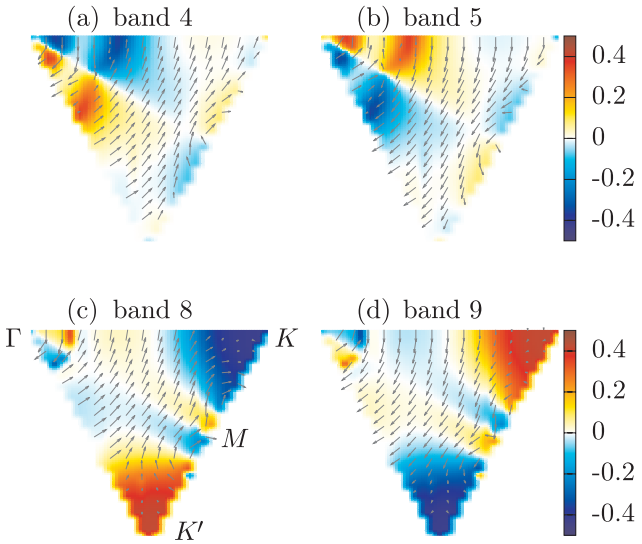

Fig. 4. Spin vector $\langle \boldsymbol{S} \rangle$ projected onto the *x*-*y* plane (arrows) and *z* axis (color bar) of the T_1 (a,b) and T_4 (c,d) configurations. Spin mapped between Γ–*K*–*K*′ (see inset Fig. 5a for reference). High symmetry points are indicated in (c). Bands 4, 5 and 8, 9 are marked in Fig. 5c and e.

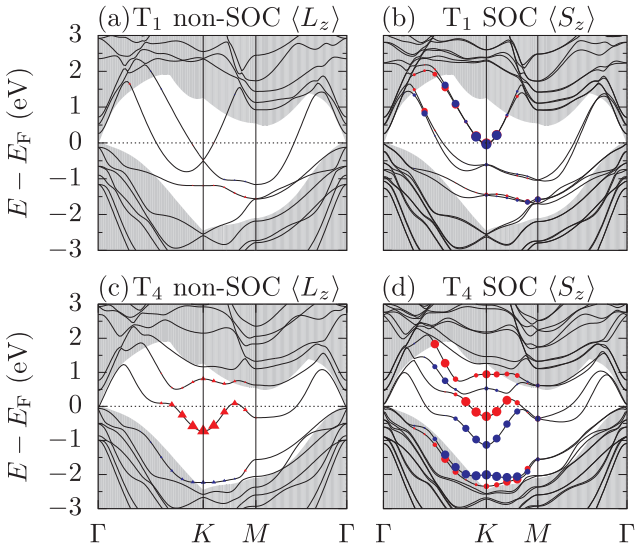

Fig. 5. Electronic structure of the Pb/Ge(1 1 1)-1×1 system in configurations T_1 (a,b), and T_4 (c,d) with the $\langle L_z \rangle$, and $\langle S_z \rangle$ projections mapped on the Pb-type bands within the Ge bulk-band gap. Red and blue indicate the up and down polarization of both vectors, respectively.

a constant determined by overlap between adjacent atomic orbitals and $\boldsymbol{E}_s$ is a surface electric field, contribute to the energetics of the spin split bands. In the latter equation the product $\boldsymbol{k}_{\|} \times \boldsymbol{L}$ represents an electric-dipole vector formed by an asymmetric charge in the direction perpendicular to the ($\boldsymbol{k}_{\|}$, $\boldsymbol{L}_z$) plane.

To take into account the effect of SOC and the dipole energy explicitly the model requires a nonzero atomic orbital momentum $\boldsymbol{L}$. In periodic systems, however, the atomic $\boldsymbol{L}$ is usually quenched due to the crystal field that facilitates mixing of wave functions with opposite m_l, forming electronic states with effective OAM ~ 0. The unquenched OAM in such systems can arise, however, due to an inversion asymmetry, which breaks the parity between atomic orbitals and facilitates the nearest-neighbor hopping between orbital pairs [17]. Fig. 5 shows the T_1 and T_4 band structures with the orbital angular momentum (Fig. 5a and c) and spin angular momentum (Fig. 5b and d) calculated for the Pb-induced gap states (the patterns for H_3 are qualitatively the same as for T_4 and are not shown). One observes that in configuration T_1 the electronic states in the gap exhibit virtually no OAM (Fig. 5a) resulting in both $\widehat{H}_{\mathrm{SOC}}$ and $\widehat{H}_{E_s}$ being zero and the corresponding electronic states spin-degenerate. By contrast, the $T_4(H_3)$ band structure of Fig. 5b has large unquenched OAM in the vicinity of the *K* point and polarized along the *z* axis, $\langle L_z \rangle$ (the $\langle L_x \rangle$ and $\langle L_y \rangle$ projections are small and present only in narrow regions along Γ-*K* and *M*-Γ). This shows that in the vicinity of *K* $\langle n, \boldsymbol{k}_{\|} | \widehat{H}_{\mathrm{SOC}} | n, \boldsymbol{k}_{\|} \rangle = \langle n, \boldsymbol{k}_{\|} | \alpha \boldsymbol{L} \cdot \boldsymbol{S} | n, \boldsymbol{k}_{\|} \rangle = \langle n, \boldsymbol{k}_{\|} | \alpha \boldsymbol{L}_z \cdot \boldsymbol{S}_z | n, \boldsymbol{k}_{\|} \rangle \neq 0$, i.e, the orientations of the $\boldsymbol{L}$ and $\boldsymbol{S}$ vectors are correlated. This is indeed the case—the unquenched $\langle L_z \rangle$ aligns with the parallel (antiparallel) SAM vector at the *K* point (compare Fig. 5b and d with a and c, respectively; see also Fig. 4c and d). The contribution to the energetics of spin-split bands from the electric dipole is expected to be negligible. The spin-split 6*p* states of Pb decoupled form the Ge(1 1 1) interface are shown not to facilitate a large assymetric charge distribution leading to the formation

of an electric dipole at the Pb/Ge surface (see Fig. 3a,b,d,e,g and h). This being a result of low overlap between the adjacent atomic orbitals [13]. However, even if a non-zero electric dipole is formed, an asymmetric charge observed in the direction perpendicular to the ($\boldsymbol{k}_{\|}$, $\boldsymbol{L}_z$) plane, interacting with the electric field $\boldsymbol{E}_s$ which has only z component gives: $\langle n, \boldsymbol{k}_{\|}|\widehat{H}_{E_s}|n, \boldsymbol{k}_{\|}\rangle = 0$. As accounted by the OAM approach, the emergence of the unquenched OAM in configuration T_4 (H_3) and its lack in configuration T_1 is the sole reason behind the qualitatively different spin-split patterns observed in the system. Here, the unquenched OAM is facilitated by the chemical interaction between the Pb monolayer and the Ge(1 1 1) surface, where one of the p_x/p_y orbitals of Pb bond covalently with the p_z orbitals of first layer Ge atom. This breaks the mirror symmetry plane within the Pb monolayer along the Γ-*K* and *K*-*M* directions effectively decoupling states comprised with wave functions of opposite m_l, which allows for unquenched $\langle L_z\rangle$. This find collaborates with our prediction of an asymmetry-induced spin splitting in a Pb/Si(1 1 1) system by means of chemical bonding at the interface[7]. It also elaborates on the proposed mechanism of the spin splitting, $\boldsymbol{\sigma}\cdot\boldsymbol{B} \sim \boldsymbol{L}\cdot\boldsymbol{S}$, expanding the physical context in which the impact of asymmetry in the system can be considered, and linking it with the unquenched OAM.

Finally, considering the substantial values of angular momentum vectors $\langle \boldsymbol{L}_z\rangle$ [0.76 $\hbar$ (T_4), 0.68 $\hbar$ (H_3)] and $\langle \boldsymbol{S}_z\rangle$ (0.5 $\hbar$) at the *K* point observed in the metallic bands, and the spin-orbit interaction strength between $6p_{1/2}$ and $6p_{3/2}$ levels of a free Pb atom[32,33] (Δ_{SOC} = 1.75 eV, $\alpha_{6p}^{Pb} = 1.17$ eV/$\hbar^2$), the predicted splittings, $\Delta = \langle\widehat{H}_{SOC}\rangle_{p_{3/2}} - \langle\widehat{H}_{SOC}\rangle_{p_{1/2}} \approx 2\alpha_{6p}^{Pb}\langle \boldsymbol{L}_z\rangle\langle \boldsymbol{S}_z\rangle$, are 0.89 (bands 8 and 9) and 0.79 eV (bands 12 and 13) for configurations T_4 and H_3, respectively, which is in good agreement with the DFT data. We conclude therefore, that within the OAM approach to Rashba effect, the splitting observed in configurations T_4 and H_3 in the vicinity of the *K* point is indeed predominantly governed by SOC, and that the OAM model predicts accurately magnitude of the spin-split it the Pb/Ge(1 1 1)-1 × 1 adsorption system.

4. Conclusions

In conclusion, we investigated the spin-split pattern observed in a number of stable surface configurations of the Pb/Ge(1 1 1)-1 × 1 adsorption system. The DFT data showed that the spin-split patterns in geometries T_4 and H_3, and its lack in configuration T_1, originate from the bonding structure at the Pb/Ge interface. These observations were also correlated with the emergence of unquenched adatom OAM. The spin split of the adatom induced electronic states was identified to be of Rashba type and its mechanism elucidated within the atom orbital magnetic moment approach. Both the OAM Rashba model and the DFT results are consistent in predicting that the observed band spin splitting originates from the atomic SOC.

5. Declarations of interest

None.

Acknowledgments

This research was supported by PL-Grid infrastructure and the Interdisciplinary Centre for Mathematical and Computational Modelling (ICM) University of Warsaw under grant nr Grant No. G44-10. M.W.R. acknowledges the Polish Ministry of Science and Higher Education for support (Grant No. 06/62/DSPB/2183). B.P. and L.J. acknowledge the support from Grant No.1010/S/IFD/17.

References

[1] I. Gierz, T. Suzuki, E. Frantzeskakis, S. Pons, S. Ostanin, A. Ernst, J. Henk, M. Grioni, K. Kern, C.R. Ast, Silicon surface with giant spin splitting, Phys. Rev. Lett. 103 (2009) 046803, https://doi.org/10.1103/PhysRevLett.103.046803 https://link.aps.org/doi/10.1103/PhysRevLett.103.046803.

[2] S. Hatta, T. Aruga, Y. Ohtsubo, H. Okuyama, Large rashba spin splitting of surface resonance bands on semiconductor surface, Phys. Rev. B 80 (2009) 113309, https://doi.org/10.1103/PhysRevB.80.113309 https://link.aps.org/doi/10.1103/PhysRevB.80.113309.

[3] J. Ibañez-Azpiroz, A. Eiguren, A. Bergara, Relativistic effects and fully spin-polarized fermi surface at the tl/Si(1 1 1) surface, Phys. Rev. B 84 (2011) 125435, https://doi.org/10.1103/PhysRevB.84.125435 https://link.aps.org/doi/10.1103/PhysRevB.84.125435.

[4] L.V. Bondarenko, D.V. Gruznev, A.A. Yakovlev, A.Y. Tupchaya, D. Usachov, O. Vilkov, A. Fedorov, D.V. Vyalikh, S.V. Eremeev, E.V. Chulkov, A.V. Zotov, A.A. Saranin, Large spin splitting of metallic surface-state bands at adsorbate-modified gold/silicon surfaces 3 (2013) 1826 EP –, article. URL: https://doi.org/10.1038/srep01826.

[5] I. Yakovkin, N. Petrova, DFT study of Sb and Pb layers on the Bi(1 1 1) surface, Appl. Surf. Sci. 445 (2018) 154–160, https://doi.org/10.1016/j.apsusc.2018.03.152 http://www.sciencedirect.com/science/article/pii/S0169433218308389.

[6] M. Kopciuszynski, M. Krawiec, R. Zdyb, M. Jalochowski, Purely one-dimensional bands with a giant spin-orbit splitting: Pb nanoribbons on si(553) surface. Scientific Reports 7 (2017) 46215 EP –, article. URL: https://doi.org/10.1038/srep46215.

[7] B. Pieczyrak, M. Szary, L. Jurczyszyn, M.W. Radny, Spin polarization of two-dimensional electronic gas decoupled from structural asymmetry environment, Phys. Rev. B 93 (2016) 195318, https://doi.org/10.1103/PhysRevB.93.195318 https://link.aps.org/doi/10.1103/PhysRevB.93.195318.

[8] K. Yaji, Y. Ohtsubo, S. Hatta, H. Okuyama, K. Miyamoto, T. Okuda, A. Kimura, H. Namatame, M. Taniguchi, T. Aruga, Large rashba spin splitting of a metallic surface-state band on a semiconductor surface 1 (2010) 17 EP –, article. URL https://doi.org/10.1038/ncomms1016.

[9] K. Sakamoto, T. Oda, A. Kimura, K. Miyamoto, M. Tsujikawa, A. Imai, N. Ueno, H. Namatame, M. Taniguchi, P.E.J. Eriksson, R.I.G. Uhrberg, Abrupt rotation of the rashba spin to the direction perpendicular to the surface, Phys. Rev. Lett. 102 (2009) 096805, https://doi.org/10.1103/PhysRevLett.102.096805 https://link.aps.org/doi/10.1103/PhysRevLett.102.096805.

[10] G. Bihlmayer, S. Blügel, E.V. Chulkov, Enhanced rashba spin-orbit splitting in BiAg (1 1 1) and PbAg(1 1 1) surface alloys from first principles, Phys. Rev. B 75 (2007) 195414, https://doi.org/10.1103/PhysRevB.75.195414 https://link.aps.org/doi/10.1103/PhysRevB.75.195414.

[11] M. Nagano, A. Kodama, T. Shishidou, T. Oguchi, A first-principles study on the rashba effect in surface systems, J. Phys.: Condens. Matter 21 (6) (2009) 064239 http://stacks.iop.org/0953-8984/21/i=6/a=064239.

[12] S.R. Park, C.H. Kim, J. Yu, J.H. Han, C. Kim, Orbital-angular-momentum based origin of rashba-type surface band splitting, Phys. Rev. Lett. 107 (2011) 156803, https://doi.org/10.1103/PhysRevLett.107.156803 https://link.aps.org/doi/10.1103/PhysRevLett.107.156803.

[13] J.-H. Park, C.H. Kim, J.-W. Rhim, J.H. Han, Orbital rashba effect and its detection by circular dichroism angle-resolved photoemission spectroscopy, Phys. Rev. B 85 (2012) 195401, https://doi.org/10.1103/PhysRevB.85.195401 https://link.aps.org/doi/10.1103/PhysRevB.85.195401.

[14] B. Kim, C.H. Kim, P. Kim, W. Jung, Y. Kim, Y. Koh, M. Arita, K. Shimada, H. Namatame, M. Taniguchi, J. Yu, C. Kim, Spin and orbital angular momentum structure of Cu(1 1 1) and Au(1 1 1) surface states, Phys. Rev. B 85 (2012) 195402, https://doi.org/10.1103/PhysRevB.85.195402 https://link.aps.org/doi/10.1103/PhysRevB.85.195402.

[15] B. Kim, P. Kim, W. Jung, Y. Kim, Y. Koh, W. Kyung, J. Park, M. Matsunami, S.-i. Kimura, J.S. Kim, J.H. Han, C. Kim, Microscopic mechanism for asymmetric charge distribution in rashba-type surface states and the origin of the energy splitting scale, Phys. Rev. B 88 (2013) 205408, https://doi.org/10.1103/PhysRevB.88.205408 https://link.aps.org/doi/10.1103/PhysRevB.88.205408.

[16] S. Jakobs, A. Ruffing, M. Cinchetti, S. Mathias, M. Aeschlimann, Orbital angular momentum structure of an unoccupied spin-split quantum-well state in Pb/Cu (1 1 1), Phys. Rev. B 87 (2013) 235438, https://doi.org/10.1103/PhysRevB.87.235438 https://link.aps.org/doi/10.1103/PhysRevB.87.235438.

[17] S. Oh, H.J. Choi, Orbital angular momentum analysis for giant spin splitting in solids and nanostructures, Scientific Reports 7 (1) (2017) 2024, https://doi.org/10.1038/s41598-017-02032-4.

[18] P. Giannozzi, S. Baroni, N. Bonini, M. Calandra, R. Car, C. Cavazzoni, D. Ceresoli, G.L. Chiarotti, M. Cococcioni, I. Dabo, A.D. Corso, S. de Gironcoli, S. Fabris, G. Fratesi, R. Gebauer, U. Gerstmann, C. Gougoussis, A. Kokalj, M. Lazzeri, L. Martin-Samos, N. Marzari, F. Mauri, R. Mazzarello, S. Paolini, A. Pasquarello, L. Paulatto, C. Sbraccia, S. Scandolo, G. Sclauzero, A.P. Seitsonen, A. Smogunov, P. Umari, R.M. Wentzcovitch, Quantum espresso: a modular and open-source software project for quantum simulations of materials, J. Phys.: Condens. Matter 21 (39) (2009) 395502 http://stacks.iop.org/0953-8984/21/i=39/a=395502.

[19] D. Vanderbilt, Soft self-consistent pseudopotentials in a generalized eigenvalue formalism, Phys. Rev. B 41 (1990) 7892–7895, https://doi.org/10.1103/PhysRevB.41.7892 https://link.aps.org/doi/10.1103/PhysRevB.41.7892.

[20] J.P. Perdew, A. Zunger, Self-interaction correction to density-functional approximations for many-electron systems, Phys. Rev. B 23 (1981) 5048–5079, https://doi.org/10.1103/PhysRevB.23.5048 https://link.aps.org/doi/10.1103/PhysRevB.23.5048.

[21] H.J. Monkhorst, J.D. Pack, Special points for brillouin-zone integrations, Phys. Rev. B 13 (1976) 5188–5192, https://doi.org/10.1103/PhysRevB.13.5188 https://link.aps.org/doi/10.1103/PhysRevB.13.5188.

[22] P. Haas, F. Tran, P. Blaha, Calculation of the lattice constant of solids with semilocal functionals, Phys. Rev. B 79 (2009) 085104, https://doi.org/10.1103/PhysRevB.

79.085104 https://link.aps.org/doi/10.1103/PhysRevB.79.085104.
[23] T. Ozaki, Variationally optimized atomic orbitals for large-scale electronic structures, Phys. Rev. B 67 (2003) 155108, https://doi.org/10.1103/PhysRevB.67.155108 https://link.aps.org/doi/10.1103/PhysRevB.67.155108.
[24] M.C. Neale, M.D. Hunter, J.N. Pritikin, M. Zahery, T.R. Brick, R.M. Kirkpatrick, R. Estabrook, T.C. Bates, H.H. Maes, S.M. Boker, OpenMx 2.0: Extended structural equation and statistical modeling, Psychometrika 81 (2) (2016) 535–549, https://doi.org/10.1007/s11336-014-9435-8.
[25] J.N. Pritikin, M.D. Hunter, S.M. Boker, Modular open-source software for Item Factor Analysis, Educ. Psychol. Measur. 75 (3) (2015) 458–474.
[26] M.D. Hunter, State space modeling in an open source, modular, structural equation modeling environment. Structural Equation Modeling (in press) 1–18. doi: 10.1080/10705511.2017.1369354.
[27] S.M. Boker, M.C. Neale, H.H. Maes, M.J. Wilde, M. Spiegel, T.R. Brick, R. Estabrook, T.C. Bates, P. Mehta, T. von Oertzen, R.J. Gore, M.D. Hunter, D.C. Hackett, J. Karch, A.M. Brandmaier, J.N. Pritikin, M. Zahery, R.M. Kirkpatrick, Y. Wang, C. Driver, Massachusetts Institute of Technology, S.G. Johnson, Association for Computing Machinery, D. Kraft, S. Wilhelm, Manjunath B G, OpenMx 2.9.6 User Guide, 2018.
[28] N. Troullier, J.L. Martins, Efficient pseudopotentials for plane-wave calculations, Phys. Rev. B 43 (1991) 1993–2006, https://doi.org/10.1103/PhysRevB.43.1993 https://link.aps.org/doi/10.1103/PhysRevB.43.1993.
[29] T. Aruga, Different types of rashba spin-split surface states on Ge(1 1 1), J. Electron. Spectrosc. Relat. Phenom. 201 (2015) 74–80, https://doi.org/10.1016/j.elspec.2014.10.004 http://ci.nii.ac.jp/naid/120005674614/en/.
[30] Y. Ohtsubo, S. Hatta, N. Kawai, A. Mori, Y. Takeichi, K. Yaji, H. Okuyama, T. Aruga, Spin-polarized surface states on br/Ge(1 1 1)-(1 × 1): surface spin polarization without heavy elements, Phys. Rev. B 86 (2012) 165325, https://doi.org/10.1103/PhysRevB.86.165325 https://link.aps.org/doi/10.1103/PhysRevB.86.165325.
[31] I.-S. Hwang, J.A. Golovchenko, Phase transition of monolayer Pb/Ge(1 1 1): β-$\sqrt{3} \times \sqrt{3}$r30° ⇆ 1 × 1 at 180°C, Phys. Rev. B 50 (1994) 18535–18542, https://doi.org/10.1103/PhysRevB.50.18535 https://link.aps.org/doi/10.1103/PhysRevB.50.18535.
[32] D.R. Wood, K.L. Andrew, Arc spectrum of lead*, J. Opt. Soc. Am. 58 (6) (1968) 818–829, https://doi.org/10.1364/JOSA.58.000818 http://www.osapublishing.org/abstract.cfm?URI=josa-58-6-818.
[33] L. Ley, S.P. Kowalczyk, F.R. McFeely, D.A. Shirley, Crystal-field effects on the apparent spin-orbit splitting of core and valence levels observed by x-ray photoemission, Phys. Rev. B 10 (1974) 4881–4888, https://doi.org/10.1103/PhysRevB.10.4881 https://link.aps.org/doi/10.1103/PhysRevB.10.4881.

P3. Role of coupling between surface orbitals in SOC enhanced spin splitting

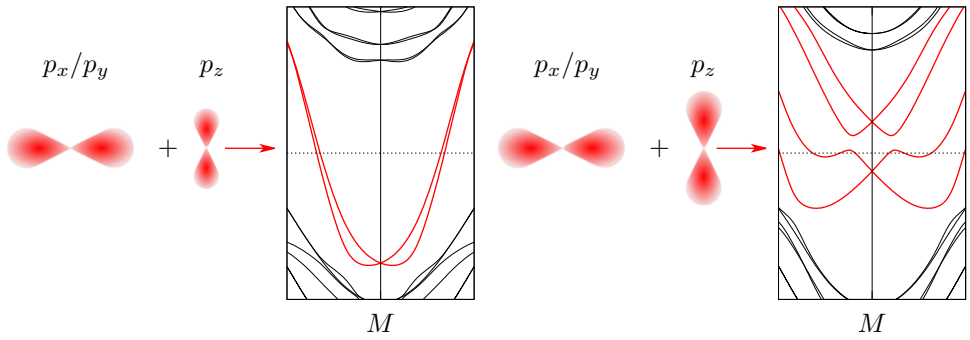

Surface Science 684 (2019) 12–17

Contents lists available at ScienceDirect

Surface Science

journal homepage: www.elsevier.com/locate/susc

Role of coupling between surface orbitals in SOC enhanced spin splitting

Maciej J. Szary

Institute of Physics, Poznan University of Technology, Poznan 62-965, Poland

ARTICLE INFO

Keywords:
Spin angular momentum
Orbital angular momentum
Spin-orbit coupling
Surface orbital coupling
Rashba effect
Density functional theory

ABSTRACT

In this study we investigate the role of coupling between surface orbitals in a giant spin splitting (GSS) observed in the Pb/Ge(111)-1 × 1 adsorption system along $\Gamma - M - \Gamma'$. We report, based on the density functional theory that, the magnitude of the GSS depends on the bonding structure of the Pb/Ge interface, varying from 242 to 667 meV for the metallic surface bands. The splitting is shown to be SOC enhanced, with ~ 93% of the effect being of SOC origin. The split-energy difference observed in the system is a result of a different coupling strength between p_x/p_y(Pb) and p_z(Pb) orbitals, which produces corresponding values of unquenched orbital angular momentum. The described spin-split pattern corresponds to those observed in Tl/Si(111)-1 × 1, Bi/Si(111)-$(\sqrt{3} \times \sqrt{3})R30°$, and 4/3ML Pb/Ge(111)-$(\sqrt{3} \times \sqrt{3})R30°$, which suggests that, their GSS may also be SOC enhanced.

1. Introduction

Spin angular momentum (SAM, or simply spin) splitting of electronic bands in nonmagnetic systems occurs when an inversion symmetry of a crystal structure is broken e.g. by an external electric field or a surface. In most systems the effect is small (typically between 0.01 and -1 meV), however, in some cases a giant spin splitting (GSS) is produce reaching values in excess of 100 meV. GSS of surface electronic states has been reported for a number of surfaces decorated with heavy atoms [1–9]. Among them Ge(111) and Si(111) surfaces with Pb overlays were shown to exhibit a spin splitting of metallic surface bands ranging between 200 and 830 meV [10–13], which makes them promising candidates for spin-polarized current transport [10,14].

SAM polarization and corresponding GSS have been commonly understood within the workframe provided by the Rashba model [15,16]. According to it electrons moving in presence of an electric field of a surface ($\boldsymbol{E}_s$) may exhibit a momentum-dependent splitting, which originates from a Zeeman-like interaction $\hat{H}_R = \alpha_R(\boldsymbol{k} \times \boldsymbol{E}_s)\cdot\boldsymbol{S}$, where α_R, $\boldsymbol{k}$, and $\boldsymbol{S}$ are the Rashba parameter, electron wavevector, and spin vector, respectively. Further studies have shown that the effect may be further enhanced by factors such as: (i) charge density distribution along the surface normal in the vicinity of the nuclei [10,17], (ii) in-plane inversion asymmetry of both structure [18] and charge [12], (iii) and strong atomic spin-orbit coupling (SOC) [19–22]. However, the exact mechanism behind the effect remains still under debate [2,23–26].

It has been shown that, for the ground-state surface configuration of the Pb/Ge(111)-1 × 1 adsorption system, the p_x/p_y bands remains spin degenerated at the K point of the surface Brillouin zone despite broken $x - y$ mirror symmetry plane of the Pb monolayer [13]. In contrast, those same states in the higher-energy configurations exhibit a GSS at K. This intriguing effect was show to originate from the unquenched orbital angular momentum (OAM or $\boldsymbol{L}$). In vicinity of K large values of $\boldsymbol{L}_z$ arise due to broken symmetry of the Pb–Pb bonding within the monolayer thus, making the effect an exclusive property of p6mm-symmetry monolayers with planar p_x/p_y-type bonding.

In this study, we investigate the role of coupling between surface orbitals in the mechanism of SOC enhanced spin splitting, which was not elucidated in our previous work [13]. We give a detailed explanation for the mechanism behind the formation of the unquenched OAM in the system, and we describe key features of electronics structures indicating SOC enhanced splitting. In this report, we investigate the spin splitting along the $\Gamma - M - \Gamma'$ direction in the Pb/Ge(111)-1 × 1 adsorption system. The study was conducted for three distinct surface configurations of the Pb/Ge interface. Contrasting the effect observed at K, in all of them a GSS of metallic surface bands has been observed. Furthermore, the split values show a large discrepancy depending on the surface configuration. It is shown that the effect does not originate from the different parity of the p_x and p_y orbitals, but rather one between p_x/p_y and p_z orbitals, which stems form the electric field of the substrate. This gives rise to large values of unquenched $\boldsymbol{L}_x/\boldsymbol{L}_y$ along $\Gamma - M - \Gamma'$, which produce GSS predominantly by SOC of 6p electrons of Pb (~ 93%). The effect does not originate from any exclusive property of the Pb monolayer, and thus the described mechanism may be applicable to other p-type adsorption systems e.g. Tl/Si(111)-1 × 1 [27–29], Bi/Si(111)-$(\sqrt{3} \times \sqrt{3})R30°$ [30], and 4/3ML Pb/

E-mail address: maciej.s.szary@doctorate.put.poznan.pl.

https://doi.org/10.1016/j.susc.2019.02.004
Received 10 November 2018; Received in revised form 6 February 2019
Available online 12 February 2019

Ge(111)-($\sqrt{3} \times \sqrt{3}$)$R30°$ [10,31], where analogous splitting of *p*-dominated bands along Γ–*M* has been reported.

2. Methods

The first-principles density-functional theory (DFT) calculations of total-energy and electronic structure have been performed using the Quantum Espresso code [32]. The plane-waves method, with Generalized Gradient Approximation (GGA) of Perdew–Burke–Ernzerhof [33,34], and Projector Augmented Wave (PAW) potentials [35,36] was used for solving the Kohn–Sham equations. A 12 × 12 × 1 Monkhorst-Pack grid scheme [37] was used to sample the surface Brillouin zone. OAM structures were calculated in OpenMX code [38–41], with norm-conserving pseudopotentials [42]. The Pb/Ge (111)-1 × 1 structure was modeled using repeated slab (see Fig. 1) and 20 Å of vacuum in the *z* axis. We employed the optimized bulk Ge lattice constant of 5.69 Å (the experimental values are reported between 5.64 and 5.66 Å [43–45]). In the total-energy calculations the five topmost slab layers were fully optimized in presence of SOC and with the adopted convergence threshold on forces of less than 10^{-5} Ry/au.

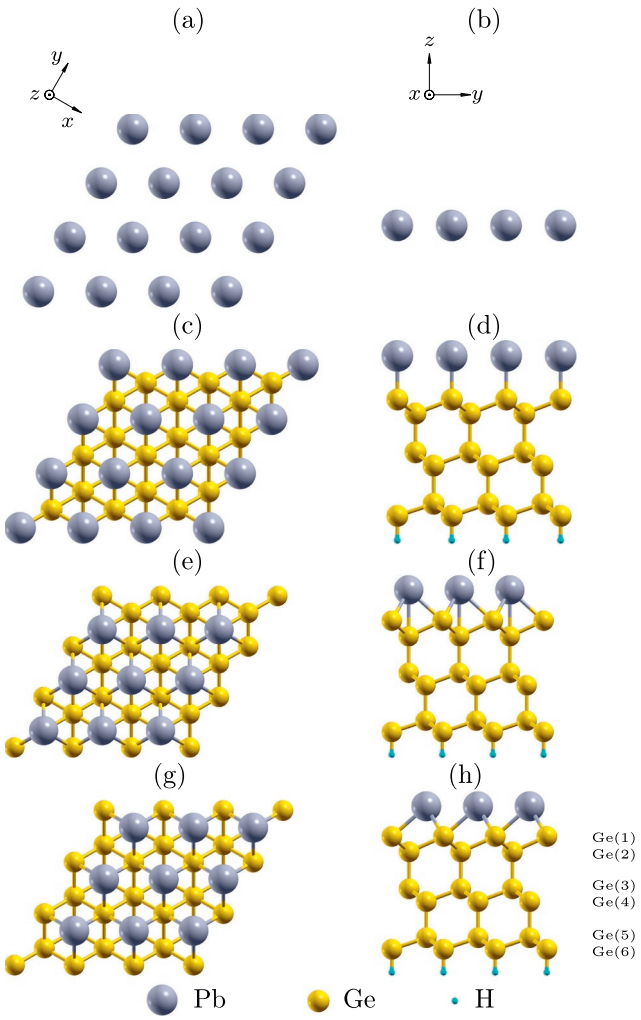

Fig. 1. Top (a,c,e,g) and side (b,d,f,h) views of atomic structures of isolated Pb monolayer (a,b) and configurations T_1 (c,d), T_4 (e,f) and H_3 (g,h) of the Pb/Ge adsorption system. The coordinate system is shown in figures (a) and (b). The numeration of Ge atoms is shown in (h).

Table 1
Atomic distances and interlayer spacings (Δz) of configurations T_1, T_4, and H_3. The atomic numeration is shown in Fig. 1h.

Atom	distance			Δz		
	T_1 (Å)	T_4	H_3	T_1	T_4	H_3
Pb–Ge(1)	2.767	3.147	3.089	2.767	2.136	2.050
Ge(1)–Ge(2)	2.489	2.533	2.521	0.925	1.038	1.008
Ge(2)–Ge(3)	2.445	2.485	2.473	2.445	2.485	2.473
Ge(3)–Ge(4)	2.467	2.457	2.457	0.865	0.833	0.835
Ge(4)–Ge(5)	2.432	2.432	2.432	2.432	2.432	2.432
Ge(5)–Ge(6)	2.437	2.437	2.437	0.774	0.774	0.774

3. Results

Fig. 2a shows non-SOC band structures of an isolated monolayer of Pb (1ML-Pb) calculated along the Γ − *M* − Γ′ path (see the bottom of Fig. 2). The monolayer has two metallic bands in vicinity of the Fermi level, both comprised of 6*p* orbitals. One band consists solely of p_z orbitals, which remain unbonded in the monolayer. The other is a combination of p_x and p_y orbitals that, take part in the formation of covalent bonds in the monolayer plane. The crystal field of 1ML-Pb does not

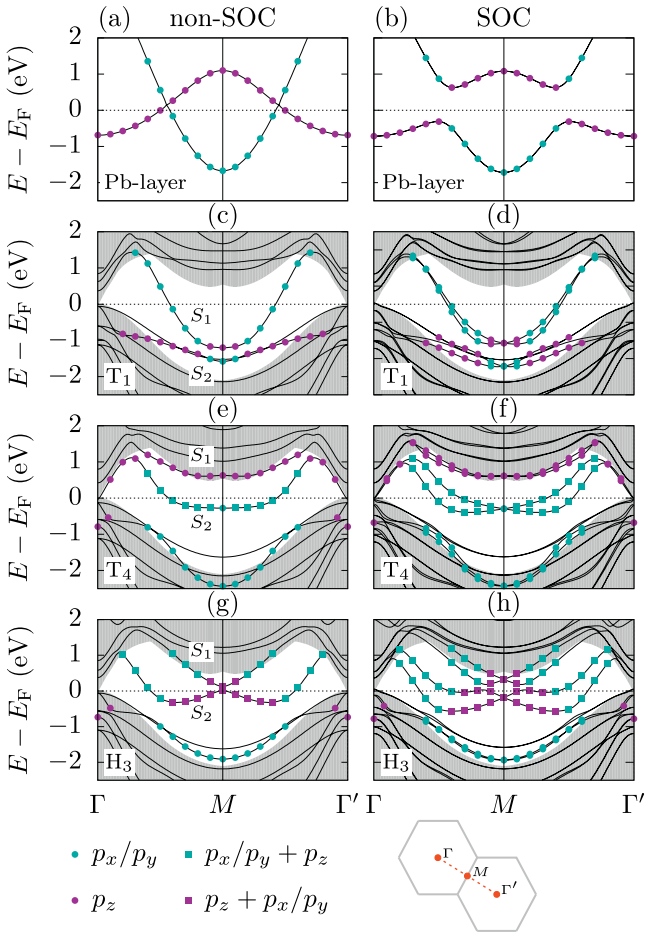

Fig. 2. Electronic band structures of 1ML-Pb (a,b), and the Pb/Ge adsorption system in configurations T_1 (c,d), T_4 (e,f) and H_3 (g,h) calculated along the Γ − *M* − Γ′ path (see bottom of the figure). The electronics structures are mapped with the projections onto the atomic orbitals of Pb. The corresponding color code is shown at the bottom of the figure. Orbital order indicates the dominant component. Mixed orbitals represent electronic states with significant coupling. The shaded area represents the projection of the bulk band gap on the [111] direction. The bands of interest are listed as S_1 (upper), and S_2 (lower).

Table 2
Electronic wavefunctions of band S_1 and S_2 projected onto p_x/p_y and p_z atomic orbitals of Pb. Values calculated at three different $\boldsymbol{k}$ points along $\Gamma - M$. Values for T_1 at 0.481 Å^{-1} represent a section where bands S_1 and S_2 overlap and orbitals comprising the electronic states are mixed.

	0.577 Å^{-1} (M)					
	T_1		T_4		H_3	
	p_x/p_y	p_z	p_x/p_y	p_z	p_x/p_y	p_z
S_1	0.05	0.31	0.06	0.72	0.18	0.58
S_2	0.80	0.05	0.38	0.04	0.44	0.48
			0.481 Å^{-1}($\Gamma - M$)			
S_1	0.4	0.17	0.06	0.56	0.32	0.32
S_2	0.46	0.21	0.42	0.16	0.28	0.67
			0.385 Å^{-1} ($\Gamma - M$)			
S_1	0.81	0.02	0.06	0.41	0.34	0.18
S_2	0.06	0.35	0.56	0.32	0.29	0.65

couple the p_z and p_x/p_y orbitals, resulting in the bands being degenerated at their crossing points. The degeneracy, however, is lifted in presence of SOC (see Fig. 2b). SOC introduces a coupling between p_z and p_x/p_y orbitals such that, the bands in the vicinity of the Fermi level still retain their dominant p_z or p_x/p_y character, however, they now have also non-zero contributions of the other p-type orbital (~ 5%). Upon adsorption the Pb/Ge(111)-1 × 1 system can be found in one of three distinct configurations: T_1, T_4, and H_3. In configuration T_1, the Pb atoms are adsorbed directly above the first-layer Ge atoms [Ge(1)], with each Pb interacting with one Ge (see Fig. 1c and d). In configurations T_4 and H_3 Pb atoms adsorb above the second [Ge(2), see Fig. 1e and f] and the fourth substrate atom [Ge(4), see Fig. 1g and h], respectively. In both configurations each Pb can interact with three nearest-neighbor Ge atoms. The relaxed structure of configuration T_1 was found to be the most stable, which agrees with other reports [13,46,47]. It has 161 and 185 meV lower energy than configurations H_3 and T_4, respectively. The corresponding atomic-structure parameters and electronic-band structures are shown in Table 1, and Fig. 2c–h, respectively.

The non-SOC band structure of the Pb/Ge(111) adsorption system in configuration T_1 is presented in Fig. 2c. The metallic band of an isolated 1ML-Pb comprising the p_x/p_y orbitals is well reproduced by band S_2 in the vicinity of M and S_1 in the sections along Γ-M and M-Γ′. These electronic states show little interaction with the germanium substrate, which suggests them not partaking in a chemical bonding at the Pb/Ge interface. Contrasting, the electronic band comprising the p_z orbitals of Pb is shown to flatten, and shift below the Fermi level (band S_1 in the vicinity of M and S_2 in the sections along Γ-M-Γ′). In the adsorption system those electronic states are a combination of p_z orbitals of Pb and Ge(1) (both unbonded when the systems are isolated). The newly emerged coupling represents a σ-type bonding between the atoms,

Table 3
The values of momentum offset (Δk), and the corresponding energy of GSS (ΔE) for bands S_1 and S_2 of configurations T_1, T_4, and H_3. The momentum offset is given with the respect to the high-symmetry point M.

	T_1		T_4		H_3	
	S_1	S_2	S_1	S_2	S_1	S_2
Δk (Å^{-1})	0.026	0.051	0.154	0.089	0.225	0.077
ΔE (meV)	52	103	309	008	546	354

which agrees with other reports of Pb adsorption on the Ge(111)-1 × 1 and Si(111)-1 × 1 surfaces [12,13,48]. The crystal field of the adsorption system affects the p_x/p_y and p_z coupling in bands S_1 and S_2 as SOC has in the case of an isolated 1ML-Pb (see Table 2). This results in lifted degeneracy at the points of overlap between the bands.

The non-SOC electronic band structures of configurations T_4 and H_3 are shown in Fig. 2e and g, respectively. The electronic structures present qualitative similarities between both configurations. The orbitals of p_x/p_y(Pb) and p_z[Ge(1)] are found coupled in the band occupying the energy levels of −2.43 and −1.91 eV at M for configurations T_4 and H_3, respectively. This coupling represents the bonding interaction emerging at the surface between interfacing atoms, which matches other reports [12,13]. The newly formed Pb–Ge(1) bond impacts also the p-orbital interaction of pristine 1ML-Pb, facilitating a prominent coupling of p_x/p_y and p_z orbitals in bands S_1 and S_2 (see Fig. 2e and g). Out of two configurations, H_3 is shown to experience a greater magnitude of the effect (see Table 2).

In periodic systems orbital coupling is imposed by symmetry of a system, i.e. the crystal electric field couples atomic orbitals of different parities, which typically results in mixing of electronic states with the opposite values of magnetic quantum number m_l. The mirror symmetry planes of the 1ML-Pb and Pb/Ge(111)-1 × 1 systems are shown in Fig. 3. The monolayer of Pb belongs to p6mm plane group. It has a mirror symmetry in the $x - y$ plane (Fig. 3a). It also has a six-fold rotational symmetry along the z axis (Fig. 3c), which results in a mirror symmetry planes along $\Gamma - M$ and $\Gamma - K$ directions. The Pb/Ge system belongs to p3m1 plane group. The adsorption on the germanium substrate brakes the mirror symmetry of the monolayer in the $x - y$ plane (Fig. 3b), and reduces the rotational symmetry to the third order (Fig. 3d). As a result, the system loses the $\Gamma - K$ mirror symmetry plane. However, it still retains the one along $\Gamma - M$. Therefore, the adsorption-induced coupling of p_x/p_y and p_z orbitals may only originate from the inversion asymmetry of the monolayer with respect to the $x - y$ plane.

Different parity of coupled orbital pairs—with respect to a symmetry of a system—has been reported to facilitate a spin splitting in a number of systems [22,49,50]. This is also the case for Pb/Ge(111)-1 × 1. All surface configurations of the system exhibit a GSS of electronic bands comprised of coupled p_x/p_y and p_z orbitals not present in

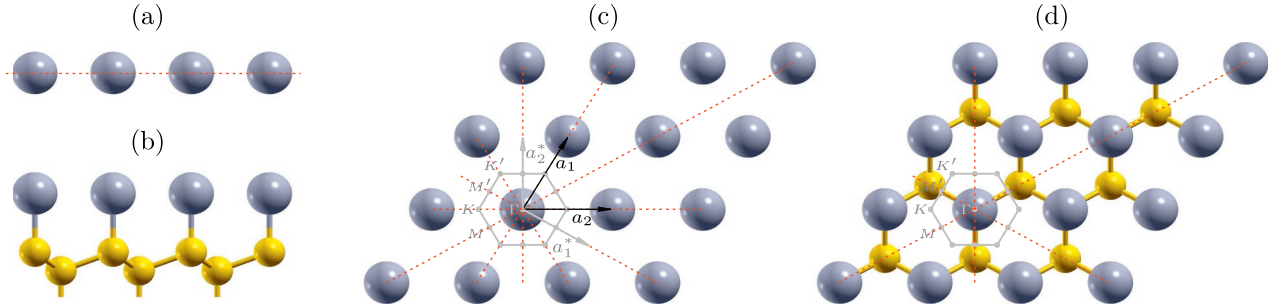

Fig. 3. Mirror symmetry plane (dashed red lines) of 1ML-Pb (a,c) and the Pb/Ge(111) adsorption system (b,d). Side (a,b) and top (c,d) views presented. For clarity only the first two layers of Ge are shown in (b) and (d). (For interpretation of the references to color in this figure legend, the reader is referred to the web version of this article.)

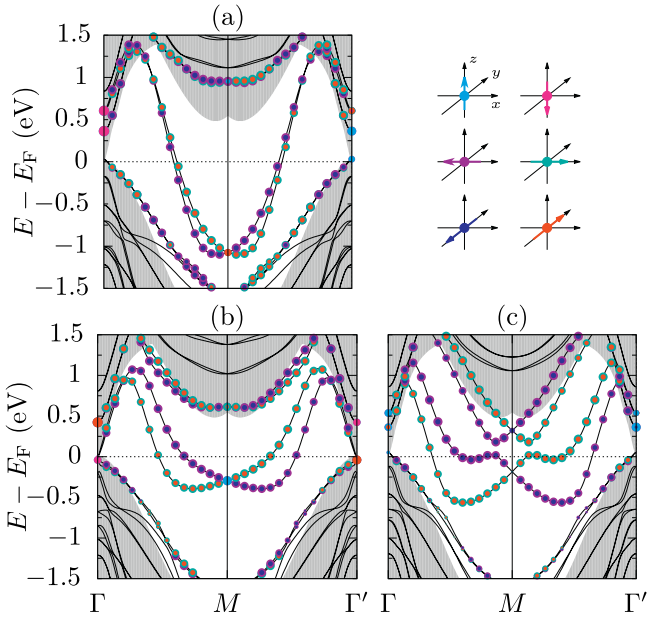

Fig. 4. SAM projections mapped onto the electronic bands in vicinity of the Fermi level for configurations T_1 (a), T_4 (b), and H_3 (c). The color code used to indicate SAM vector components is shown in the upper-right corner of the figure.

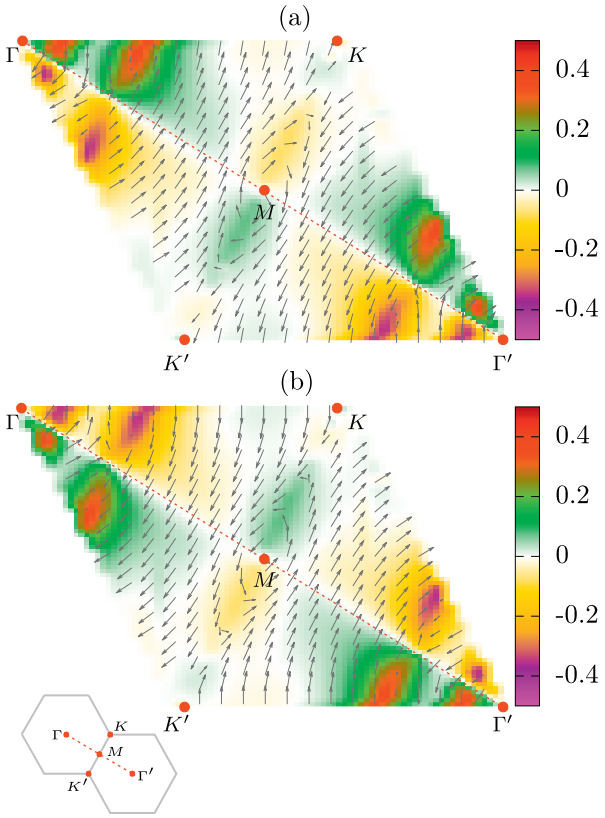

Fig. 5. SAM vector projected onto the $x - y$ plane (arrows) and the z axis (color bar) for the upper (a) and lower (b) bands split in presence of SOC from band S_1 (see Fig. 2c and d). In the lower-left corner of the figure the insert presents two neighboring surface Brillouin zones with relevant high-symmetry points indicated.

the isolated 1ML-Pb (see Fig. 2d,f,h, and compare with b). The SAM vectors projected onto the SOC band structure of configuration T_1 are shown in Fig. 4a. The electronic states in the vicinity of the Fermi level have an in-plane polarization of the spin vector, and the $p_x/p_y - p_z$ comprised band S_1 exhibits a GSS around the M point (see Table 3, for the values of momentum offset Δk, and the corresponding energy offset ΔE). Configuration T_4 is presented in Fig. 4b. Again the electronic states are shown to have an $x - y$ polarization of spin, however, the $p_x/p_y - p_z$ intermix band S_2 exhibits a significantly grater splitting, when compared to band S_1 in configuration T_1 (see Table 3). Band S_1 in configuration T_4 consists mostly of p_z(Pb) orbitals, and shows virtually no splitting. On the other hand, when configuration H_3 is considered both S_1 and S_2 are comprised of strongly coupled p_x/p_y and p_z orbitals, and both bands exhibit a large SAM splitting after the inclusion of SOC (see Fig 4c). Clearly the emergence and magnitude of the spin splitting are correlated with the strength of $p_x/p_y - p_z$ orbital coupling in the Pb bands.

In all configurations electronic states show only a polarization in the $x - y$ plane. This is a direct result of the p3m1 plane symmetry group of the Pb/Ge(111)-1 × 1 surface. In it M point belongs to C_{1h} point group, and the corresponding mirror symmetry plane zeros out the $\langle S_z \rangle$ component of SAM [23]. This results in a full in-plane polarization of the spin vector in the $\Gamma - M - \Gamma'$ direction; see Fig. 5 for the spin texture map of the spin-split metallic bands in configuration T_1. Other configurations have qualitatively the same spin pattern along $\Gamma - M - \Gamma'$, and in the vicinity of M. Alongside the splitting we observe a rotation of SAM centered at the M point. The effect stems from the time reversal symmetry being preserved at the M point, and the anti-unitary character of the SAM operator.

The spin-split values presented in Table 3 exceed those associated with the model Rashba Hamiltonian $\hat{H}_R$; the latter giving the splitting energy $\Delta E \sim 10^{-6}$ eV [22]. The Zeeman-like picture also has difficulty elucidating the large differences in the spin splitting between the surface configurations because the strength of the surface electric field should not vary much between them. The observed splitting can, however, be enhanced by SOC. Typically spin-orbit coupling in periodic systems is small due to near-zero values of $\boldsymbol{L}$, but large non-zero values can be induced by the interatomic hopping between different-parity orbital pairs [49]. OAM vectors projected onto the non-SOC band structures of Pb/Ge(111)-1 × 1 are shown in Fig. 6. The OAM in the spin-split bands is large and its magnitude correlates with the strength of $p_x/p_y - p_z$ coupling.

The unquenched $\boldsymbol{L}$ contributes to $\hat{H}_{SOC} = \alpha \boldsymbol{L} \cdot \boldsymbol{S}$, where α is a SOC coupling strength. Fig. 7 shown the splitting energy calculated along $M - \Gamma'$. Our DFT data is confronted with the split values estimated by the $\hat{H}_{SOC}$ i.e. $\Delta E = \langle \hat{H}_{SOC} \rangle_{up} - \langle \hat{H}_{SOC} \rangle_{down} \approx 2\alpha \boldsymbol{L} \cdot \boldsymbol{S}$. The values show strong correlation. The $\hat{H}_{SOC}$ splitting is ∼ 93% of the one predicted by DFT, which indicates that, the effect is predominantly of SOC origin. This illustrates that, the surface spin splitting can be greatly enhanced by atomic SOC in presence of unquenched OAM. Interestingly, the GSS of 200 meV reported for a 4/3ML Pb/Ge(111)-$(\sqrt{3} \times \sqrt{3})R30°$ system also occurs along $\Gamma - M$ in bands with strong p_x/p_y(Pb) character. Furthermore, analogous splittings have also been reported for Tl/Si (111)-1 × 1, and Bi/Si(111)-$(\sqrt{3} \times \sqrt{3})R30°$. This suggests that, SOC may also enhance spin splitting along $\Gamma - M$ in other adsorption systems.

In principle produced splitting can be as large as those observe in free atoms (1.75 eV for 6p orbital in Pb). The effect, however, is noticeably smaller in the adsorption system as OAM remains partially quenched. The magnitude of $\boldsymbol{L}$ directly correlates with the hopping energy of the coupled orbitals, which originates from an external perturbation that brake a symmetry of a system. Our study demonstrates that a perturbation stems not only from the atomic configuration of the surface, but also the bonding configuration that arises at the interface, as it can impact the strength of coupling between surface orbitals.

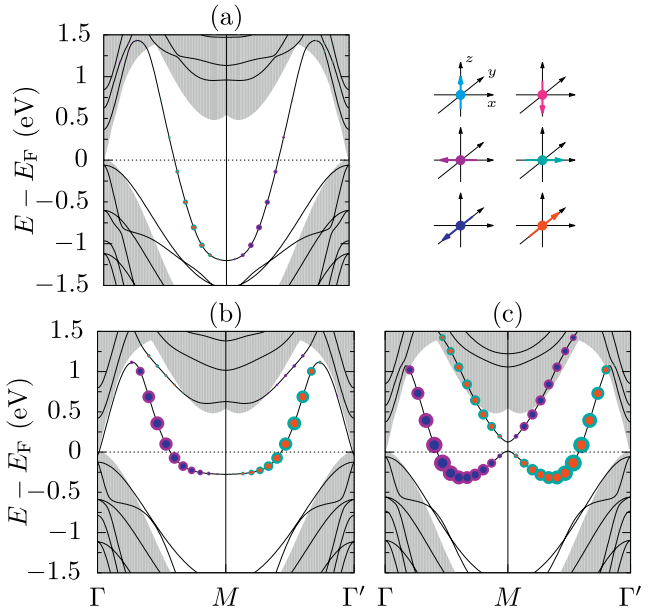

Fig. 6. OAM projections mapped onto the electronic bands in vicinity of the Fermi level for configurations T_1 (a), T_4 (b), and H_3 (c). The color code used to indicate OAM vector components is shown in the upper-right corner of the figure. Size of points correlates with the value of the respective OAM component.

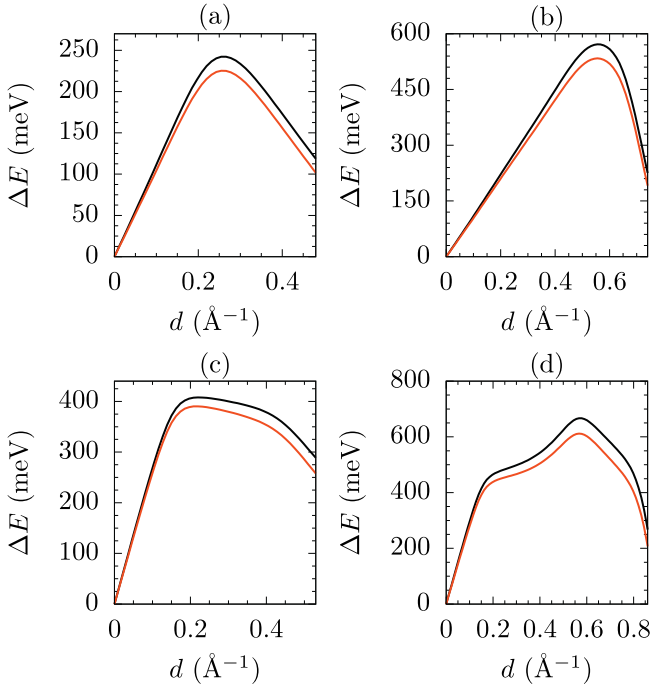

Fig. 7. The spin splitting energy ΔE calculated along $M - \Gamma'$ for band S_1 of configuration T_1 (a), S_2 of T_4 (b), and S_1 (c) and S_2 (d) of H_3. The black and red curves represent the DFT data and those obtained from the Hamiltonian $\hat{H}_{SOC}$, respectively. The band section d is in reference to the M point (at 0 Å^{-1}). (For interpretation of the references to color in this figure legend, the reader is referred to the web version of this article.)

4. Conclusions

In Conclusion, we investigated the role of coupling between surface orbitals in a SOC enhanced spin splitting observed in the Pb/Ge(111)-1 × 1 system along $\Gamma - M - \Gamma'$. We have shown that, the analysis of surface-band composition, and parity of the comprising orbitals—in respect to the symmetry-breaking electric field of the surface—is of key importance when searching for indicators of SOC enhanced spin splitting. It is demonstrated that the bonding configuration of the Pb/Ge interface impacts the coupling of p_x/p_y and p_z in the Pb monolayer, which produces electronic states with different values of unquenched OAM. The spin-orbit interaction enhances the magnitude of splitting energy, facilitating a GSS of the order of hundreds of meV. The coupling of p_x/p_y and p_z orbitals by an external electric field is not limited to the Pb/Ge(111)-1 × 1 system, and thus our findings suggest that, other adsorption systems (e.g. Tl/Si(111)-1 × 1, Bi/Si(111)-($\sqrt{3} \times \sqrt{3}$)$R30°$ or 4/3ML Pb/Ge(111)-($\sqrt{3} \times \sqrt{3}$)$R30°$) may have their GSS also originating from SOC.

Acknowledgments

This research was supported by PL-Grid infrastructure. M.J.S. acknowledges the Polish Ministry of Science and Higher Education for support (Grant no. 06/62/DSPB/2183).

References

[1] I. Barke, F. Zheng, T.K. Rügheimer, F.J. Himpsel, Experimental evidence for spin-split bands in a one-dimensional chain structure, Phys. Rev. Lett. 97 (2006) 226405, https://doi.org/10.1103/PhysRevLett.97.226405.
[2] K. Sakamoto, T. Oda, A. Kimura, K. Miyamoto, M. Tsujikawa, A. Imai, N. Ueno, H. Namatame, M. Taniguchi, P.E.J. Eriksson, R.I.G. Uhrberg, Abrupt rotation of the rashba spin to the direction perpendicular to the surface, Phys. Rev. Lett. 102 (2009) 096805, https://doi.org/10.1103/PhysRevLett.102.096805.
[3] I. Gierz, T. Suzuki, E. Frantzeskakis, S. Pons, S. Ostanin, A. Ernst, J. Henk, M. Grioni, K. Kern, C.R. Ast, Silicon surface with giant spin splitting, Phys. Rev. Lett. 103 (2009) 046803, https://doi.org/10.1103/PhysRevLett.103.046803.
[4] S. Hatta, T. Aruga, Y. Ohtsubo, H. Okuyama, Large rashba spin splitting of surface resonance bands on semiconductor surface, Phys. Rev. B 80 (2009) 113309, https://doi.org/10.1103/PhysRevB.80.113309.
[5] J. Ibañez-Azpiroz, A. Eiguren, A. Bergara, Relativistic effects and fully spin-polarized fermi surface at the tl/si(111) surface, Phys. Rev. B 84 (2011) 125435, https://doi.org/10.1103/PhysRevB.84.125435.
[6] L.V. Bondarenko, D.V. Gruznev, A.A. Yakovlev, A.Y. Tupchaya, D. Usachov, O. Vilkov, A. Fedorov, D.V. Vyalikh, S.V. Eremeev, E.V. Chulkov, A.V. Zotov, A.A. Saranin, Large spin splitting of metallic surface-state bands at adsorbate-modified gold/silicon surfaces 3(2013) 1826 EP –, Article. 10.1038/srep01826.
[7] I. Yakovkin, N. Petrova, Dft study of sb and pb layers on the bi(111) surface, Appl. Surf. Sci. 445 (2018) 154–160, https://doi.org/10.1016/j.apsusc.2018.03.152. URL http://www.sciencedirect.com/science/article/pii/S0169433218308389
[8] M. Kopciuszynski, M. Krawiec, R. Zdyb, M. Jalochowski, Purely one-dimensional bands with a giant spin-orbit splitting: pb nanoribbons on si(553) surface, Sci. Rep. 7 (2017), https://doi.org/10.1038/srep46215. 46215 EP –, Article
[9] Y. Ohtsubo, S. Hatta, N. Kawai, A. Mori, Y. Takeichi, K. Yaji, H. Okuyama, T. Aruga, Spin-polarized surface states on br/ge(111)-(1 × 1): surface spin polarization without heavy elements, Phys. Rev. B 86 (2012) 165325, https://doi.org/10.1103/PhysRevB.86.165325.
[10] K. Yaji, Y. Ohtsubo, S. Hatta, H. Okuyama, K. Miyamoto, T. Okuda, A. Kimura, H. Namatame, M. Taniguchi, T. Aruga, Large Rashba spin splitting of a metallic surface-state band on a semiconductor surface, Nat. Commun. 1 (2010), https://doi.org/10.1038/ncomms1016. 17 EP –, Article
[11] T. Aruga, Different types of rashba spin-split surface states on ge(111), J. Electron Spectrosc. Relat. Phenom. 201 (2015) 74–80, https://doi.org/10.1016/j.elspec.2014.10.004. Special issue on electron spectroscopy for Rashba spin-orbit interaction.URL http://www.sciencedirect.com/science/article/pii/S0368204814002254
[12] B. Pieczyrak, M. Szary, L. Jurczyszyn, M.W. Radny, Spin polarization of two-dimensional electronic gas decoupled from structural asymmetry environment, Phys. Rev. B 93 (2016) 195318, https://doi.org/10.1103/PhysRevB.93.195318.
[13] M.J. Szary, B. Pieczyrak, L. Jurczyszyn, M.W. Radny, Suppressed and enhanced spin polarization in the 1ml-pb/ge(111) − 1 × 1 system, Appl. Surf. Sci. 466 (2019) 224–229, https://doi.org/10.1016/j.apsusc.2018.10.028. URL http://www.sciencedirect.com/science/article/pii/S0169433218327247
[14] B. Slomski, G. Landolt, G. Bihlmayer, J. Osterwalder, J.H. Dil, Tuning of the Rashba effect in pb quantum well states via a variable Schottky barrier, Sci. Rep. 3 (2013), https://doi.org/10.1038/srep01963. 1963 EP –, Article
[15] E.I. Rashba, Symmetry of energy bands in crystals of wurtzite type: i. symmetry of bands disregarding spin-orbit interaction, Sov. Phys.-Solid State 1 (1959) 368.
[16] G. Bihlmayer, O. Rader, R. Winkler, Focus on the Rashba effect, New J. Phys. 17 (5) (2015) 050202. URL http://stacks.iop.org/1367-2630/17/i=5/a=050202
[17] M. Nagano, A. Kodama, T. Shishidou, T. Oguchi, A first-principles study on the Rashba effect in surface systems, J. Phys. 21 (6) (2009) 064239. URL http://stacks.iop.org/0953-8984/21/i=6/a=064239
[18] J. Premper, M. Trautmann, J. Henk, P. Bruno, Spin-orbit splitting in an anisotropic two-dimensional electron gas, Phys. Rev. B 76 (2007) 073310, https://doi.org/10.

1103/PhysRevB.76.073310.
[19] G. Nicolay, F. Reinert, S. Hüfner, P. Blaha, Spin-orbit splitting of the l-gap surface state on au(111) and ag(111), Phys. Rev. B 65 (2001) 033407, https://doi.org/10.1103/PhysRevB.65.033407.
[20] C.R. Ast, J. Henk, A. Ernst, L. Moreschini, M.C. Falub, D. Pacilé, P. Bruno, K. Kern, M. Grioni, Giant spin splitting through surface alloying, Phys. Rev. Lett. 98 (2007) 186807, https://doi.org/10.1103/PhysRevLett.98.186807.
[21] H. Lee, H.J. Choi, Role of *d* orbitals in the Rashba-type spin splitting for noble-metal surfaces, Phys. Rev. B 86 (2012) 045437, https://doi.org/10.1103/PhysRevB.86.045437.
[22] L. Petersen, P. Hedegøard, A simple tight-binding model of spin-orbit splitting of sp-derived surface states, Surf. Sci. 459 (1) (2000) 49–56, https://doi.org/10.1016/S0039-6028(00)00441-6. URL http://www.sciencedirect.com/science/article/pii/S0039602800004416
[23] T. Oguchi, T. Shishidou, The surface rashba effect: a k â·p perturbation approach, J. Phys. 21 (9) (2009) 092001. URL http://stacks.iop.org/0953-8984/21/i=9/a=092001
[24] M. Michiardi, M. Bianchi, M. Dendzik, J.A. Miwa, M. Hoesch, T.K. Kim, P. Matzen, J. Mi, M. Bremholm, B.B. Iversen, P. Hofmann, Strongly anisotropic spin-orbit splitting in a two-dimensional electron gas, Phys. Rev. B 91 (2015) 035445, https://doi.org/10.1103/PhysRevB.91.035445.
[25] S.R. Park, C.H. Kim, J. Yu, J.H. Han, C. Kim, Orbital-angular-momentum based origin of Rashba-type surface band splitting, Phys. Rev. Lett. 107 (2011) 156803, https://doi.org/10.1103/PhysRevLett.107.156803.
[26] B. Kim, P. Kim, W. Jung, Y. Kim, Y. Koh, W. Kyung, J. Park, M. Matsunami, S.-i. Kimura, J.S. Kim, J.H. Han, C. Kim, Microscopic mechanism for asymmetric charge distribution in rashba-type surface states and the origin of the energy splitting scale, Phys. Rev. B 88 (2013) 205408, https://doi.org/10.1103/PhysRevB.88.205408.
[27] S.D. Stolwijk, K. Sakamoto, A.B. Schmidt, P. Krüger, M. Donath, Spin texture with a twist in momentum space for tl/si(111), Phys. Rev. B 91 (2015) 245420, https://doi.org/10.1103/PhysRevB.91.245420.
[28] J. Lafuente-Bartolome, I.G. Gurtubay, A. Eiguren, Relativistic response and novel spin-charge plasmon at the tl/si(111) surface, Phys. Rev. B 96 (2017) 035416, https://doi.org/10.1103/PhysRevB.96.035416.
[29] P. Garcia-Goiricelaya, I.G. Gurtubay, A. Eiguren, Coupled spin and electron-phonon interaction at the tl/si(111) surface from relativistic first-principles calculations, Phys. Rev. B 97 (2018) 201405, https://doi.org/10.1103/PhysRevB.97.201405.
[30] K. Sakamoto, H. Kakuta, K. Sugawara, K. Miyamoto, A. Kimura, T. Kuzumaki, N. Ueno, E. Annese, J. Fujii, A. Kodama, T. Shishidou, H. Namatame, M. Taniguchi, T. Sato, T. Takahashi, T. Oguchi, Peculiar Rashba splitting originating from the two-dimensional symmetry of the surface, Phys. Rev. Lett. 103 (2009) 156801, https://doi.org/10.1103/PhysRevLett.103.156801.
[31] X.-Y. Ren, H.-J. Kim, S. Yi, Y. Jia, J.-H. Cho, Spin-orbit coupling effects on the stability of two competing structures in pb/si(111) and pb/ge(111), Phys. Rev. B 94 (2016) 075436, https://doi.org/10.1103/PhysRevB.94.075436.
[32] P. Giannozzi, S. Baroni, N. Bonini, M. Calandra, R. Car, C. Cavazzoni, D. Ceresoli, G.L. Chiarotti, M. Cococcioni, I. Dabo, A.D. Corso, S. de Gironcoli, S. Fabris, G. Fratesi, R. Gebauer, U. Gerstmann, C. Gougoussis, A. Kokalj, M. Lazzeri, L. Martin-Samos, N. Marzari, F. Mauri, R. Mazzarello, S. Paolini, A. Pasquarello, L. Paulatto, C. Sbraccia, S. Scandolo, G. Sclauzero, A.P. Seitsonen, A. Smogunov, P. Umari, R.M. Wentzcovitch, Quantum espresso: a modular and open-source software project for quantum simulations of materials, J. Phys. 21 (39) (2009) 395502. URL http://stacks.iop.org/0953-8984/21/i=39/a=395502
[33] J.P. Perdew, K. Burke, M. Ernzerhof, Generalized gradient approximation made simple, Phys. Rev. Lett. 77 (1996) 3865–3868.
[34] J.P. Perdew, A. Ruzsinszky, G.I. Csonka, O.A. Vydrov, G.E. Scuseria, L.A. Constantin, X. Zhou, K. Burke, Restoring the density-gradient expansion for exchange in solids and surfaces, Phys. Rev. Lett. 100 (2008) 136406.
[35] P.E. Blöchl, Projector augmented-wave method, Phys. Rev. B 50 (1994) 17953–17979.
[36] G. Kresse, D. Joubert, From ultrasoft pseudopotentials to the projector augmented-wave method, Phys. Rev. B 59 (1999) 1758–1775.
[37] H.J. Monkhorst, J.D. Pack, Special points for Brillouin-zone integrations, Phys. Rev. B 13 (1976) 5188–5192.
[38] M.C. Neale, M.D. Hunter, J.N. Pritikin, M. Zahery, T.R. Brick, R.M. Kirkpatrick, R. Estabrook, T.C. Bates, H.H. Maes, S.M. Boker, Openmx 2.0: extended structural equation and statistical modeling, Psychometrika 81 (2) (2016) 535–549, https://doi.org/10.1007/s11336-014-9435-8.
[39] J.N. Pritikin, M.D. Hunter, S.M. Boker, Modular open-source software for item factor analysis, Educ. Psychol. Meas. 75 (3) (2015) 458–474.
[40] M.D. Hunter, State space modeling in an open source, modular, structural equation modeling environment, Struct. Equ. Model. Multidisciplinary J. 25 (2) (2018) 307–324, https://doi.org/10.1080/10705511.2017.1369354.
[41] S.M. Boker, M.C. Neale, H.H. Maes, M.J. Wilde, M. Spiegel, T.R. Brick, R. Estabrook, T.C. Bates, P. Mehta, T. von Oertzen, R.J. Gore, M.D. Hunter, D.C. Hackett, J. Karch, A.M. Brandmaier, J.N. Pritikin, M. Zahery, R.M. Kirkpatrick, Y. Wang, C. Driver, Massachusetts Institute of Technology, S.G. Johnson, Association for Computing Machinery, D. Kraft, S. Wilhelm, Manjunath B G, OpenMx 2.9.6 User Guide, 2018.
[42] N. Troullier, J.L. Martins, Efficient pseudopotentials for plane-wave calculations, Phys. Rev. B 43 (1991) 1993–2006, https://doi.org/10.1103/PhysRevB.43.1993.
[43] P. Haas, F. Tran, P. Blaha, Calculation of the lattice constant of solids with semilocal functionals, Phys. Rev. B 79 (2009) 085104, https://doi.org/10.1103/PhysRevB.79.085104.
[44] T. Hom, W. Kiszenik, B. Post, Accurate lattice constants from multiple reflection measurements. II. lattice constants of germanium silicon, and diamond, J. Appl. Crystallogr. 8 (4) (1975) 457–458, https://doi.org/10.1107/S0021889875010965.
[45] A. Yoshiasa, K. Koto, H. Maeda, T. Ishii, The mean-square relative displacement and displacement correlation functions in tetrahedrally and octahedrally coordinated a n b 8- n crystals, Jpn. J. Appl. Phys. 36 (2R) (1997) 781. URL http://stacks.iop.org/1347-4065/36/i=2R/a=781
[46] I.-S. Hwang, J.A. Golovchenko, Tunneling microscope observation of a structural surface phase transition: structure, fluctuations, and local effects, Phys. Rev. Lett. 71 (1993) 255–258, https://doi.org/10.1103/PhysRevLett.71.255.
[47] I.-S. Hwang, J.A. Golovchenko, Phase transition of monolayer pb/ge(111): $\beta - \sqrt{3} \times \sqrt{3}$r30° ⇆ 1 × 1 at 180°c, Phys. Rev. B 50 (1994) 18535–18542, https://doi.org/10.1103/PhysRevB.50.18535.
[48] M. Rafiee, S.J. Asadabadi, Quantum size effects in pb/si(111) thin films from density functional calculations, Comput. Mater. Sci 47 (2) (2009) 584–592, https://doi.org/10.1016/j.commatsci.2009.09.027. URL http://www.sciencedirect.com/science/article/pii/S0927025609003711
[49] S. Oh, H.J. Choi, Orbital angular momentum analysis for giant spin splitting in solids and nanostructures, Sci. Rep. 7 (1) (2017) 2024, https://doi.org/10.1038/s41598-017-02032-4.
[50] G. Khalsa, B. Lee, A.H. MacDonald, Theory of t_{2g} electron-gas Rashba interactions, Phys. Rev. B 88 (2013) 041302, https://doi.org/10.1103/PhysRevB.88.041302.

P4. Giant Rashba spin splitting induced by heavy element adsorption at germanene

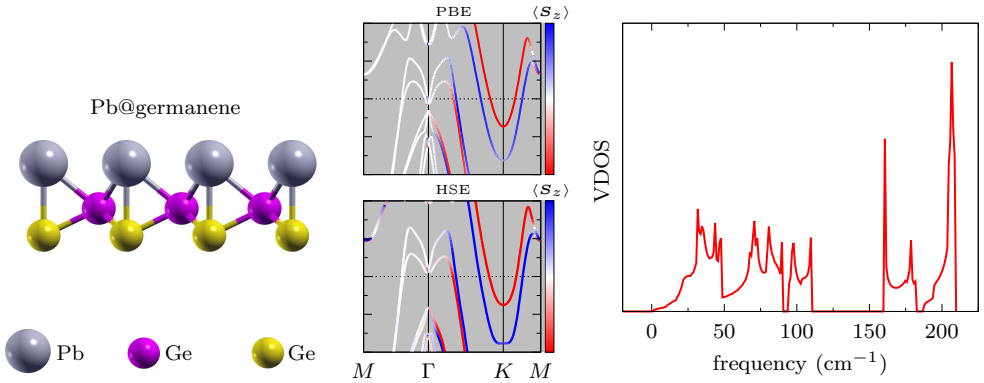

FlatChem 18 (2019) 100141

Contents lists available at ScienceDirect

FlatChem

journal homepage: www.elsevier.com/locate/flatc

Giant Rashba spin splitting induced by heavy element adsorption at germanene

Maciej J. Szary

Institute of Physics, Poznan University of Technology, ul. Piotrowo 3, 61-138 Poznan, Poland

ARTICLE INFO

Keywords:
Germanene
Lead
2D materials
Spin splitting
Adsorption
Density functional theory

ABSTRACT

Density functional theory calculations have been performed to investigate the structural and electronic properties of the Pb@germanene adsorption system. By employing equilibrium ab initio atomistic thermodynamics and phonon spectra analysis a dynamically stable configuration have been found. It is a (1 × 1) structure with coverage of 1 monolayer [(1 × 1)′@germanene]. The surface configuration shares some structural similarities with the sTable (1 × 1) phase of Pb@Ge(1 1 1), however, it favors a different adsorption site, and facilitates more Pb–Ge bonds per adsorbed atom. This results in (1 × 1)′@germanene having lower surface free energy than its Ge (1 1 1) counterpart. The electronics have been investigate using both GGA-type PBE and hybrid HSE functionals in order to ensure the accuracy. In both cases the system is a metal. Strong spin-orbit interaction of electrons in Pb facilitates a giant spin splitting of metallic bands up to 646 meV at the Fermi level, which makes the system an interesting platform for two-dimensional spintronics.

1. Introduction

Two-dimensional (2D) layered materials have been a continuous topic of interest in physics, chemistry, and material science due to their exotic properties coupled with high surface area. Recent advancements in their fabrication have made them promising prospects for nanoelectronics, energy storage, catalysis and sensing [1–9]. Among them germanene has become an interesting platform for advanced electronic devices. It was successfully fabricated on substrates such as: Pt(1 1 1) [10], Au(1 1 1) [11], Ag(1 1 1) [12], Al(1 1 1) [13–15], Ge_2Pt [16,17], and MoS_2 [18]. Pristine germanene is a zero-gap semiconductor and its charge carriers are massless Dirac fermions, which results in a very high intrinsic carrier mobility of $\sim 6 \cdot 10^5\,cm^2\,V^{-1}\,s^{-1}$ at room temperature [19]. Electronic properties of germanene are also tunable, its band gap was reported to open via an externally applied electrical field, atom adsorption and substrate interaction [20–23]. This, however, impacts the mass of electrons and holes reducing their mobility. The system is predicted to exhibit a quantum spin Hall effect [24,25] similarly to other 2D systems e.g.: SnC_2H [26], AsO [27], and Bi@Sb(1 1 1) [28]. On the other hand due to low atomic number of comprising atoms, spin-orbit coupling (SOC) is weak in germanene, which limits its application in spintronics.

For an effective spin transport at room temperature, a metallic surface band with a giant spin splitting (GSS) of at least 100 meV is required. In surface systems a GSS is formed via Rashba-type effect, when the orbital angular momentum is unquenched [29–33]. This gives rise to two non-zero energy terms in the split Hamiltonian [34]: (i) $\widehat{H}_{SOC} = \alpha \boldsymbol{L}\cdot\boldsymbol{S}$, were α is SOC strength, while $\boldsymbol{L}$ and $\boldsymbol{S}$ are orbital and spin angular momentum, respectively, and (ii) $\widehat{H}_{E_s} = -\alpha_K(\boldsymbol{L}\times\boldsymbol{k})\cdot\boldsymbol{E}_s$, where α_K is a proportionality constant, $\boldsymbol{k}$ is a wave vector, and $\boldsymbol{E}_s$ is the surface electrostatic field. The first term represents the atomic SOC, while the second gives the interaction between the asymmetric charge distribution and the surface electrostatic field. This microscopic mechanism for Rashba-type band splitting has been successful in predicting the accurate energy scale in systems such as: Au(1 1 1) [34,35], Bi_2Te_3 [30], Bi_2Te_2Se [34], Bi_2Se_3 [36] $WeSe_2$ [35], Pb@Ge(1 1 1) [37,38], and Pb@$MoTe_2$ [39].

In case of graphene, spin splitting can be facilitated by adsorption on a substrate [40,41], intercalation [42–44] or decoration by heavy elements [45], however, low chemical activity of graphene limits the thermal stability of such systems, and thus their application in room temperature spintronics. In contrast germanene is more chemically active as the comprising Ge atoms favor a mixed sp^2-sp^3 hybridization over flat sp^2 of graphene. Thus, germanene is more likely to support stable adsorption configurations, which could facilitate a GSS in the system. Furthermore, GSS was successfully induced at (1 1 1) surfaces of Ge and Si—which are structurally similar to germanene—by elements such as Tl [46,47], Pb [37,47,48], and Bi [47,49].

Conflicts of interest: The authors declare no conflicts of interest.

E-mail address: maciej.szary@put.poznan.pl.

https://doi.org/10.1016/j.flatc.2019.100141
Received 29 June 2019; Received in revised form 9 October 2019; Accepted 30 October 2019
Available online 05 November 2019

This work investigates adsorption of Pb at germanene. Different surface configurations are considered based on the phases of Pb@Ge (1 1 1). The latter is a well-known adsorption system [37,38,47,50,51]. Its surface structure depends on the temperature and Pb coverage. There are two different $(\sqrt{3} \times \sqrt{3})R30°$ structures at room temperature: dilute phase α and dense phase β. The coverage of α-Pb@Ge(1 1 1)-$(\sqrt{3} \times \sqrt{3})R30°$ [α@Ge(1 1 1) for short] and β-Pb@Ge(1 1 1)-$(\sqrt{3} \times \sqrt{3})R30°$ [β@Ge(1 1 1)] is 1/3 and 4/3 monolayer (ML), respectively. The surface also favors a (1×1) structure [(1×1)@Ge (1 1 1)] at high-temperature, which has the coverage of 1 ML. In phases β@Ge(1 1 1) and (1×1)@Ge(1 1 1) a GSS of metallic surface bands has been reported [37,38,50].

It is shown, based on the density functional theory (DFT) calculations and equilibrium ab initio atomistic thermodynamics that, Pb forms a dynamically stable surface configuration at germanene. It is a (1×1) configuration with a coverage of 1 ML. Its surface geometry share some structural similarities with (1×1)@Ge(1 1 1), however, it favors a different adsorption side, and forms more Pb–Ge bonds per adsorbed atom. The Pb@germanene system is a metal. Strong SOC of electrons in Pb facilitates GSS of metallic bands, with its maximum value of 646 meV at the Fermi level. The intrinsic GSS makes the system an attractive platform for spin transport and accumulation in 2D spintronics.

2. Methods

DFT calculations of total energy and electronic structure were performed using Quantum Espresso code [52,53]. The generalized gradient approximation of Perdew, Burke, and Ernzerhof (GGA-PBE) [54,55] and norm-conserving potentials [56] were employed. This work adopted the smearing parameter of 1 mRy and the cutoff energies for the wave function and density of 55 and 500 Ry, respectively. The $12 \times 12 \times 1$ grid was used in Monkhorst-Pack k-point sampling method for the surface-Brillouin zone (SBZ) integration [57]. Semi-empirical Grimme's DFT-D2 van der Waals correction was included, and in spin-polarized calculations full-relativistic potentials were used [58,59]. All dynamical-matrix calculations were performed using Density-Functional Perturbation Theory (DFPT) as implemented PHonon package, which is a part of Quantum Espresso distribution. The phonon density-of-states spectra were calculated with a dense q-grid of $60 \times 60 \times 1$. In order to ensure the accuracy of band structures, the self-consistent calculations (SCF) were also conducted employing Heyd-Scuseria-Ernzerhof (HSE) hybrid exchange-correlation functional [60]. The $12 \times 12 \times 1$ mesh was used for the sampling of the Fock operator. In this case the band structure was produced by unfolding of the reduced grid from the SCF onto the full grid, and then wannierizing the obtained wave-functions using wannier90 code for generating maximally-localized Wannier functions [61].

The monolayer of germanene and the Ge(1 1 1) surface were modeled within the repeated periodic slab model in (1×1) and $(\sqrt{3} \times \sqrt{3})R30°$ cells. For Ge(1 1 1), 10 atomic layers of Ge formed the slab, with one side passivated by H atoms. The cell height of 40 Å [$\sim$34 Å of vacuum along z for germanene and $\sim$25 Å for Ge (1 1 1)] and truncation of the Coulomb interaction in the z direction were employed to avoid artificial interactions between the neighboring systems [62]. The atomic positions of all the atoms in the system were fully optimized with the adopted convergence threshold on forces (less than 10^{-5} Ry/au).

3. Results

3.1. Isolated germanene

An isolated monolayer of germanene is shown in Fig. 1a and b. The sheet comprised two atomic layers of germanium: upper Ge(1), and lower Ge(2). They form a hexagonal honeycomb structure, which belongs to the p3m1 plane-symmetry group. The sheet has three mirror-symmetry planes normal to the surface, with one along x–z, and a broken mirror symmetry in the x–y plane. The relaxed structure of germanene has a lattice constant of 4.0 Å, with Ge–Ge bonding distance of 2.38 Å, and Ge(1)–Ge(2) interlayer spacing of 0.69 Å. This coincides with other reports where the structure parameters were reported between 3.87 and 4.07 Å [63–65,10,66], 2.31–2.44 Å [64,66], and 0.64–0.75 Å [64,10,67,66], respectively. Lattice vectors for (1×1) ($\boldsymbol{a}_1$, $\boldsymbol{a}_2$) and $(\sqrt{3} \times \sqrt{3})R30°$ ($\boldsymbol{b}_1$, $\boldsymbol{b}_2$) cells are shown in Fig. 1b. The length of $\boldsymbol{a}_1$ is 4.0 Å, while $\boldsymbol{b}_1$ is 6.83 Å. The vectors are at 30° angle, which also translates to the reciprocal lattices having rotated SBZs.

Fig. 1c and d show the non-SOC and SOC electronic band structures of germanene calculated for (1×1) unit cell. Without SOC, the system is a zero-gap semiconductor with its conduction and valence bands meeting at K points of SBZ. The bands have a linear energy dispersion in close vicinity of the Fermi level. They comprised predominantly p_z states of Ge(1) and Ge(2), which contrasts the p_x/p_y composition of the valence bands at Γ. Due to low atomic number the inclusion of SOC has a little impact on the electronic band structure of germanene. It introduces a negligible band gap of 23 meV, and lifts the degeneracy of

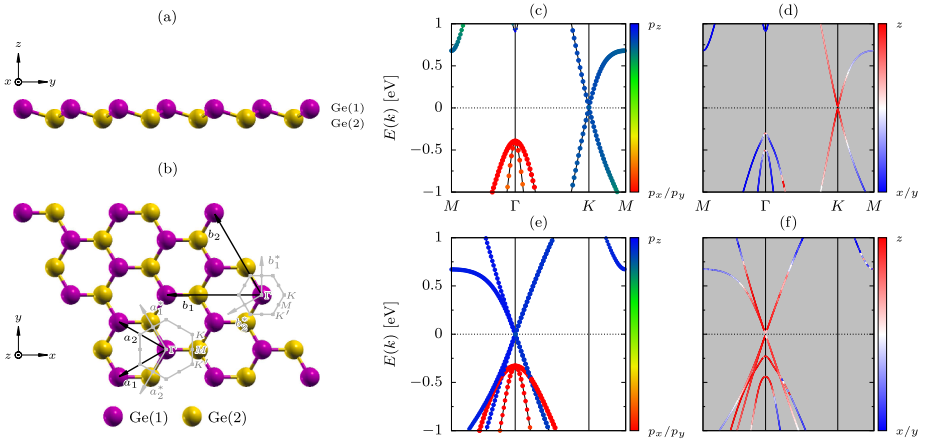

Fig. 1. Atomic-structure schematics of an isolated germanene (a, b). The coordinate system is shown in (a) and (b), atomic notation is given in (b). Lattice vectors of (1×1) (a_1, a_2) and $(\sqrt{3} \times \sqrt{3})R30°$ (b_1, b_2) cells are presented in (b). Non-SOC and SOC electronic band structures calculated in (1×1) cell are given in (c) and (d), respectively. Electronics of $(\sqrt{3} \times \sqrt{3})R30°$ are shown in (e), and (f). In (c) and (e), the radii of the circles are proportional to the total contribution of 4p Ge, and the colour index represents the relative contributions of $4/4p_y$ and $4p_z$. In (d) and (f), the line color indicates the relative polarization of the spin vector between z (red) and x/y (blue) polarizations.

valence bands at Γ separating them by 205 meV. In vicinity of K the spin vector has predominantly z polarization, while the rest of the band structure shows mostly x/y polarity. No GSS is observed in the system. Similar electronics are shown for the germanene calculated in $(\sqrt{3} \times \sqrt{3})R30°$ unit cell (see Fig. 1e and f). The only notable difference is a shift of the Dirac cones form K to Γ, which results in the z polarization of spin vector near Γ.

3.2. Pb@germanene adsorption system

Germanene has been successfully fabricated on a number of surfaces [10–14,16,17] among them MoS_2 [18]. Chemically inactive MoS_2 offers a limited interaction with the adsorbate, preserving the bonding configuration of germanene. Following the fabrication of germanene the deposition of Pb can be attempted with similar vacuum methods used for the heavy-element deposition on Ge(1 1 1) and Si(1 1 1) [49,47,50,68]. In order to investigate the stability of this adsorption system a number of different surface adsorption configurations has to be considered. For that pursue the Pb@Ge(1 1 1) phases will be used as a reference. Both pristine (1 1 1)–1 × 1 surface of germanium, and germanene have three distance adsorption sites: T_1, T_4, and H_3. At T_1 atoms adsorb on top of the first-layer Ge, and have one nearest-neighbor Ge(1). In the case of T_4, an adsorbate is located above the second layer of Ge, while at H_3 it is positioned at the center of the hexagonal ring. In both cases an adsorbate has three nearest-neighbor Ge(1) atoms.

In phase α@Ge(1 1 1) a Pb atom occupies site T_4 of the $(\sqrt{3} \times \sqrt{3})R30°$ unit cell. For (1 × 1)@Ge(1 1 1), Pb adsorbs at T_1. In β@Ge(1 1 1) one Pb atom is located at H_3, while remaining three are positioned at the off-centered bridge positions between T_1 and T_4 of $(\sqrt{3} \times \sqrt{3})R30°$. In the case of Pb adsorbing at germanene all three phases are investigated and for each, adsorption at all of the sites is considered. The binding energies per atom of Pb at germanene and Ge (1 1 1) are given in Table 1. It is shown that, $T_1 - \alpha$@germanene, T_4–(1 × 1)@germanene and $T_1 - \beta$@germanene are the most energetically favorable configurations of their respective phases. For α@germanene Pb atom adsorbing at T_1 has 204 meV lower binding energy than at T_4, while in (1 × 1)@germanene adsorption at T_4 has 496 meV lower energy than at T_1. In β@germanene the Pb pattern centered at T_1 has 135 meV lower binding energy per atom than at H_3. As the phases at germanene favor different adsorption sites, their preferred configurations will be named α'@germanene (T_1– α@germanene), $(1 \times 1)'$@germanene [T_4–(1 × 1)@germanene], and β'@germanene (T_1–β@germanene).

Fig. 2a–i shows the atomic-structure schematics of phases α', $(1 \times 1)'$, and β'. In α'@germanene, both Pb–Ge(1) and Pb–Ge(2) bonding distances are ≈3.02 Å (see Fig. 2a and d), while the Ge(1)–Ge (2) distances are 2.498 and 2.573 Å (Fig. 2d). It should be noted that the Ge(1) atoms directly above the Pb shift 2.181 Å below remaining Ge(1), and 1.1 Å below Ge(2) (Fig. 2g), which produces a significant corrugation of the germanene substrate. The effect is similar to the one observed for germanene@Al(1 1 1), where Ge atoms above threefold hollow sites of Al(1 1 1) are shifted up and down resulting in 1.96 and 2.13 Å buckling [15]. In $(1 \times 1)'$@germanene, Pb–Ge(1) distance is 2.982 Å, while Pb–Ge(2) is 3.092 Å (see Fig. 2e and h). The Ge(1)–Ge (2) bond length is 2.555 Å, and the buckling of germanene is 1.159 Å (Fig. 2e and h). Interestingly, the atomic structure of $(1 \times 1)'$@ germanene resembles that of a transition metal dichalcogenide monolayer (i.e. MoS_2 and $MoSe_2$). Atoms bond in a trigonal-prismatic geometry, however, without the mirror symmetry in the x–y plane. β'@ germanene has one upper-layer [Pb(1)] and three lower-layer Pb atoms [Pb(2)]. Pb(1)–Pb(2) bonding length is 3.208 Å, while Pb(2)–Pb(2) is 3.522 Å (Fig. 2c and f). Pb(1)–Ge(1) and Pb(2)–Ge(1) distances are 2.904, and 3.101 Å, respectively. The Ge(1)–Ge(2) bond length is 2.555 Å, and the buckling is 1.511 Å (Fig. 2f and i). The large corrugation of germanene results form the upward shift of the Ge(1) atoms directly below Pb(1), the Ge(1) atoms move 0.773 Å towards Pb(1).

Table 1
Binding energy (E_b) of Pb per atom adsorbed at germanene and Ge(1 1 1). Values are calculated for three adsorption sited of germanene for α, β and (1 × 1) configurations of Pb@germanene. For Pb@Ge(1 1 1) only stable structures are shown.

Phase	T_1–Pb@ germanene	T_4–Pb@ germanene	H_3–Pb@ germanene	Pb@Ge (1 1 1)
	(eV/atom)			
α	− 2.50	− 2.30	− 1.96	− 2.56
1 × 1	− 2.19	− 2.69	− 2.36	− 2.37
β	− 2.47	− 2.38	− 2.34	− 2.11

Stability of the relaxed structures can be ascertained from the phase diagram of surface free energy (γ_{ads}) and the chemical potential of Pb (μ_{Pb}). When the system is in thermal equilibrium—i.e. adsorption at the substrate and desorption to a Pb environment occur at even rates without changing either temperature or pressure of the system—its thermodynamic properties can be described by Gibbs free energy G, which is a function of temperature (T), pressure (p), and a number of Pb and Ge atoms in the system (N_{Pb} and N_{Ge}). The most stable adsorption configuration has the lowest γ_{ads}:

$$\gamma_{ads} = \frac{1}{A}\left[\Delta G\left(T, p, N_{Pb}, N_{Ge}\right) - N_{Pb}\mu_{Pb}\left(T, p\right)\right], \quad (1)$$

where A is the area of the unit cell, and ΔG is the Gibbs free energy difference between Pb@germanene and pristine germanene. The latter is approximated as the difference between the ground state DFT total energies of the adsorption system $E_{Pb@ger}$, and the clean substrate E_{ger} [69–72]. Also, chemical potential of the adsorbate is reference to the ground state of an isolated Pb atom E_{Pb}. Thus (1) can be rewritten as:

$$\gamma_{ads} = \frac{1}{A}\left[E_{Pb@ger} - E_{ger} - N_{Pb}E_{Pb} - N_{Pb}\Delta\mu_{Pb}\right], \quad (2)$$

where $\Delta\mu_{Pb} = \mu_{Pb} - E_{Pb}$.

The phase diagram of Pb@germanene plotted using (2) is given in Fig. 2j. Phases of Pb@Ge(1 1 1) are also presented. The figure shows that, β' and $(1 \times 1)'$ are the energetically favorable configurations of Pb@germanene, and that they have noticeably lower surface free energy than their Pb@Ge(1 1 1) counterparts. For high values of $\Delta\mu_{Pb}$ the most energetically favorable configuration is β'@germanene. This phase is stable between − 1.83 and 0 eV/Å^2. At lower values, $(1 \times 1)'$@ germanene becomes the energetically favorable phase having the lowest surface free energy between − 2.69 and − 1.83 eV/Å^2. Phase α' is predicted not to form as below − 2.69 eV/Å pristine germanene has a lower γ_{ads} than Pb@germanene making the adsorption system unstable.

The atomistic thermodynamic investigation of stability of the interface was conducted with the Gibbs free energy difference approximated with the difference between the ground state DFT total energies of the adsorption system and the clean substrate, and as such it does not include any contributions from: the pV term, entropy, and the vibrational energy. Thus the analysis does not considered the dynamical stability of the system, which is of key importance for room temperature applications. This, however, can be derived out of the phonon density of states (VDOS) spectra. VDOS of $(1 \times 1)'$@germanene and β'@ germanene are shown in Fig. 2k and l, respectively. It is shown that, phase $(1 \times 1)'$ is dynamically stable as the VDOS spectrum has only real and positive frequencies, which indicates that for this configuration its potential energy always increases against any combinations of atomic displacements. On the other hand, the VDOS spectrum of phase β' shows imaginary frequencies indicating dynamic instability of the system. This makes only phase $(1 \times 1)'$ a suitable candidate for room-temperature applications.

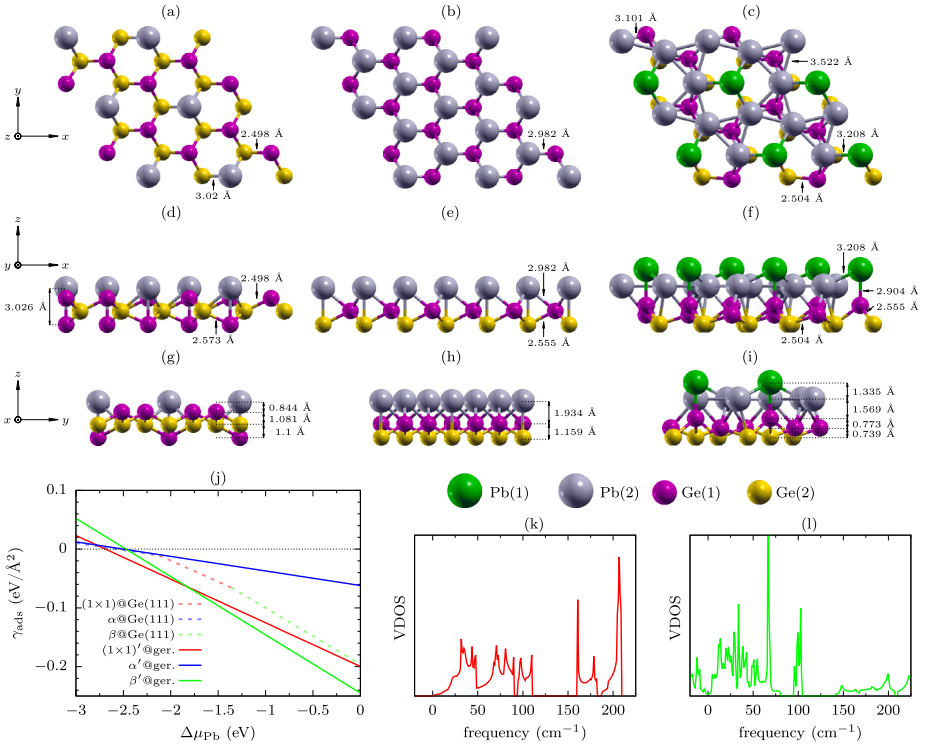

Fig. 2. Atomic-structure schematics of α'@germanene (a,d,g), $(1 \times 1)'$@germanene (b,e,h), and β'@germanene (c,f,i). The coordinate system is shown in (a), (d) and (g), and the atomic notations is presented below (h) and (i). Figure (j) shows the phase diagram $\gamma_{ads}(\Delta_{Pb})$. Solid lines represent phases of germanene, while dashed mark phases of Ge(1 1 1). The horizontal dashed line at 0 eV/Å^2 represents a clean surface of the substrate. Figures (k) and (l) show the phonon density of states spectra of $(1 \times 1)'$@germanene and β'@germanene, respectively.

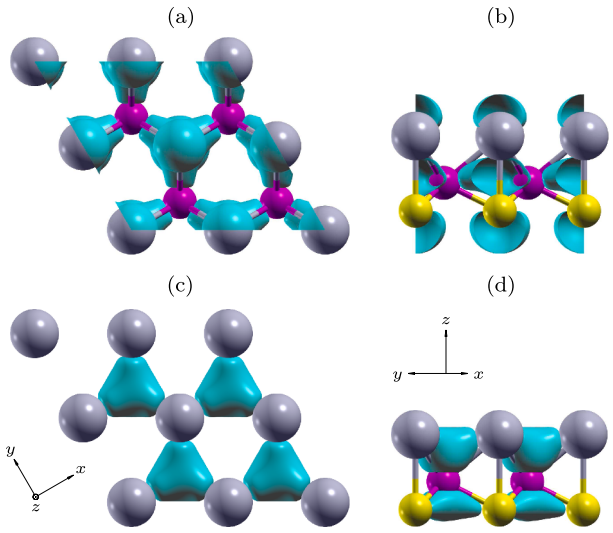

Fig. 3. Charge density contour calculated at K for two new hybrid states of Pb and Ge in $(1 \times 1)'$@germanene. Calculations where performed in (1×1) unit cell. The coordinate system is shown in (c), (d). Isosurface value: 0.0037 e/a.u.^{3}.

Stability of $(1 \times 1)'$@germanene and its lower binding energy in comparison with (1×1)@Ge(1 1 1) must have its origin in the Pb–Ge boding interaction. In the stable configuration of (1×1)@Ge(1 1 1), p_z orbitals of Pb and Ge overlap forming a covalent σ-type bond, while less stable off-centered configurations facilitate a bonding between p_x/p_y Pb and p_z Ge [37,38]. In $(1 \times 1)'$@germanene both p_x/p_y and p_z states of Pb show a strong coupling with states of Ge due to small interlayer spacing between the substrate and the adsorbate. The electronic wave functions of p_z Pb and p_z Ge(2) overlap forming a new hybrid state with the charge density present between the atoms indicative of a covalent bond (see Fig. 3a and b). This new state shows also a small contribution of p_x/p_y Ge(1) atomic wave function (8.6%). Similarly p_x/p_y orbitals of Pb hybridize with p_z of Ge(1) (see Fig. 3c and d). Interestingly, the Pb–Ge (1) bond mirrors a p_z–p_x/p_y bonding between Ge(1) and Ge(2) atoms forming an asymmetrical trigonal-prismatic geometry akin to that of transition metal dichalcogenide monolayers.

Strong hybridization of electronic states observed between interfacing atoms, and the large SOC of electrons in Pb have a significant impact on the electronic properties of the adsorption system. SOC and non-SOC electronic band structure of $(1 \times 1)'$@germanene are shown in Fig. 4. In order to ensure the accuracy of the band structure analysis the electronics were calculated with both PBE (Fig. 4a–d), and HSE exchange-correlation functionals (Fig. 4e–f). In both cases the system is a metal with a large contribution of 6p states to the electronic bands in vicinity of the Fermi level (see Fig. 4a and e). Bands have mostly p_x/p_y character except band sections with dominant p_z contribution around Γ. Similar metallic band comprising p_x/p_y states of Pb was also reported along Γ-K-M [37]. Both PBE and HSE functional produce qualitatively similar band structures, with mostly matching band composition and shape. Bands do experience some energy shift, however, the only notable difference observed for the Pb-dominated bands is the upward shift of the band section with p_z composition in vicinity of Γ, which puts it above Fermi level in the HSE band structure.

Inclusion of SOC has a significant impact on the electronic band structure of $(1 \times 1)'$@germanene. A GSS with an in-plane polarization of the spin vector is observed above the Fermi level for a metallic band near Γ (see Fig. 4b–d). In the case of PBE the maximum values of the spin splitting are 332 and 341 meV along M–Γ and Γ–K, respectively. The same values for the HSE calculations are 348 and 323 meV. GSS is also observed for a metallic band that, comprised predominantly p_x/p_y states of Pb. The splitting arises along Γ–K–M. In case of PBE it is 540 meV at the Fermi for Γ–K, 448 meV at K, and 508 meV at Fermi for K–M. The same splitting in the HSE bands structure has the values of 646, 508, and 582 meV, respectively. The spin vector has the out-of-

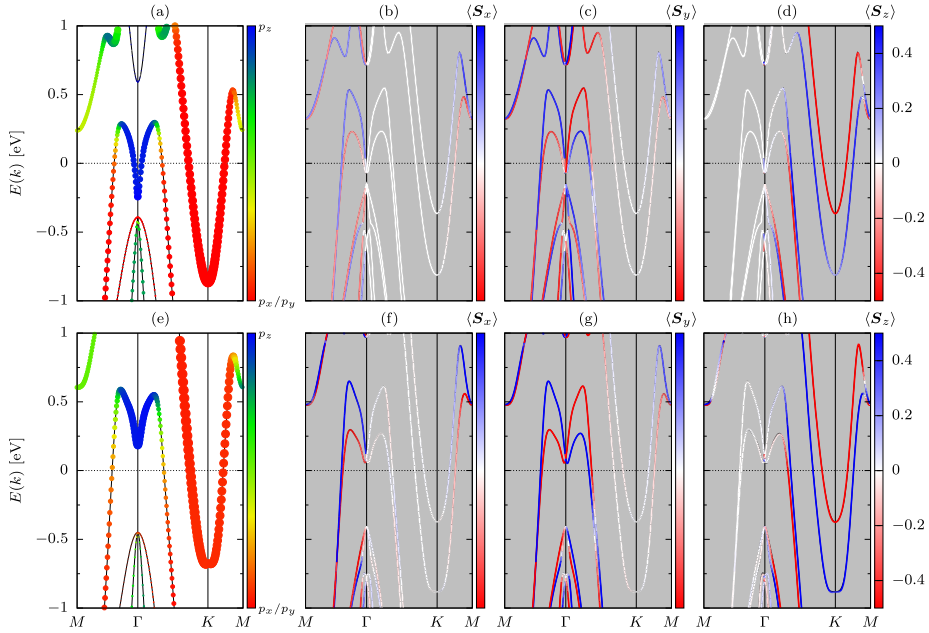

Fig. 4. Non-SOC electronic band structure of $(1 \times 1)'$@germanene calculated with PBE (a) and HSE (e) functionals. The radii of the circles are proportional to the total contribution of 6*p* Pb, and the color index represents the relative contributions of $6/6p_y$ and $6p_z$. SOC electronic band structure of $(1 \times 1)'$@germanene for PBE (b–d) and HSE (f–g) calculations. The line color indicates the value of spin vector projections: $\langle \boldsymbol{S}_x \rangle$, $\langle \boldsymbol{S}_y \rangle$, and $\langle \boldsymbol{S}_z \rangle$.

plane polarization. Such splitting was also reported for the off-centered configurations of Pb@Ge(1 1 1), where it was associated with the strong electronic SOC of Pb facilitated by an unquenched orbital-angular momentum present in the split states [37]. Its values, however, are shown to be ~800 meV at *K*, which suggests that, the germanium surface introduces a greater electrostatic gradient at the interface than germanene.

GSS of metallic surface-state bands has been pursued and widely discussed for semiconductor surfaces decorated with heavy elements in context of spintronics [37,38,46–49], with particular interest in spin-polarized transport and accumulation [47,50,73–75]. The intrinsic GSS of metallic surface bands in Pb@germanene is shown to be large enough for room-temperature spintronics offering an interesting platform for spin-polarized transport, accumulation, and filtering in 2D systems. Furthermore, both germanene [20–23] and plumbene [76,77] were reported to have highly tunable electronic structures, which suggests that the electronics of Pb@germanene may also prove susceptible to strain engineering or electric field.

4. Conclusions

In conclusion, adsorption of Pb at germanene has been investigated for a number of surface configurations based on the stable phases of Pb@Ge(1 1 1). With the use of equilibrium ab initio atomistic thermodynamics, and phonon spectra analysis, one dynamically stable interface configurations have been found. It is a (1×1) structure with coverage of 1 monolayer, where Pb adsorbs directly above the second layer Ge atoms. The structure shares some similarities with its Ge(1 1 1) counterpart, however, at germanene the Pb is shown to have more bond with the substrate, which produces noticeably lower binding energy. Adsorption of Pb makes the Pb@germanene system a metal. Strong SOC of electrons in Pb facilitates GSS of metallic bands making the Pb@germanene an attractive prospect for spin transport and accumulation in 2D spintronics.

Declaration of Competing Interest

The authors declare that they have no known competing financial interests or personal relationships that could have appeared to influence the work reported in this paper.

Acknowledgments

M.J.S. acknowledges the Ministry of Science and Higher Education in Poland for financial support within Project No 06/62/SBAD/1923 realized at Faculty of Technical Physics, Poznan University of Technology. VDOS calculations reported in this work have been performed at the Interdisciplinary Centre of Mathematical and Computational Modeling of the University of Warsaw under Grant No. GB77-35.

References

[1] J. Shim, D.-H. Kang, Y. Kim, H. Kum, W. Kong, S.-H. Bae, I. Almansouri, K. Lee, J.-H. Park, J. Kim, Recent progress in van der waals (vdw) heterojunction-based electronic and optoelectronic devices, Carbon 133 (2018) 78–89, https://doi.org/10.1016/j.carbon.2018.02.104 URL: http://www.sciencedirect.com/science/article/pii/S0008622318302409.

[2] K.K. Kim, H.S. Lee, Y.H. Lee, Synthesis of hexagonal boron nitride heterostructures for 2d van der waals electronics, Chem. Soc. Rev. 47 (2018) 6342–6369, https://doi.org/10.1039/C8CS00450A.

[3] S. shi Li, C. wen Zhang, W. xiao Ji, Novel electronic properties in silicene on MoSe2 monolayer: an excellent prediction for FET, Mater. Chem. Phys. 164 (2015) 150–156, https://doi.org/10.1016/j.matchemphys.2015.08.036.

[4] Q. Li, J. Yang, R. Quhe, Q. Zhang, L. Xu, Y. Pan, M. Lei, J. Lu, Ohmic contacts between monolayer WSE2 and two-dimensional titanium carbides, Carbon 135 (2018) 125–133, https://doi.org/10.1016/j.carbon.2018.04.043 URL: http://www.sciencedirect.com/science/article/pii/S0008622318304020.

[5] Z.J. Han, A.T. Murdock, D.H. Seo, A. Bendavid, Recent progress in plasma-assisted synthesis and modification of 2d materials, 2D Mater. 5 (3) (2018) 032002, https://doi.org/10.1088/2053-1583/aabb81.

[6] J. Pang, R.G. Mendes, A. Bachmatiuk, L. Zhao, H.Q. Ta, T. Gemming, H. Liu, Z. Liu, M.H. Rummeli, Applications of 2d MXenes in energy conversion and storage systems, Chem. Soc. Rev. 48 (2019) 72–133, https://doi.org/10.1039/C8CS00324F.

[7] X. Gong, X. Zhao, M.E. Pam, H. Yao, Z. Li, D. Geng, S.J. Pennycook, Y. Shi, H.Y. Yang, Location-selective growth of two-dimensional metallic/semiconducting transition metal dichalcogenide heterostructures, Nanoscale 11 (2019) 4183–4189, https://doi.org/10.1039/C8NR08744J.

[8] H.-F. Zhang, D.-P. Wu, X.-J. Ning, Atomistic mechanism for graphene based gaseous sensor working, Appl. Surf. Sci. 470 (2019) 448–453, https://doi.org/10.1016/j.apsusc.2018.11.149 URL:http://www.sciencedirect.com/science/article/pii/S0169433218332276.

[9] Y. Seekaew, C. Wongchoosuk, A novel graphene-based electroluminescent gas sensor for carbon dioxide detection, Appl. Surf. Sci. 479 (2019) 525–531, https://

doi.org/10.1016/j.apsusc.2019.02.100 URL: http://www.sciencedirect.com/science/article/pii/S0169433219304441.
[10] L. Li, S.-Z. Lu, J. Pan, Z. Qin, Y.-Q. Wang, Y. Wang, G.-Y. Cao, S. Du, H.-J. Gao, Buckled germanene formation on pt(1 1 1), Adv. Mater. 26(28) 4820–4824. arXiv:https://onlinelibrary.wiley.com/doi/pdf/10.1002/adma.201400909,https://doi.org/10.1002/adma.201400909. URL: https://onlinelibrary.wiley.com/doi/abs/10.1002/adma.201400909.
[11] M.E. Dávila, L. Xian, S. Cahangirov, A. Rubio, G.L. Lay, New J. Phys. 16 (9) (2014) 095002, https://doi.org/10.1088/1367-2630/16/9/095002.
[12] C.-H. Lin, A. Huang, W.W. Pai, W.-C. Chen, T.-Y. Chen, T.-R. Chang, R. Yukawa, C.-M. Cheng, C.-Y. Mou, I. Matsuda, T.-C. Chiang, H.-T. Jeng, S.-J. Tang, Single-layer dual germanene phases on ag(111), Phys. Rev. Mater. 2 (2018) 024003, https://doi.org/10.1103/PhysRevMaterials. 2.024003.
[13] M. Derivaz, D. Dentel, R. Stephan, M.-C. Hanf, A. Mehdaoui, P. Sonnet, C. Pirri, Continuous germanene layer on al(111), Nano Lett. 15 (4) (2015) 2510–2516, https://doi.org/10.1021/acs.nanolett.5b00085 pMID: 25802988. arXiv:https://doi.org/10.1021/acs.nanolett.5b00085.
[14] S. Endo, O. Kubo, N. Nakashima, S. Iwaguma, R. Yamamoto, Y. Kamakura, H. Tabata, M. Katayama, Appl. Phys. Exp. 11 (1) (2017) 015502, https://doi.org/10.7567/apex.11.015502.
[15] W. Wang, R.I.G. Uhrberg, Coexistence of strongly buckled germanene phases on al (111), Beilstein J. Nanotechnol. 8 (2017) 1946–1951, https://doi.org/10.3762/bjnano.8.195.
[16] P. Bampoulis, L. Zhang, A. Safaei, R. van Gastel, B. Poelsema, H.J.W. Zandvliet, J. Phys.: Condensed Matter 26 (44) (2014) 442001, https://doi.org/10.1088/0953-8984/26/44/442001.
[17] R. van Bremen, P. Bampoulis, J. Aprojanz, M. Smithers, B. Poelsema, C. Tegenkamp, H.J.W. Zandvliet, Ge2pt hut clusters: a substrate for germanene, J. Appl. Phys. 124 (12) (2018) 125301, https://doi.org/10.1063/1.5046997 arXiv: https://doi.org/10.1063/1.5046997.
[18] L. Zhang, P. Bampoulis, A.N. Rudenko, Q. Yao, A. van Houselt, B. Poelsema, M.I. Katsnelson, H.J.W. Zandvliet, Structural and electronic properties of germanene on mos_2, Phys. Rev. Lett. 116 (2016) 256804, https://doi.org/10.1103/PhysRevLett. 116.256804.
[19] X.-S. Ye, Z.-G. Shao, H. Zhao, L. Yang, C.-L. Wang, Intrinsic carrier mobility of germanene is larger than graphene's: first-principle calculations, RSC Adv. 4 (2014) 21216–21220, https://doi.org/10.1039/C4RA01802H.
[20] Z. Ni, Q. Liu, K. Tang, J. Zheng, J. Zhou, R. Qin, Z. Gao, D. Yu, J. Lu, Tunable bandgap in silicene and germanene, Nano Lett. 12 (1) (2012) 113–118, https://doi.org/10.1021/nl203065e pMID: 22050667. arXiv: https://doi.org/10.1021/nl203065e.
[21] M. Ye, R. Quhe, J. Zheng, Z. Ni, Y. Wang, Y. Yuan, G. Tse, J. Shi, Z. Gao, J. Lu, Tunable band gap in germanene by surface adsorption, Physica E: Low-dimensional Syst. Nanostruct. 59 (2014) 60–65, https://doi.org/10.1016/j.physe.2013.12.016 URL http://www.sciencedirect.com/science/article/pii/S1386947713004530.
[22] A. Acun, L. Zhang, P. Bampoulis, M. Farmanbar, A. van Houselt, A.N. Rudenko, M. Lingenfelder, G. Brocks, B. Poelsema, M.I. Katsnelson, H.J.W. Zandvliet, Germanene: the germanium analogue of graphene, J. Phys.: Condensed Matter 27 (44) (2015) 443002, https://doi.org/10.1088/0953-8984/27/44/443002.
[23] R. Singh, Spin-orbit coupling in graphene, silicene and germanene: dependence on the configuration of full hydrogenation and fluorination, Bull. Mater. Sci. 41 (6) (2018) 158, https://doi.org/10.1007/s12034-018-1655-6.
[24] L. Seixas, J.E. Padilha, A. Fazzio, Quantum spin hall effect on germanene nanorod embedded in completely hydrogenated germanene, Phys. Rev. B 89 (2014) 195403, https://doi.org/10.1103/PhysRevB.89.195403.
[25] C.J. Tabert, E.J. Nicol, Ac/dc spin and valley hall effects in silicene and germanene, Phys. Rev. B 87 (2013) 235426, https://doi.org/10.1103/PhysRevB.87.235426.
[26] R.-W. Zhang, C.-W. Zhang, W.-X. Ji, S.-S. Li, S.-J. Hu, S.-S. Yan, P. Li, P.-J. Wang, F. Li, New J. Phys. 17 (8) (2015) 083036, https://doi.org/10.1088/1367-2630/17/8/083036.
[27] Y.-P. Wang, W.-X. Ji, C.-W. Zhang, P. Li, S.-F. Zhang, P.-J. Wang, S.-S. Li, S.-S. Yan, Two-dimensional arsenene oxide: a realistic large-gap quantum spin hall insulator, Appl. Phys. Lett. 110 (21) (2017) 213101, https://doi.org/10.1063/1.4983781 arXiv: https://doi.org/10.1063/1.4983781.
[28] S.-S. Li, W.-X. Ji, S.-J. Hu, C.-W. Zhang, S.-S. Yan, Effect of amidogen functionalization on quantum spin hall effect in bi/sb(111) films, ACS Appl. Mater. Interfaces 9 (47) (2017) 41443–41453, https://doi.org/10.1021/acsami.7b13179 pMID: 29140070. arXiv: https://doi.org/10.1021/acsami.7b13179.
[29] S.R. Park, C.H. Kim, J. Yu, J.H. Han, C. Kim, Orbital-angular-momentum based origin of rashba-type surface band splitting, Phys. Rev. Lett. 107 (2011) 156803, https://doi.org/10.1103/PhysRevLett. 107.156803.
[30] W. Jung, Y. Kim, B. Kim, Y. Koh, C. Kim, M. Matsunami, S.-I. Kimura, M. Arita, K. Shimada, J.H. Han, J. Kim, B. Cho, C. Kim, Warping effects in the band and angular-momentum structures of the topological insulator bi_2te_3, Phys. Rev. B 84 (2011) 245435, https://doi.org/10.1103/PhysRevB.84.245435.
[31] J.-H. Park, C.H. Kim, J.-W. Rhim, J.H. Han, Orbital rashba effect and its detection by circular dichroism angle-resolved photoemission spectroscopy, Phys. Rev. B 85 (2012) 195401, https://doi.org/10.1103/PhysRevB.85.195401.
[32] B. Kim, C.H. Kim, P. Kim, W. Jung, Y. Kim, Y. Koh, M. Arita, K. Shimada, H. Namatame, M. Taniguchi, J. Yu, C. Kim, Spin and orbital angular momentum structure of cu(111) and au(111) surface states, Phys. Rev. B 85 (2012) 195402, https://doi.org/10.1103/PhysRevB.85.195402.
[33] S. Jakobs, A. Ruffing, M. Cinchetti, S. Mathias, M. Aeschlimann, Orbital angular momentum structure of an unoccupied spin-split quantum-well state in PB/CU (111), Phys. Rev. B 87 (2013) 235438, https://doi.org/10.1103/PhysRevB.87.235438.
[34] B. Kim, P. Kim, W. Jung, Y. Kim, Y. Koh, W. Kyung, J. Park, M. Matsunami, S.-I. Kimura, J.S. Kim, J.H. Han, C. Kim, Microscopic mechanism for asymmetric charge distribution in rashba-type surface states and the origin of the energy splitting scale, Phys. Rev. B 88 (2013) 205408, https://doi.org/10.1103/PhysRevB.88.205408.
[35] S. Oh, H.J. Choi, Orbital angular momentum analysis for giant spin splitting in solids and nanostructures, Sci. Rep. 7 (1) (2017) 2024, https://doi.org/10.1038/s41598-017-02032-4.
[36] S.R. Park, J. Han, C. Kim, Y.Y. Koh, C. Kim, H. Lee, H.J. Choi, J.H. Han, K.D. Lee, N.J. Hur, M. Arita, K. Shimada, H. Namatame, M. Taniguchi, Chiral orbital-angular momentum in the surface states of bi_2se_3, Phys. Rev. Lett. 108 (2012) 046805, https://doi.org/10.1103/PhysRevLett. 108.046805.
[37] M.J. Szary, B. Pieczyrak, L. Jurczyszyn, M.W. Radny, Suppressed and enhanced spin polarization in the 1ML-Pb/Ge(111)-11 system, Appl. Surf. Sci. 466 (2019) 224–229, https://doi.org/10.1016/j.apsusc.2018.10.028 URL http://www.sciencedirect.com/science/article/pii/S0169433218327247.
[38] M.J. Szary, Role of coupling between surface orbitals in soc enhanced spin splitting, Surf. Sci. 684 (2019) 12–17, https://doi.org/10.1016/j.susc.2019.02.004 URL http://www.sciencedirect.com/science/article/pii/S0039602818309646.
[39] M.J. Szary, M.T. Michalewicz, M.W. Radny, Giant spin splitting induced by a symmetry-braking van der waals interaction, Appl. Surf. Sci. 494 (2019) 619–626, https://doi.org/10.1016/j.apsusc.2019.07.189 URL http://www.sciencedirect.com/science/article/pii/S0169433219322251.
[40] A.M. Shikin, A.A. Rybkina, A.G. Rybkin, I.I. Klimovskikh, P.N. Skirdkov, K.A. Zvezdin, A.K. Zvezdin, Spin current formation at the graphene/pt interface for magnetization manipulation in magnetic nanodots, Appl. Phys. Lett. 105 (4) (2014) 042407, https://doi.org/10.1063/1.4891361 arXiv: https://doi.org/10.1063/1.4891361.
[41] I.I. Klimovskikh, S.S. Tsirkin, A.G. Rybkin, A.A. Rybkina, M.V. Filianina, E.V. Zhizhin, E.V. Chulkov, A.M. Shikin, Nontrivial spin structure of graphene on pt (111) at the fermi level due to spin-dependent hybridization, Phys. Rev. B 90 (2014) 235431, https://doi.org/10.1103/PhysRevB.90.235431.
[42] M. Krivenkov, E. Golias, D. Marchenko, J. Sánchez-Barriga, G. Bihlmayer, O. Rader, A. Varykhalov, Nanostructural origin of giant rashba effect in intercalated graphene, 2D Mater. 4 (3) (2017) 035010, https://doi.org/10.1088/2053-1583/aa7ad8.
[43] I.I. Klimovskikh, M.M. Otrokov, V.Y. Voroshnin, D. Sostina, L. Petaccia, G. Di Santo, S. Thakur, E.V. Chulkov, A.M. Shikin, Spin-orbit coupling induced gap in graphene on pt(111) with intercalated pb monolayer, ACS Nano 11 (1) (2017) 368–374, https://doi.org/10.1021/acsnano.6b05982 pMID: 28005333. arXiv: https://doi.org/10.1021/acsnano.6b05982.
[44] M.M. Otrokov, I.I. Klimovskikh, F. Calleja, A.M. Shikin, O. Vilkov, A.G. Rybkin, D. Estyunin, S. Muff, J.H. Dil, A.L.V. de Parga, R. Miranda, H. Ochoa, F. Guinea, J.I. Cerdá, E.V. Chulkov, A. Arnau, Evidence of large spin-orbit coupling effects in quasi-free-standing graphene on pb/ir(111), 2D Mater. 5 (3) (2018) 035029, https://doi.org/10.1088/2053-1583/aac596 URL: https://doi.org/10.1088/2F2053-1583/2Faac596.
[45] L. Brey, Spin-orbit coupling in graphene induced by adatoms with outer-shell p orbitals, Phys. Rev. B 92 (2015) 235444, https://doi.org/10.1103/PhysRevB.92.235444.
[46] K. Sakamoto, T. Oda, A. Kimura, Y. Takeichi, J. Fujii, R. Uhrberg, M. Donath, H.W. Yeom, Symmetry induced peculiar rashba effect on thallium adsorbed si(111) surfaces, J. Electron Spectrosc. Related Phenomena 201 (2015) 88–91, https://doi.org/10.1016/j.elspec.2014.09.008 special issue on electron spectroscopy for Rashba spin-orbit interaction. URL http://www.sciencedirect.com/science/article/pii/S0368204814001923.
[47] T. Aruga, Different types of rashba spin-split surface states on ge(111), J. Electron Spectrosc. Related Phenomena 201 (2015) 74–80, https://doi.org/10.1016/j.elspec.2014.10.004 special issue on electron spectroscopy for Rashba spin-orbit interaction. URL http://www.sciencedirect.com/science/article/pii/S0368204814002254.
[48] B. Pieczyrak, M. Szary, L. Jurczyszyn, M.W. Radny, Spin polarization of two-dimensional electronic gas decoupled from structural asymmetry environment, Phys. Rev. B 93 (2016) 195318, https://doi.org/10.1103/PhysRevB.93.195318.
[49] S. Hatta, T. Aruga, Y. Ohtsubo, H. Okuyama, Large rashba spin splitting of surface resonance bands on semiconductor surface, Phys. Rev. B 80 (2009) 113309, https://doi.org/10.1103/PhysRevB.80.113309.
[50] K. Yaji, Y. Ohtsubo, S. Hatta, H. Okuyama, K. Miyamoto, T. Okuda, A. Kimura, H. Namatame, M. Taniguchi, T. Aruga, Large rashba spin splitting of a metallic surface-state band on a semiconductor surface, Nat. Commun. 1 (2010) 17 EP –, article.
[51] K. Yaji, S. Hatta, T. Aruga, H. Okuyama, Structural and electronic properties of the PB/GE(111)-$\beta)\sqrt{3}\,\sqrt{3}$)r30 surface studied by photoelectron spectroscopy and first-principles calculations, Phys. Rev. B 86 (2012) 235317, https://doi.org/10.1103/PhysRevB.86.235317.
[52] P. Giannozzi, S. Baroni, N. Bonini, M. Calandra, R. Car, C. Cavazzoni, D. Ceresoli, G.L. Chiarotti, M. Cococcioni, I. Dabo, A. Dal Corso, S. de Gironcoli, S. Fabris, G. Fratesi, R. Gebauer, U. Gerstmann, C. Gougoussis, A. Kokalj, M. Lazzeri, L. Martin-Samos, N. Marzari, F. Mauri, R. Mazzarello, S. Paolini, A. Pasquarello, L. Paulatto, C. Sbraccia, S. Scandolo, G. Sclauzero, A.P. Seitsonen, A. Smogunov, P. Umari, R.M. Wentzcovitch, Quantum espresso: a modular and open-source software project for quantum simulations of materials, J. Phys.: Condensed Matter 21 (39) (2009) 395502 .
[53] P. Giannozzi, O. Andreussi, T. Brumme, O. Bunau, M.B. Nardelli, M. Calandra, R. Car, C. Cavazzoni, D. Ceresoli, M. Cococcioni, N. Colonna, I. Carnimeo, A.D. Corso, S. de Gironcoli, P. Delugas, R.A.D. Jr, A. Ferretti, A. Floris, G. Fratesi,

G. Fugallo, R. Gebauer, U. Gerstmann, F. Giustino, T. Gorni, J. Jia, M. Kawamura, H.-Y. Ko, A. Kokalj, E. Kkbenli, M. Lazzeri, M. Marsili, N. Marzari, F. Mauri, N.L. Nguyen, H.-V. Nguyen, A.O. de-la Roza, L. Paulatto, S. Poncé, D. Rocca, R. Sabatini, B. Santra, M. Schlipf, A.P. Seitsonen, A. Smogunov, I. Timrov, T. Thonhauser, P. Umari, N. Vast, X. Wu, S. Baroni, Advanced capabilities for materials modelling with quantum espresso, J. Phys.: Condensed Matter 29 (46) (2017) 465901.

[54] J.P. Perdew, K. Burke, M. Ernzerhof, Generalized gradient approximation made simple, Phys. Rev. Lett. 77 (1996) 3865.

[55] J.P. Perdew, A. Ruzsinszky, G.I. Csonka, O.A. Vydrov, G.E. Scuseria, L.A. Constantin, X. Zhou, K. Burke, Restoring the density-gradient expansion for exchange in solids and surfaces, Phys. Rev. Lett. 100 (2008) 136406 .

[56] N. Troullier, J.L. Martins, Efficient pseudopotentials for plane-wave calculations, Phys. Rev. B 43 (1991) 1993–2006, https://doi.org/10.1103/PhysRevB.43.1993.

[57] H.J. Monkhorst, J.D. Pack, Special points for brillouin-zone integrations, Phys. Rev. B 13 (1976) 5188–5192.

[58] S. Grimme, Semiempirical GGA-type density functional constructed with a long-range dispersion correction, J. Computat.Chem. 27 (15) (2006) 1787.

[59] V. Barone, M. Casarin, D. Forrer, M. Pavone, M. Sambi, A. Vittadini, Role and effective treatment of dispersive forces in materials: polyethylene and graphite crystals as test cases, J. Computat. Chem. 30 (6) (2009) 934.

[60] J. Heyd, G.E. Scuseria, M. Ernzerhof, Hybrid functionals based on a screened coulomb potential, J. Chem. Phys. 118 (18) (2003) 8207–8215, https://doi.org/10.1063/1.1564060.

[61] G. Pizzi, V. Vitale, R. Arita, S. Blügel, F. Freimuth, G. Géranton, M. Gibertini, D. Gresch, C. Johnson, T. Koretsune, J. Ibaez-Azpiroz, H. Lee, J.-M. Lihm, D. Marchand, A. Marrazzo, Y. Mokrousov, J.I. Mustafa, Y. Nohara, Y. Nomura, L. Paulatto, S. Poncé, T. Ponweiser, J. Qiao, F. Thle, S.S. Tsirkin, M. Wierzbowska, N. Marzari, D. Vanderbilt, I. Souza, A.A. Mostofi, J.R. Yates, Wannier90 as a community code: new features and applications (2019). arXiv:1907.09788.

[62] T. Sohier, M. Calandra, F. Mauri, Density functional perturbation theory for gated two-dimensional heterostructures: theoretical developments and application to flexural phonons in graphene, Phys. Rev. B 96 (2017) 075448, https://doi.org/10.1103/PhysRevB.96.075448.

[63] H. Li, Y. Yu, X. Xue, J. Xie, H. Si, J.Y. Lee, A. Fu, Electronic and optical properties of germanene/MoS2 heterobilayers: first principles study, J. Mol. Model. 24 (12) (2018) 333, https://doi.org/10.1007/s00894-018-3855-9.

[64] N.H. Giang, T.T.H. Tran, V.V. Hoang, Structural and thermodynamic properties of two-dimensional confined germanene: a molecular dynamics and DFT study, Mater. Res. Express 6 (8) (2019) 086411, https://doi.org/10.1088/2053-1591/ab1d12.

[65] Y. Fan, X. Liu, J. Wang, H. Ai, M. Zhao, Silicene and germanene on InSe substrates: structures and tunable electronic properties, Phys. Chem. Chem. Phys. 20 (2018) 11369–11377, https://doi.org/10.1039/C8CP00610E.

[66] D.K. Sharma, S. Kumar, A. Laref, S. Auluck, Mono and bi-layer germanene as prospective anode material for li-ion batteries: a first-principles study, Computat. Condensed Matter 16 (2018) e00314, https://doi.org/10.1016/j.cocom.2018.e00314 URL http://www.sciencedirect.com/science/article/pii/S2352214318301382.

[67] M.O. Ne, A.E. hachimi, M. Boujnah, A. Benyoussef, A.E. Kenz, Comparative study of electronic and optical properties of graphene and germanene: DFT study, Optik 158 (2018) 693–698, https://doi.org/10.1016/j.ijleo.2017.12.089 URL http://www.sciencedirect.com/science/article/pii/S0030402617317163.

[68] K. Sakamoto, T. Oda, A. Kimura, K. Miyamoto, M. Tsujikawa, A. Imai, N. Ueno, H. Namatame, M. Taniguchi, P.E.J. Eriksson, R.I.G. Uhrberg, Abrupt rotation of the Rashba spin to the direction perpendicular to the surface, Phys. Rev. Lett. 102 (2009) 096805, https://doi.org/10.1103/PhysRevLett. 102.096805.

[69] S. Peljhan, A. Kokalj, Adsorption of chlorine on cu(111): a density-functional theory study, J. Phys. Chem. C 113 (32) (2009) 14363–14376, https://doi.org/10.1021/jp902273k arXiv: https://doi.org/10.1021/jp902273k.

[70] I.A. Suleiman, M.W. Radny, M.J. Gladys, P.V. Smith, J.C. Mackie, E.M. Kennedy, B.Z. Dlugogorski, An equilibrium ab initio atomistic thermodynamics study of chlorine adsorption on the cu(001) surface, Phys. Chem. Chem. Phys. 13 (2011) 10306–10311, https://doi.org/10.1039/C0CP02211J.

[71] M. Zhang, W. Wang, Y. Chen, Insight of DFT and ab initio atomistic thermodynamics on the surface stability and morphology of In2O3, Appl. Surf. Sci. 434 (2018) 1344–1352, https://doi.org/10.1016/j.apsusc.2017.11.258 URL http://www.sciencedirect.com/science/article/pii/S0169433217335511.

[72] Y.-R. Yin, C.-L. Ren, H. Han, J.-X. Dai, H. Wang, P. Huai, Z.-Y. Zhu, First-principle atomistic thermodynamic study on the early-stage corrosion of NiCr alloy under fluoride salt environment, Phys. Chem. Chem. Phys. 20 (2018) 28832–28839, https://doi.org/10.1039/C8CP05045G.

[73] J. Ibañez Azpiroz, A. Eiguren, A. Bergara, Relativistic effects and fully spin-polarized fermi surface at the TL/SI(111) surface, Phys. Rev. B 84 (2011) 125435.

[74] N. Arzate, R.A. Vázquez-Nava, B.S. Mendoza, Optical spin- and current-injection study on si(111)-in surfaces, Phys. Rev. B 90 (2014) 205310, https://doi.org/10.1103/PhysRevB.90.205310.

[75] J. Gou, L.-J. Kong, W.-B. Li, S.-X. Sheng, H. Li, S. Meng, P. Cheng, K.-H. Wu, L. Chen, Scanning tunneling microscopy investigations of unoccupied surface states in two-dimensional semiconducting-3 3-bi/si(111) surface, Phys. Chem. Chem. Phys. 20 (2018) 20188–20193, https://doi.org/10.1039/C8CP01356J.

[76] H. Zhao, C.-W. Zhang, W.-X. Ji, R.-W. Zhang, S.-S. Li, S.-S. Yan, B.-M. Zhang, P. Li, P.-J. Wang, Unexpected giant-gap quantum spin hall insulator in chemically decorated plumbene monolayer, Sci. Rep. 6 (2016), https://doi.org/10.1038/srep20152.

[77] X.-L. Yu, L. Huang, J. Wu, From a normal insulator to a topological insulator in plumbene, Phys. Rev. B 95 (2017) 125113, https://doi.org/10.1103/PhysRevB.95.125113.

P5. Giant spin splitting induced by a symmetry-braking van der Waals interaction

Applied Surface Science 494 (2019) 619–626

Contents lists available at ScienceDirect

Applied Surface Science

journal homepage: www.elsevier.com/locate/apsusc

Full length article

Giant spin splitting induced by a symmetry-braking van der Waals interaction

Maciej J. Szary[a,*], Marek T. Michalewicz[b,c], Marian W. Radny[a,d,**]

[a] Institute of Physics, Poznan University of Technology, Piotrowo 3A, Poznan, 61-138, Poland
[b] Interdisciplinary Centre for Mathematical and Computational Modelling, ul. Kupiecka 32, Warsaw, 03-046, Poland
[c] Institute for Advanced Computational Science, Stony Brook University, New York, USA
[d] School of Mathematical and Physical Sciences, The University of Newcastle, Callaghan 2308, Australia

ARTICLE INFO

Keywords:
Dichalcogenides
Lead
Spin-orbit coupling
Spin splitting
Orbital angular momentum
Density functional theory

ABSTRACT

It is shown, based on the density functional theory (DFT) calculations, that weak van der Waals interaction between monolayers of Pb and $MoTe_2$ introduce a symmetry breaking that gives rise to spin polarized interface states. This is a departure from a conventional picture of band spin splitting in the adsorption systems as it is usually associated with the strong surface interactions e.g. covalent bonds, which results in electronic charge asymmetry in the vicinity of the adatom's nuclei. The analysis based on the effective Hamiltonian within the orbital-angular-momentum approach to the Rashba effect indicates that the observed spin splitting originates directly from the atomic spin-orbit coupling, with the orbital angular momentum unquenched due to broken inversion symmetry.

1. Introduction

Transition-metal dichalcogenides (TMDs) have a “sandwich” type, three-layer structure—X-M-X—where X represents chalcogen atoms (S, Se, or Te) and M is a transition metal from groups IV–VI (e.g. Mo, Nb, W, Ta, and Ti). The elements within these three layers bond covalently, while individual three-layer films interact with each other by weak van der Waals (vdW) forces. The latter allows for a mechanical or solvent based exfoliation of single, isolated three-layer films (a TMD monolayer) from the bulk, similarly to graphene [1-4].

The isolated TMD monolayers can be either semiconducting (MoX_2 and WX_2) [4-7] or metallic (NbX_2 and TaX_2) [7-9]. The size and type of the gap in semiconducting monolayers can be tuned by a mechanical strain [10-12] or by a number of TMD monolayers stacked [12-14] thus, making the system a promising candidate for nanoelectronics [15-19]. The mechanical strain has also been shown to enhance the chemical activity of the TMD's surface, facilitating formation of covalent bonds that wouldn't be formed otherwise [20, 21]. Furthermore, within a TMD monolayer, each M atom has six nearest-neighbor X atoms in the trigonal prismatic geometry that, breaks inversion symmetry of the system. This, along with the strong spin-orbit coupling (SOC) of electrons in heavy elements comprising the monolayers, leads to a spin splitting of the valence bands within the range of 0.15–0.46 eV [22-24], which makes TMD monolayers suitable for spintronic applications [19,25-28].

In this paper we demonstrate, based on the density functional theory (DFT) calculations, that the weak van der Waals (vdW) forces acting between the monolayers of Pb adatoms (1ML-Pb) and the unstrained $MoTe_2$ monolayer (1ML-$MoTe_2$) break the in-plane symmetry of the monolayers, which induces the spin angular momentum (SAM, or simply spin) polarization of electronic state and facilitates the split of these spin-polarized bands within both systems, not observed when isolated. These effects are present in the Pb/$MoTe_2$ system independently of its adsorption configuration. An insight into the mechanism behind the observed phenomena is provided within the angular orbital momentum (OAM) approach to Rashba effect, which has been shown to predict a correct energy scale of the spin splitting in a variety of systems [29-36]. It is shown that, the spin splitting and spin polarization originate explicitly from the atomic spin-orbit coupling via the term $\boldsymbol{L}\cdot\boldsymbol{S}$, with the unquenched orbital angular momentum $\boldsymbol{L}$ arising due to broken inversion symmetry of the system.

2. Methods

Total-energy and electronic structure calculations were performed based on the density functional theory as implemented in the Quantum

* Corresponding author.
** Correspondence to: M.W. Radny, Institute of Physics, Poznan University of Technology, Piotrowo 3A, Poznan, 61-138, Poland.
E-mail addresses: maciej.s.szary@doctorate.put.poznan.pl (M.J. Szary), marian.radny@newcastle.edu.au (M.W. Radny).

https://doi.org/10.1016/j.apsusc.2019.07.189
Received 22 May 2019; Received in revised form 12 July 2019; Accepted 20 July 2019
Available online 24 July 2019
0169-4332/

Espresso code [37] with the generalized gradient approximation of Perdew Burke Ernzerhof (GGA-PBE) [38,39]. Three types of vdW correction have been employed in the study: semiempirical Grimme's (DFT-D2) [40,41], exchange-hole dipole-moment model (XDM) [42,43] and Tkatchenko-Scheffler (TS-vdW) [44]. First two were used with the Projector Augmented Wave (PAW) potentials [45,46], while for the latter norm-conserving pseudopotentials [47] were employed. The smearing parameter of 1 mRy, and the kinetic energy cut-offs of 55 and 500 Ry for the wave functions and densities, respectively, were also used in the study. The 12 × 12 × 1 Monkhorst-Pack *k*-point sampling set [48] was employed for the surface-Brillouin-zone (SBZ) integrations. The expectation values of the OAM and SAM-vector components, $\langle L_x \rangle$, $\langle L_y \rangle$ etc., for specific *k*-points were calculated using the linear combination of pseudoatomic orbitals (LCPAO) [49] coefficients of local atoms calculated in OpenMX code [50,51].

The monolayer of $MoTe_2$ was modeled within the repeated periodic slab model and a 1 × 1 surface unit cell. The one side of the 1ML-$MoTe_2$ was covered by the Pb atoms and the other remained pristine. The atomic positions of all the atoms in the system were fully optimized with the adopted convergence threshold on forces (less than 10^{-5} Ry/au). All calculations were performed with the optimized 1ML-$MoTe_2$ lattice constant of 3.532 Å; the value for the $MoTe_2$ system are reported between 3.47–3.56 Å [9,12,52], and 3.5 Å for a hexagonal Pb(111) layer [53,54]. The separation between the slabs (vacuum) of 20 Å was found to be sufficient.

3. Results and discussion

3.1. Geometry and energetics

A hexagonal surface of the $MoTe_2$ monolayer has three distinct adsorption sites shown in Fig. 1. The Pb adatoms adsorbed at the H_3 and T_4 sites have three nearest-neighbor Te atoms. The difference between these geometries is that in T_4, the Pb adatoms are located directly above the Mo atoms, while in H_3, the adatoms are placed at the hollow center of the Mo-Te hexagonal rings (see Fig. 1e and i). In configuration T_1, the Pb adatoms are placed directly above the top-layer Te and each Pb has one nearest-neighbor Te atom.

The relaxed, pristine surface of a TMD monolayer is expected to bond with adsorbates via the vdW forces [7,20,55] thus, making it crucial to select an accurate vdW correction method when performing DFT calculations. In order to determine the correct functional for our system we confronted relaxation data of bulk $MoTe_2$ for three different correction methods: Grimme's DFT-D2, TS-vdW dispersion correction, and XDM model (see Section 2). The relaxed structure parameters are given in Table 1. As shown, all functionals produce good lattice constants; TS-vdW and XDM carrying ~2% error, while DFT-D2 method showing only ~0.5% deviation from the experimental data. All of the methods give consistent Mo–Te distances, however, the XDM method produces the noticeably larger Te–Te separation between neighboring layers, with the error of ~10%. By contrast, DFT-D2 and TS-vdW yield much more accurate values, with only ~2% error. On average, DFT-D2 gives structural parameters most closely matching those reported based on experiment thus, we've selected this method for our in depth study of the Pb/$MoTe_2$ interface.

VdW heterostructures usually lack a single, distinct, energetically favorable configuration due to the dispersive nature of the interactions at the interface. Therefore, in search for the stable Pb adatom geometries of the adsorption system, the Pb/$MoTe_2$ interface was sampled by locating the Pb adatoms at the points of a homogeneous 9 × 9 mesh (81 points in total) including the H_3, T_1, and T_4 sites. At each point of the mesh the unrestricted relaxation of the Pb atom was allowed. Our calculations reveal that, the Pb atoms on the $MoTe_2$ monolayer tend to relax along the [110], or equivalent, surface direction (see Fig. 1g), independently of the starting Pb adatom configuration. Fig. 2 shows the total energy plotted as a function of the position of Pb along the [110]

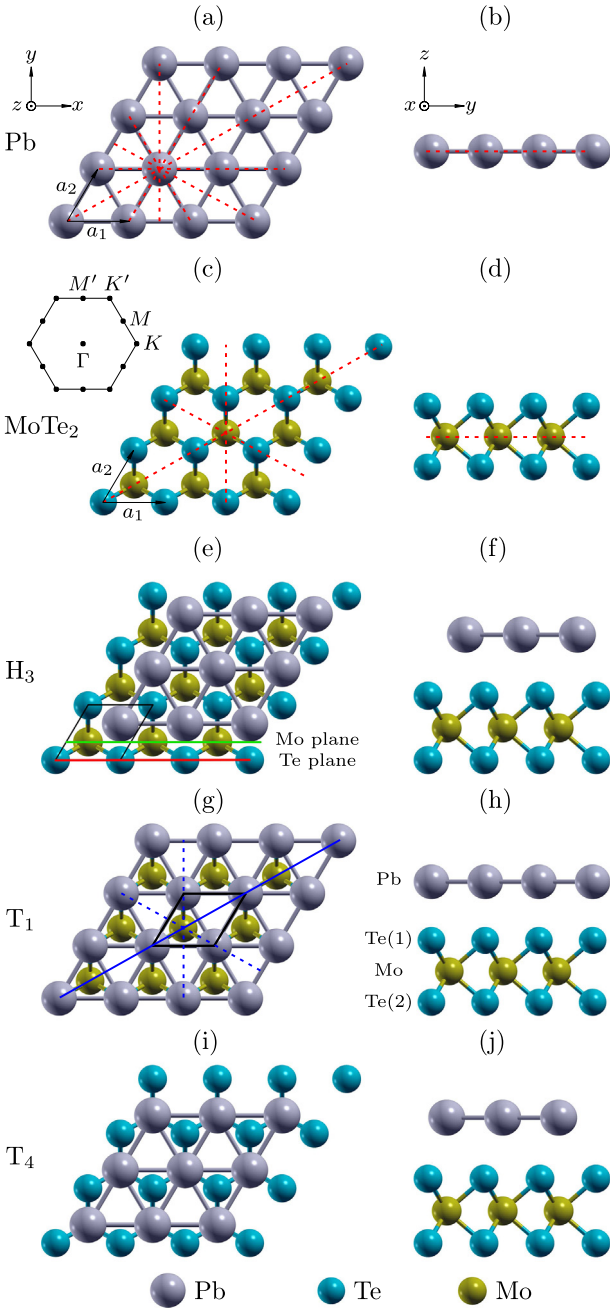

Fig. 1. Top (left) and side (right) views of the atomic structures of isolated Pb and $MoTe_2$ monolayers, and Pb/$MoTe_2$ in configuration H_3, T_1, and T_4. Pb, and $MoTe_2$ MLs belong to p6mm and p3m1 plane symmetry groups, respectively. Inset in (c) shows SBZ, where the Γ-*M* direction is along the *y* axis. Red dashed lines indicate mirror symmetry planes. The surface unit cell of a $MoTe_2$-1 × 1 monolayer is shown in (e) and (g). The [110] (solid blue line) and the equivalent (dashed blue) surface directions of the $MoTe_2$-1 × 1 system are shown in (g). The atomic-layer notations is presented on the left-hand side of (h). The Mo and Te planes (projected onto in Fig. 7) are indicated by green and red lines, respective, in (e).

direction, relative to the ground state of the Pb/$MoTe_2$ system. Geometry H_3' was found to be the most stable. This structure is an off-center variation of configuration H_3 tilted 0.72 Å along the [110] direction towards the Te atom. It is by 7.5 meV lower in energy than H_3, with the latter being a state of unstable equilibrium. This is in contrast to the study of X Du et al. [54] where structure H_3 was reported to be the ground state of the interface. Configuration T_1', where the Pb atom is tilted 1.0 Å of the T_1 position towards T_4, is the second lowest energy

Table 1
Lattice properties of hexagonal bulk $MoTe_2$ (2H): lattice constants a, c, Te–Mo layer separation in the monolayer ($\Delta z_{Mo\text{-}Te}$), vdW gap ($\Delta z_{Te\text{-}Te}$), Mo–Te distance in the monolayer ($d_{Mo\text{-}Te}$), and Te–Te distance for neighboring monolayer ($d_{Te\text{-}Te}$). Data sets for three vdW functionals (DFT-D2, TS-vdW, and XDM) are confronted with the experimental values.

	a	c	c/a	$\Delta z_{Mo\text{-}Te}$ (Å)	$\Delta z_{Te\text{-}Te}$	$d_{Mo\text{-}Te}$	$d_{Te\text{-}Te}$
DFT-D2	3.532	13.956	3.951	1.843	3.307	2.749	3.885
TS-vdW	3.574	14.217	3.978	1.848	3.413	2.769	3.988
XDM	3.466	13.594	3.859	1.863	3.069	2.734	3.664
exp.[a]	3.518	13.974	3.972	1.802	3.384	2.716	3.945
exp.[b]	3.519	13.964	3.968	1.815	3.352	2.730	3.920

[a] Ref. [56].
[b] Ref. [57].

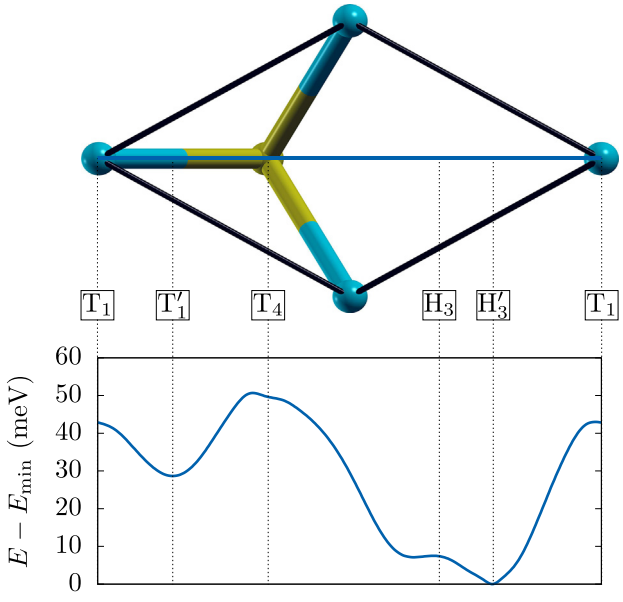

Fig. 2. (Top) Schematics of the 1 × 1 surface unit cell of $MoTe_2$ with the blue line indicating the [110] surface direction. (Bottom) The total energy of the Pb/$MoTe_2$ system calculated for the Pb adatom adsorbed at different points along [110] surface direction relative to the ground state configuration (H_3'). Configurations other than H_3, H_3', T_1, T_1' and T_4, are unstable (relaxing into H_3' or T_1'), and therefore at these points the Pb atoms were relaxed along the normal to the $MoTe_2$ surface. The graph is composed of 31 points in total.

geometry. This configuration is by 29 meV higher in energy than H_3'. The neighboring T_1 and T_4 configurations were found, similarly to H_3, to be the states of unstable equilibria with energies, respectively, 43 meV and 50 meV higher than H_3'. These results indicate that, the stable T_1' and H_3' configurations can be transformed into one another by horizontal sliding of the Pb monolayer along the [110] direction with the negligible activation barriers of 43 meV and 14 meV for the H_3'-to-T_1' and T_1'-to-H_3' transitions, respectively. It shows that position of the Pb atoms on $MoTe_2$ has a limited impact on the binding energy of the Pb/$MeTe_2$ heterostructures, which is between −0.47 and −0.42 eV. Low binding energy, and a lack of strongly localized adsorption site are indicative of vdW interface, and suggest a lack of covalent bonding between the systems.

The inter-atomic and inter-layer distances of the Pb/$MoTe_2$ system are given in Table 2. One observes that the changes in the bond lengths within the $MoTe_2$ monolayer upon adsorption are negligible in reference to the isolated monolayer (up to 0.02 Å). On the other hand, the Pb–Te(1) distance varies significantly depending on the adsorption site (e.g. 0.69 Å between T_1 and T_4), however, this is shown to have very little impact on the binding energy of the heterostructure (50 meV).

Table 2
Calculated bonding lengths and interlayer spacings of the Pb/MoTe2 interface in configurations H_3, H_3', T_1, T_1', and T_4. The enumeration of Te atoms is shown in Fig. 1.

	Ref.	T_1	T_1'	T_4	H_3	H_3'
			(Å)			
			Interlayer spacings			
Pb-Te(1)	–	3.079	3.117	3.172	3.025	2.948
Te(1)-Mo	1.830[b]	1.806	1.806	1.829	1.825	1.826
Mo-Te(2)	1.830[b]	1.829	1.829	1.826	1.826	1.826
			Atomic distances			
Pb-Te(1)	2.93[a]	3.079	3.221	3.768	3.644	3.228
Te(1)-Mo	2.736[b]	2.720	2.720	2.735	2.732	2.731
Mo-Te(2)	2.736[b]	2.732	2.735	2.732	2.732	2.731

[a] Ref. [58], PbTe(111)-(2 × 1), Pb terminated, LDA-PZ.
[b] Present work, isolated $MoTe_2$, GGA-PBE, DFT-D2.

This again suggests a lack of strong chemical interaction at the interface. Finally, it should also be noted that the Pb–Te(1) distance of 3.22 Å calculated for the most stable geometry is much larger than the sum of the covalent radii of the Te and Pb atoms (2.84 Å), and it is clearly beyond the covalent bonding range of Pb–Te.

3.2. Electronics of $MoTe_2$

Fig. 3 shows the electronic band structures of the isolated Pb and $MoTe_2$ monolayers with and without SOC. The non-SOC electronic structure of the Pb monolayer is metallic (Fig. 3a). In the vicinity of the Fermi level (E_F) the bands are comprised of the unbonded p_z states and the coupled p_x and p_y states, with the latter forming covalent bonds within the Pb-monolayer plane [35,36,59]. The spin-orbit interaction opens the gaps at all crossing points in the non-SOC band structure (Fig. 3b), however, the system remains metallic, which agrees with other studies [35,58].

The isolated $MoTe_2$ monolayer is a direct-band-gap semiconductor, with the gap of 1.19 and 1.05 eV for non-SOC and SOC regime, respectively—see the band structures of Fig. 3c and d. In the non-SOC case, the top valence band at Γ (− 1.04 eV) consists of the Te $5p_z$ (35%) and $4d_{z^2}$ (65%) atomic orbitals, which changes to the Mo $4d_{x^2y^2}$ (40%) and Mo $4d_{xy}$ (40%) states with small contribution of Te $5p_x/5p_y$ (8%) at the K point (− 0.48 eV). This band in the SOC band structure of Fig. 3d exhibits the spin-dependent splitting along Γ-K-M with the maximum split of 216 meV at K. As shown in Fig. 3f the spin in the split bands in the vicinity of K is oriented along the z axis. Also, the OAM in Fig. 3e is represented by the non-zero expectation value of the $\boldsymbol{L}_z$ component only, as the projections of $\langle \boldsymbol{L}_x \rangle$ and $\langle \boldsymbol{L}_y \rangle$ are calculated to be virtually zero. Comparing the $\langle \boldsymbol{L}_z \rangle$ and $\langle \boldsymbol{S}_z \rangle$ projections (see Fig. 3e and f) it is clear that the direction of SAM, and the magnitude of spin splitting correlates with the direction and value of the unquenched atomic OAM. In periodic systems the OAM is usually quenched due to symmetry of the crystal field. However, in the presence of a surface or other factors that break the inversion symmetry of a system the OAM can be large [33,34]. The unquenched OAM in the non-SOC band structure of $MoTe_2$ arises due to the inversion asymmetry of the monolayer in the z-x plane; the x-y and z-y are mirror symmetry planes of the monolayer (the mirror symmetry planes are along the z and y axes, but not along x; see Fig. 1c and d, and also for details Ref. [34]).

3.3. Mechanism of spin splitting in $MoTe_2$

The energetics of the spin split bands can be discussed by evaluating the matrix element:

$$\langle n, \boldsymbol{k}_{||} | \hat{H} | n, \boldsymbol{k}_{||} \rangle, \quad (1)$$

where $|n,k_{||}\rangle$ denotes the state in the band structure with the band index n and the momentum $\boldsymbol{k}_{||}$, with $\hat{H}$ being the effective Hamiltonian

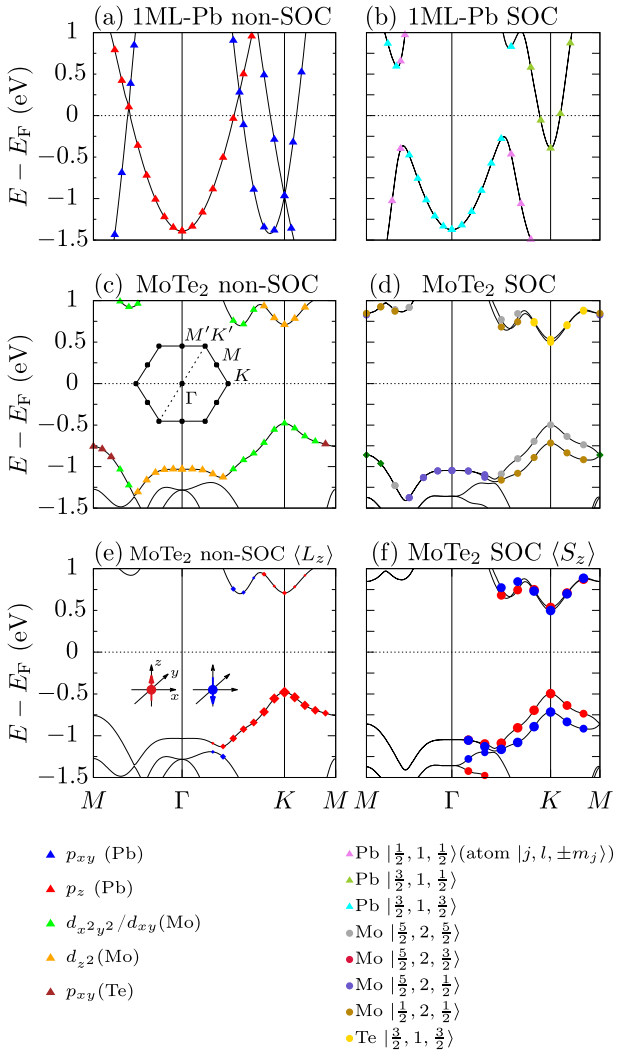

Fig. 3. SOC and non-SOC electronic band structure of the isolated Pb (a, b) and $MeTe_2$ (c, d) monolayers. The color code in (a)–(d) maps the orbital composition of the bands. The color codes in (e) and (f) maps the $\boldsymbol{L}$ and $\boldsymbol{S}$ contribution to the bands of the $MoTe_2$ monolayer. The corresponding projections for the isolated Pb monolayer as well as $\langle \boldsymbol{L}_{x(y)} \rangle$ and $\langle \boldsymbol{S}_{x(y)} \rangle$ for isolated $MoTe_2$ were calculated to be virtually zero and are not shown. In all figures the Fermi level is at 0 eV.

operator of the form [29,30,33]:

$$\hat{H} = \alpha \boldsymbol{L}\cdot\boldsymbol{S} + \beta(\boldsymbol{k}\times\boldsymbol{L})\cdot\boldsymbol{E} = \hat{H}_{SOC} + \hat{H}_{E}. \quad (2)$$

The first term in Eq. (2) is the atomic SOC interaction with α as a SOC coupling strength, and the second term is the electric dipole energy. In the latter β is a constant determined by the overlap between adjacent, coupled atomic orbitals, $\boldsymbol{k}\times\boldsymbol{L}$ gives the vector of the electric charge imbalance, and $\beta(\boldsymbol{k}\times\boldsymbol{L})$ expresses the dipole momentum originating from it; $\boldsymbol{E}$ is an external electric field vector.

As $\boldsymbol{L}_z$ is the only non-zero component of $\boldsymbol{L}$ (see Fig. 3e), the charge imbalance, correlated with the splitting at K, would be formed within the x-y plane of the monolayer. As shown in Fig. 4 the calculated electronic charge is distributed predominantly in the Mo plane centered at the Mo atoms. However, for any non-zero x-y component of the electric field vector $\boldsymbol{E}$, the three-fold symmetry of the imbalanced charge results in the net electric dipole energy being zero. This makes the splitting in the isolated $MoTe_2$ governed exclusively by $\hat{H}_{SOC}$.

Fig. 5 shows the energetics of spin splitting along Γ-K-M for the $d_{x^2y^2}/d_{xy}$ band (see Fig. 3d and f) obtained directly from DFT (black curve) and that estimated from the $\hat{H}_{SOC}$ Hamiltonian of Eq.

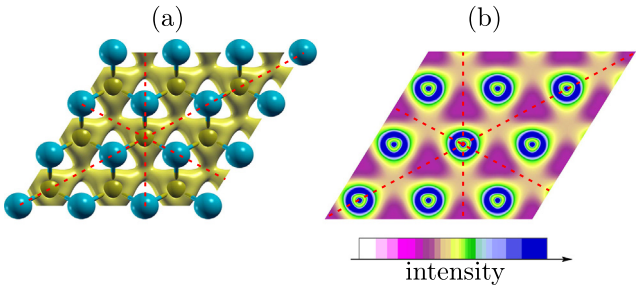

Fig. 4. Charge density contours, and the corresponding cross section taken in the atomic x-y plane of Mo calculated at the K point for the spin split bands of the isolated $MoTe_2$ monolayer. Isosurface value: 0.005 e/au^3. Red dashed lines indicate mirror symmetry planes. Atoms are represented as in Fig. 1.

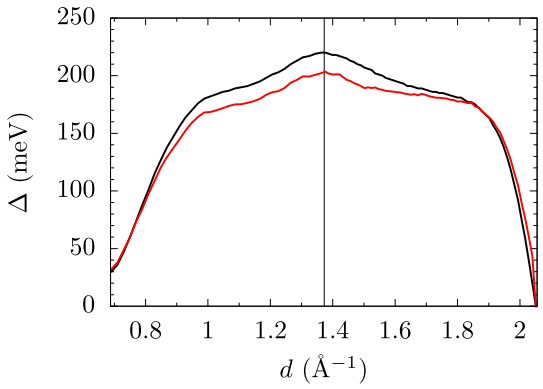

Fig. 5. Isolated $MoTe_2$ monolayer—energetics of the spin split $d_{x^2y^2}/d_{xy}$ band calculated along Γ-K-M on the section where the split states do not overlap with the neighboring bands (see Fig. 3d and f). The black and red curves represent the DFT data and those obtained from the effective $\hat{H}_{SOC}$ Hamiltonian, respectively. The K point in SBZ is represented by the vertical black line; M is at 2.06 Å^{-1}.

(2);$\Delta = \langle \hat{H}_{SOC} \rangle_{5/2} - \langle \hat{H}_{SOC} \rangle_{3/2} \approx 2\alpha\langle \boldsymbol{L}_z \rangle\langle \boldsymbol{S}_z \rangle$ (red curve); parameter α has been taken from the theoretical prediction and spectroscopic data in Refs. [60]and [61]. Both sets of data are observed to be well correlated, with the maximal numerical difference of 6% at K.

3.4. Electronics of Pb/$MoTe_2$

Fig. 6 shows the non-SOC electronic band structures of the Pb/$MoTe_2$ heterostructure in configurations H_3' (a), H_3 (b), T_1 (c), T_1' (d), and T_4(e). The configurations have the vdW gap of ~3 Å (see Table 2). We also show the evolution of the electronic band structure depending on the size of vdW gap (see Fig. 6f–i).

We observe that the band structures of adsorption configurations are very similar. This similarity suggests that the interaction at the Pb/$MeTe_2$ interface is dispersive in nature and as such uniform across the interface independently of the adsorption geometry resulting in similar band structures for all of them. We also observe that the bands in the electronic structures of Pb/$MoTe_2$ are preserved everywhere in the SBZ except the vicinity of the Γ point where the new features are observed. In particular, the coupling of the unbonded $6p_z$ (Pb) orbital (at − 1.38 eV in 1ML-Pb) with the $5p_z$ [Te(1)] and $4d_{z^2}$ (Mo) states (band S_2, at − 1.04 eV in 1ML-$MoTe_2$) in band S_1 at 0.11–0.46 eV above the Fermi (see Table 3). This band is formed predominantly by unbonded orbitals of Pb that experience an upward energy shift of 1.49–1.94 eV upon adsorption. Also, this coupling reduces the contribution of the $5p_z$ [Te(1)] and $4d_{z^2}$ (Mo) states of band S_2 in the vicinity of Γ in the adsorption system, lowering its energy by ~0.2 eV when compared to 1ML-$MoTe_2$ (see Fig. 6a and h).

These new features are not commonly associated with vdW

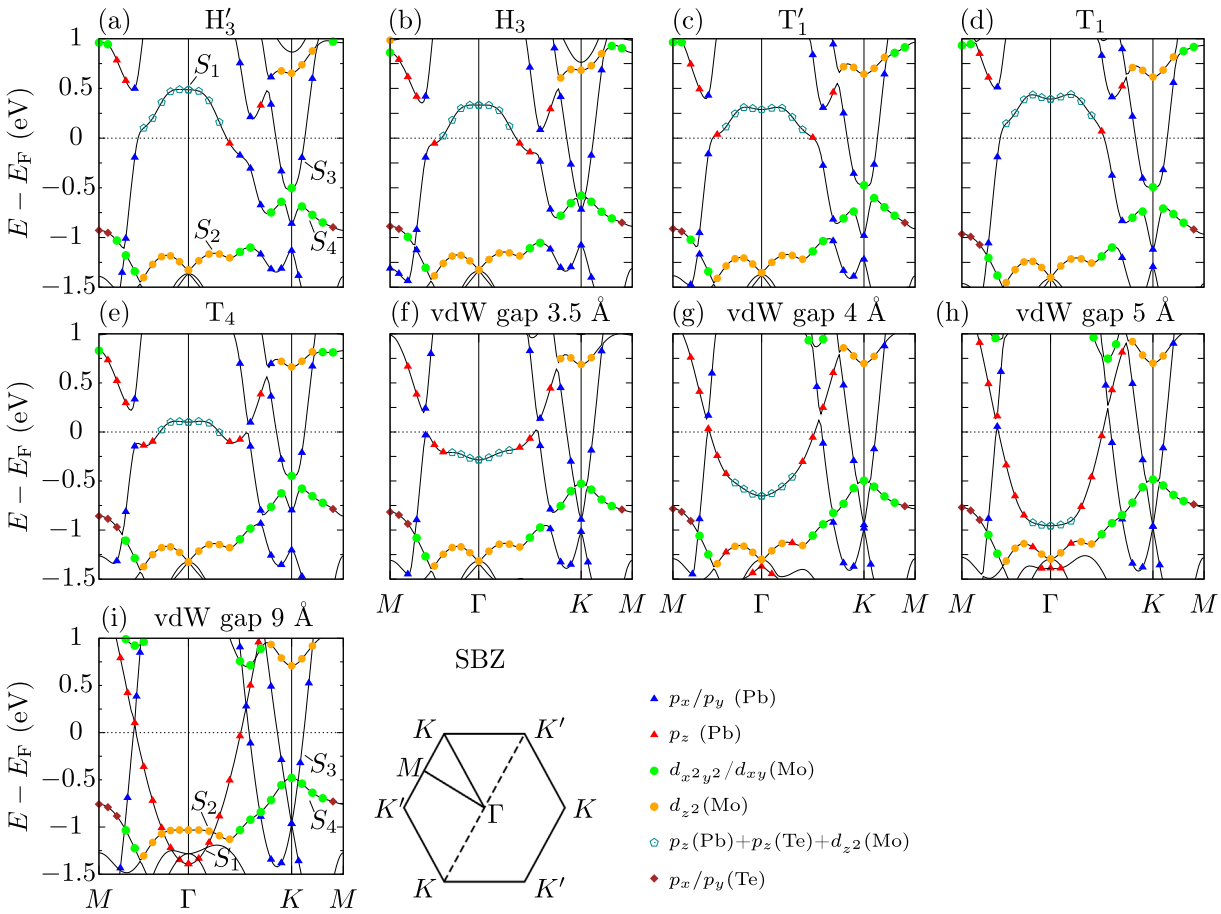

Fig. 6. Non-SOC electronic band structures of the Pb/$MoTe_2$ heterostructure in configurations H_3' (a), H_3 (b), T_1' (c), T_1 (d), T_4 (e). Electronic structures of the system with increased size of vdW gap are shown in f–i. Fig. (a) and (i) indicate the bands of interest (S_1–S_4). The color code maps the orbital composition of the bands. In all figures the Fermi level is at 0 eV.

Table 3
The electronic states of band S_1 for configuration H_3, H_3', T_1, T_1' and T_4 projected onto orthogonalized atomic wave functions for k values of 0 and 0.35 Å^{-1}; non-SOC case.

	Γ					
	p_z (Pb)	p_z (Te)	d_{z^2} (Mo)	p_{xy} (Pb)	p_{xy} (Te)	$d_{x^2y^2}/d_{xy}$ (Mo)
H_3	0.506	0.25	0.124	0	0	0
H_3'	0.506	0.248	0.122	0	0	0
T_1	0.496	0.262	0.126	0	0	0
T_1'	0.500	0.256	0.149	0	0	0
T_4	0.497	0.255	0.165	0	0	0
				0.35 Å^{-1} (Γ-K)		
H_3	0.431	0.083	0.005	0.14	0.128	0.046
H_3'	0.427	0.081	0.005	0.123	0.133	0.045
T_1	0.402	0.091	0.004	0.151	0.161	0.095
T_1'	0.448	0.070	0.003	0.12	0.136	0.056
T_4	0.518	0.132	0.022	0.092	0.08	0.022

interfaces as typically the electronic band structure of such systems is a combination of well preserved electronic bands of their components (see for example the MoS_2/PbI_2 heterostructure reported in Ref. [62]). The peculiar behavior of band S_1 observed around Γ was discussed in Ref. [54] as a result of strong hybridization of the Pb and Te orbitals and the formation of bonding and antibonding states. However, the band-decomposition analysis shows that the bands below the Fermi level shows no coupling of the Pb–Te(1), i.e., they cannot represent a bonding state of a chemical Pb-Te bond. Furthermore, the suggested localized, directional interaction at the Pb/$MoTe_2$ interface does not coincide with the calculated energetics of the system and its structural properties. Moreover, S_1 is observed for all adsorption sites and at Γ those bands have virtually identical composition. Therefore, it is hard to see how the same covalent bond could be formed at distinct adsorption sites of the surface.

Fig. 7 shows the probability density contours calculated for the empty band S_1 at Γ. One can observe that, the contributing densities retain their Pb, Te and Mo atomic characters (as they are localized predominantly in the vicinity of the respective atoms) with their x-y symmetries affected by the interface formation. Furthermore, as shown in Fig. 6i band S_1 around Γ is initially occupied when two systems are isolated, and it moves towards E_F when the distance between the Pb and $MoTe_2$ layers is reduced (Fig. 6f–h), This continues until the equilibrium distance is achieved, at which point band S_1 ends above the Fermi level (Fig. 6a–d). The increase of the binding energy of this occupied band results in the higher energy of the Pb/$MoTe_2$ system reflecting the repulsive interaction between the orbitals comprising the band.

Repulsive interactions in atomic systems are typically discussed in terms of exchange interaction where electrons are repulsed due to Pauli exclusion principle. This becomes a major term when atoms are in close proximity i.e. less than their bonding distance. Such effect could contribute to the repulsive interactions indicated by band S_1 when layers are close, but if only limited to Pauli repulsion this interaction should vanish quickly with a small increase of the layer spacing. This however, is not the case as the Pb-Te-Mo coupling and the upward shift of the band is still observed at 5 Å separation between layers of Pb and $MoTe_2$ (see Fig. 6h). This far exceeds a distance at which any significant electronic overlap could be considered, which indicates that the

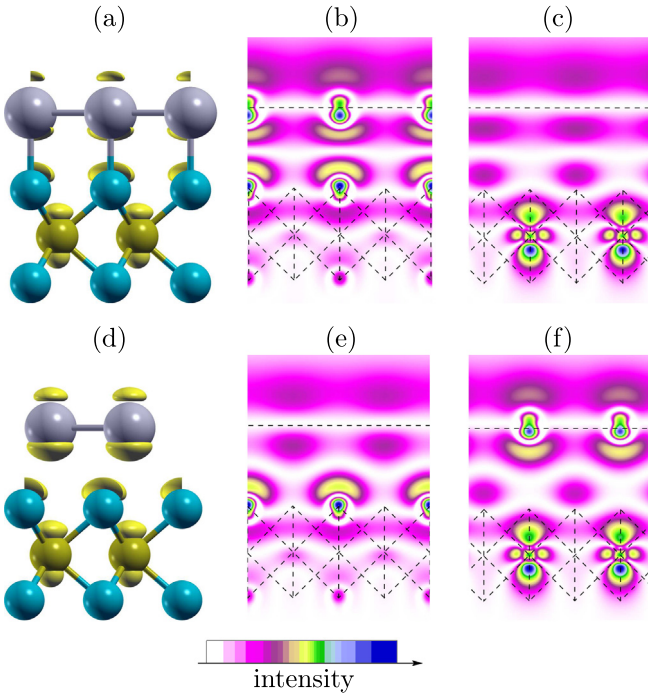

Fig. 7. Probability density contours (a, d) and their cross sections (b, c, e, f) calculated at Γ for band S_1 for the T_1 (a–c) and T_4 (d–f) geometries. The distributions calculated for other configurations exhibit very similar features. Configurations T_1 and T_4 were chosen as the Pb, Te and Mo atoms can be viewed on the same planes and corresponding cross sections—the contours (a, d) and the cross sections (b, c, e, f) are projected onto the (110) and (100) planes, respectively. The cross sections represent the charge density profiles crossing Te (b, e) and Mo (c, f) atoms along (100) (shown in Fig. 1e, red and green lines, respectively). The isosurface value is $-0.0026\, e/\text{au}^3$.

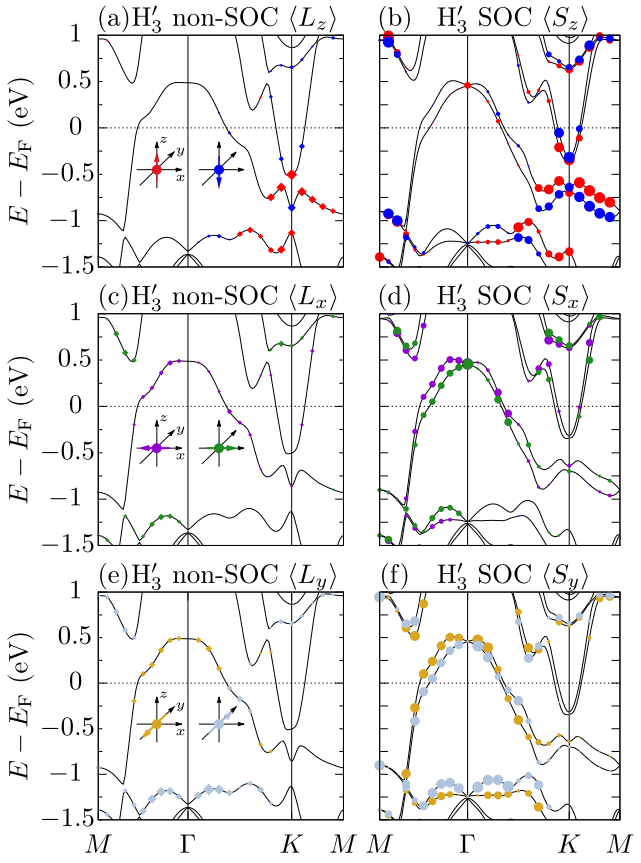

Fig. 8. Projections of the unquenched OAM (triangles) and spin (circles) vectors onto the electronic structures of the H_3' adsorption configuration. The color coding of the projected vectors is shown in Fig. 3.

repulsion has to be also supplemented by the dipole term of vdW interactions.

In general, the dipole term of vdW interaction in three-dimensions (3D) between two polarizable media with the r^{-1} coulombic intrapotential is described by an attractive r^{-6} potential that, results in lowering the energy of the interacting system. However, as discussed in Ref. [63], if the electronic motion is restricted to lower dimension (1D or 2D), with the r^{-1} coulombic potential within the interacting parts and no overlap of the electronic wave functions retained, the r-dependence for dipole interactions will change from attractive r^{-6} to repulsive r^{-5}. In 2D materials the electrons are confined to an extreme degree, and thus they should share similarities with model 2D system. Indeed, the theoretically predicted repulsion between not overlapping, electronic states coincides with our DFT calculations for band S_1. We conclude therefore, that coupling between Pb, Te and Mo orbitals at Γ is facilitated by the electric field induced at the interface by the restricted electronic motion in the 2D layers, and it reflects the repulsive Pb/$MoTe_2$ dispersive interactions rather than directional in nature strong chemical bonding. Similar atomic orbital coupling mechanism was discussed in Ref. [34] for the isolated TMD monolayers exposed to an external electric field.

The electric field at the Pb/$MoTe_2$ interface arises due to the gradient of the interface potential which breaks the x-y mirror symmetry in both the Pb and $MoTe_2$ monolayers (see Fig. 1a–d and it compare with Fig. 1e–j). This field induces the inversion asymmetry in Pb/$MoTe_2$ and is manifested in the corresponding band structures (Fig. 8) via the presence of spin-split electronic bands.

3.5. Mechanism of spin splitting in Pb/$MoTe_2$

As in all of the identified adsorption configurations the splitting are observed between the same pairs of bands we will analyze the observed effects based on the H_3' configuration. Fig. 8 presents the calculated projections of the SAM and OAM vectors onto the H_3' SOC electronic band structure. Along Γ-K-M the split of 220 meV of the $d_{x^2y^2}$(Mo)/d_{xy}(Mo) band around K (S_4, see Fig. 6a) is facilitated by the non-zero $\boldsymbol{L}_z$ component of OAM and is the same as for the isolated monolayer (0.216 meV; compare Figs. 8a and b with Fig. 3e and f), and therefore it is not considered as an adsorption induced feature. On the other hand, the non-zero OAM ($\boldsymbol{L}_z$) is also responsible for the spin-split metallic band of the Pb origin at -0.86 eV at K (S_3, see Fig. 6a). For this band, the $\boldsymbol{L}_x$ and $\boldsymbol{L}_y$ components show near-zero values in the vicinity of K (Fig. 8c and e), and thus $\langle \hat{H}_E \rangle \approx 0$ $[(\boldsymbol{k}_{||} \times \boldsymbol{L}_z) \perp \boldsymbol{E}]$. We conclude, therefore that, similarly to 1ML-$MoTe_2$, the spin splittings observed along the Γ-K-M direction in the Pb/$MoTe_2$ system are also governed exclusively by $\hat{H}_{SOC}$.

For band S_1, the split states are comprised by both x-y and z-type orbitals originating from three different-type atoms, namely: Pb (47–54%) followed by Te(1) (19–24%) and Mo (10–20%). The band's composition correlates with small projections of OAM for Mo and Te—first being prominent within band S_2 (see Fig. 6, and the $\boldsymbol{L}$ projections in Fig. 8c and e) with virtually no OAM of Mo origin in band S_1, and the other exhibiting small non-zero values of $\langle \boldsymbol{L} \rangle$ across bands S_1 and S_2. In the vicinity of the Γ point, the spin splitting of the empty S_1 is induced by the non-zero $\langle \boldsymbol{L}_x \rangle$ and $\langle \boldsymbol{L}_y \rangle$ components (Fig. 8c and f). As the $\boldsymbol{L}_x$ and $\boldsymbol{L}_y$ are the only non-zero components of the unquenched OAM, both the OAM and SAM vectors in the spin-split bands have a chiral structure in x-y plane (see the first term in Eq. (2)). Also, considering the second term in Eq. (2) and the non-zero values of $\boldsymbol{L}_x$ and $\boldsymbol{L}_y$ in vicinity of Γ, the charge imbalance originating from unquenched OAM should be observed in the z-x and z-y planes. For this band,

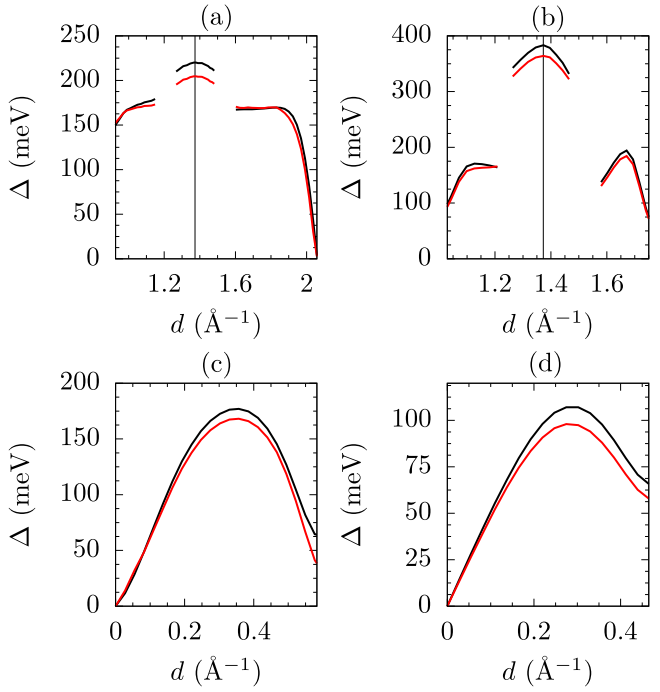

Fig. 9. Configuration H_3'—energetics of the spin-split S_4 (a) and S_3 (b) bands (along Γ-*K*-*M*), and S_2 (c), and S_1 (d) (along Γ-*K*). The black and red curves represent the DFT data and those obtained from the effective $\hat{H}_{SOC}$ Hamiltonian, respectively. The *K* point in SBZ is represented by the vertical black line. Figs.(a) and (b); Γ is at 0.0 Å^{-1}, and *M* is at 2.06 Å^{-1}.

however, the charge asymmetry becomes the probability density asymmetry indicating that the observed splitting must be governed exclusively by $\hat{H}_{SOC}$.

The splitting in vicinity of Γ also occurs for band S_2 (−1.26 eV). The band is dominated by Mo states and represents the bonding between top and bottom Te atoms with Mo. In this case, the adsorbate/substrate interaction of p_z(Pb), p_z([Te(1)] and d_{z^2}(Mo)—represented by the S_1 band—brakes the out-of-plane symmetry of the Mo-Te bonding, $\langle \boldsymbol{L}_y \rangle$, $\langle \boldsymbol{L}_x \rangle$, and $\langle \boldsymbol{L}_y \rangle$, $\langle \boldsymbol{L}_z \rangle$ components in S_2 along the Γ-*M*, and Γ-*K* directions, respectively thus, allowing for non-zero contributions from$\hat{H}_E$. However, for an atom of Mo mass it is still expected that, the splitting will be governed predominantly by $\hat{H}_{SOC}$ [29-33]. Similar SOC effect was also reported for a WSe_2 monolayer in presence of an external electric field [34].

Fig. 9 shows the energetics of spin splitting of the discussed above bands as predicted by the effective Hamiltonian of Eq. (2) along with the DFT values. Both sets of data are in good agreement, with DFT showing consistently slightly higher values. For the bands in the vicinity of Γ, the splitting values form a characteristic parabolic dispersion for non-zero values of $\boldsymbol{k}$, with momentum offset of 0.35 and 0.27 Å^{-1} for S_2 and S_1 bands, respectively. The corresponding split values are 168 (177 for DFT), and 98 (107) meV. The split along Γ-*K*-*M* has the maximal values at *K* point of 204 (220) meV for S_4, and 364 (383) meV for band S_3.

4. Conclusions

It was shown that spin polarization of electronics states in the Pb/$MoTe_2$ adsorption system can be induced by a broken symmetry due to van der Waals interactions between monolayers of Pb and $MoTe_2$ independently of the adsorption configuration. By applying the effective Hamiltonian we have demonstrated that, the observed splitting can be understood as the phenomenon resulting from the unquenched atomic orbital momentum. We have also shown that, the spin splitting is predominantly of the SOC origin with the negligible contribution from the charge asymmetry at the interface. This analysis also shows that, the observed spin splitting can be classified as Rashba effect and demonstrates that, the weak forces are strong enough to facilitate a non-negligible SOC-enhanced spin splitting in 2D TMD-based systems. Furthermore, as there is no chemical bonding between the spin polarized system components, they can be seen as two quasi-independent spin-polarized media, with the magnitude of spin splitting tunable by eg. the monolayer distance.

Acknowledgments

M.J.S. and M.W.R. acknowledge the Ministry of Science and Higher Education in Poland for financial support within Project No. 06/62/SBAD/1923 realized at Faculty of Technical Physics, Poznan University of Technology. A*STAR Computational Resource Centre, Singapore is acknowledged for access to the high performance computing facilities.

References

[1] M.M. Benameur, B. Radisavljevic, J.S. Hron, S. Sahoo, H. Berger, A. Kis, Visibility of dichalcogenide nanolayers, Nanotechnology 22 (12) (2011) 125706 http://stacks.iop.org/0957-4484/22/i=12/a=125706.

[2] J.N. Coleman, M. Lotya, A. O'Neill, S.D. Bergin, P.J. King, U. Khan, K. Young, A. Gaucher, S. De, R.J. Smith, I.V. Shvets, S.K. Arora, G. Stanton, H.-Y. Kim, K. Lee, G.T. Kim, G.S. Duesberg, T. Hallam, J.J. Boland, J.J. Wang, J.F. Donegan, J.C. Grunlan, G. Moriarty, A. Shmeliov, R.J. Nicholls, J.M. Perkins, E.M. Grieveson, K. Theuwissen, D.W. McComb, P.D. Nellist, V. Nicolosi, Two-dimensional nanosheets produced by liquid exfoliation of layered materials, Science 331 (6017) (2011) 568–571, https://doi.org/10.1126/science.1194975 http://science.sciencemag.org/content/331/6017/568 arXiv: http://science.sciencemag.org/content/331/6017/568.full.pdf.

[3] C. Lee, Q. Li, W. Kalb, X.-Z. Liu, H. Berger, R.W. Carpick, J. Hone, Frictional characteristics of atomically thin sheets, Science 328 (5974) (2010) 76–80, https://doi.org/10.1126/science.1184167 http://science.sciencemag.org/content/328/5974/76 arXiv:http://science.sciencemag.org/content/328/5974/76.full.pdf.

[4] B. Radisavljevic, A. Radenovic, J. Brivio, V. Giacometti, A. Kis, Single-layer MoS_2 transistors, Nat. Nanotechnol. 6 (2011), https://doi.org/10.1038/nnano.2010.279 147 EP –.

[5] T. Roy, M. Tosun, J.S. Kang, A.B. Sachid, S.B. Desai, M. Hettick, C.C. Hu, A. Javey, Field-effect transistors built from all two-dimensional material components, ACS Nano 8 (6) (2014) 6259–6264, https://doi.org/10.1021/nn501723y pMID: 24779528.

[6] A. Ramasubramaniam, Large excitonic effects in monolayers of molybdenum and tungsten dichalcogenides, Phys. Rev. B 86 (2012) 115409, https://doi.org/10.1103/PhysRevB.86.115409 https://link.aps.org/doi/10.1103/PhysRevB.86.115409.

[7] Q.H. Wang, K. Kalantar-Zadeh, A. Kis, J.N. Coleman, M.S. Strano, Electronics and optoelectronics of two-dimensional transition metal dichalcogenides, Nat. Nanotechnol. 7 (2012), https://doi.org/10.1038/nnano.2012.193 699 EP –, review Article.

[8] A. Kuc, N. Zibouche, T. Heine, Influence of quantum confinement on the electronic structure of the transition metal sulfide ts_2, Phys. Rev. B 83 (2011) 245213, https://doi.org/10.1103/PhysRevB.83.245213.

[9] Y. Ding, Y. Wang, J. Ni, L. Shi, S. Shi, W. Tang, First principles study of structural, vibrational and electronic properties of graphene-like mx2 (m = Mo, Nb, W, Ta; x = S, Se, Te) monolayers, Physica B: Condensed Matter 406 (11) (2011) 2254–2260, https://doi.org/10.1016/j.physb.2011.03.044 http://www.sciencedirect.com/science/article/pii/S0921452611002651.

[10] P. Johari, V.B. Shenoy, Tuning the electronic properties of semiconducting transition metal dichalcogenides by applying mechanical strains, ACS Nano 6 (6) (2012) 5449–5456, https://doi.org/10.1021/nn301320r https://doi.org/10.1021/nn301320r pMID: 22591011.

[11] S. Song, D.H. Keum, S. Cho, D. Perello, Y. Kim, Y.H. Lee, Room temperature semiconductormetal transition of $MoTe_2$ thin films engineered by strain, Nano Letters 16 (1) (2016) 188–193, https://doi.org/10.1021/acs.nanolett.5b03481 https://doi.org/10.1021/acs.nanolett.5b03481 pMID: 26713902.

[12] W.S. Yun, S.W. Han, S.C. Hong, I.G. Kim, J.D. Lee, Thickness and strain effects on electronic structures of transition metal dichalcogenides: 2h-mX_2 semiconductors (m = Mo, W; x = S, Se, Te), Phys. Rev. B 85 (2012) 033305, https://doi.org/10.1103/PhysRevB.85.033305 https://link.aps.org/doi/10.1103/PhysRevB.85.033305.

[13] K.F. Mak, C. Lee, J. Hone, J. Shan, T.F. Heinz, Atomically thin MoS_2: a new direct-gap semiconductor, Phys. Rev. Lett. 105 (2010) 136805, https://doi.org/10.1103/PhysRevLett.105.136805.

[14] K. Dileep, R. Sahu, S. Sarkar, S.C. Peter, R. Datta, Layer specific optical band gap measurement at nanoscale in MoS_2 and ReS_2 van der Waals compounds by high resolution electron energy loss spectroscopy, J. Appl. Phys. 119 (11) (2016) 114309, https://doi.org/10.1063/1.4944431.

[15] H.-L. Tang, M.-H. Chiu, C.-C. Tseng, S.-H. Yang, K.-J. Hou, S.-Y. Wei, J.-K. Huang,

Y.-F. Lin, C.-H. Lien, L.-J. Li, Multilayer graphene-WSe_2 heterostructures for WSe_2 transistors, ACS Nano 11 (12) (2017) 12817–12823, https://doi.org/10.1021/acsnano.7b07755 pMID: 29182852.
[16] Q. Li, J. Yang, R. Quhe, Q. Zhang, L. Xu, Y. Pan, M. Lei, J. Lu, Ohmic contacts between monolayer WSe_2 and two-dimensional titanium carbides, Carbon 135 (2018) 125–133, https://doi.org/10.1016/j.carbon.2018.04.043 http://www.sciencedirect.com/science/article/pii/S0008622318304020.
[17] J.-W. Chen, S.-T. Lo, S.-C. Ho, S.-S. Wong, T.-H.-Y. Vu, X.-Q. Zhang, Y.-D. Liu, Y.-Y. Chiou, Y.-X. Chen, J.-C. Yang, Y.-C. Chen, Y.-H. Chu, Y.-H. Lee, C.-J. Chung, T.-M. Chen, C.-H. Chen, C.-L. Wu, A gate-free monolayer WSe_2 pn diode, Nat. Commun. 9 (1) (2018) 3143, https://doi.org/10.1038/s41467-018-05326-x.
[18] Q. Peng, C. Si, J. Zhou, Z. Sun, Modulating the Schottky barriers in MoS_2/mxenes heterostructures via surface functionalization and electric field, Appl. Surf. Sci. 480 (2019) 199–204, https://doi.org/10.1016/j.apsusc.2019.02.249 http://www.sciencedirect.com/science/article/pii/S0169433219306063.
[19] L. Zhang, X. Dai, T. Li, H. Li, Chemical modification, field effect transistors and voltage-driven spin logic gates of tailored monolayer MoS_2 nanoflakes, Appl. Surf. Sci. 481 (2019) 910–918, https://doi.org/10.1016/j.apsusc.2019.03.202 http://www.sciencedirect.com/science/article/pii/S0169433219308244.
[20] M.J. Szary, M.T. Michalewicz, M.W. Radny, Bonding and electronics of the $MoTe_2$/Ge interface under strain, Phys. Rev. B 95 (2017) 205421, https://doi.org/10.1103/PhysRevB.95.205421.
[21] M.J. Szary, Bonding and electronics of the silicene/MoTe2 interface under strain, Appl. Surf. Sci. 491 (2019) 469–477, https://doi.org/10.1016/j.apsusc.2019.06.156 http://www.sciencedirect.com/science/article/pii/S0169433219318653.
[22] Z.Y. Zhu, Y.C. Cheng, U. Schwingenschlögl, Giant spin-orbit-induced spin splitting in two-dimensional transition-metal dichalcogenide semiconductors, Phys. Rev. B 84 (2011) 153402, https://doi.org/10.1103/PhysRevB.84.153402.
[23] Y.C. Cheng, Z.Y. Zhu, M. Tahir, U. Schwingenschlögl, Spin-orbitinduced spin splittings in polar transition metal dichalcogenide monolayers, EPL (Europhysics Letters) 102 (5) (2013) 57001 http://stacks.iop.org/0295-5075/102/i=5/a=57001.
[24] G.-B. Liu, W.-Y. Shan, Y. Yao, W. Yao, D. Xiao, Three-band tight-binding model for monolayers of group-vib transition metal dichalcogenides, Phys. Rev. B 88 (2013) 085433, https://doi.org/10.1103/PhysRevB.88.085433.
[25] X. Li, S. Zhang, Q. Wang, Topological insulating states in 2D transition metal dichalcogenides induced by defects and strain, Nanoscale 9 (2017) 562–569, https://doi.org/10.1039/C6NR07851F.
[26] S. Kansara, S.K. Gupta, Y. Sonvane, Effect of strain engineering on 2D dichalcogenides transition metal: a DFT study, Computational Materials Science 141 (2018) 235–242, https://doi.org/10.1016/j.commatsci.2017.09.037 http://www.sciencedirect.com/science/article/pii/S0927025617305177.
[27] X. Xue, X. Wang, W. Mi, Electric field effects on electronic structure of tantalum dichalcogenides van der Waals TaS2/TaSe2 and TaSe2/TaTe2 heterostructures, Applied Surface Science 455 (2018) 963–969, https://doi.org/10.1016/j.apsusc.2018.06.004 http://www.sciencedirect.com/science/article/pii/S0169433218315708.
[28] Y. Miao, Y. Li, Q. Fang, Y. Huang, Y. Sun, K. Xu, F. Ma, P.K. Chu, Effects of dopant separation on electronic states and magnetism in monolayer MoS_2, Applied Surface Science 0169-4332, 428 (2018) 226–232, https://doi.org/10.1016/j.apsusc.2017.09.128 http://www.sciencedirect.com/science/article/pii/S0169433217327769.
[29] S.R. Park, C.H. Kim, J. Yu, J.H. Han, C. Kim, Orbital-angular-momentum based origin of Rashba-type surface band splitting, Phys. Rev. Lett. 107 (2011) 156803, https://doi.org/10.1103/PhysRevLett.107.156803.
[30] J.-H. Park, C.H. Kim, J.-W. Rhim, J.H. Han, Orbital Rashba effect and its detection by circular dichroism angle-resolved photoemission spectroscopy, Phys. Rev. B 85 (2012) 195401, https://doi.org/10.1103/PhysRevB.85.195401.
[31] B. Kim, C.H. Kim, P. Kim, W. Jung, Y. Kim, Y. Koh, M. Arita, K. Shimada, H. Namatame, M. Taniguchi, J. Yu, C. Kim, Spin and orbital angular momentum structure of Cu(111) and Au(111) surface states, Phys. Rev. B 85 (2012) 195402, https://doi.org/10.1103/PhysRevB.85.195402.
[32] S. Jakobs, A. Ruffing, M. Cinchetti, S. Mathias, M. Aeschlimann, Orbital angular momentum structure of an unoccupied spin-split quantum-well state in Pb/Cu (111), Phys. Rev. B 87 (2013) 235438, https://doi.org/10.1103/PhysRevB.87.235438.
[33] B. Kim, P. Kim, W. Jung, Y. Kim, Y. Koh, W. Kyung, J. Park, M. Matsunami, S.-i. Kimura, J.S. Kim, J.H. Han, C. Kim, Microscopic mechanism for asymmetric charge distribution in Rashba-type surface states and the origin of the energy splitting scale, Phys. Rev. B 88 (2013) 205408, https://doi.org/10.1103/PhysRevB.88.205408.
[34] S. Oh, H.J. Choi, Orbital angular momentum analysis for giant spin splitting in solids and nanostructures, Sci. Rep. 7 (1) (2017) 2024, https://doi.org/10.1038/s41598-017-02032-4.
[35] M.J. Szary, B. Pieczyrak, L. Jurczyszyn, M.W. Radny, Suppressed and enhanced spin polarization in the 1ml-Pb/Ge(111)-11 system, Appl. Surf. Sci. 466 (2019) 224–229, https://doi.org/10.1016/j.apsusc.2018.10.028 http://www.sciencedirect.com/science/article/pii/S0169433218327247.
[36] M.J. Szary, Role of coupling between surface orbitals in SOC enhanced spin splitting, Surface Science 684 (2019) 12–17, https://doi.org/10.1016/j.susc.2019.02.004 http://www.sciencedirect.com/science/article/pii/S0039602818309646.
[37] P. Giannozzi, S. Baroni, N. Bonini, M. Calandra, R. Car, C. Cavazzoni, D. Ceresoli, G.L. Chiarotti, M. Cococcioni, I. Dabo, A. Dal Corso, S. de Gironcoli, S. Fabris, G. Fratesi, R. Gebauer, U. Gerstmann, C. Gougoussis, A. Kokalj, M. Lazzeri, L. Martin-Samos, N. Marzari, F. Mauri, R. Mazzarello, S. Paolini, A. Pasquarello, L. Paulatto, C. Sbraccia, S. Scandolo, G. Sclauzero, A.P. Seitsonen, A. Smogunov, P. Umari, QUANTUM ESPRESSO: a modular and open-source software project for quantum simulations of materials, J. Phys. Condens. Matter 21 (39) (2009) 395502.
[38] J.P. Perdew, K. Burke, M. Ernzerhof, Generalized gradient approximation made simple, Phys. Rev. Lett. 77 (1996) 3865.
[39] J.P. Perdew, A. Ruzsinszky, G.I. Csonka, O.A. Vydrov, G.E. Scuseria, L.A. Constantin, X. Zhou, K. Burke, Restoring the density-gradient expansion for exchange in solids and surfaces, Phys. Rev. Lett. 100 (2008) 136406.
[40] S. Grimme, Semiempirical GGA-type density functional constructed with a long-range dispersion correction, J. Comput. Chem. 27 (15) (2006) 1787.
[41] V. Barone, M. Casarin, D. Forrer, M. Pavone, M. Sambi, A. Vittadini, Role and effective treatment of dispersive forces in materials: polyethylene and graphite crystals as test cases, J. Comput. Chem. 30 (6) (2009) 934.
[42] A.D. Becke, E.R. Johnson, Exchange-hole dipole moment and the dispersion interaction revisited, The Journal of Chemical Physics 127 (15) (2007) 154108, https://doi.org/10.1063/1.2795701.
[43] A. Otero-de-la Roza, E.R. Johnson, Van der Waals interactions in solids using the exchange-hole dipole moment model, J. Chem. Phys. 136 (17) (2012) 174109, https://doi.org/10.1063/1.4705760.
[44] A. Tkatchenko, M. Scheffler, Accurate molecular van der Waals interactions from ground-state electron density and free-atom reference data, Phys. Rev. Lett. 102 (2009) 073005, https://doi.org/10.1103/PhysRevLett.102.073005 https://link.aps.org/doi/10.1103/PhysRevLett.102.073005.
[45] P.E. Blöchl, Projector augmented-wave method, Phys. Rev. B 50 (1994) 17953.
[46] G. Kresse, D. Joubert, From ultrasoft pseudopotentials to the projector augmented-wave method, Phys. Rev. B 59 (1999) 1758.
[47] N. Troullier, J.L. Martins, Efficient pseudopotentials for plane-wave calculations, Phys. Rev. B 43 (1991) 1993–2006, https://doi.org/10.1103/PhysRevB.43.1993 https://link.aps.org/doi/10.1103/PhysRevB.43.1993.
[48] H.J. Monkhorst, J.D. Pack, Special points for Brillouin-zone integrations, Phys. Rev. B 13 (1976) 5188–5192.
[49] T. Ozaki, Variationally optimized atomic orbitals for large-scale electronic structures, Phys. Rev. B 67 (2003) 155108, https://doi.org/10.1103/PhysRevB.67.155108.
[50] M.C. Neale, M.D. Hunter, J.N. Pritikin, M. Zahery, T.R. Brick, R.M. Kirkpatrick, R. Estabrook, T.C. Bates, H.H. Maes, S.M. Boker, OpenMx 2.0: extended structural equation and statistical modeling, Psychometrika 81 (2) (2016) 535–549, https://doi.org/10.1007/s11336-014-9435-8.
[51] J.N. Pritikin, M.D. Hunter, S.M. Boker, Modular open-source software for item factor analysis, Educational and Psychological Measurement 75 (3) (2015) 458–474, https://doi.org/10.1177/0013164414554615 pMID: 27065479.
[52] T. Böker, R. Severin, A. Müller, C. Janowitz, R. Manzke, D. Voß, P. Krüger, A. Mazur, J. Pollmann, Band structure of MoS_2, $MoSe_2$, and α-$MoTe_2$: angle-resolved photoelectron spectroscopy and ab initio calculations, Phys. Rev. B 64 (2001) 235305, https://doi.org/10.1103/PhysRevB.64.235305.
[53] J. Zemann, Crystal structures 2nd edn. Vol. 1 by R. W. G. Wyckoff, Acta Crystallogr. 18 (1) 139–139 10.1107/S0365110X65000361.
[54] X. Du, Z.Y. Wang, G.Q. Huang, Rashba-type spin splitting and the electronic structure of ultrathin Pb/$MoTe_2$ heterostructure, Materials Research Express 3 (11) (2016) 116302 http://stacks.iop.org/2053-1591/3/i=11/a=116302.
[55] X. Li, S. Wu, S. Zhou, Z. Zhu, Structural and electronic properties of germanene/MoS_2 monolayer and silicene/MoS_2 monolayer superlattices, Nanoscale Res. Lett. 9 (1) (2014) 110, https://doi.org/10.1186/1556-276X-9-110 https://doi.org/10.1186/1556-276X-9-110.
[56] O. Knop, R.D. MacDonald, Chalkogenides of the transition elements: III. Molybdenum ditelluride, Can. J. Chem. Eng. 39 (4) (1961) 897–904, https://doi.org/10.1139/v61-110.
[57] D. Puotinen, R.E. Newnham, The crystal structure of $MoTe_2$, Acta Crystallogr. 14 (6) (1961) 691–692, https://doi.org/10.1107/S0365110X61002084.
[58] V.L. Deringer, R. Dronskowski, Stabilities and reconstructions of PbTe crystal surfaces from density-functional theory, J. Phys. Chem. C 117 (46) (2013) 24455–24461, https://doi.org/10.1021/jp408699a.
[59] B. Pieczyrak, M. Szary, L. Jurczyszyn, M.W. Radny, Spin polarization of two-dimensional electronic gas decoupled from structural asymmetry environment, Phys. Rev. B 93 (2016) 195318, https://doi.org/10.1103/PhysRevB.93.195318 https://link.aps.org/doi/10.1103/PhysRevB.93.195318.
[60] W.C. Martin, Table of spin-orbit energies for p-electrons in neutral atomic (core)np configurations, J. Res. of NBS, Section A: Phys. Chem. 75A (1971) 109, https://doi.org/10.6028/jres.075A.010.
[61] C. Moore, Atomic Energy Levels as Derived From the Analyses of Optical Spectra, pkt 3, Atomic Energy Levels as Derived From the Analyses of Optical Spectra, U.S. Department of Commerce, National Bureau of Standards, 1958, https://books.google.dk/books?id=wvURAAAAIAAJ.
[62] Y. Ma, X. Zhao, T. Wang, W. Li, X. Wang, S. Chang, Y. Li, M. Zhao, X. Dai, Band structure engineering in a MoS_2/PbI_2 van der Waals heterostructure via an external electric field, Phys. Chem. Chem. Phys. 18 (41) (2016) 2846628473, https://doi.org/10.1039/c6cp06046c.
[63] A.C. Ipsen, K. Splittorff, The van der Waals interaction in one, two, and three dimensions, American Journal of Physics 83 (2) (2015) 150–155, https://doi.org/10.1119/1.4896248.

P6. Bonding and electronics of the $MoTe_2$/Ge interface under strain

PHYSICAL REVIEW B **95**, 205421 (2017)

Bonding and electronics of the $MoTe_2$/Ge interface under strain

Maciej J. Szary*
Institute of Physics, Poznan University of Technology, 62-965 Poznan, Poland

Marek T. Michalewicz
*A*STAR Computational Resource Centre, Singapore 138632, Singapore;*
Interdisciplinary Centre for Mathematical and Computational Modelling, ulica Kupiecka 32, 03-046 Warsaw, Poland;
and Institute for Advanced Computational Science, Stony Brook University, New York, USA

Marian W. Radny†
Institute of Physics, Poznan University of Technology, 62-965 Poznan, Poland
and School of Mathematical and Physical Sciences, The University of Newcastle, Callaghan 2308, Australia
(Received 19 November 2016; revised manuscript received 24 April 2017; published 17 May 2017)

Understanding the interface formation of a conventional semiconductor with a monolayer of transition-metal dichalcogenides provides a necessary platform for the anticipated applications of dichalcogenides in electronics and optoelectronics. We report here, based on the density functional theory, that under in-plane tensile strain, a 2H semiconducting phase of the molybdenum ditelluride ($MoTe_2$) monolayer undergoes a semiconductor-to-metal transition and in this form bonds covalently to bilayers of Ge stacked in the [111] crystal direction. This gives rise to the stable bonding configuration of the $MoTe_2$/Ge interface with the $\pm$K valley metallic, electronic interface states exclusively of a Mo 4*d* character. The atomically sharp Mo layer represents therefore an electrically active (conductive) subsurface δ-like two-dimensional profile that can exhibit a valley-Hall effect. Such system can develop into a key element of advanced semiconductor technology or a novel device concept.

DOI: 10.1103/PhysRevB.95.205421

I. INTRODUCTION

Since the discovery of graphene and surprises that emerged from exploring its low-dimensional physics, such as massless Dirac electrons or anomalous quantum Hall effect [1], the interest in other two-dimensional (2D) layered materials has grown rapidly [2–4]. Among them, exfoliated layers of transition-metal dichalcogenides (TMDs) have gained particular interest due to their intrinsic properties that are distinct from those of graphene. This includes the coexistence of *s*, *p*, and *d* electrons, absence of dangling bonds, inherent direct/indirect band gaps in semiconducting TMDs [4,5], and spin-split electronic bands due to inversion symmetry breaking [6]. Many features that are important in the realization of electronic or optoelectronic devices, such as electrostatics control or tunable optical properties, directly arise from such effects. On top of that, TMDs share important similarity with graphene—high elasticity with predicted strain resistance up to 20% [7]—adding further application perspectives.

A TMD monolayer consists of strongly bonded $X-M-X$ hexagonal layers, with M being a layer of transition-metal atoms of groups IV–VI (most common are Mo, Nb, W, Ta, and Ti) and X being a layer of chalcogen atoms (S, Se, or Te). Each M atom is coordinated by six nearest-neighbor X atoms in the trigonal prismatic geometry that breaks inversion symmetry of the monolayer. In bulk TMDs, the monolayers interact with each other by weak van der Waals (vdW) forces due to the lack of unsaturated (dangling) bonds on their surfaces. While the pristine surfaces of a TMD monolayer allow for engineering novel van der Waals heterostructures [8], they make it difficult to form strong interface bonds. The latter is important in electronics where the quality of (electrical) contacts within the device's circuitry controls the charge flow within the device and governs its overall performance. Typically, the pristine surface of TMDs interfaced with a metal increases the contact resistance and limits the charge transfer within the device [9]. Substitutional doping that is usually adopted in conventional semiconductors to reduce the contact resistance is not applicable in the 2D limit as it modifies the material and its properties. The latter also applies to TMDs with defects that are known to facilitate local electron transfer and covalent bond formation. The phase engineering approach, in which the octahedral 1T metallic phase was chemically modified to covalently functionalize TMD semiconductors, was demonstrated recently for $MoSe_2$, MoS_2, and VS_2 [10]. Phase engineering was proven to be particularly effective for $MoTe_2$ due to the small energy difference between the 2H phase and the metastable 1T′ phase for Mo- and W-based TMD monolayers. Other studies also predict that $MoTe_2$ monolayers undergo 2H-1T′ transitions induced by tensile strains [11,12], atoms and molecules adsorption [13], and electronic excitation [14]. The phase change from 2H to 1T′ in $MoTe_2$ induced by biaxial tensile strain up to 15% produces the 1T′ phase as a more stable structure; however, the activation barrier for this transition was calculated to be of 0.9 eV [12].

In this paper, we report the emergence of covalent bonding at the interface between a film of conventional semiconductor (Ge) and a $MoTe_2$ monolayer facilitated by strain applied to the monolayer in the 2H phase. The strain induces a semiconductor-to-metal transition in 2H-$MoTe_2$ and when such system is interfaced with bilayers of Ge stacked in the [111] crystal direction, it gives rise to the most stable atomic configuration of the $MoTe_2$/Ge interface. The *p*-type covalent

*Corresponding author: maciejjanszary@gmail.com
†Corresponding author: marian.radny@newcastle.edu.au

bonds at the interface result in seamless contact between the $MoTe_2$ monolayer and the Ge film. The system is metallic with the electronic states of a Mo 4*d* character crossing the Fermi level at the *K* points of the surface Brillouin zone (SBZ). The atomically sharp Mo layer represents, therefore, an electrically active δ-like 2D profile that can lead to a valley-Hall effect, which may significantly enrich the functionality of similar components present in conventional semiconductor-based electronics, such as in GaAs- and InP-based photonic devices [15].

II. METHODS

Total-energy and electronic structure calculations were performed based on the density functional theory as implemented in the QUANTUM ESPRESSO code [16]. The Projector augmented wave (PAW) potentials [17,18] and the kinetic-energy cutoff of 750 and 6800 eV for wave functions and densities, respectively, were used in the study. The vdW interaction was included and treated within a dispersion-corrected density functional theory (DFT-D) approach [19,20]. For exchange and correlation, the generalized gradient approximation–Perdew-Burke-Ernzerhof (GGA-PBEsol) functional was adopted [21,22]. The irreducible part of the surface Brillouin zone was sampled by a $12 \times 12 \times 1$ grid of *k* points generated using the Monkhorst-Pack scheme [23]. All calculations were performed in full-relativistic regime.

The systems were modeled by repeated asymmetric slabs that consist of up to seven bilayers of Ge subsequently stacked in the [111] crystal direction and interfaced with the $MoTe_2$ monolayer in three distinct interface configurations, shown in Fig. 2. The open surface of the Ge film was terminated by hydrogen atoms to prevent the electronic states at the interface from being contaminated by the states that might occur on this free surface (see Fig. 2). In the total-energy calculations, atomic positions were relaxed for all the atoms in the system with the adopted convergence threshold on forces (less than 10^{-5} Ry/a.u.). The separation between the slabs (vacuum) of 20 Å was found to be sufficient.

All of the calculations were performed with the relaxed lattice constant of bulk Ge equal to 5.658 Å, which for the $MoTe_2$ monolayer is equivalent to 14% homogeneous biaxial strain. Hence, in this approach, both systems share the same primitive hexagonal unit-cell equivalent to that of the Ge(111)-1×1 surface. Preliminary calculations for clean $MoTe_2$ conducted within 2×2 and 3×3 supercells under tensile strain exhibited no surface structural phase transitions. Similar calculations performed for strained $MoTe_2$ interfaced with one bilayer and six bilayers of Ge did not show any atomic reconstruction at the interface. Therefore, all of the reported calculations were performed within the 1×1 surface unit cell.

III. RESULTS

We first consider the structural and electronic properties of an isolated, strained $MoTe_2$ monolayer and compare them to those of the unstrained one. Upon relaxation within the Ge(111)-1×1 unit cell (see Sec. II), which is equivalent to 14% homogeneous biaxial strain, the atomic structure of $MoTe_2$ preserves its 2H phase. The calculations performed for the strained 2H phase of $MoTe_2$ within 2×2 and 3×3 supercells provide no evidence for any structural phase changes or deformations due to, for example, bond breaking or atom movement. The lack of the 2H to 1T′ transition in our calculations can be understood in the context of the results presented in Ref. [12], where the 2H-1T′ phase transition was identified to be due to simultaneous movement of the TM atom and Te atoms in their planes, associated with the activation barrier of ~ 0.9 eV. Structurally, the strained 2H phase of $MoTe_2$ is characterized by the increased Mo-Te bond lengths, from 2.71 to 2.82 Å, and the decreased Te-Mo-Te angles, from 82.9° to 70.8°, both resulting in the monolayer thickness reduced from 3.59 to 3.28 Å.

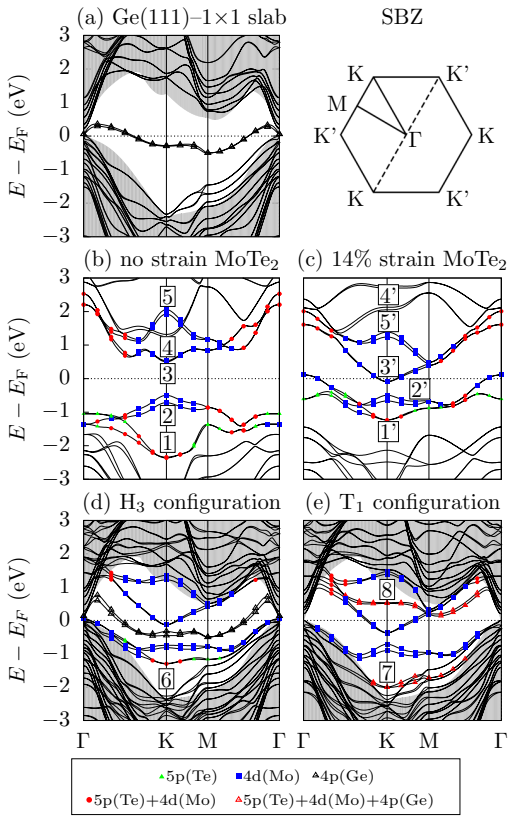

FIG. 1. Electronic band structures of (a) the isolated Ge(111) seven bilayers film (solid lines) with the bulk Ge band structure projected on the [111] direction (shaded area), (b) the isolated unstrained $MoTe_2$ monolayer, (c) the isolated strained $MoTe_2$ monolayer, (d) the $MoTe_2$/Ge interface in configuration H_3, and (e) the $MoTe_2$/Ge interface in configuration T_1. A schematic of SBZ with high symmetry points indicated is shown next to (a). The shaded area in (d) and (e) represents the bulk Ge band structure projected on the [111] direction.

These structural changes affect the electronic structure of the $MoTe_2$ monolayer, as shown in Fig. 1. The electronic band structure shown in Fig. 1(b) demonstrates that the unstrained monolayer is a direct-gap (1.05 eV) semiconductor with both the valence and conduction bands in the vicinity of the Fermi level (E_F) predominantly of the Te 5*p* and Mo 4*d* character (Te 5*s* states are localized at -12 eV and do not contribute to the bands near E_F). The valence and conduction bands' extrema are predominantly of the Mo $4d_{xy}/d_{x^2-y^2}$ and Mo d_{z^2} character [bands 2 and 3 in Fig. 1(b)], consistent with other reports [6].

TABLE I. Calculated binding energies of the H, Ge, Pb, and Si atoms on $MoTe_2$ adsorbed at three adsorption sites, T_1, T_4, and H_3 [these sites are equivalent to those of the $MoTe_2$ surface shown in Fig. 2].

	No strain			Strain		
Atom	H_3	T_1	T_4	H_3	T_1	T_4
	(eV)					
H	−1.66	−1.14	−1.08	−2.78	−2.41	−3.04
Ge	−0.66	−0.73	−0.42	−1.11	−1.38	−1.66
Pb	−0.62	−0.63	−0.52	−0.95	−1.17	−0.98
Si	−0.80	−0.86	−0.52	−1.32	−1.49	−1.96

As a result of inversion symmetry breaking, spin-orbit-induced spin splitting is observed in some of the bands with the largest splitting of 0.17 and 0.22 eV at the top of the valence band at the K point for strain and unstrain $MoTe_2$, respectively. This is also consistent with previous reports [6,24].

Under strain, the system undergoes a semiconductor-to-metal transition [see Fig. 1(c)] as a result of reduced dispersion of the Mo 4d bands. Similar electronic effects were reported in [14,25–27]. In particular, conduction band 3 at point K and valence band 2 in the Γ point, which are of the same Mo d_{z^2} character at these points, cross the Fermi level. These changes are consistent with the results of Johari and Shenoy [28], where the gap-size reduction and the transition from direct to indirect gap were reported for $MoTe_2$ under 10% strain. The dispersion of the band of predominantly Te $5p_z$ character at the K point [band 1 in Fig. 1(b)] is also reduced with its minimum at −2.0 eV (point K) shifted up in energy to −1.0 eV [band 1′ in Fig. 1(c)].

The impact of strain on the chemical activity of $MoTe_2$ is demonstrated first by calculating the binding energy of the H, Si, Pb, and Ge atoms adsorbed on the monolayer (see Table I). The binding energy was calculated as a total energy of the system upon adsorption (at three possible adsorption sites) minus the sum of the energies of the isolated components calculated in equivalent unit cells. The calculations were performed in the nonrelativistic regime with the vdW correction (DFT-D) included.

The data in Table I shows that for the equilibrium bonding configuration, the values of the adatoms binding energies calculated for $MoTe_2$ under strain are, on average, two times higher than the ones obtained for the unstrained $MoTe_2$ sample. This indicates that $MoTe_2$ under strain forms strong chemical bonds with the adatoms. The Lödwin charge analysis presented in Table II shows that isolated $MoTe_2$ under 14% strain exhibits a net charge transfer of 0.13e from Mo to Te when compared to the unstrained monolayer. The same trend is observed for the $MoTe_2$/adatom systems (Ge in Table II). These observations are in line with recently reported strain-induced charge excess around dichalcogen atoms (and the consequent depletion around transition-metal atoms) for MoS_2 and WS_2 [30]. Our data also shows that negative charge is accumulated on the dichalcogen atoms and the adatom (Ge in Table II), which illustrates that the strained TMD surface favors the formation of strong chemical (covalent) bonds. This results in higher adatom binding energies (see Table I).

TABLE II. Atom and l-resolved Lödwin charge distribution [29] (in $-e$) calculated within the unstrained and strained isolated $MoTe_2$ monolayer and the corresponding $MoTe_2$/Ge adsorption system.

			Partial charge		
	Atom	Total charge	s	p	d
		No strain			
	Te	15.33	1.57	3.77	10.00
	Mo	15.11	2.42	7.12	5.57
	Te	15.33	1.57	3.77	10.00
$MoTe_2$		Strain			
	Te	15.42	1.60	3.81	10.00
	Mo	14.98	2.51	7.14	5.33
	Te	15.42	1.60	3.81	10.00
		No strain			
	Ge	14.10	1.87	2.23	10.00
	Te	15.15	1.49	3.67	10.00
	Mo	15.13	2.42	7.12	5.60
	Te	15.33	1.57	3.77	10.00
T_1		Strain			
	Ge	15.04	1.90	2.14	10.00
	Te	15.25	1.52	3.74	10.00
	Mo	15.05	2.51	7.14	5.40
	Te	15.42	1.60	3.82	10.00

The $MoTe_2$/Ge interface formation was investigated by subsequent adsorption of Ge bilayers (germanene) on strained (14%) $MoTe_2$. The Te layers of the $MoTe_2$ monolayer under 14% strain have the hexagonal unit cells equivalent to that of the surface of a Ge(111)-1 × 1 film so the adsorbed bilayers of Ge are in their equilibrium atomic configurations. The subsequent adsorption of such bilayers results in the formation of the multilayered Ge(111) film interfaced with $MoTe_2$.

The interface configurations under study are schematically shown in Fig. 2 with strained $MoTe_2$ interfaced with the Ge(111) film of six bilayers of Ge. In the H_3 and T_4 geometries,

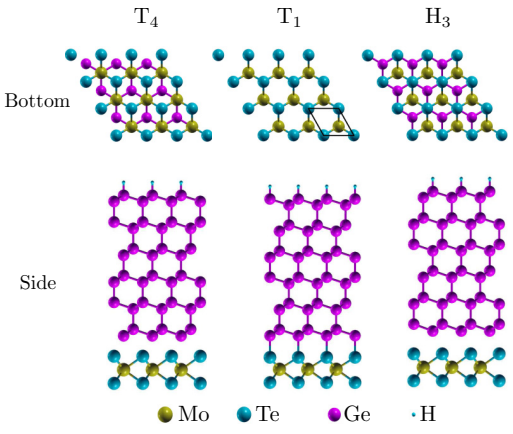

FIG. 2. Schematics of atomic structures (bottom and side views) of $MoTe_2$/Ge(111) interfaces in configuration H_3, T_1, and T_4. The surface unit cell, equivalent to that for Ge(111)-1 × 1, is shown in configuration T_1. The bottom view presents $MoTe_2$ and the first bilayer of the Ge film.

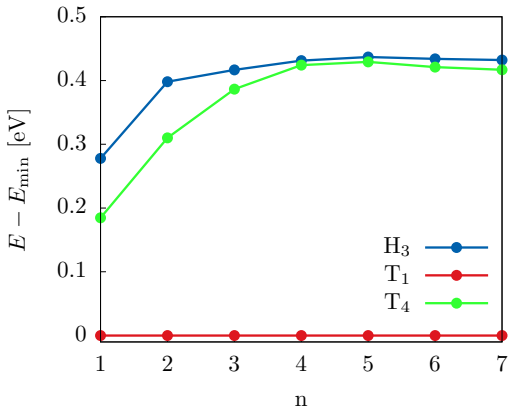

FIG. 3. Relative energetics of the $MoTe_2$/Ge interfaces as a function of a number of bilayers (n) in the Ge film. The reference energy is that of configuration T_1.

each bottom-most Ge adatom is located at the hollow site of the Te atomic layer and interacts with three top Te atoms. The difference between these geometries is that in T_4, the bottom-most Ge adatoms are located above the Mo atoms, while in H_3, the Ge adatoms are placed at the hollow sites of the $MoTe_2$ monolayer (at the center of honeycomb hexagons). In configuration T_1, the Ge atoms are placed directly above the top-layer Te atoms and each Ge interacts with one Te atom.

The calculated energetics of the systems is shown in Fig. 3. Geometry T_1 was found to be the most stable independently of the number of Ge bilayers interfaced with $MoTe_2$. The interface configuration with one bilayer of Ge is lower in energy by 0.18 and 0.28 eV than the corresponding H_3 and T_4 structures, respectively. Interestingly, the adsorption of more bilayers of Ge makes the $MoTe_2$/Ge interface more stable—the data in Fig. 3 shows that the energy separation between T_1, and T_4/H_3 increases to 0.42 eV and remains unchanged for the films with four or more bilayers of Ge. Inclusion of the van der Waals (vdW) interactions preserves this energetic order with the energy separation between T_1 and T_4 remaining at 0.4 eV. However, the vdW corrections clearly separate configurations T_4 and H_3, with the latter being ~ 0.1 eV lower in energy for the films with four or more bilayers of Ge. The dependence of the energetic stability on the number of bilayers of Ge in the $MoTe_2$/Ge interfaces is also reflected in the geometries of the systems (see Table III). In the most stable configuration, T_1, the Te-Ge bond length of 2.84 Å for one Ge bilayer is reduced to 2.67 Å for seven bilayers. In the T_4/H_3 geometries, the Te-Ge distances of 4.05 Å (H_3) and 3.68 Å (T_4) for one bilayer of Ge are reduced to 3.53 Å (H_3) and 3.44 Å (T_4) for seven bilayers.

The observed significant difference in the structural parameters between the T_4/H_3 and T_1 interface configurations indicates a different type of bonding in these structures. The nature of bonding at the $MoTe_2$/Ge interfaces is revealed in the electronic structures calculated for geometries H_3 [Fig. 1(d)] and T_1 [Fig. 1(e)] with seven bilayers of Ge (the structure for configuration T_4 is very similar to that for H_3 and is not shown). The electronic band structure of the $MoTe_2$/Ge interface with seven bilayers of Ge develops to the one that can be presented within the bulk Ge band structure projected on the reciprocal

TABLE III. Calculated bond lengths and interlayer spacings (in brackets) of the $MoTe_2$/Ge(111) interface in configurations H_3, T_1, and T_4. The corresponding data for the isolated Ge slab and $MoTe_2$ monolayer are given in the first column (Ref.). Atoms are numbered from the bottom of the monolayer to the top of the Ge slab (see Fig. 2).

Bilayers	Atoms	Ref.	H_3	T_1	T_4
			(Å)		
1	Ge(1)-Ge(2)	2.46	2.41	2.45	2.41
		(0.83)	(0.67)	(0.81)	(0.69)
	Te(2)-Ge(1)		4.05	2.84	3.68
			(3.32)	(2.84)	(2.87)
	Mo-Te(2)	2.71	2.83	2.81	2.83
		(1.64)	(1.64)	(1.60)	(1.63)
	Te(1)-Mo	2.71	2.83	2.82	2.82
		(1.64)	(1.63)	(1.62)	(1.62)
7	Ge(2)-Ge(3)	2.46	2.46	2.47	2.47
		(2.46)	(2.46)	(2.47)	(2.47)
	Ge(1)-Ge(2)	2.46	2.49	2.45	2.46
		(0.83)	(0.92)	(0.8)	(0.85)
	Te(2)-Ge(1)		3.53	2.67	3.44
			(2.66)	(2.67)	(2.55)
	Mo-Te(2)	2.71	2.83	2.74	2.83
		(1.64)	(1.64)	(1.48)	(1.63)
	Te(1)-Mo	2.71	2.83	2.82	2.82
		(1.64)	(1.63)	(1.62)	(1.62)

space [111] direction [shaded areas in Figs. 1(e) and 1(f)]. In this scheme, the electronic structure of an isolated Ge film [Fig. 1(a)] has a metallic surface band located in the bulk Ge energy gap. This band is of a Ge $4p_z$ character and originates from the unsaturated, dangling bonds on the Ge(111)-1 × 1 surface of the film.

The electronic structure of configuration H_3 [Fig. 1(d)] is a simple combination of the band structure of the strained, isolated $MoTe_2$ monolayer [Fig. 1(c)] and the Ge slab [Fig. 1(a)] with the dispersion of the bands and their atomic characters preserved. By contrast, in the electronic structure of configuration T_1 [Fig. 1(e)], the bands of the Mo $4d$ character in the vicinity of E_F remain intact, but the Te $5p$ states [band 1' in Fig. 1(c)] and the Ge $4p$ states [metallic band in Fig. 1(a)] interact, resulting in the formation of two new bands, 8 and 7, in Fig. 1(e).

The origin of these new bands is resolved by inspecting the partial (pseudo-)charge density distribution for band 7 and the probability density distribution for band 8 calculated at the K point, are shown in Fig. 4. A significant bonding charge

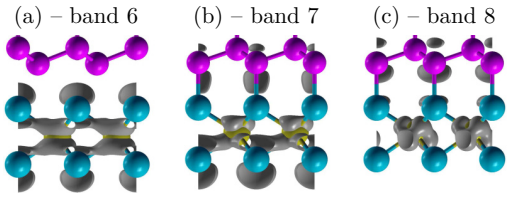

FIG. 4. Partial (pseudo-)charge densities ($|\psi|^2$) calculated for the states at point K for bands (a) 6, (b) 7, and (c) 8 in Figs. 1(d) and 1(e). Isosurface value: $0.0025e$/a.u.^{3}.

can be seen midway along the Te-Ge bonds for band 7 in Fig. 4(b), which corresponds to covalent bonds resulting from the bonding combination of the Te $5p_z$ and Ge $4p_z$ states. By contrast, the probability density for unoccupied band 8 [Fig. 4(c)] is significant only around the Te and Ge atoms with a nodal plane within the Te-Ge bond; this is a result of the antibonding combination of the Te $5p_z$ and Ge $4p_z$ states. Figure 4(a) shows that the charge distribution calculated at point K for band 6 in Fig. 1(d) for configuration H_3 is mirror symmetric with respect to the Mo layer, indicating that there is no influence of the Ge layer on the $MoTe_2$ states in this geometry. This is also equivalent to the charge distribution calculated for band 1 in Fig. 1(c) for the isolated monolayer.

The presented results are intriguing for a number of reasons. First, the calculated Te-Ge covalent bond of 2.7 Å at the MoTe2/Ge interface with seven bilayers of Ge in the most stable interface geometry, T_1, is significantly shorter than those found in the GeTe compounds (2.85–3.25 Å) [31]. As the covalency of the Ge-Te bonds is considered to be greater for the shorter bonds [32], our results suggest very strong covalent bonding at the $MoTe_2$/Ge interface. The data on Fig. 3 also show that the adsorption of just a single bilayer of Ge atoms on the 14% strained $MoTe_2$ monolayer produces the T_1 configuration as the most stable structure, with the adsorption of more layers of Ge making the covalent bonds at the interface even stronger. As the TMD monolayers are predicted to withstand 10–20% strain and Te atoms are known surfactants for the epitaxial growth of thick, low-defect Ge layers on Si, the epitaxial growth of Ge layers on the strained $MoTe_2$ monolayer, while challenging, may be a feasible task.

Second, both the isolated, strained $MoTe_2$ monolayer and the $MoTe_2$/Ge interface are metallic due to the electronic states at E_F of the Mo $4d_{z^2}$ character. However, the interface formation transfers the monolayer's conduction- and valence-band extrema localized interface states, as they are located in the (bulk) energy gap of the Ge film [see Figs. 1(d) and 1(e)]. Therefore, the Mo atoms are located beneath the open surface of the interface (Te) and are confined to a single atomic plane; they form the subsurface, conductive δ-like 2D profile. In addition to that, the Fermi level of the interface is located such that the Mo $4d_{z^2}$ states cross E_F exclusively at the K points of the surface Brillouin zone [SBZ; see Fig. 1(e) and the inset in Fig. 1]. However, the K points in the SBZ are not equivalent, and the equivalent pairs (K, K) or (K', K') are separated by a large distance in the momentum (k) space. The separation is such that when an electric field is applied to the system, the charge may flow in opposite directions, giving rise to the so-called valley-Hall effect (similar results can be obtained by exposing the interface to a circularly polarized light). While the quantitative accounts of these effects involve the calculations and analysis of a Berry curvature [6,33] and are outside the scope of this paper, the reported results highlight some intriguing consequences of a semiconductor-dichalcogenide interface formation on the electronic and optical properties of the formed systems.

IV. CONCLUSIONS

So far, mechanical strain has been shown to be an effective way to induce and tune the band gaps and structural phase transitions in TMD monolayer materials. Our density functional theory study reveals a surprising occurrence of strong covalent bonding at the strained 2H-$MoTe_2$/Ge interface and the formation of an atomically sharp δ-like 2D profile with conductive d electrons. The latter arises from the interaction of the Mo $4d$ orbitals in the strained $MoTe_2$ monolayer not affected by the interface formation with Ge. The results suggest a way for utilizing the strain-induced chemical activity of the TMD materials, d-electron physics, and valley electronics of dichalcogenides, and may evolve to develop novel electronic materials with unique applications.

ACKNOWLEDGMENTS

A*STAR Computational Resource Centre, Singapore, is acknowledged for access to the high-performance computing facilities. M.W.R. acknowledges the Polish Ministry of Science and Higher Education for support (Grant No. 06/62/DSPB/2173).

[1] K. S. Novoselov, D. Jiang, F. Schedin, T. J. Booth, V. V. Khotkevich, S. V. Morozov, and A. K. Geim, Proc. Nat. Acad. Sci. USA **102**, 10451 (2005).
[2] B. Aufray, A. Kara, S. Vizzini, H. Oughaddou, C. Léandri, B. Ealet, and G. Le Lay, Appl. Phys. Lett. **96**, 183102 (2010).
[3] M. E. Dàvila, L. Xian, S. Cahangirov, A. Rubio, and G. L. Lay, New J. Phys. **16**, 095002 (2014).
[4] K. F. Mak, C. Lee, J. Hone, J. Shan, and T. F. Heinz, Phys. Rev. Lett. **105**, 136805 (2010).
[5] A. Splendiani, L. Sun, Y. Zhang, T. Li, J. Kim, C.-Y. Chim, G. Galli, and F. Wang, Nano Lett. **10**, 1271 (2010).
[6] G.-B. Liu, W.-Y. Shan, Y. Yao, W. Yao, and D. Xiao, Phys. Rev. B **88**, 085433 (2013).
[7] R. C. Cooper, C. Lee, C. A. Marianetti, X. Wei, J. Hone, and J. W. Kysar, Phys. Rev. B **87**, 035423 (2013).
[8] A. K. Geim and I. V. Grigorieva, Nature (London) **499**, 419 (2013).
[9] A. Allain, J. Kang, K. Banerjee, and A. Kis, Nat. Mater. **14**, 1195 (2015).
[10] D. Voiry, A. Goswami, R. Kappera, S. d. C. C. e, D. Kaplan, T. Fujita, M. Chen, T. Asefa, and M. Chhowalla, Nat. Chem. **7**, 45 (2015).
[11] K.-A. N. Duerloo, Y. Li, and E. J. Reed, Nat. Commun. **5**, 4214 (2014).
[12] H. H. Huang, X. Fan, D. J. Singh, H. Chen, Q. Jiang, and W. T. Zheng, Phys. Chem. Chem. Phys. **18**, 4086 (2016).
[13] Y. Zhou and E. J. Reed, J. Phys. Chem. C **119**, 21674 (2015).
[14] A. V. Kolobov, P. Fons, and J. Tominaga, Phys. Rev. B **94**, 094114 (2016).
[15] J. J. Harris, J. Mater. Sci.: Mater. Electron. **4**, 93 (1993).

[16] P. Giannozzi, S. Baroni, N. Bonini, M. Calandra, R. Car, C. Cavazzoni, D. Ceresoli, G. L. Chiarotti, M. Cococcioni, I. Dabo, A. Dal Corso, S. de Gironcoli, S. Fabris, G. Fratesi, R. Gebauer, U. Gerstmann, C. Gougoussis, A. Kokalj, M. Lazzeri, L. Martin-Samos, N. Marzari, F. Mauri, R. Mazzarello, S. Paolini, A. Pasquarello, L. Paulatto, C. Sbraccia, S. Scandolo, G. Sclauzero, A. P. Seitsonen, A. Smogunov, P. Umari, and R. M. Wentzcovitch, J. Phys. Condens. Matter **21**, 395502 (2009).
[17] P. E. Blöchl, Phys. Rev. B **50**, 17953 (1994).
[18] G. Kresse and D. Joubert, Phys. Rev. B **59**, 1758 (1999).
[19] S. Grimme, J. Comput. Chem. **27**, 1787 (2006).
[20] V. Barone, M. Casarin, D. Forrer, M. Pavone, M. Sambi, and A. Vittadini, J. Comput. Chem. **30**, 934 (2009).
[21] J. P. Perdew, K. Burke, and M. Ernzerhof, Phys. Rev. Lett. **77**, 3865 (1996).
[22] J. P. Perdew, A. Ruzsinszky, G. I. Csonka, O. A. Vydrov, G. E. Scuseria, L. A. Constantin, X. Zhou, and K. Burke, Phys. Rev. Lett. **100**, 136406 (2008).
[23] H. J. Monkhorst and J. D. Pack, Phys. Rev. B **13**, 5188 (1976).
[24] Y. C. Cheng, Z. Y. Zhu, M. Tahir, and U. Schwingenschlögl, Europhys. Lett. **102**, 57001 (2013).
[25] S. Song, D. H. Keum, S. Cho, D. Perello, Y. Kim, and Y. H. Lee, Nano Lett. **16**, 188 (2016).
[26] S. Bhattacharyya and A. K. Singh, Phys. Rev. B **86**, 075454 (2012).
[27] W. S. Yun, S. W. Han, S. C. Hong, I. G. Kim, and J. D. Lee, Phys. Rev. B **85**, 033305 (2012).
[28] P. Johari and V. B. Shenoy, ACS Nano **6**, 5449 (2012).
[29] D. Sanchez-Portal, E. Artacho, and J. M. Soler, Solid State Commun. **95**, 685 (1995).
[30] M. Ghorbani-Asl, S. Borini, A. Kuc, and T. Heine, Phys. Rev. B **87**, 235434 (2013).
[31] J. L. F. Da Silva, A. Walsh, and H. Lee, Phys. Rev. B **78**, 224111 (2008).
[32] A. Kolobov, M. Krbal, P. Fons, J. Tominaga, and T. Uruga, Nat. Chem. **3**, 311 (2011).
[33] W. Feng, Y. Yao, W. Zhu, J. Zhou, W. Yao, and D. Xiao, Phys. Rev. B **86**, 165108 (2012).

P7. Bonding and electronics of the silicene/$MoTe_2$ interface under strain

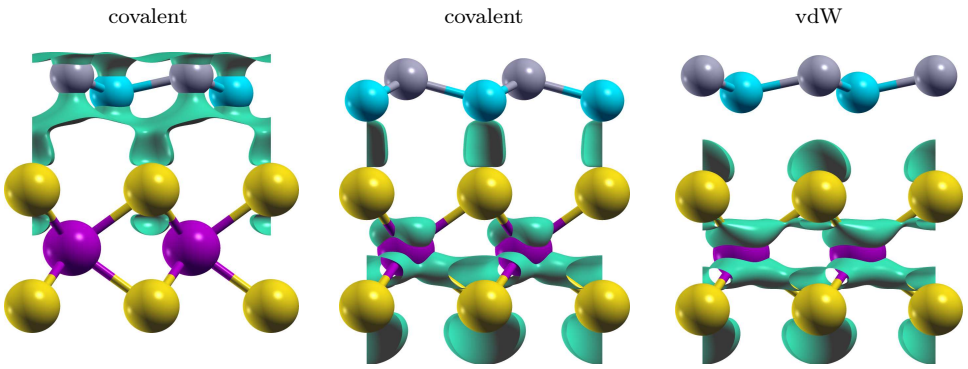

Applied Surface Science 491 (2019) 469–477

Contents lists available at ScienceDirect

Applied Surface Science

journal homepage: www.elsevier.com/locate/apsusc

Full Length Article

Bonding and electronics of the silicene/$MoTe_2$ interface under strain

Maciej J. Szary

Institute of Physics, Poznan University of Technology, Poznan 61-138, Poland

ARTICLE INFO

Keywords:
2D materials
Diachalcogenides
Silicene
Heterostructure
Strain
Electric contacts

ABSTRACT

Density functional theory calculations have been performed to investigate the structural and electronic properties of silicene/$MoTe_2$ heterostructure under strain. The results show three different interaction cases depending on the interface configuration. The interactions can be weak and limited to van der Waals forces, or strong and covalent producing hybrid states between p_z–p_z and p_x/p_y–p_z orbital pairs of Si and Te. Covalent bonding gives rise to well-defined, energetically favorable configurations with properties distinguishably different from those observed in vdW-only configurations. The new hybrid states shared between the layers allow for more effective charge transfer between them, which is critical for the performance of electronic and optoelectronic devices.

1. Introduction

Silicene (Sil) is a two-dimensional (2D) allotropic form of silicon. Similar to graphene it has a hexagonal honeycomb structure, however, unlike graphene, a silicene sheet is periodically buckled. Both systems have an s^2p^2 valence configuration, and thus share a number of electronic similarities. They are zero-gap semiconductors [1-3], with a linear electronic dispersion forming Dirac cones [4], and both exhibit a quantum spin Hall effect [5,6]. Still, the systems differ in *s-p* hybridizations, which correlates with their structure. Si atoms in silicene adopt a mixed sp^2-sp^3 hybridization responsible for its buckling [4], contrasting flat sp^2 observed in graphene [7]. This makes silicene more chemically active than graphene, and thus easier to chemically functionalize [4,8-10].

Transition-metal dichalcogenide (TMD) monolayers are compounds of MX_2, where X is a chalcogen (S, Se, or Te) and M is a transition metal (e.g. Ti, Nb, Mo, Ta and W). Each TMD monolayer consists of three strongly bonded atomic layers X–M–X. Atoms within a TMD monolayer are bonded covalently in either trigonal prismatic or disordered octahedral symmetry with no unsaturated bond present at the surface. This makes them chemically inactive in most cases, with the external interactions limited to van der Waals (vdW) forces.

TMD monolayers show a wide variety of electronic properties. Depending on a transition metal comprising the system it can be either semiconducting (e.g. MoX_2 and WX_2) [11,12] or metallic (e.g. NbX_2 and TaX_2) [12,13]. Furthermore, the size and type of the band gap in semiconducting TMDs can be tuned by a number of monolayers stack [14,15] or by a mechanical strain [16,17]. The latter also impacts the chemical activity of TMDs making their chemical functionalization more feasible [17,18]. In addition, because of the D_{3h} point group, the trigonal-prismatic TMDs exhibit broken inversion symmetry allowing for an intrinsic spin splitting of the valence bands within the range of 0.15–0.46 eV, which is large enough for room temperature spintronics [19-21].

Due to novel properties of 2D materials and advancements in their fabrication, 2D heterostructures have gained much interest in context of nanotechnology, spintronics, elastic electronics, and energy storage [21-27]. Among them graphene, silicene, germanene, and TMD based systems were shown to be attractive prospects for field-effect transistors (FET) and tunable metal-semiconductor contacts. It was reported that external electric filed can enhance the interaction strength between the layers, and control size of the Schottky barrier in graphene/MoS_2 [28], silicene/MoS_2 [29] and germanene/MoS_2 [30] heterostructures. Tunable size of the band gap was also shown for MoS_2/Nb_2CO_2 and MoS_2/Nb_2CF_2 [31]. Silicene/MoS_2 heterostructure was employed in a back-gated FET reported in Ref. [32,33], and a high-performance photodetector based on graphene/MoS_2/graphene was shown in Ref. [34]. In those studies [28-34] the interactions between layers are reported to be weak i.e. limited to vdW forces. However, under some conditions strong chemical bonding may be facilitated. This problem was partially discussed for Sil and Ger at unstrained MoS_2 [35]. It was reported that, upon interface formation distortions of the atomic geometry was small suggesting relatively weak interactions between the layers. However, the intra-layer charge transfer hinted more than just the vdW interactions between Sil (Ger) and MoS_2. The strength of such interface can be further enhanced by strain, which was reported to impact the chemical activity of TMDs [17].

This work investigates the interaction character between low-

E-mail addresses: maciejjanszary@gmail.com, maciej.s.szary@doctorate.put.poznan.pl.

https://doi.org/10.1016/j.apsusc.2019.06.156
Received 25 March 2019; Received in revised form 28 May 2019; Accepted 14 June 2019
Available online 19 June 2019

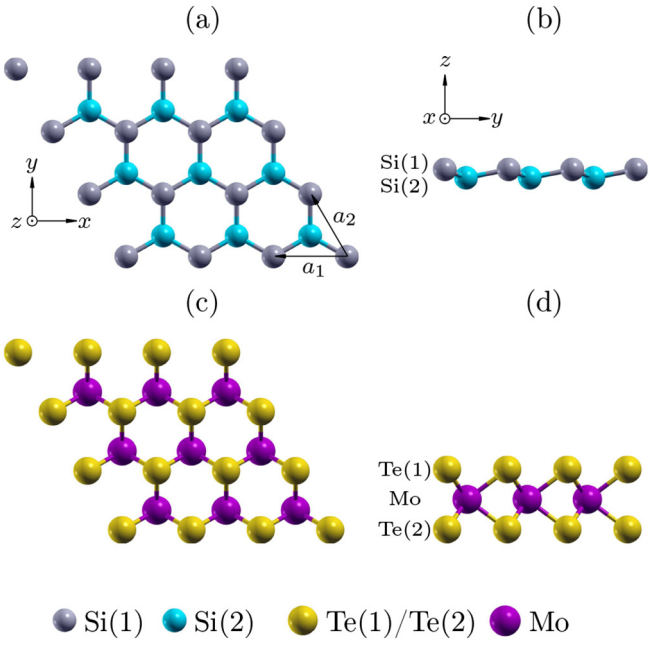

Fig. 1. Atomic-structure schematics of an isolated sheet of Sil (a,b) and $MoTe_2$ (c,d). The coordinate system system is shown in (a) and (b), atomic notations is presented in (b) and (d). Lattice vectors are presented in (a).

buckled silicene (LB-Sil or simply Sil) and a hexagonal monolayer of $MoTe_2$ under 6% of homogeneous biaxial (HB) strain (6% HB 1ML 2H-$MoTe_2$ or simply $MoTe_2$). The value of strain was selected to match the lattice constant of $MoTe_2$ with that of unstrained LB-Sil. This is far below the 20% strain limit predicted for the monolayer [36]. Also, while under 6% HB strain the hexagonal phase 2H is still reported to be more stable than the disordered octahedral phase 1T′ [37,38].

It is shown, based on the density functional theory (DFT) calculations, that the LB-Sil/2H-$MoTe_2$ heterostructure (abbreviated to Sil/$MoTe_2$) can have distinctly different interactions at the interface depending on its configuration. On the one hand, the dominant interaction can be local and directional in nature with a hybridization between p_z–p_z (or p_x/p_y–p_z) orbitals of interfacing Si and Te atoms. On the other hand, it can be limited to vdW forces. Covalent bond formation has not only an impact on both stability and electronics of the system, but also on the efficiency of charge transfer between the sheets. Effective contacts between metallic electrodes and semiconductors are critical for the performance of electronic and optoelectronic devices [25,27].

2. Methods

The first-principles DFT calculations of total-energy and electronic structure have been performed using PWSCF code of the Quantum Espresso package [39]. Generalized gradient approximation of Perdew, Burke, and Ernzerhof (GGA-PBE) [40, 41] was used in combination with three types of vdW correction: semiempirical Grimme's (DFT-D2) [42, 43], exchange-hole dipole-moment model (XDM) [44, 45], and Tkatchenko-Scheffler [46]. With the first two methods Projector Augmented Wave (PAW) potentials [47, 48] were employed, while for the latter norm-conserving pseudopotentials were used [49]. The study adopts a smearing parameter of 0.1 mRy and the cutoff energies for the wave function and density of 55 and 500 Ry, respectively. The 12× 12 ×1 grid was used in Monkhorst-Pack *k*-point sampling method for the surface-Brillouin-zone (SBZ) integration [50].

Different vdW correction methods were employed for the relaxation of bulk $MoTe_2$, and the calculated parameters were confronted with the experimental values [51, 52]. The DFT data have shown that the DFT-D2 method produces structure parameters most closely matching those

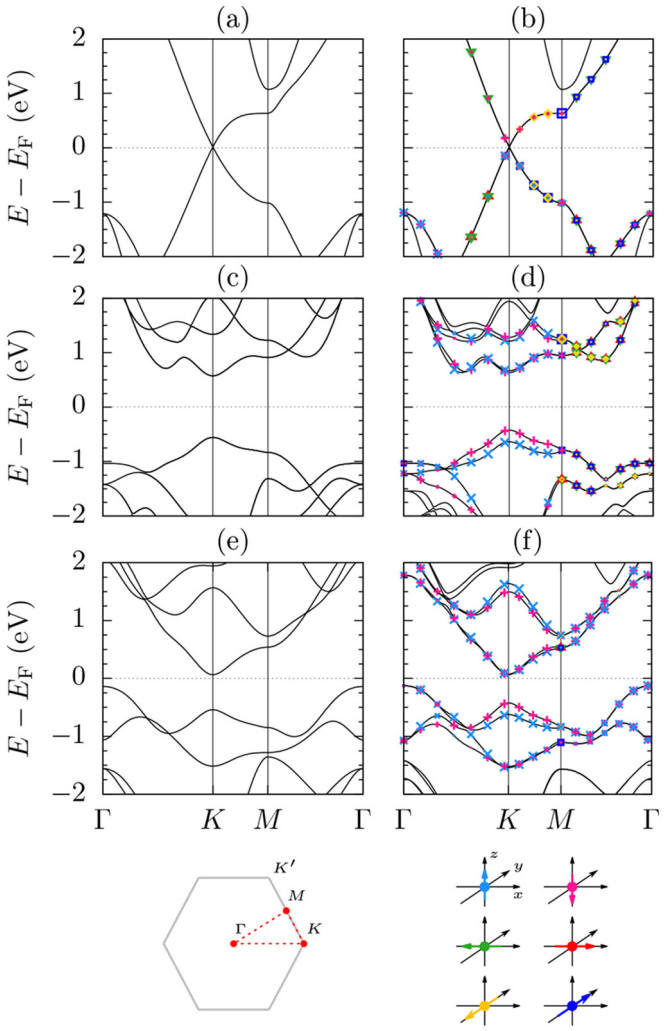

Fig. 2. Non-SOC (left) and SOC (right) electronic band structures of isolated Sil (a,b), unstrained $MoTe_2$ (c,d), and 6% HB strained $MoTe_2$ (c,d). The SBZ with high symmetry points is shown in the bottom-left corner of the figure. The expectation value of SAM $\langle \boldsymbol{S} \rangle$ are projected onto the SOC electronic band structures. The color code of the $\langle \boldsymbol{S} \rangle$ projections is shown in the bottom-right corner of the figure. The Fermi energy is at 0.0 eV.

reported in the experiment, and thus it was used for the Sil/$MoTe_2$ calculations. The monolayer of Sil and $MoTe_2$ were modeled within the repeated periodic slab model and a 1×1 surface unit cell. The cell height of 30 Å (~23 Å of vacuum along *z*) and truncation of the Coulomb interaction in the *z* direction [53] were employed to avoid artificial interactions between the neighboring systems. The atomic positions of all the atoms in the system were fully optimized with the adopted convergence threshold on forces (less than 10^{-5} Ry/au).

3. Results

3.1. Isolated Sil and $MoTe_2$

An isolated sheet of silicene is shown in Fig. 1a and b. The sheet comprised two atomic layers of silicon: upper Si(1), and lower Si(2), see Fig. 1b. Its surface belongs to p3m1 plane group, with no mirror symmetry in *x*-*y* plane. Its geometry has been fully optimized, and the calculated Si–Si distance, interlayer spacing and lattice constant are 2.264, 0.444, and 3.844 Å, respectively. Values reported for LB-Sil are between 2.2 and 2.4 Å for the Si–Si distance [54-56], 0.39–0.48 Å for the interlayer spacing [54,56,35,57], and 3.83–3.89 Å for the lattice constant [55,35,57,58].

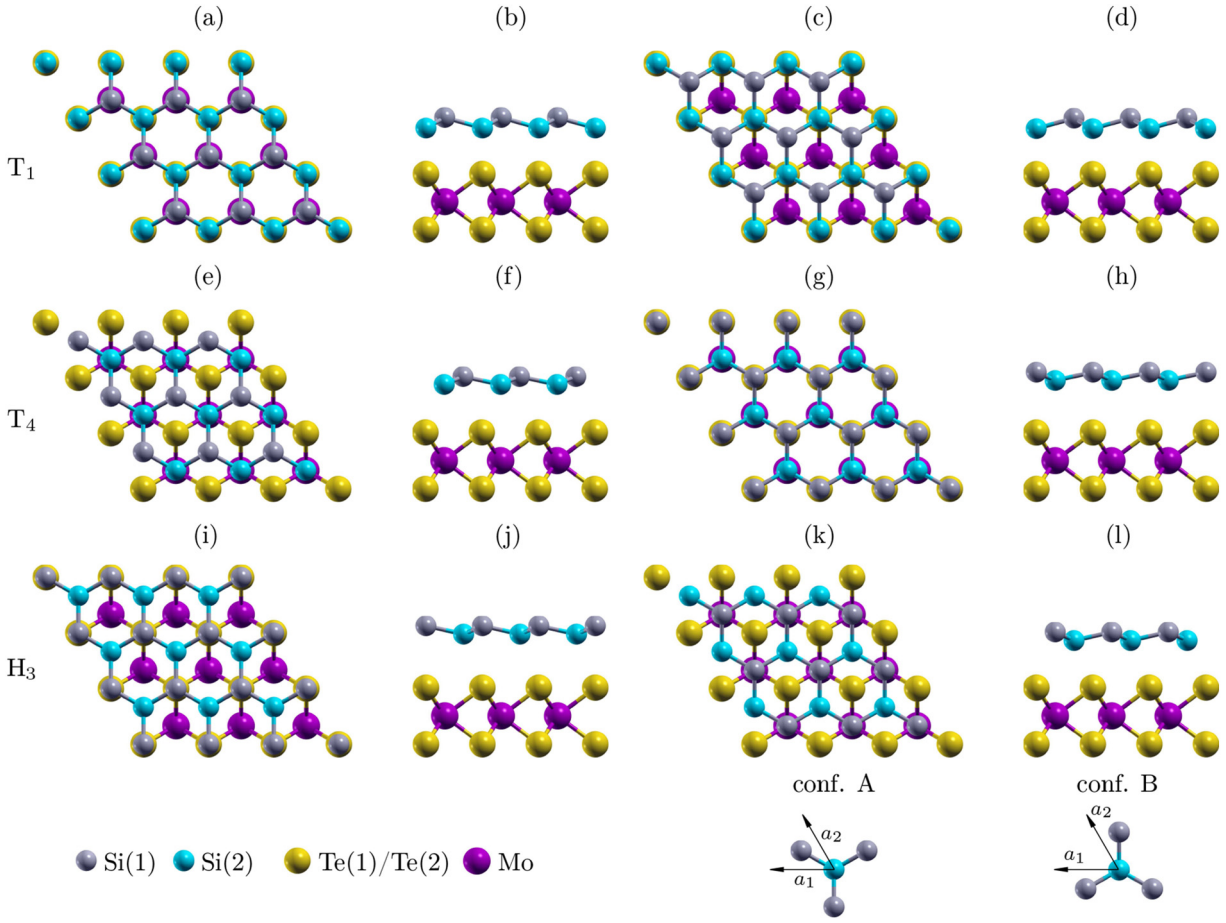

Fig. 3. Atomic-structures schematics of the heterostructure in configuration T_1–A (a,b), T_1–B (c,d), T_4–A (e,f), T_4–B (g,h), H_3–A (i,j), and H_3–B (k,l). Configurations A and B are transformed in one another with 60° rotation along *z* axis centered at a Si(2) atom see the bottom-right corner of the figure.

The non-SOC and SOC electronic structures of low-buckled silicene are given in Fig. 2a and b, respectively. Spin-orbit interaction is shown to have little impact on the electronic properties of the system. In non-SOC case Sil is a zero-gap semiconductor with its conduction and valence bands meeting at $K(K')$ points of SBZ. The inclusion of SOC introduces a negligible splitting of 1.3 meV between them. In the presence of SOC, the electronic states in the vicinity of Fermi level remain spin degenerated, with spin angular momentum (SAM) vector of the lowest-conductive and highest-valence bands (see Fig. 2b) exhibiting mostly *x*-*y* polarization; *z*-type polarization is observed for sections of the bands in vicinity of Γ and *K* points.

An isolated monolayer of hexagonal $MoTe_2$ is shown in Fig. 1c and d. The monolayer consists of two atomic layers of Te [Te(1) and Te(2)] and one of Mo between them. The surface belongs to p3m1 plane group with the *x*-*y* mirror symmetry plane located at the Mo atomic layer. When unstrained, the relaxed lattice constant, Te(1)–Te(2) spacing, and Mo–Te distance are respectively: 3.523, 3.594, and 2.713 Å. The values reported for $MoTe_2$ are between 3.47 and 3.56 Å for lattice constant [59-61], 3.59–3.62 Å for Te(1)–Te(2) spacing [17,61,62], and 2.69–2.74 for Mo–Te distance [17,61]. Under 6% HB strain, the lattice constant of $MoTe_2$ increases its value to 3.844 Å while the Te(1)–Te(2) spacing and Mo–Te distance change to 3.383 and 2.791 Å, respectively.

The non-SOC electronic structures of unstrained and strained $MoTe_2$ are shown in Fig. 2c and e. The unstrained system is a direct-gap (1.19 eV at *K*) semiconductor with both the conducive and valence bands in the vicinity of the Fermi level being predominantly comprised by 4*d* orbitals of Mo. Under strain the system undergoes a direct-to-indirect gap transition reducing its size to 0.21 eV. This correlates with other reports of TMDs under strain, where the band gap of TMDs is shown to be highly tunable [17,63,64]. When SOC is introduced to the system, a large Rashba-type spin splitting of the highest-valence band is observed along Γ–*K*–*M* in both strained and unstrained systems (see Fig. 2d and f). The effect in TMDs has been reported to originate from spin-orbit interaction facilitated by large unquenched orbital angular momentum present in the spit states [65]. The latter can be associated with the broken parity of $d_{x^2y^2}$ and d_{xy} orbitals of Mo, which stems from the p3m1 plane symmetry group, for which the mirror symmetries along Γ–*K* and *K*–*M* are absent [65,66]. Strain is shown to have a limited impact on the magnitude of the split. Its maximum values are 219 and 201 meV for unstrained and strained $MoTe_2$, respectively (see the top-valence band at *K* in Fig. 2d and f). Projections of the expectation values of SAM $\langle \boldsymbol{S} \rangle$ onto the electronic states in vicinity of Fermi level also reveal that, strain does no affect on the polarization of spin vector along Γ–*K*–*M*; in both cases spin is *z* polarized. Strain however, has an effect on the SAM vector along *M*–Γ where spin changes its polarization form *x*-*y* to *z*. This is not accompanied by a new spin splitting as in this direction, $MoTe_2$ has a *y*-*z* mirror symmetry plane (see Fig. 1c).

3.2. *Sil/$MoTe_2$ heterostructure*

The surface of $MoTe_2$ has three distinct adsorption sites all along [110]: T_1, T_4, and H_3. In T_1 atoms adsorb on top of the Te, and have one nearest-neighbor Te. In the case of T_4, an adsorbate is located above the Mo atoms, while at H_3 its positioned at the hollow center of the monolayer. In both cases an adsorbate has three nearest-neighbor Te atoms. When under 6% HB strain $MoTe_2$ matches the lattice constant of Sil, and thus in each unit cell an interfacing Si atom can occupy one of

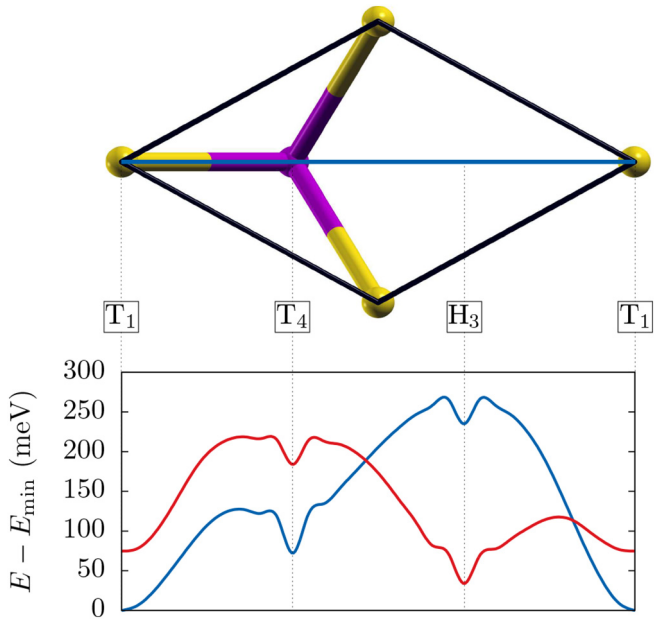

Fig. 4. (Top) Schematics of the 1 × 1 surface unit cell of $MoTe_2$ with the blue line indicating the [110] surface direction. (Bottom) The total energy of the Sil/$MoTe_2$ heterostructure calculated for different positions of Si(2) along [110] for configurations A (blue) and B (red). Energies are presented in relation to the ground states configuration (T_1–A). Interface geometries other than A and B forms of T_1, T_4 and H_3 are unstable (relaxing into one of the stable configuration), and thus at this points Si atoms were allowed only relaxation along *z* axis. The graph is comprised by 31 points per line.

Table 1
Atomic distances and interlayer spacings (Δ*z*) of configurations T_1–A, T_4–A, H_3–A, T_1–B, T_4–B, and H_3–B. The atomic numeration is shown in Fig. 1b and d.

Atom	Distance				Δz			
	izol.	T_1–A	T_4–A	H_3–A	izol.	T_1–A	T_4–A	H_3–A
				(Å)				
Si(1)–Si(2)	2.264	2.309	2.269	2.275	0.444	0.635	0.474	0.498
Si(2)–Te(1)	–	2.705	3.623	3.890	–	2.705	2.869	3.194
Te(1)–Mo	2.791	2.771	2.794	2.790	1.692	1.659	1.696	1.690
Mo–Te(2)	2.791	2.781	2.790	2.791	1.692	1.675	1.690	1.691
	izol.	T_1–B	T_4–B	H_3–B	izol.	T_1–B	T_4–B	H_3–B
Si(1)–Si(2)	2.264	2.307	2.275	2.279	0.444	0.629	0.497	0.510
Si(2)–Te(1)	–	2.739	3.835	3.583	–	2.739	3.116	2.813
Te(1)–Mo	2.791	2.768	2.791	2.795	1.692	1.654	1.690	1.698
Mo–Te(2)	2.791	2.787	2.788	2.789	1.692	1.686	1.687	1.689

those sites (see Fig. 3). Furthermore, at each site silicene can have two distinct configurations; both transforming into each other with a 60° rotation along the *z* axis centered at a Si(2) atom (A and B see the bottom-right corner of Fig. 3). This results in six distinct configurations of Sil/$MoTe_2$ system, which are shown in Fig. 3. For all of them a full structural relaxation was performed.

The binding energy of the Sil/$MoTe_2$ heterostructure was found to be between –523 and –288 meV. The values coincide with the low chemical activity of TMDs, which would suggest that, the interaction at the interface is weak. However, the energy difference observed between surface configurations is uncharacteristically large for a vdW heterostructure (235 meV) suggesting more complex interplay between the layers.

Fig. 4 shows the total energy plotted as a function of the position of Si(2) along the [110] direction, relative to the ground state of the Sil/$MoTe_2$ heterostructure. The calculations reveal that, the most stable configuration of the interface is T_1–A, where Si(1) and Si(2) atoms are directly above Te and Mo (see Fig. 3a and b). It has 72, and 235 meV lower energy than configurations T_4–A and H_3–A. It has also 34, 75, and 184 eV lower energy than configurations H_3–B, T_1–B and T_4–B. The height of the activation barrier varies greatly between surface configurations, with the lowest and highest having the values of 31 (H_3–A to T_1–A) and 266 meV (T_1–A to H_3–A), respectively. The energy barrier between A- and B-type configurations also depends on the position of Sil at the $MoTe_2$ ranging between 27 (T_1–B to T_1–A) and 251 meV (H_3–B to H_3–A). Interestingly, both global and local minima are highly localized at the points of the surface, which reviles local, non-uniform character of interactions at the interface.

Distinct differences between the surface configurations are also observed in the atomic structure of the system (see Table 1). While $MoTe_2$ across all configurations of the heterostructure remains mostly unaffected—Mo–Te distance having maximum of 0.023 Å length difference in comparison to the isolated sheet—the atomic structure of silicene is shown to change more significantly. The Si(1)–Si(2) interlayer spacing increases in comparison to the isolated system by 0.03–0.19 Å. Larger buckling of Sil is usually a result of increased contribution of sp^3 hybridization in the bonding of the monolayer. The large value of Si(1)–Si(2) interlayer separation correlates with the relatively short Si(2)–Te(1) distance observed for T_1–A and T_1–B. This suggests that Si(2)–Te(1) interaction affects the hybridization of Si (1)–Si(2) bonds in Sil.

The short distance of Si(2)–Te(1) in T_1–A and T_1–B correlates with their low total energy further supporting a strong chemical bonding in those configurations. Interestingly, T_4–A and H_3–B also have relatively low energy, while having significantly longer Si(2)–Te(1) distance than T_1–A and T_1–B (~3.6 in comparison to ~2.7 Å, see Table 1). This indicates a different interaction type in both cases. Furthermore, T_4–B and H_3–A have the highest total energy and the greatest Si(2)–Te(1) distance making them distinguishable from other configurations. The observed differences demonstrate that the layers interact with each other differently at different configurations.

Strong surface interactions can impact the bonding configuration of a system, and thus their nature should be reflected in the electronics. Fig. 5 shows the non-SOC electronic band structures of the isolated layers and configurations T_1–A, T_4–B, and H_3–B. The configurations were selected to represent one of each interaction cases observed at the interface. Remaining structures have similar features to those presented, and thus are not shown. The projections of atomic wave functions onto the electronic band structure of $MoTe_2$ are shown in Fig. 5b and c. When isolated the electronic states that comprised p_z orbitals of Te show even contribution from both Te(1) and Te(2), however, in configuration T_1–A this symmetry is affected (see Fig. 5e and f). This is further demonstrated by the partial charge differences ($\Delta\delta$) obtained from the Löwdin population analysis (see Fig. 6a). Te(2), which is on the pristine side of $MoTe_2$, shows only negligible deviation of charge, while Te(1) becomes 0.11*e* more electropositive with large depopulation of p_z electronic states (0.21*e*) partially countered by increased population of p_x/p_y-type states (–0.13*e*). The change imbalance in the TMD monolayer is offset by Mo, which becomes more electronegative (–0.11*e*). This is a result of large increase in population of d_{z^2} states (–0.19*e*), which is partially compensated by the depopulation of d_{zx}/d_{zx} states (0.08*e*). Those changes correlate with the features of the band structure. While states of d_{z^2} Mo are well reproduced in the electronics of configuration T_1–A they experience a downward shift moving below the Fermi level in vicinity of *K* (see Fig. 5c, and f). On the other hand, the p_z orbital contributions of Te(2) move upwards, with notable present between –2 and –3 eV (band S_1), and a limited one below –4 eV (see Fig. 5b, and e).

Broken bonding symmetry is also observed in Sil. When isolated electronic states that comprised p_x/p_y and p_z orbitals show even contribution from both Si(1) and Si(2) (see Fig. 5a). In T_1–A the p_x/p_y orbital coupling remains unaffected, however, the p_z orbitals become

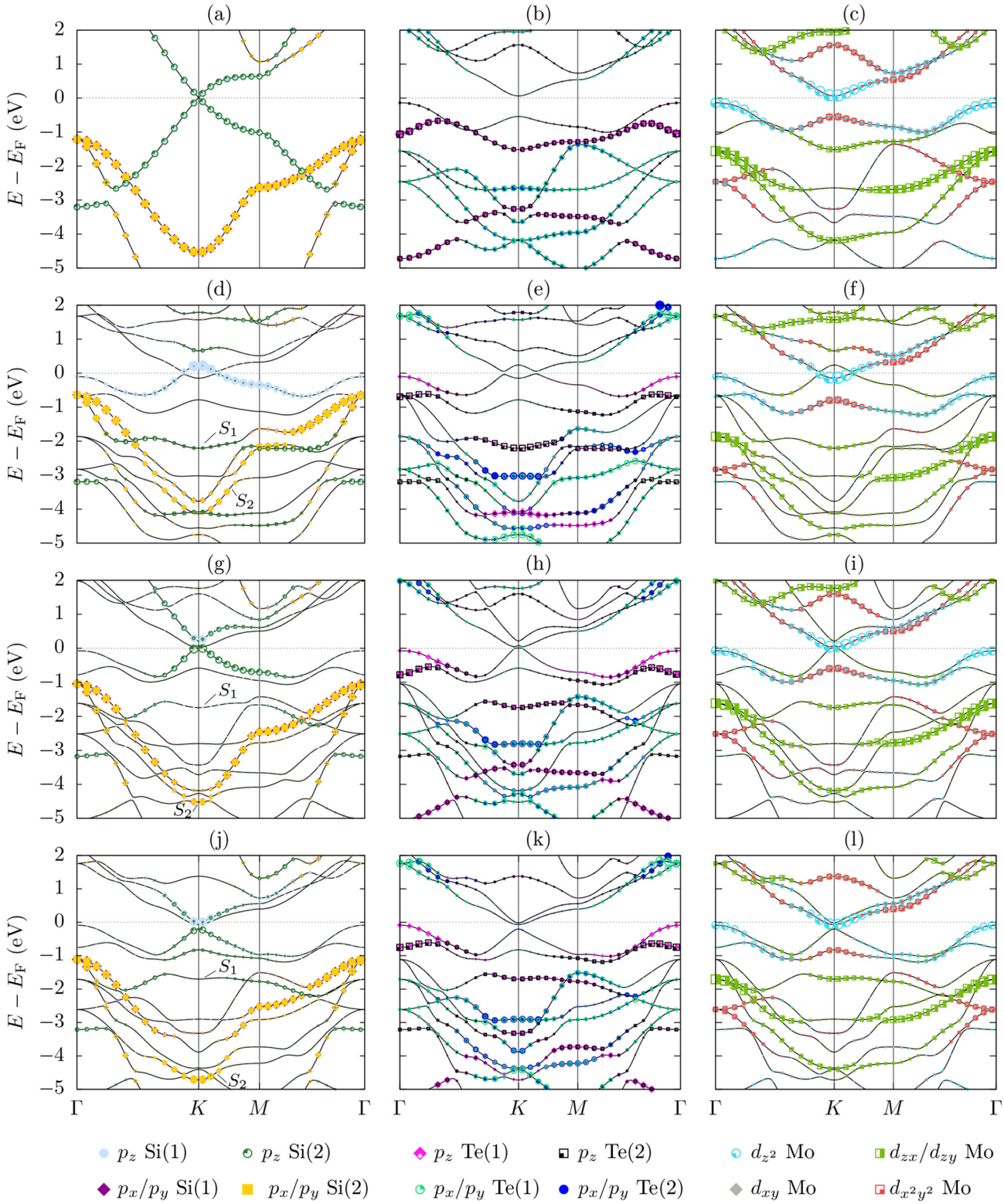

Fig. 5. Atomic orbital projections onto the electronic bands of isolated SiI (a), $MoTe_2$ (b,c), and configurations T_1–A (d–f), T_4–B (g–i), and H_3–B (j–l). Color code for the atomic orbitals is shown in the bottom of the figure. Bands S_1 and S_2 are shown in (d), (g) and (j). In all figures the Fermi level is at 0 eV.

decoupled. The p_z Si(1) are present almost exclusively in vicinity of Fermi level in a band, which devolved from the lower Dirac cone. In contrast, the p_z Si(2) orbitals have only a small presence in vicinity of Fermi, while the majority of its projections are found between –2 and –4 eV. The decoupling coincides with the changes in orbital population of Si atoms (see Fig. 6a). The population p_z of Si(1) increases (–0.06e), while the p_x/p_y orbitals depopulate (0.10e). For the Si(2) atoms trend is reversed, the p_z orbitals depopulate (0.12e), while p_x/p_y populate (0.10e). Interestingly the projections of the most affected atomic orbitals—p_z Si(2) and p_z Te(1)—are shown to coincide with each other (see Fig. 5d and e). This coupling is particularly strong for band S_1, which represents a Mo–Te bonding in an isolated $MoTe_2$. The charge density

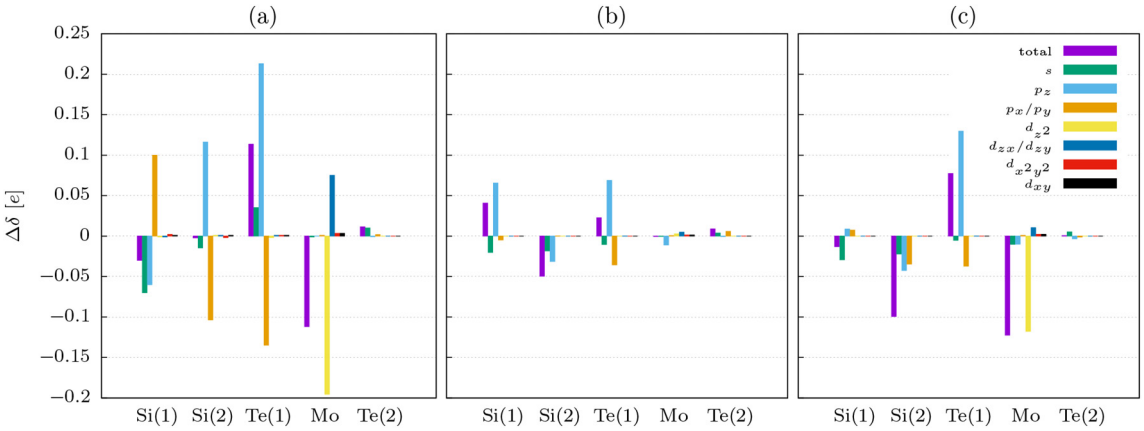

Fig. 6. Partial charge differences ($\Delta\delta$) obtained form the Löwdin population analysis for configuration T_1–A (a), T_4–B (b), and H_3–B (c). The values are in reference to the charges calculated for atoms in an isolated Sil and $MoTe_2$.

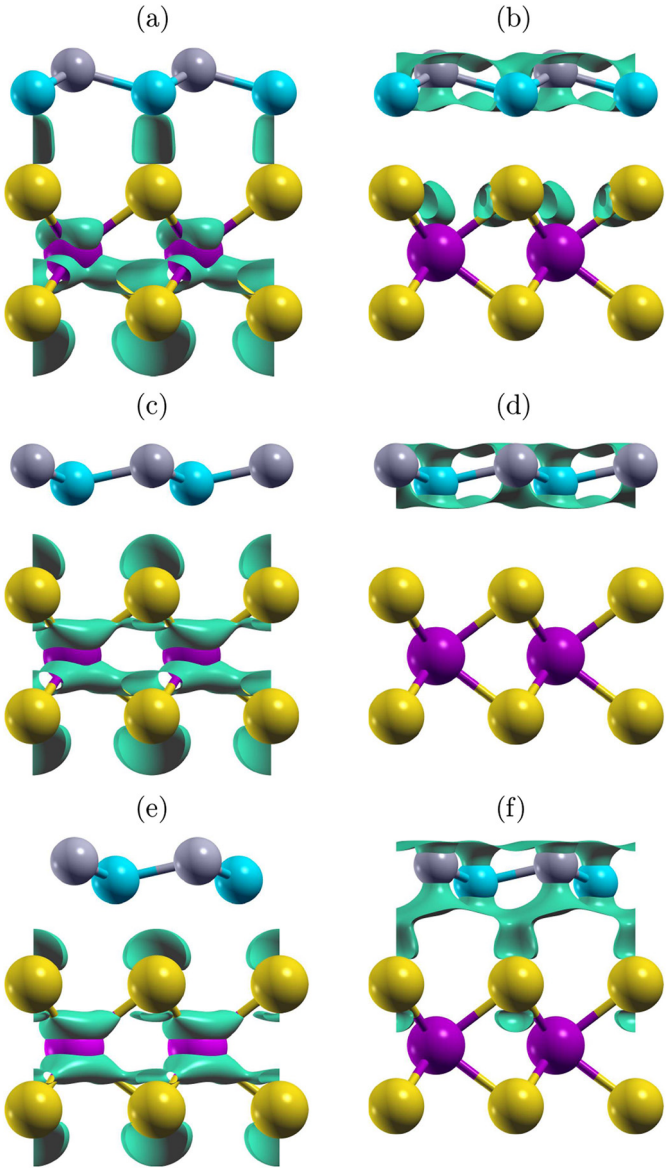

Fig. 7. Electronic-charge contours calculated for band S_1 (left) and S_2 (right) at K for configurations T_1–A (a,b), T_4–B (c,d), and H_3–B (e,f). Isosurface value: 0.0027 e/a.u.^{3}.

contour of the band in configuration T_1–A is given in Fig. 7a. It shows that, the electronic charge of both Si(2) and Te(1) overlaps forming hybrid states with the charge density present between the atoms. As the interaction is local and directional due to to orbital overlap it is clear that in T_1–A Si(2) and Te(1) form a covalent σ-type bonding, which coincides with a downward shift of the band in the heterostructure (–0.69 eV at K). The new bond formation comes at the experience of one of the Mo–Te(1) bonds, which brakes the intrinsic symmetry of the boding configuration of the isolated $MoTe_2$. This explains the decoupling of Te(1) and Te(2) orbitals in the system and the relatively low binding energy of the configuration.

Atomic orbitals projected onto the electronic structure of configuration H_3–B are shown in Fig. 5j–l. Interestingly, despite configurations T_1–A and H_3–B having similar total energies, the chemical interactions between Si(2) and Te(1) outlined by their electronic structures are vastly different. While in both cases Mo orbitals remain mostly unaffected, in H_3–B p_z orbitals of Te(1) and Te(2) remain partially coupled. This coincides with a smaller variation of orbital population in H_3–B when compared with T_1–A (see Fig. 6a and 6c). Furthermore, the coupling of p_z orbitals of Si(1) and Si(2) in the vicinity of Fermi is also mostly unaffected suggesting the lack of binding interaction between those orbitals. This is indeed the cases for H_3–B. The p_z orbitals of Si(2) and Te(1) do not couple, and as shown by the contours of electronic charge of band S_1 (see Fig. 7e), no new Si(2)–Te(1) bond is present. Still, the Te(1)–Mo bonding is broken. The electronic charges of both atoms do no overlap and the bonding symmetry of $MoTe_2$ is affected. Also, the projections of the p_x/p_y Si(2) and p_z Te(1) are shown to coincide with each other more than in configuration T_1–A (see Fig. 5d–e and j–k). This coupling is most pronounced in band S_2, which represents the Si(1)–Si(2) bonding in an isolated Sil. The charge density contour of the band in configuration H_3–B is given in Fig. 7f. It shows that, the electronic charge of both Si(2) and Te(1) overlaps forming new hybrid states. This localized interaction is also clearly directional, with rise of p_x/p_y–p_z coupling instead of p_z–p_z due to position of interfacing atoms, which is indicative of a covalent-type bonding. This interaction is responsible for the low energy of the configuration. It also elucidates on the electronic population changes in Si(2) and Te(1) atoms. Furthermore, it is exclusive to configuration H_3–B. It is not present in configuration T_1–A, as shown by the contours of electronic charge of band S_2 (see Fig. 7b), the electronic charge is localized at the monolayer, with no overlap with electronic states of p_z Te(2).

Atomic orbitals projected onto the electronic structure of unfavorable configuration T_4–B are shown in Fig. 5g–i. In this configuration the electronic structure presents well reproduced electronic bands of the isolated systems with very little deviation in terms of orbital composition. This is indicative of weak interactions at interface, which is further supported by small changes in the electronic population (see Fig. 6b).

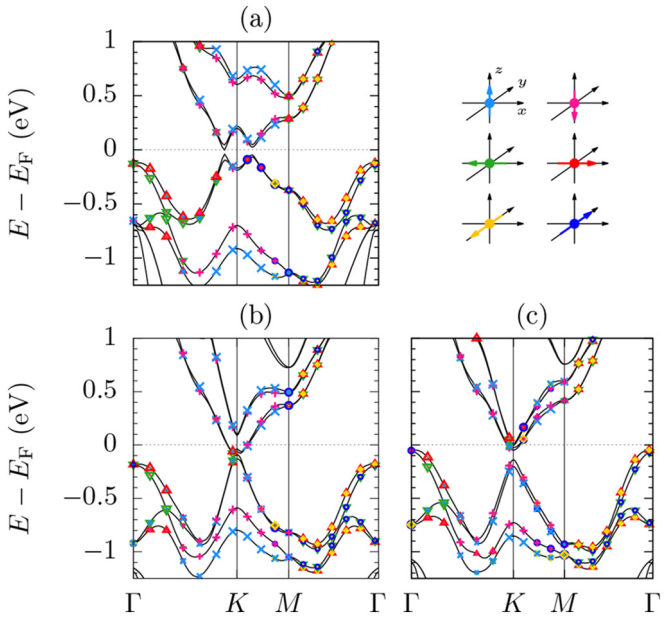

Fig. 8. SOC electronic band structures of configurations T_1–A (a), T_4–B (b), and H_3–B (c) with expectation values of SAM projected on the bands. Color code of the $\langle S \rangle$ components is presented in the top-right corner of the figure. In all figures the Fermi level is at 0 eV.

Also in this configuration there is no p_z–p_z or p_x/p_y–p_z coupling between Si(2) and Te(1) atom. Electronic charge distribution of both bands S_1 and S_2 shows that, Si(1)–Si(2) and Mo–Te(1) bonding remains unaffected by formation of the interface. Therefore, configuration T_4–B represents a case where the interaction between Sil and $MoTe_2$ is limited to weak vdW forces.

The character of the interface interaction has a significant impact on properties of the Sil/$MoTe_2$ heterostructure. It affects geometry and energetics of the system, as well as electronic population of atoms in the layers, and the shape of electronic bands in the vicinity of Fermi level and their orbital composition. It also has a great impact on the charge transfer between layers. On the one hand, when the interactions are limited only to dispersive forces, there is no orbital hybridization of interfacing atoms (configuration T_4–B). This forms vdW gap, with no overlapping electronic-charge clouds (see Fig. 7c and d), which facilitates high potential energy barrier for electrons to pass between the systems, and thus limiting electrical conductivity of the contact [25,59]. On the other hand, covalent bonds (configuration T_1–A and H_3–B) form hybrid states with overlapping electronic-charge clouds between the interfacing atoms (see Fig. 7a and f). This lowers the energy barrier for electrons to pass between the systems [25], which is beneficial for carrier injections.

An isolated monolayer of $MoTe_2$ has an intrinsic spin splitting along Γ–*K*–*M* thus, it is instructive to investigate also the impact of interface interactions in the presence of SOC. The electronic band structures of configurations T_1–A, T_4–B, and H_3–B with projections of SAM onto the electronic bands are given in Fig. 8. It shows that the intrinsic splitting of $MoTe_2$ is preserved in Sil/$MoTe_2$ regardless of the interface configuration. The $d_{xy}/d_{x^2y^2}$ dominated band splits along Γ–*K*–*M* retaining the out-of-plane polarization of the spin vector (compare Figs. 8 with 2f). The maximum of spin splitting is observed at *K*, and the values are 213, 209 and 135 meV in configurations T_1–A, T_4–B, and H_3–B, respectively. Only the p_x/p_y–p_z bonding interaction between Si(2) and Te(1) atom is shown to significantly affect the value of spin splitting. The effect coincides with composition of the band as the contribution of $d_{xy}/d_{x^2y^2}$ Mo orbitals is reduced due to mixing with states of p_z Si(2) (see Fig. 5j and l). The coupling does not produce a covalent bonding, there is no overlap between the orbitals. The effect stems, however, from surface electric field that couples those states in the vicinity of *K*.

Interestingly, the interface formation also induces a spin splitting in the vicinity of Γ for the electronic band that comprised predominantlyd_{z^2} orbitals of Mo with non-zero contributions from p_z Te and d_{xy} Mo. This effect coincides with other reports where a spin splitting is induced due to broken out-of-plane symmetry introduced by an external electric field or an adsorbate [65,67]. In the system, the observed splitting is, however, small with momentum offset of $\sim 0.08\ \text{Å}^{-1}$ and corresponding splitting of ~ 40 meV, which indicates that, the electric field gradient introduced by Sil is smaller in comparison to those produced by adsorption of heavy elements e.g. Pb [67].

4. Conclusions

In conclusion, the interaction mechanism between silicene and strained $MoTe_2$ has been investigated. This report illustrates that depending on the adsorption configuration, the interface interaction can take one of three forms. In the energetically unfavorable configurations the interactions are weak and limited to vdW forces. In contrast, the favorable configurations are shown to facilitate new covalent bonds with the hybridization between p_z–p_z or p_x/p_y–p_z orbitals of interfacing Si and Te atoms. New covalent bonds have a significant impact on the electronic population of atoms in the monolayer, which also affect the electronic band structure in the vicinity of Fermi level. Directional character of the interaction produces well-defined and energetically favorable configuration of the Sil/$MoTe_2$ interface, where overlapping electronic-charge clouds lower the energy barrier for electrons to pass between the layers thus, making charge transfer between them more effective.

Acknowledgments

M.J.S. acknowledges the Ministry of Science and Higher Education in Poland for the financial support within project no 06/62/SBAD/1923 realized at the Faculty of Technical Physics, Poznan University of Technology.

References

[1] Z. Ni, Q. Liu, K. Tang, J. Zheng, J. Zhou, R. Qin, Z. Gao, D. Yu, J. Lu, Tunable bandgap in silicene and germanene, Nano Lett. 12 (1) (2012) 113–118, https://doi.org/10.1021/nl203065e pMID: 22050667.
[2] Z. Ni, H. Zhong, X. Jiang, R. Quhe, G. Luo, Y. Wang, M. Ye, J. Yang, J. Shi, J. Lu, Tunable band gap and doping type in silicene by surface adsorption: towards tunneling transistors, Nanoscale 6 (13) (2014) 7609–7618, https://doi.org/10.1039/C4NR00028E.
[3] R. Singh, Spin-orbit coupling in graphene, silicene and germanene: dependence on the configuration of full hydrogenation and fluorination, Bull. Mater. Sci. 41 (6) (2018) 158, https://doi.org/10.1007/s12034-018-1655-6.
[4] A. Molle, C. Grazianetti, L. Tao, D. Taneja, M.H. Alam, D. Akinwande, Silicene, silicene derivatives, and their device applications, Chem. Soc. Rev. 47 (2018) 6370–6387, https://doi.org/10.1039/C8CS00338F.
[5] R. Yu, W. Zhang, H.-J. Zhang, S.-C. Zhang, X. Dai, Z. Fang, Quantized anomalous hall effect in magnetic topological insulators, Science 329 (5987) (2010) 61–64, https://doi.org/10.1126/science.1187485 http://science.sciencemag.org/content/329/5987/61.
[6] C.L. Kane, E.J. Mele, Quantum spin hall effect in graphene, Phys. Rev. Lett. 95 (2005) 226801, https://doi.org/10.1103/PhysRevLett.95.226801 https://link.aps.org/doi/10.1103/PhysRevLett.95.226801.
[7] S. Rajasekaran, F. Abild-Pedersen, H. Ogasawara, A. Nilsson, S. Kaya, Interlayer carbon bond formation induced by hydrogen adsorption in few-layer supported graphene, Phys. Rev. Lett. 111 (2013) 085503, https://doi.org/10.1103/PhysRevLett.111.085503 https://link.aps.org/doi/10.1103/PhysRevLett.111.085503.
[8] F.-b. Zheng, C.-w. Zhang, The electronic and magnetic properties of functionalized silicene: a first-principles study, Nanoscale Res. Lett. 7 (1) (2012) 422, https://doi.org/10.1186/1556-276X-7-422.
[9] J. Sivek, H. Sahin, B. Partoens, F.M. Peeters, Adsorption and absorption of boron, nitrogen, aluminum, and phosphorus on silicene: stability and electronic and phonon properties, Phys. Rev. B 87 (2013) 085444, https://doi.org/10.1103/PhysRevB.87.085444 https://link.aps.org/doi/10.1103/PhysRevB.87.085444.

[10] D.W. Boukhvalov, M.I. Katsnelson, Chemical functionalization of graphene, J. Phys. Condens. Matter 21 (34) (2009) 344205, https://doi.org/10.1088/0953-8984/21/34/344205.

[11] M. Nayeri, M. Moradinasab, M. Fathipour, The transport and optical sensing properties of MoS2, MoSe2, WS2 and WSe2 semiconducting transition metal dichalcogenides, Semicond. Sci. Technol. 33 (2) (2018) 025002, https://doi.org/10.1088/1361-6641/aaa168.

[12] Q.H. Wang, K. Kalantar-Zadeh, A. Kis, J.N. Coleman, M.S. Strano, Electronics and optoelectronics of two-dimensional transition metal dichalcogenides, Nature Nanotechnology 7 (2012) 699, https://doi.org/10.1038/nnano.2012.193 EP –, review Article.

[13] G.H. Han, D.L. Duong, D.H. Keum, S.J. Yun, Y.H. Lee, van der Waals metallic transition metal dichalcogenides, Chem. Rev. 118 (13) (2018) 6297–6336, https://doi.org/10.1021/acs.chemrev.7b00618 pMID: 29957928.

[14] Z.G. Yu, B.I. Yakobson, Y.-W. Zhang, Realizing indirect-to-direct band gap transition in few-layer two-dimensional MX2 (M = Mo, W; X = S, Se), ACS Appl. Energy Mater. 1 (8) (2018) 4115–4121, https://doi.org/10.1021/acsaem.8b00774.

[15] R. Dong, I. Kuljanishvili, Review article: progress in fabrication of transition metal dichalcogenides heterostructure systems, J. Vac. Sci. Technol. B 35 (3) (2017) 030803, https://doi.org/10.1116/1.4982736.

[16] P. Sreeparvathy, V. Kanchana, P. Anees, G. Vaitheeswaran, Emergence of strain induced two dimensional metallic state in ReS2, J. Solid State Chem. 269 (2019) 138–144, https://doi.org/10.1016/j.jssc.2018.09.008 http://www.sciencedirect.com/science/article/pii/S0022459618303931.

[17] M.J. Szary, M.T. Michalewicz, M.W. Radny, Bonding and electronics of the $MoTe_2$/Ge interface under strain, Phys. Rev. B 95 (2017) 205421, https://doi.org/10.1103/PhysRevB.95.205421 https://link.aps.org/doi/10.1103/PhysRevB.95.205421.

[18] X. Hu, Q. Zhang, S. Yu, Theoretical insight into the hydrogen adsorption on MoS2 (MoSe2) monolayer as a function of biaxial strain/external electric field, Appl. Surf. Sci. 478 (2019) 857–865, https://doi.org/10.1016/j.apsusc.2019.01.276 http://www.sciencedirect.com/science/article/pii/S0169433219303071.

[19] Q. Wang, J. Li, J. Besbas, C.-H. Hsu, K. Cai, L. Yang, S. Cheng, Y. Wu, W. Zhang, K. Wang, T.-R. Chang, H. Lin, H. Chang, H. Yang, Room-temperature nanoseconds spin relaxation in WTe2 and MoTe2 thin films, Adv. Sci. 5 (6) (2018) 1700912, https://doi.org/10.1002/advs.201700912 https://onlinelibrary.wiley.com/doi/abs/10.1002/advs.201700912.

[20] J. Quereda, T.S. Ghiasi, J.-S. You, J. van den Brink, B.J. van Wees, C.H. van der Wal, Symmetry regimes for circular photocurrents in monolayer MoSe2, Nat. Commun. 9 (1) (2018) 3346, https://doi.org/10.1038/s41467-018-05734-z.

[21] X. Li, Y. Dai, C. Niu, Y. Ma, W. Wei, B. Huang, MoTe2 is a good match for GeI by preserving quantum spin Hall phase, Nano Res. 10 (8) (2017) 2823–2832, https://doi.org/10.1007/s12274-017-1488-4.

[22] X. Chen, R. Meng, J. Jiang, Q. Liang, Q. Yang, C. Tan, X. Sun, S. Zhang, T. Ren, Electronic structure and optical properties of graphene/stanene heterobilayer, Phys. Chem. Chem. Phys. 18 (2016) 16302–16309, https://doi.org/10.1039/C6CP02424F.

[23] J. Shim, D.-H. Kang, Y. Kim, H. Kum, W. Kong, S.-H. Bae, I. Almansouri, K. Lee, J.-H. Park, J. Kim, Recent progress in Van der Waals (vdW) heterojunction-based electronic and optoelectronic devices, Carbon 133 (2018) 78–89, https://doi.org/10.1016/j.carbon.2018.02.104 http://www.sciencedirect.com/science/article/pii/S0008622318302409.

[24] K.K. Kim, H.S. Lee, Y.H. Lee, Synthesis of hexagonal boron nitride heterostructures for 2D van der Waals electronics, Chem. Soc. Rev. 47 (2018) 6342–6369, https://doi.org/10.1039/C8CS00450A.

[25] Q. Li, J. Yang, R. Quhe, Q. Zhang, L. Xu, Y. Pan, M. Lei, J. Lu, Ohmic contacts between monolayer WSe2 and two-dimensional titanium carbides, Carbon 135 (2018) 125–133, https://doi.org/10.1016/j.carbon.2018.04.043 http://www.sciencedirect.com/science/article/pii/S0008622318304020.

[26] J. Pang, R.G. Mendes, A. Bachmatiuk, L. Zhao, H.Q. Ta, T. Gemming, H. Liu, Z. Liu, M.H. Rummeli, Applications of 2D MXenes in energy conversion and storage systems, Chem. Soc. Rev. 48 (2019) 72–133, https://doi.org/10.1039/C8CS00324F.

[27] X. Gong, X. Zhao, M.E. Pam, H. Yao, Z. Li, D. Geng, S.J. Pennycook, Y. Shi, H.Y. Yang, Location-selective growth of two-dimensional metallic/semiconducting transition metal dichalcogenide heterostructures, Nanoscale 11 (2019) 4183–4189, https://doi.org/10.1039/C8NR08744J.

[28] X. Liu, Z. Li, Electric field and strain effect on graphene-MoS2 hybrid structure: ab initio calculations, J. Phys. Chem. Lett. 6 (16) (2015) 3269–3275, https://doi.org/10.1021/acs.jpclett.5b01233.

[29] S. shi Li, C. wen Zhang, W. xiao Ji, Novel electronic properties in silicene on MoSe2 monolayer: an excellent prediction for FET, Mater. Chem. Phys. 164 (2015) 150–156, https://doi.org/10.1016/j.matchemphys.2015.08.036 http://www.sciencedirect.com/science/article/pii/S0254058415302959.

[30] H. Li, Y. Yu, X. Xue, J. Xie, H. Si, J.Y. Lee, A. Fu, Electroic and optical properties of germanene/MoS2 heterobilayers: first principles study, J. Mol. Model. 24 (12) (2018) 333, https://doi.org/10.1007/s00894-018-3855-9.

[31] Q. Peng, C. Si, J. Zhou, Z. Sun, Modulating the Schottky barriers in MoS2/MXenes heterostructures via surface functionalization and electric field, Appl. Surf. Sci. 480 (2019) 199–204, https://doi.org/10.1016/j.apsusc.2019.02.249 http://www.sciencedirect.com/science/article/pii/S0169433219306063.

[32] A. Molle, A. Lamperti, D. Rotta, M. Fanciulli, E. Cinquanta, C. Grazianetti, Electron confinement at the Si/MoS2 heterosheet interface, Adv. Mater. Interfaces 3 (10) (2016) 1500619, https://doi.org/10.1002/admi.201500619 https://onlinelibrary.wiley.com/doi/abs/10.1002/admi.201500619.

[33] E. Scalise, K. Iordanidou, V.V. Afanas'ev, A. Stesmans, M. Houssa, Silicene on non-metallic substrates: recent theoretical and experimental advances, Nano Res. 11 (3) (2018) 1169–1182, https://doi.org/10.1007/s12274-017-1777-y.

[34] B. Liu, Y. Chen, C. You, Y. Liu, X. Kong, J. Li, S. Li, W. Deng, Y. Li, H. Yan, Y. Zhang, High performance photodetector based on graphene/MoS2/graphene lateral heterostrurcture with Schottky junctions, J. Alloys Compd. 779 (2019) 140–146, https://doi.org/10.1016/j.jallcom.2018.11.165 http://www.sciencedirect.com/science/article/pii/S0925838818342944.

[35] X. Li, S. Wu, S. Zhou, Z. Zhu, Structural and electronic properties of germanene/MoS2 monolayer and silicene/MoS2 monolayer superlattices, Nanoscale Res. Lett. 9 (1) (2014) 110, https://doi.org/10.1186/1556-276X-9-110.

[36] R.C. Cooper, C. Lee, C.A. Marianetti, X. Wei, J. Hone, J.W. Kysar, Nonlinear elastic behavior of two-dimensional molybdenum disulfide, Phys. Rev. B 87 (2013) 035423, https://doi.org/10.1103/PhysRevB.87.035423 https://link.aps.org/doi/10.1103/PhysRevB.87.035423.

[37] H.H. Huang, X. Fan, D.J. Singh, H. Chen, Q. Jiang, W.T. Zheng, Controlling phase transition for single-layer MTe2 (M = Mo and W): modulation of the potential barrier under strain, Phys. Chem. Chem. Phys. 18 (2016) 4086–4094, https://doi.org/10.1039/C5CP06706E.

[38] K.-A.N. Duerloo, Y. Li, E.J. Reed, Structural phase transitions in two-dimensional Mo- and W-dichalcogenide monolayers, Nature Communications 5 (2014) 4214, https://doi.org/10.1038/ncomms5214 EP –, article.

[39] P. Giannozzi, S. Baroni, N. Bonini, M. Calandra, R. Car, C. Cavazzoni, D. Ceresoli, G.L. Chiarotti, M. Cococcioni, I. Dabo, A. Dal Corso, S. de Gironcoli, S. Fabris, G. Fratesi, R. Gebauer, U. Gerstmann, C. Gougoussis, A. Kokalj, M. Lazzeri, L. Martin-Samos, N. Marzari, F. Mauri, R. Mazzarello, S. Paolini, A. Pasquarello, L. Paulatto, C. Sbraccia, S. Scandolo, G. Sclauzero, A.P. Seitsonen, A. Smogunov, P. Umari, R.M. Wentzcovitch, Quantum Espresso: a modular and open-source software project for quantum simulations of materials, J. Phys. Condens. Matter 21 (39) (2009) 395502.

[40] J.P. Perdew, K. Burke, M. Ernzerhof, Generalized gradient approximation made simple, Phys. Rev. Lett. 77 (1996) 3865.

[41] J.P. Perdew, A. Ruzsinszky, G.I. Csonka, O.A. Vydrov, G.E. Scuseria, L.A. Constantin, X. Zhou, K. Burke, Restoring the density-gradient expansion for exchange in solids and surfaces, Phys. Rev. Lett. 100 (2008) 136406.

[42] S. Grimme, Semiempirical GGA-type density functional constructed with a long-range dispersion correction, J. Comput. Chem. 27 (15) (2006) 1787.

[43] V. Barone, M. Casarin, D. Forrer, M. Pavone, M. Sambi, A. Vittadini, Role and effective treatment of dispersive forces in materials: polyethylene and graphite crystals as test cases, J. Comput. Chem. 30 (6) (2009) 934.

[44] A.D. Becke, E.R. Johnson, Exchange-hole dipole moment and the dispersion interaction revisited, J. Chem. Phys. 127 (15) (2007) 154108, https://doi.org/10.1063/1.2795701.

[45] A. Otero-de-la Roza, E.R. Johnson, Van der Waals interactions in solids using the exchange-hole dipole moment model, J. Chem. Phys. 136 (17) (2012) 174109, https://doi.org/10.1063/1.4705760.

[46] A. Tkatchenko, M. Scheffler, Accurate molecular van der Waals interactions from ground-state electron density and free-atom reference data, Phys. Rev. Lett. 102 (2009) 073005, https://doi.org/10.1103/PhysRevLett.102.073005 https://link.aps.org/doi/10.1103/PhysRevLett.102.073005.

[47] P.E. Blöchl, Projector augmented-wave method, Phys. Rev. B 50 (1994) 17953.

[48] G. Kresse, D. Joubert, From ultrasoft pseudopotentials to the projector augmented-wave method, Phys. Rev. B 59 (1999) 1758.

[49] N. Troullier, J.L. Martins, Efficient pseudopotentials for plane-wave calculations, Phys. Rev. B 43 (1991) 1993–2006, https://doi.org/10.1103/PhysRevB.43.1993 https://link.aps.org/doi/10.1103/PhysRevB.43.1993.

[50] H.J. Monkhorst, J.D. Pack, Special points for Brillouin-zone integrations, Phys. Rev. B 13 (1976) 5188–5192.

[51] D. Puotinen, R.E. Newnham, The crystal structure of $MoTe_2$, Acta Crystallographica 14 (6) (1961) 691–692, https://doi.org/10.1107/S0365110X61002084.

[52] O. Knop, R.D. MacDonald, Chalkogenides of the transition elements: III. molybdenum ditelluride, Can. J. Chem. 39 (4) (1961) 897–904, https://doi.org/10.1139/v61-110.

[53] T. Sohier, M. Calandra, F. Mauri, Density functional perturbation theory for gated two-dimensional heterostructures: theoretical developments and application to flexural phonons in graphene, Phys. Rev. B 96 (2017) 075448, https://doi.org/10.1103/PhysRevB.96.075448 https://link.aps.org/doi/10.1103/PhysRevB.96.075448.

[54] J. Zhao, H. Liu, Z. Yu, R. Quhe, S. Zhou, Y. Wang, C.C. Liu, H. Zhong, N. Han, J. Lu, Y. Yao, K. Wu, Rise of silicene: a competitive 2D material, Prog. Mater. Sci. 83 (2016) 24–151, https://doi.org/10.1016/j.pmatsci.2016.04.001 http://www.sciencedirect.com/science/article/pii/S0079642516300068.

[55] S. Cahangirov, M. Topsakal, E. Aktürk, H. Şahin, S. Ciraci, Two- and one-dimensional honeycomb structures of silicon and germanium, Phys. Rev. Lett. 102 (2009) 236804, https://doi.org/10.1103/PhysRevLett.102.236804 https://link.aps.org/doi/10.1103/PhysRevLett.102.236804.

[56] C. Hogan, O. Pulci, P. Gori, F. Bechstedt, D.S. Martin, E.E. Barritt, A. Curcella, G. Prevot, Y. Borensztein, Optical properties of silicene, Si/Ag(111), and Si/Ag (110), Phys. Rev. B 97 (2018) 195407, https://doi.org/10.1103/PhysRevB.97.195407 https://link.aps.org/doi/10.1103/PhysRevB.97.195407.

[57] G.S.L. Fabris, N.L. Marana, E. Longo, J.R. Sambrano, Porous silicene and silicon graphenylene-like surfaces: a DFT study, Theor. Chem. Accounts 137 (1) (2018) 13, https://doi.org/10.1007/s00214-017-2188-6.

[58] Y. Li, H.B. Zhu, G.Q. Wang, Y.Z. Peng, J.R. Xu, Z.H. Qian, R. Bai, G.H. Zhou, C. Yesilyurt, Z.B. Siu, M.B.A. Jalil, Strain-controlled valley and spin separation in silicene heterojunctions, Phys. Rev. B 97 (2018) 085427, https://doi.org/10.1103/PhysRevB.97.085427 https://link.aps.org/doi/10.1103/PhysRevB.97.085427.

[59] H. Li, Y. Cui, T. Wang, H. Luo, The band alignments modulation of g-MoTe2/WTe2 van der Waals heterostructures, Applied Physics A 125 (2) (2019) 147, https://doi.

org/10.1007/s00339-019-2458-3.
[60] N. Li, J. Zhang, Y. Xue, T. Zhou, Z. Yang, Large valley polarization in monolayer MoTe2 on a magnetic substrate, Phys. Chem. Chem. Phys. 20 (2018) 3805–3812, https://doi.org/10.1039/C7CP07610J.
[61] Y. Ding, Y. Wang, J. Ni, L. Shi, S. Shi, W. Tang, First principles study of structural, vibrational and electronic properties of graphene-like MX2 (M = Mo, Nb, W, Ta; X = S, Se, Te) monolayers, Phys. B Condens. Matter 406 (11) (2011) 2254–2260, https://doi.org/10.1016/j.physb.2011.03.044 http://www.sciencedirect.com/science/article/pii/S0921452611002651.
[62] A. Ramasubramaniam, Large excitonic effects in monolayers of molybdenum and tungsten dichalcogenides, Phys. Rev. B 86 (2012) 115409, https://doi.org/10.1103/PhysRevB.86.115409 https://link.aps.org/doi/10.1103/PhysRevB.86.115409.
[63] P. Johari, V.B. Shenoy, Tuning the electronic properties of semiconducting transition metal dichalcogenides by applying mechanical strains, ACS Nano 6 (6) (2012) 5449–5456, https://doi.org/10.1021/nn301320r pMID: 22591011.
[64] D. Lloyd, X. Liu, J.W. Christopher, L. Cantley, A. Wadehra, B.L. Kim, B.B. Goldberg, A.K. Swan, J.S. Bunch, Band gap engineering with ultralarge biaxial strains in suspended monolayer MoS2, Nano Lett. 16 (9) (2016) 5836–5841, https://doi.org/10.1021/acs.nanolett.6b02615 pMID: 27509768.
[65] S. Oh, H.J. Choi, Orbital angular momentum analysis for giant spin splitting in solids and nanostructures, Sci. Rep. 7 (1) (2017) 2024, https://doi.org/10.1038/s41598-017-02032-4.
[66] M.J. Szary, B. Pieczyrak, L. Jurczyszyn, M.W. Radny, Suppressed and enhanced spin polarization in the 1ML-Pb/Ge(111)-11 system, Appl. Surf. Sci. 466 (2019) 224–229, https://doi.org/10.1016/j.apsusc.2018.10.028 http://www.sciencedirect.com/science/article/pii/S0169433218327247.
[67] M.J. Szary, Role of coupling between surface orbitals in SOC enhanced spin splitting, Surf. Sci. 684 (2019) 12–17, https://doi.org/10.1016/j.susc.2019.02.004 http://www.sciencedirect.com/science/article/pii/S0039602818309646.

Oświadczenia współautorów

Wrocław, dn. 15.04.2021

dr Barbara Pieczyrak
Uniwersytet Wrocławski
Instytut Fizyki Doświadczalnej

Oświadczenie współautora

dotyczy pracy doktorskiej mgr Macieja Szarego

Oświadczam, że w ramach współpracy naukowej opublikowałam z mgr M. Szarym następujące prace:

P1 Barbara Pieczyrak, Maciej J. Szary, Leszek Jurczyszyn, and Marian W. Radny, "Spin polarization of two-dimensional electronic gas decoupled from structural asymmetry environment", Physical Review B 93, 195318 (2016)

P2 Maciej J. Szary, Barbara Pieczyrak, Leszek Jurczyszyn, Marian W. Radny, "Suppressed and enhanced spin polarization in the 1ML-Pb/Ge(111)-1 × 1 system", Applied Surface Science 466 224–229 (2019)

W pracy P1 mój wkład polegał na wykonaniu obliczeń DFT, współudziale w opracowaniu i interpretacji wyników pomiarów oraz pisaniu manuskryptu. W pracy P2 mój wkład polegał na wykonaniu części obliczeń DFT, współudziale w opracowaniu i interpretacji wyników pomiarów.

B. Pieczyrak
dr Barbara Pieczyrak

prof. dr hab. Leszek Jurczyszyn
Uniwersytet Wrocławski
Instytut Fizyki Doświadczalnej

Wrocław, dn. 21.04.2021

Oświadczenie współautora

dotyczy pracy doktorskiej mgr Macieja Szarego

Oświadczam, że w ramach współpracy naukowej opublikowałem z mgr M. Szarym następujące prace:

P1 Barbara Pieczyrak, Maciej J. Szary, Leszek Jurczyszyn, and Marian W. Radny, "Spin polarization of two-dimensional electronic gas decoupled from structural asymmetry environment", Physical Review B 93, 195318 (2016)

P2 Maciej J. Szary, Barbara Pieczyrak, Leszek Jurczyszyn, Marian W. Radny, "Suppressed and enhanced spin polarization in the 1ML-Pb/Ge(111)-1 × 1 system", Applied Surface Science 466 224–229 (2019)

W pracy P1 mój wkład polegał na współudziale w opracowaniu i interpretacji wyników obliczeń oraz przygotowaniu manuskryptu. W przypadku pracy P2 brałem udział w interpretacji otrzymanych wyników.

prof. dr hab. Leszek Jurczyszyn

Marek Michalewicz, PhD
Dyrektor
Interdysciplinarne Centrum Modelowania
Matematycznego i Komputerowego,
Uniwersytet Warszawski

Warszawa, 26 kwiecień 2021

Do zainteresowanych

Oświadczam, że od września 2015 roku do czasu złożenia pracy doktorskiej przez pana Macieja Szarego pełniłem rolę opiekuna naukowego, w trakcie jego studiów doktoranckich.

Pan Maciej Szary spędził ok. pół roku na przłomie 2015/2016 w Singapurze jako stażysta naukowy w A*STAR Computational Resource Center, które prowadziłem jako dyrektor naczelny (CEO).

W okresie tym zaangażowani byliśmy w częste rozmowy na temat ciekawych układów doświadczalnych, metod teoretycznych oraz obliczeniowych. Przez cały czas współpracy starałem się podsuwać Panu Maciejowi ciekawe prace oraz dyskutować z nim metody obliczeniowe. Wynikiem pracy Pana Macieja z tamtego okresu jest artykuł:

Maciej J. Szary, ***Marek T. Michalewicz***, Marian W. Radny “Bonding and electronics of the MoTe2/Ge interface under strain”, Physical Review B 95, 205421 (2017)

Moja rola w tym zespole ograniczała się do regularnych dyskusji nad postępami pracy, efektywnym użyciem zasobow obliczeniowych, oraz tekstem i prezentacją wyników.

Cały wysiłek obliczeniowy, prezentacja wyników i większość analizy i wniosków należą do pana Macieja Szarego.

Siedziba główna ICM:
ul. Tyniecka 15/17 • 02-630 Warszawa
tel. +48 22 874 91 00 • sekretariat@icm.edu.pl

W drugiej pracy której jestem współautorem z panem Maciejem Szarym:

Maciej J. Szary, ***Marek T. Michalewicz***, Marian W. Radny “Giant spin splitting induced by a symmetry-braking van der Waals interaction”, Applied Surface Science 494 619–626 (2019)

moja rola sprowadzała się znowu do dyskusji nad systemem fizycznym i zjawiskiem, które studiowaliśmy, znaczeniem i interpretacją wyników oraz tekstem i wykresami, które w całości wykonał pan Maciej Szary.

W obu przypadkach byłem raczej bardziej doświadczonym mentorem i partnerem do ważkich dyskusji. Pan Maciej Szary jest głównym i bezsprzecznym głównym twórcą obu tych prac.

Z wyrazami szacunku,

Marek Michalewicz, MSc (LaTrobe), PhD (ANU), FAIP

Siedziba główna ICM:
ul. Tyniecka 15/17 • 02-630 Warszawa
tel. +48 22 874 91 00 • sekretariat@icm.edu.pl

Prof. dr hab. Marian W. Radny
University of Newcastle, Australia
I.C.D.G.W (de Technologie en Sciences) EU, France

Lyon, 12.05.2022

Oświadczenie współautora

dotyczące pracy doktorskiej magistra Macieja Szarego

Oświadczam, że w ramach współpracy naukowej z doktorantem, byłem współautorem następujących publikacji:

P1 Barbara Pieczyrak, Maciej J. Szary, Leszek Jurczyszyn, and **Marian W. Radny** *"Spin polarization of two-dimensional electronic gas decoupled from structural asymmetry environment"*, Physical Review B 93, 195318 (2016)

P2 Maciej J. Szary, Barbara Pieczyrak, Leszek Jurczyszyn, **Marian W. Radny** *"Suppressed and enhanced spin polarization in the 1ML-Pb/Ge(111)-1 × 1 system"*, Applied Surface Science 466 224–229 (2019)

P5 Maciej J. Szary, Marek T. Michalewicz, **Marian W. Radny** *"Giant spin splitting induced by a symmetry-braking van der Waals interaction"*, Applied Surface Science 494 619–626 (2019)

P6 Maciej J. Szary, Marek T. Michalewicz, **Marian W. Radny** *"Bonding and electronics of the $MoTe_2$/Ge interface under strain"*, Physical Review B 95, 205421 (2017)

W wymienionych publikacjach byłem inicjatorem problemu badawczego i współpomysłodawcą jego rozwiązania. Mój wkład polegał również na współudziale w interpretacji wyników, pisaniu manuskryptów i opiece merytorycznej.

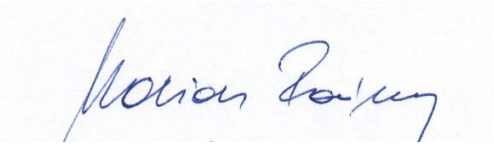

.....
prof. dr hab. Marian W. Radny

Bibliografia

[1] Rojas, J. P.; Torres Sevilla, G. A.; Ghoneim, M. T.; Inayat, S. B.; Ahmed, S. M.; Hussain, A. M.; Hussain, M. M. Transformational Silicon Electronics. *ACS Nano* **2014**, *8*, 1468–1474, PMID: 24476361.

[2] Sah Chih-Tang, Evolution of the MOS transistor-from conception to VLSI. *Proceedings of the IEEE* **1988**, *76*, 1280–1326.

[3] Arora, N. D.; Hauser, J. R.; Roulston, D. J. Electron and hole mobilities in silicon as a function of concentration and temperature. *IEEE Transactions on Electron Devices* **1982**, *29*, 292–295.

[4] Dabrowski, J.; Müssig, H.-J. *Silicon Surfaces and Formation of Interfaces*; WORLD SCIENTIFIC, 2000.

[5] Siffert, P.; Krimmel, E. F. D. Silicon : evolution and future of a technology. 2004.

[6] Hwang, C. New Paradigms in the Silicon Industry. 2006 International Electron Devices Meeting. 2006; pp 1–8.

[7] Ludwig, G. W.; Watters, R. L. Drift and Conductivity Mobility in Silicon. *Phys. Rev.* **1956**, *101*, 1699–1701.

[8] Li, S. S. The dopant density and temperature dependence of hole mobility and resistivity in boron doped silicon. *Solid-State Electronics* **1978**, *21*, 1109 – 1117.

[9] Neudeck, P. G.; Okojie, R. S.; Liang-Yu Chen, High-temperature electronics - a role for wide bandgap semiconductors? *Proceedings of the IEEE* **2002**, *90*, 1065–1076.

[10] Singh, P.; Singh, S.; Lal, M.; Husain, M. Temperature dependence of I–V characteristics and performance parameters of silicon solar cell. *Solar Energy Materials and Solar Cells* **2008**, *92*, 1611 – 1616.

[11] Perret, C.; Boussey, J.; Schaeffer, C.; Coyaud, M. Analytic modeling, optimization, and realization of cooling devices in silicon technology. *IEEE Transactions on Components and Packaging Technologies* **2000**, *23*, 665–672.

[12] Jen-Hau Cheng,; Chun-Kai Liu,; Yu-Lin Chao,; Ra-Min Tain, Cooling performance of silicon-based thermoelectric device on high power LED. ICT 2005. 24th International Conference on Thermoelectrics, 2005. 2005; pp 53–56.

[13] Chowdhury, I.; Prasher, R.; Lofgreen, K.; Chrysler, G.; Narasimhan, S.; Mahajan, R.; Koester, D.; Alley, R.; Venkatasubramanian, R. On-chip cooling by superlattice-based thin-film thermoelectrics. *Nature Nanotechnology* **2009**, *4*, 235–238.

[14] Council, N. R. *Materials for High-Temperature Semiconductor Devices*; The National Academies Press: Washington, DC, 1995.

[15] Hornberger, J.; Lostetter, A. B.; Olejniczak, K. J.; McNutt, T.; Lal, S. M.; Mantooth, A. Silicon-carbide (SiC) semiconductor power electronics for extreme high-temperature environments. 2004 IEEE Aerospace Conference Proceedings (IEEE Cat. No.04TH8720). 2004; pp 2538–2555 Vol.4.

[16] Precker, J. W.; da Silva, M. A. Experimental estimation of the band gap in silicon and germanium from the temperature–voltage curve of diode thermometers. *American Journal of Physics* **2002**, *70*, 1150–1153.

[17] Edmond, J. A.; Kong, H.-S.; Carter, C. H. Blue LEDs, UV photodiodes and high-temperature rectifiers in 6H-SiC. *Physica B: Condensed Matter* **1993**, *185*, 453–460.

[18] Nakamura, S.; Mukai, T.; Senoh, M. Candela-class high-brightness InGaN/AlGaN double-heterostructure blue-light-emitting diodes. *Applied Physics Letters* **1994**, *64*, 1687–1689.

[19] Dadgar, A.; Poschenrieder, M.; Bläsing, J.; Fehse, K.; Diez, A.; Krost, A. Thick, crack-free blue light-emitting diodes on Si(111) using low-temperature AlN interlayers and in situ SixNy masking. *Applied Physics Letters* **2002**, *80*, 3670–3672.

[20] Wolf, S. A.; Awschalom, D. D.; Buhrman, R. A.; Daughton, J. M.; von Molnár, S.; Roukes, M. L.; Chtchelkanova, A. Y.; Treger, D. M. Spintronics: A Spin-Based Electronics Vision for the Future. *Science* **2001**, *294*, 1488–1495.

[21] Žutić, I.; Fabian, J.; Das Sarma, S. Spintronics: Fundamentals and applications. *Rev. Mod. Phys.* **2004**, *76*, 323–410.

[22] Yaji, K.; Ohtsubo, Y.; Hatta, S.; Okuyama, H.; Miyamoto, K.; Okuda, T.; Kimura, A.; Namatame, H.; Taniguchi, M.; Aruga, T. Large Rashba spin splitting of a metallic surface-state band on a semiconductor surface. *Nature Communications* **2010**, *1*, 17.

[23] Kim, B.; Kim, P.; Jung, W.; Kim, Y.; Koh, Y.; Kyung, W.; Park, J.; Matsunami, M.; Kimura, S.-i.; Kim, J. S.; Han, J. H.; Kim, C. Microscopic mechanism for asymmetric charge distribution in Rashba-type surface states and the origin of the energy splitting scale. *Phys. Rev. B* **2013**, *88*, 205408.

[24] Pieczyrak, B.; Szary, M.; Jurczyszyn, L.; Radny, M. W. Spin polarization of two-dimensional electronic gas decoupled from structural asymmetry environment. *Phys. Rev. B* **2016**, *93*, 195318.

[25] Oh, S.; Choi, H. J. Orbital angular momentum analysis for giant spin splitting in solids and nanostructures. *Scientific Reports* **2017**, *7*, 2024.

[26] Szary, M. J.; Pieczyrak, B.; Jurczyszyn, L.; Radny, M. W. Suppressed and enhanced spin polarization in the 1ML-Pb/Ge(111)-1$\times$1 system. *Applied Surface Science* **2019**, *466*, 224 – 229.

[27] Szary, M. J.; Michalewicz, M. T.; Radny, M. W. Giant spin splitting induced by a symmetry-braking van der Waals interaction. *Applied Surface Science* **2019**, *494*, 619 – 626.

[28] Barke, I.; Zheng, F.; Rügheimer, T. K.; Himpsel, F. J. Experimental Evidence for Spin-Split Bands in a One-Dimensional Chain Structure. *Phys. Rev. Lett.* **2006**, *97*, 226405.

[29] Sakamoto, K.; Oda, T.; Kimura, A.; Miyamoto, K.; Tsujikawa, M.; Imai, A.; Ueno, N.; Namatame, H.; Taniguchi, M.; Eriksson, P. E. J.; Uhrberg, R. I. G. Abrupt Rotation of the Rashba Spin to the Direction Perpendicular to the Surface. *Phys. Rev. Lett.* **2009**, *102*, 096805.

[30] Gierz, I.; Suzuki, T.; Frantzeskakis, E.; Pons, S.; Ostanin, S.; Ernst, A.; Henk, J.; Grioni, M.; Kern, K.; Ast, C. R. Silicon Surface with Giant Spin Splitting. *Phys. Rev. Lett.* **2009**, *103*, 046803.

[31] Hatta, S.; Aruga, T.; Ohtsubo, Y.; Okuyama, H. Large Rashba spin splitting of surface resonance bands on semiconductor surface. *Phys. Rev. B* **2009**, *80*, 113309.

[32] Ibañez-Azpiroz, J.; Eiguren, A.; Bergara, A. Relativistic effects and fully spin-polarized Fermi surface at the Tl/Si(111) surface. *Phys. Rev. B* **2011**, *84*, 125435.

[33] Bondarenko, L. V.; Gruznev, D. V.; Yakovlev, A. A.; Tupchaya, A. Y.; Usachov, D.; Vilkov, O.; Fedorov, A.; Vyalikh, D. V.; Eremeev, S. V.; Chulkov, E. V.; Zotov, A. V.; Saranin, A. A. Large spin splitting of metallic surface-state bands at adsorbate-modified gold/silicon surfaces. **2013**, *3*, 1826 EP –, Article.

[34] Yakovkin, I.; Petrova, N. DFT study of Sb and Pb layers on the Bi(111) surface. *Applied Surface Science* **2018**, *445*, 154 – 160.

[35] Kopciuszynski, M.; Krawiec, M.; Zdyb, R.; Jalochowski, M. Purely one-dimensional bands with a giant spin-orbit splitting: Pb nanoribbons on Si(553) surface. *Scientific Reports* **2017**, *7*, 46215 EP –, Article.

[36] Aruga, T. Different types of Rashba spin-split surface states on Ge(111). *Journal of Electron Spectroscopy and Related Phenomena* **2015**, *201*, 74 – 80, Special issue on electron spectroscopy for Rashba spin-orbit interaction.

[37] Bychkov, Y. A.; Rashba, É. I. Properties of a 2D electron gas with lifted spectral degeneracy. *Soviet Journal of Experimental and Theoretical Physics Letters* **1984**, *39*, 78.

[38] LaShell, S.; McDougall, B. A.; Jensen, E. Spin Splitting of an Au(111) Surface State Band Observed with Angle Resolved Photoelectron Spectroscopy. *Phys. Rev. Lett.* **1996**, *77*, 3419–3422.

[39] Ast, C. R.; Höchst, H. Fermi Surface of Bi(111) Measured by Photoemission Spectroscopy. *Phys. Rev. Lett.* **2001**, *87*, 177602.

[40] Koroteev, Y. M.; Bihlmayer, G.; Gayone, J. E.; Chulkov, E. V.; Blügel, S.; Echenique, P. M.; Hofmann, P. Strong Spin-Orbit Splitting on Bi Surfaces. *Phys. Rev. Lett.* **2004**,

93, 046403.

[41] Ast, C. R.; Henk, J.; Ernst, A.; Moreschini, L.; Falub, M. C.; Pacilé, D.; Bruno, P.; Kern, K.; Grioni, M. Giant Spin Splitting through Surface Alloying. *Phys. Rev. Lett.* **2007**, *98*, 186807.

[42] Hasan, M. Z.; Kane, C. L. Colloquium: Topological insulators. *Rev. Mod. Phys.* **2010**, *82*, 3045–3067.

[43] Nitta, J.; Akazaki, T.; Takayanagi, H.; Enoki, T. Gate Control of Spin-Orbit Interaction in an Inverted $In_{0.53}Ga_{0.47}As/In_{0.52}Al_{0.48}As$ Heterostructure. *Phys. Rev. Lett.* **1997**, *78*, 1335–1338.

[44] Nagano, M.; Kodama, A.; Shishidou, T.; Oguchi, T. A first-principles study on the Rashba effect in surface systems. *Journal of Physics: Condensed Matter* **2009**, *21*, 064239.

[45] Premper, J.; Trautmann, M.; Henk, J.; Bruno, P. Spin-orbit splitting in an anisotropic two-dimensional electron gas. *Phys. Rev. B* **2007**, *76*, 073310.

[46] Frantzeskakis, E.; Pons, S.; Grioni, M. Band structure scenario for the giant spin-orbit splitting observed at the Bi/Si(111) interface. *Phys. Rev. B* **2010**, *82*, 085440.

[47] Park, S. R.; Kim, C. H.; Yu, J.; Han, J. H.; Kim, C. Orbital-Angular-Momentum Based Origin of Rashba-Type Surface Band Splitting. *Phys. Rev. Lett.* **2011**, *107*, 156803.

[48] Kim, B.; Kim, C. H.; Kim, P.; Jung, W.; Kim, Y.; Koh, Y.; Arita, M.; Shimada, K.; Namatame, H.; Taniguchi, M.; Yu, J.; Kim, C. Spin and orbital angular momentum structure of Cu(111) and Au(111) surface states. *Phys. Rev. B* **2012**, *85*, 195402.

[49] Li, X.; Dai, Y.; Niu, C.; Ma, Y.; Wei, W.; Huang, B. $MoTe_2$ is a good match for GeI by preserving quantum spin Hall phase. *Nano Research* **2017**, *10*, 2823–2832.

[50] Chen, X.; Meng, R.; Jiang, J.; Liang, Q.; Yang, Q.; Tan, C.; Sun, X.; Zhang, S.; Ren, T. Electronic structure and optical properties of graphene/stanene heterobilayer. *Phys. Chem. Chem. Phys.* **2016**, *18*, 16302–16309.

[51] Shim, J.; Kang, D.-H.; Kim, Y.; Kum, H.; Kong, W.; Bae, S.-H.; Almansouri, I.; Lee, K.; Park, J.-H.; Kim, J. Recent progress in Van der Waals (vdW) heterojunction-based electronic and optoelectronic devices. *Carbon* **2018**, *133*, 78 – 89.

[52] Kim, K. K.; Lee, H. S.; Lee, Y. H. Synthesis of hexagonal boron nitride heterostructures for 2D van der Waals electronics. *Chem. Soc. Rev.* **2018**, *47*, 6342–6369.

[53] Li, Q.; Yang, J.; Quhe, R.; Zhang, Q.; Xu, L.; Pan, Y.; Lei, M.; Lu, J. Ohmic contacts between monolayer WSe2 and two-dimensional titanium carbides. *Carbon* **2018**, *135*, 125 – 133.

[54] Pang, J.; Mendes, R. G.; Bachmatiuk, A.; Zhao, L.; Ta, H. Q.; Gemming, T.; Liu, H.; Liu, Z.; Rummeli, M. H. Applications of 2D MXenes in energy conversion and storage systems. *Chem. Soc. Rev.* **2019**, *48*, 72–133.

[55] Gong, X.; Zhao, X.; Pam, M. E.; Yao, H.; Li, Z.; Geng, D.; Pennycook, S. J.; Shi, Y.; Yang, H. Y. Location-selective growth of two-dimensional metallic/semiconducting transition metal dichalcogenide heterostructures. *Nanoscale* **2019**, *11*, 4183–4189.

[56] Liu, X.; Li, Z. Electric Field and Strain Effect on Graphene-MoS_2 Hybrid Structure: Ab Initio Calculations. *The Journal of Physical Chemistry Letters* **2015**, *6*, 3269–3275.

[57] shi Li, S.; wen Zhang, C.; xiao Ji, W. Novel electronic properties in silicene on MoSe2 monolayer: An excellent prediction for FET. *Materials Chemistry and Physics* **2015**, *164*, 150 – 156.

[58] Li, H.; Yu, Y.; Xue, X.; Xie, J.; Si, H.; Lee, J. Y.; Fu, A. Electroic and optical properties of germanene/MoS_2 heterobilayers: first principles study. *Journal of Molecular Modeling* **2018**, *24*, 333.

[59] Peng, Q.; Si, C.; Zhou, J.; Sun, Z. Modulating the Schottky barriers in MoS_2/MXenes heterostructures via surface functionalization and electric field. *Applied Surface Science* **2019**, *480*, 199 – 204.

[60] Molle, A.; Lamperti, A.; Rotta, D.; Fanciulli, M.; Cinquanta, E.; Grazianetti, C. Electron Confinement at the Si/MoS_2 Heterosheet Interface. *Advanced Materials Interfaces* **2016**, *3*, 1500619.

[61] Scalise, E.; Iordanidou, K.; Afanas'ev, V. V.; Stesmans, A.; Houssa, M. Silicene on non-metallic substrates: Recent theoretical and experimental advances. *Nano Research* **2018**, *11*, 1169–1182.

[62] Liu, B.; Chen, Y.; You, C.; Liu, Y.; Kong, X.; Li, J.; Li, S.; Deng, W.; Li, Y.; Yan, H.; Zhang, Y. High performance photodetector based on graphene/MoS_2/graphene lateral heterostrurcture with Schottky junctions. *Journal of Alloys and Compounds* **2019**, *779*, 140 – 146.

[63] Li, X.; Wu, S.; Zhou, S.; Zhu, Z. Structural and electronic properties of germanene/MoS_2 monolayer and silicene/MoS_2 monolayer superlattices. *Nanoscale Research Letters* **2014**, *9*, 110.

[64] Giannozzi, P. et al. QUANTUM ESPRESSO: a modular and open-source software project for quantum simulations of materials. *Journal of Physics: Condensed Matter* **2009**, *21*, 395502.

[65] Giannozzi, P. et al. Advanced capabilities for materials modelling with QUANTUM ESPRESSO. *Journal of Physics: Condensed Matter* **2017**, *29*, 465901.

[66] Blöchl, P. E. Projector augmented-wave method. *Phys. Rev. B* **1994**, *50*, 17953.

[67] Kresse, G.; Joubert, D. From ultrasoft pseudopotentials to the projector augmented-wave method. *Phys. Rev. B* **1999**, *59*, 1758.

[68] Vanderbilt, D. Soft self-consistent pseudopotentials in a generalized eigenvalue formalism. *Phys. Rev. B* **1990**, *41*, 7892–7895.

[69] Troullier, N.; Martins, J. L. Efficient pseudopotentials for plane-wave calculations. *Phys. Rev. B* **1991**, *43*, 1993–2006.

[70] Perdew, J. P.; Zunger, A. Self-interaction correction to density-functional approximations for many-electron systems. *Phys. Rev. B* **1981**, *23*, 5048–5079.

[71] Perdew, J. P.; Burke, K.; Ernzerhof, M. Generalized Gradient Approximation Made Simple. *Phys. Rev. Lett.* **1996**, *77*, 3865.

[72] Perdew, J. P.; Ruzsinszky, A.; Csonka, G. I.; Vydrov, O. A.; Scuseria, G. E.; Constantin, L. A.; Zhou, X.; Burke, K. Restoring the Density-Gradient Expansion for Exchange in Solids and Surfaces. *Phys. Rev. Lett.* **2008**, *100*, 136406.

[73] Heyd, J.; Scuseria, G. E.; Ernzerhof, M. Hybrid functionals based on a screened Coulomb potential. *The Journal of Chemical Physics* **2003**, *118*, 8207–8215.

[74] Grimme, S. Semiempirical GGA-type density functional constructed with a long-range dispersion correction. *Journal of Computational Chemistry* **2006**, *27*, 1787–1799.

[75] Barone, V.; Casarin, M.; Forrer, D.; Pavone, M.; Sambi, M.; Vittadini, A. Role and effective treatment of dispersive forces in materials: Polyethylene and graphite crystals as test cases. *Journal of Computational Chemistry* **2009**, *30*, 934.

[76] Grimme, S.; Antony, J.; Ehrlich, S.; Krieg, H. A consistent and accurate ab initio parametrization of density functional dispersion correction (DFT-D) for the 94 elements H-Pu. *The Journal of Chemical Physics* **2010**, *132*, 154104.

[77] Tkatchenko, A.; Scheffler, M. Accurate Molecular Van Der Waals Interactions from Ground-State Electron Density and Free-Atom Reference Data. *Phys. Rev. Lett.* **2009**, *102*, 073005.

[78] Becke, A. D.; Johnson, E. R. Exchange-hole dipole moment and the dispersion interaction revisited. *The Journal of Chemical Physics* **2007**, *127*, 154108.

[79] Otero-de-la Roza, A.; Johnson, E. R. Van der Waals interactions in solids using the exchange-hole dipole moment model. *The Journal of Chemical Physics* **2012**, *136*, 174109.

[80] Monkhorst, H. J.; Pack, J. D. Special points for Brillouin-zone integrations. *Phys. Rev. B* **1976**, *13*, 5188–5192.

[81] Sohier, T.; Calandra, M.; Mauri, F. Density functional perturbation theory for gated two-dimensional heterostructures: Theoretical developments and application to flexural phonons in graphene. *Phys. Rev. B* **2017**, *96*, 075448.

[82] Johari, P.; Shenoy, V. B. Tuning the Electronic Properties of Semiconducting Transition Metal Dichalcogenides by Applying Mechanical Strains. *ACS Nano* **2012**, *6*, 5449–5456, PMID: 22591011.